

# A Complete Study of Radio Galaxies at $z \sim 0.5$

Peter David Herbert

School of Physics, Astronomy & Mathematics

Submitted to the  
University of Hertfordshire  
in partial fulfilment of the requirements  
of the degree of  
Doctor of Philosophy  
October 2011



## Abstract

In this thesis I investigate the hosts and cluster environments of a sample of 41 radio galaxies between  $z = 0.4$  and  $z = 0.6$ . I use spectroscopic data for a 24 object subsample to investigate their star formation histories via the strength of the  $4000\text{\AA}$  break. I find that the higher radio luminosity or high excitation objects in the sample have evidence for young stellar populations, but the lower radio luminosity or low excitation objects do not.

My investigations into the Fundamental Plane (FP) of 18 of the radio galaxies, using the same spectroscopic data as well as data from the literature, show that the Fanaroff-Riley type I objects (FRIs) lie on the FP of local radio galaxies once corrected for passive evolution but the Fanaroff-Riley type II objects (FRIIs) do not. I suggest that an evolution in the size of the host galaxies, aided by a combination of passive evolution and a mass-dependent evolution in the mass-to-light ratios, may explain the observed offsets.

Finally, I use wide field multi-band imaging to investigate the cluster environments of the full  $z \sim 0.5$  sample. I find that the environmental overdensity is positively correlated with the radio luminosity and observe a greater number of close companions around the FRIIs than the FRIs (albeit with only nine FRIs in the sample). The cluster environments of the radio galaxies with the greatest host luminosities show tentative evidence for an alignment between the major axis of a galaxy and that of its cluster, whilst there are hints that the objects with the highest radio luminosities have clusters whose major axis is aligned with the position angle of the radio jet.

My results suggest a picture in which FRII type radio sources reside in particularly rich cluster environments at  $z \sim 0.5$  but FRI type radio sources in less rich environments. The environment plays a key role in determining both the radio properties of the galaxy and the evolution of its host. The effect of the environment on the emission line properties and star formation histories of the galaxies leads to the overlap seen in the morphological and spectral properties of radio galaxies.



# Acknowledgements

Thanks are first and foremost due to my supervisor, Matt Jarvis, who has patiently guided, helped, taught and encouraged me with a commitment beyond what I could have expected.

I also thank those who have made a particular contribution to the work described here: Dan Smith and Dave Bonfield for their instruction on the observing trips; to Eduardo Gonzalez-Solares for his help with the CASU INT pipeline; and to Jon Davies for his proof-reading at the end. I am also grateful to the Centre for Astrophysics Research for supporting me in attending various conferences.

Thank you to all those who have encouraged me along the way: to all at the University of Hertfordshire who have made the Centre for Astrophysics Research such a friendly and supportive place in which to study; to friends at St Andrew the Great, St Matthew's and Oak Hill College; and of course to my Mum and Dad and to my siblings, Steven and Elizabeth, for their unstinting support and encouragement.

Finally, special thanks are reserved for my wife, Caroline, who has been the most wonderful tower of strength, ready to assist wherever she could, and patiently persevering throughout. Thank you.



# Contents

<b>Abstract</b>	<b>i</b>
<b>Acknowledgements</b>	<b>iii</b>
<b>Contents</b>	<b>v</b>
<b>1 Introduction</b>	<b>1</b>
1.1 Active Galactic Nuclei . . . . .	1
1.2 Unification of AGNs . . . . .	7
1.2.1 The Orientation-based Unification Scheme . . . . .	7
1.2.2 The Receding Torus Model . . . . .	10
1.2.3 Evolutionary Unification . . . . .	12
1.3 Classification of Radio Galaxies . . . . .	14
1.4 The Evolution of AGNs . . . . .	18
1.5 Host Galaxies of AGNs . . . . .	19
1.5.1 Star Formation Histories of AGNs . . . . .	20
1.5.2 The Fundamental Plane . . . . .	22
1.6 Environments of AGNs . . . . .	27
1.6.1 Environmental Densities . . . . .	27
1.6.2 Alignment Effects . . . . .	29

---

1.7	AGN-driven Feedback . . . . .	31
1.8	This Thesis . . . . .	33
<b>2</b>	<b>GMOS Spectroscopy</b>	<b>39</b>
2.1	Observations . . . . .	39
2.2	Data Reduction . . . . .	42
2.2.1	Flatfielding, Bias Subtraction & Cosmic Ray Removal . . . . .	42
2.2.2	Wavelength Calibration . . . . .	46
2.2.3	Background Subtraction . . . . .	47
2.2.4	De-fringing and Frame Combination . . . . .	48
2.2.5	Flux Calibration . . . . .	49
2.2.6	Aperture Extraction . . . . .	50
2.2.7	Spectrum Combination and Noise . . . . .	51
2.3	WHT Observations & Data Reduction . . . . .	54
2.4	Summary . . . . .	56
<b>3</b>	<b>Star Formation Histories</b>	<b>65</b>
3.1	Spectroscopic Data . . . . .	65
3.2	Analysis . . . . .	66
3.2.1	4000Å Break Strength . . . . .	66
3.2.2	Spectral and Morphological Classifications . . . . .	68
3.3	Discussion . . . . .	70
3.3.1	$D_n(4000)$ versus Radio Luminosity . . . . .	70
3.3.2	$D_n(4000)$ versus Emission-line Classification . . . . .	73
3.3.3	Contamination by Scattered Quasar Light? . . . . .	75
3.4	Conclusions . . . . .	78

---

---

<b>4</b>	<b>The Fundamental Plane</b>	<b>81</b>
4.1	The ZP5 Sub-sample . . . . .	82
4.2	Spectral Fitting . . . . .	85
4.2.1	The Fitting Procedure . . . . .	85
4.2.2	Aperture Correction . . . . .	91
4.2.3	Resolution Tests & Fitting Corrections . . . . .	91
4.3	Fundamental Plane Fitting . . . . .	92
4.3.1	Initial Plane Fitting . . . . .	92
4.3.2	Monte Carlo Simulations . . . . .	95
4.3.3	Local Plane Fitting . . . . .	96
4.4	Discussion . . . . .	98
4.4.1	The Local Fundamental Plane . . . . .	98
4.4.2	The ZP5 Fundamental Plane . . . . .	100
4.4.3	Evolution of the Host Galaxies? . . . . .	103
4.4.4	A Link with Recent Star Formation? . . . . .	109
4.4.5	Correlations with Radio Luminosity . . . . .	110
4.5	Conclusions . . . . .	113
<b>5</b>	<b>Imaging Data</b>	<b>117</b>
5.1	INT Observations . . . . .	117
5.2	INT Data Reduction . . . . .	118
5.2.1	Further Photometric Calibrations . . . . .	123
5.3	Data Processing . . . . .	124
5.3.1	Source Extraction . . . . .	124
5.3.2	Completeness . . . . .	126
5.4	Summary . . . . .	127

---

<b>6</b>	<b>The Radio Galaxy Environments</b>	<b>133</b>
6.1	Environmental Densities . . . . .	134
6.1.1	INT Wide Field Imaging Data . . . . .	134
6.1.2	Colour Selection . . . . .	134
6.1.3	Background Density . . . . .	135
6.2	Annular Overdensities . . . . .	137
6.2.1	Overdensity and Radio Luminosity . . . . .	138
6.2.2	Overdensity and Host Magnitude . . . . .	148
6.2.3	Overdensity and Radio Morphology . . . . .	154
6.2.4	Overdensity and Spectral Classification . . . . .	156
6.3	An Alternative Overdensity Measurement . . . . .	157
6.3.1	Calculating $B_{gq}$ . . . . .	158
6.3.2	$B_{gq}$ and Radio Luminosity . . . . .	162
6.3.3	$B_{gq}$ and Host Magnitude . . . . .	166
6.4	Overdensities and Radio Jet Position Angle . . . . .	169
6.5	Overdensities and Host Position Angle . . . . .	173
6.6	Conclusions . . . . .	175
<b>7</b>	<b>Conclusions</b>	<b>177</b>
7.1	Host Galaxies . . . . .	177
7.2	Environments . . . . .	179
7.3	Radio Galaxies, Hosts & Environments . . . . .	180
7.4	Future Work . . . . .	181
	<b>Bibliography</b>	<b>185</b>
<b>A</b>	<b>WHT Spectra</b>	<b>199</b>

---

# Chapter 1

## Introduction

### 1.1 Active Galactic Nuclei

Active Galactic Nuclei (AGNs) are the most powerful objects yet discovered in the universe. They are believed, in essence, to be supermassive black holes (of mass  $10^7$ – $10^{10}$  solar masses,  $M_{\odot}$ ), the immediate environments of which are exceedingly luminous. It is believed that, in the majority of AGNs, this central supermassive black hole is surrounded by a hot accretion disc which emits the majority of the continuum emission (see Section 1.2). However, it is now thought that in some AGNs the accretion onto the central supermassive black hole proceeds via an alternative and less efficient mechanism, and therefore the hot accretion disc may not represent the full picture for all AGNs (see Section 1.3).

The first observation of an AGN was made in 1908 by E. A. Fath, who found strong emission lines in his spectrum of NGC 1086. The next notable contribution to the field was made by Carl Seyfert (1943), who observed a group of spiral galaxies which contained unusually bright, point-like, nuclei. He discovered that several of them were dominated by high-excitation emission lines. Another wartime discovery was that of the first known radio galaxy, Cygnus A, which was discovered accidentally by radar engineers.

The following decades saw the rise of radio astronomy, including the third Cambridge radio catalogue (3C; Edge et al. 1959) and the discovery of quasars, whose optical counterparts initially appeared to be point-like but with unusual emission spectra (Matthews & Sandage 1963). Schmidt (1963) realised that the similar spectrum of 3C273 contained familiar emission lines (including the hydrogen Balmer series) redshifted to  $z = 0.158$ , leading to the identification of the lines in the star-like optical counterparts of other such quasi-stellar objects (quasars).

Today, AGNs are typically divided into six main classes: quasars, radio galaxies, obscured quasars, Seyfert galaxies, LINERs and blazars. I briefly describe below the main observed characteristics of each and in Section 1.2 I describe how the observed properties of these objects fit into a ‘unified scheme’. Further detail concerning radio galaxies (which are the main focus of this thesis) is given in Section 1.3.

## Quasars

Quasars comprise the most optically luminous class of AGNs, and are generally hosted by massive elliptical galaxies with scalelengths of  $\sim 10$  kpc (e.g. McLure et al. 1999). The majority of the light originates in the nucleus, which outshines the entire host galaxy. The spectrum extends from the radio through to  $\gamma$ -rays, peaking at blue wavelengths, and contains prominent broad ( $\sim 5000\text{kms}^{-1}$ ) permitted lines as well as weaker narrow ( $\lesssim 1000\text{kms}^{-1}$ ) forbidden lines. Variability is observed across the spectrum of many quasars, on timescales of months down to days. Quasars are subdivided, based on their radio luminosity, into radio-loud quasars (RLQs) and radio-quiet quasars (RQQs). Observationally it is found that there are 10 to 20 times the number of RQQs as RLQs (e.g. Goldschmidt et al. 1999; Dunlop et al. 2003), but otherwise their properties appear to be the same. There have been suggestions that RLQs are found preferentially in elliptical or interacting host galaxies whereas RQQs tend to inhabit ellipticals or spirals (e.g. Bahcall

---

et al. 1997), but the relationship between radio luminosity and host galaxy is far from clear.

## **Radio Galaxies**

Radio galaxies are AGNs hosted by luminous elliptical galaxies (e.g. Best, Longair & Röttgering 1998; McLure et al. 1999) and marked out by their radio emission. In many respects they are similar to the RLQs described above but with no evidence of a bright nuclear point source. Most do not show evidence of broad lines either, although there exists a population of broad-line radio galaxies that do (and which thus appear to form a class intermediate between RLQs and the majority of radio galaxies). The spectra of these broad-line radio galaxies contain broad permitted lines as well as narrow forbidden and permitted lines whereas the spectra of (the more common) narrow-line radio galaxies only contain narrow lines. Radio galaxies may contain a radio core, and may also display lobes, jets and hotspots at radio wavelengths. The radio core is a compact region associated with the nucleus and with a flat radio spectrum which arises due to the superposition of relativistic optically thick synchrotron spectra (e.g. Scheuer 1987). The lobes are a radio galaxy's largest feature (sometimes extending to a Mpc scale) and emit optically thin synchrotron radiation. X-ray observations have shown large cavities in the inter-galactic medium (IGM), filled by the radio lobes and with associated shock fronts. This suggests that the IGM is being displaced by the radio source as the lobes expand (e.g. McNamara et al. 2005; McNamara & Nulsen 2007). Hotspots are bright and compact regions within lobes which have steep radio spectra. The jets link the core to the lobes.

## **Obscured Quasars**

In addition to the quasars described above, there also exists a population of obscured quasars (e.g. Norman et al. 2002; Zakamska et al. 2003). Obscured quasars do not exhibit

---

the blue continua or broad lines seen in unobscured quasars, and nor do they outshine their host galaxies in optical or ultraviolet (UV) radiation. They therefore resemble normal, inactive galaxies in optical imaging surveys (Martínez-Sansigre et al. 2006) and due to this fact were until recently very difficult to discover. Most studies concentrated on using X-ray observations to select hard-spectrum sources, i.e. those with an excess of emission at higher energies (e.g. Almaini et al. 1995; Ohta et al. 1996; Akiyama et al. 2002). However, the arrival of the *Spitzer Space Telescope* opened up the field since an obscured quasar would by definition heat up the dust that is obscuring it and this dust would then emit thermal radiation at a wavelength dictated by the dust temperature. Given that quasars emit powerfully at X-ray and UV wavelengths we would expect the dust to be relatively hot but still below the sublimation temperature of approximately 1500 K for graphite and approximately 1000 K for silicate grains (e.g. Granato et al. 1997). Furthermore, we would expect the majority of the dust in the torus of unified models (Section 1.2) to be at a lower temperature than the sublimation temperature (since we expect the outer regions of the torus to be cooler than the inner regions), and using Wien's law we find that the peak of the thermal black body radiation occurs at  $2 - 30 \mu\text{m}$  for temperatures spanning 100–1500 K. Therefore targeting objects that peak at mid-infrared wavelengths, where *Spitzer* was very sensitive, allows the identification of large samples of obscured AGN (e.g. Lacy et al. 2004; Stern et al. 2005; Martínez-Sansigre et al. 2005; Martínez-Sansigre et al. 2006; Poletta et al. 2006; Villar-Martín et al. 2011). Obscured quasars are sometimes referred to as type 2 quasars in accordance with the naming convention of Seyfert galaxies (see below).

## **Seyfert Galaxies**

Seyfert galaxies are similar to radio galaxies and to quasars, but have a lower luminosity than quasars and their radio emission is generally at a lower luminosity than the powerful

---

radio galaxies. A distinction between Seyferts and quasars is usually made on the basis of absolute nuclear B-band luminosity ( $M_B$ ), where Seyferts have  $M_B > -21.5 + 5 \log h_0$  (Schmidt & Green 1983), where  $h_0$  is the Hubble constant ( $H_0$ ) divided by 100. Seyferts tend to reside in spiral galaxies, and were originally classified on a morphological basis as galaxies with a bright nucleus. Now, however, a galaxy is classified as a Seyfert if its spectrum possesses strong, high-ionisation emission lines. Seyferts are typically divided into two groups: type 1 and type 2 (Khachikian & Weedman 1974). Examples of the spectra of each type are shown in Figure 1.1. The spectra of type 1 Seyferts contain both narrow lines and broad lines. The narrow lines (which are predominantly forbidden lines) have widths of  $\sim 400 \text{ km s}^{-1}$ , whereas the broad lines (permitted lines only) have widths of  $\lesssim 10,000 \text{ km s}^{-1}$ . Type 2 Seyferts, on the other hand, only exhibit the narrow lines in their spectra. However, these categories do not seem to be as distinct as was once thought, since some objects classified as type 2 Seyferts have now been found to possess weak broad lines. In unified models (Section 1.2) type 1 Seyferts can be associated with quasars and broad-line radio galaxies and type 2 Seyferts with narrow-line radio galaxies and obscured quasars, at lower luminosities and with no requirement for radio emission.

## LINERs

Low-ionisation nuclear emission line region galaxies (LINERs) were first identified by Heckman (1980), although there are conflicting views on whether they are actually a class of AGNs (e.g. Filippenko 1996). LINERs have spectra similar to Seyferts (e.g. Ho, Filippenko & Sargent 1997) and as defined by Heckman (1980) they are marked out by spectra dominated by low-ionization lines (e.g.  $[\text{OII}]_{3727}$ ,  $[\text{OI}]_{6300}$ ,  $[\text{NII}]_{6584}$ ,  $[\text{SII}]_{6717}$  and  $[\text{SII}]_{6731}$ ) and with relatively weak high ionization lines (e.g.  $[\text{OIII}]_{5007}$ ,  $[\text{NeIII}]_{3869}$  and  $[\text{HeII}]_{4686}$ ). In order to distinguish LINERs from Seyferts, Heckman defined a LINER as an object with  $[\text{OII}]_{3727}/[\text{OIII}]_{5007} \geq 1$  and  $[\text{OIII}]_{5007}/[\text{OI}]_{6300} \leq 3$ . In addition, the spectra

---

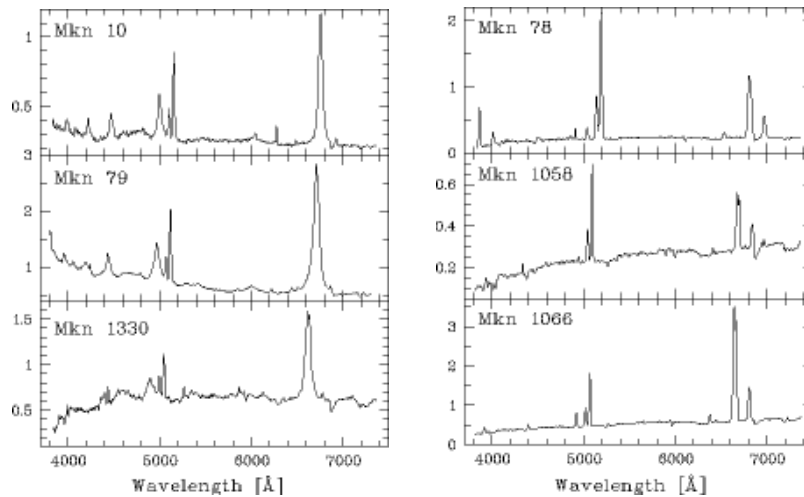


Figure 1.1: Examples of the spectra of type 1 Seyferts (left) and type 2 Seyferts (right), taken from the Astronomy & Astrophysics Supplement Series website (<http://aas.aanda.org/>). The broad lines are visible for the type 1 Seyferts, but not the type 2 Seyferts, as discussed in Section 1.1.

of LINERs do not show strong optical continua or X-ray emission (Heckman 1980, Ho 2009), and in this way are found to differ from other classes of AGNs such as quasars and Seyferts. LINERs have been found to be common in all types of local galaxies, most particularly in early-type spirals (e.g. Ho 1996) and may be either radio-loud or radio-quiet (e.g. Chiaberge, Capetti & Macchetto 2005).

## Blazars

In a similar fashion to quasars, blazars are star-like in their appearance, but are all high-luminosity radio sources, variable on timescales of days or shorter. Blazars are divided into two groups: BL Lac objects and optically violent variables (OVVs). BL Lac objects are named after BL Lacertae, the first such object studied, and have spectra with very weak or no emission lines. OVVs are similar to BL Lac objects, but have stronger broad emission lines and exhibit larger variations in optical luminosity, as well as often displaying variation in the magnitude and angle of their polarisation. They are only  $\sim 1.5 - 3$  times more powerful than BL Lac objects (Smith et al. 1987).

## 1.2 Unification of AGNs

### 1.2.1 The Orientation-based Unification Scheme

It is widely believed that the different types of AGN (Section 1.1) are not distinct objects but rather different manifestations of one underlying phenomenon. Various schemes have been proposed for the unification of AGNs, including evolutionary schemes (see Section 1.2.3). However, the current most basic and commonly accepted unification scheme is one of orientation-based unification. Here I describe this scheme, as illustrated in Figure 1.2. In this scheme, the centre of the AGN houses a supermassive black hole, typically of mass  $10^7$ – $10^{10} M_{\odot}$ . Surrounding this is a gaseous accretion disc, in which the viscosity of the gas removes angular momentum from the gas and heats it. The accretion disc is extremely hot, with an approximate temperature of  $10^5$ – $10^6$  K (e.g. Bonning et al. 2007). It is exceedingly luminous from optical to X-ray wavelengths (particularly its inner region) and is the source of the radiation which originates in the centre of the AGN.

The accretion disc is surrounded by dense, fast-moving gas clouds that make up the broad line region (BLR). Their density means only permitted emission lines are seen, whilst the high velocity (typically  $\sim 5000 \text{ km s}^{-1}$ ) gives rise to the width of the lines.

Beyond the central engine of the AGN there is a dusty torus composed, it is thought, of graphite particles in view of the observed temperatures of 100–1500 K (see Section 1.1). The dust in the torus absorbs UV and X-ray radiation from the central engine and re-emits it in the infrared. The toroidal shape of this component is important since it permits a view of the central engine to some observers but not to others, depending on their viewing angle, which is key for the orientation-based unification model (Figure 1.2).

Beyond the torus (and thus visible to all observers) is the narrow line region (NLR), comprised of slower moving ( $200$ – $900 \text{ km s}^{-1}$ ) gas clouds with a lower density than those in the BLR. This lower density means that both permitted and forbidden emission lines

---

are seen in the spectra from these regions.

The final components in this unified picture of AGNs are the radio structures, which appear in some AGNs but not in others. The question of why some AGNs are radio-loud whilst others are not is, as yet, unresolved. Where they do occur, it is believed that radio jets originate very close to the central black hole, where infalling material is ejected along the axis of rotation at relativistic speeds by some as yet unknown mechanism. In some examples of radio-loud AGNs we only observe one jet. However, it is believed that two jets are actually present, but only one is visible due to the effects of relativistic beaming.

In this picture, the type of AGN observed is primarily governed by the viewing angle of the observer, as illustrated in Figure 1.2. The transition between type 1 and type 2 AGNs appears to take place at a viewing angle of  $\sim 45^\circ$  to the axis of rotation (Barthel 1989; Simpson 1998), although evidence exists for a luminosity-dependent variation in the opening angle as incorporated in the ‘receding torus model’ (see Section 1.2.2). However, in the radio-quiet case of the simple unification picture (the bottom half of Figure 1.2), an observer whose line of sight is approaching  $90^\circ$  to the axis of rotation will see the NLR but not the radiation direct from the accretion disc or the BLR (because of the obscuring torus). They will thus observe a type 2 Seyfert galaxy or an obscured quasar, depending on the luminosity. On the other hand, an observer whose line of sight is approaching  $0^\circ$  to the axis of rotation will see the BLR and the emission from the central engine as well as the NLR, and thus observe a type 1 Seyfert or a RQQ. The primary difference between Seyferts and RQQs appears to be one of luminosity (as discussed in Section 1.1).

In the radio-loud case (the top half of Figure 1.2) we see a similar pattern. An observer whose line of sight is approaching  $90^\circ$  to the axis of rotation will again see the NLR but not the BLR or the direct emission from the accretion disc and thus observe a narrow-line radio galaxy. An observer whose line of sight is close to  $0^\circ$  to the axis of rotation can see

---

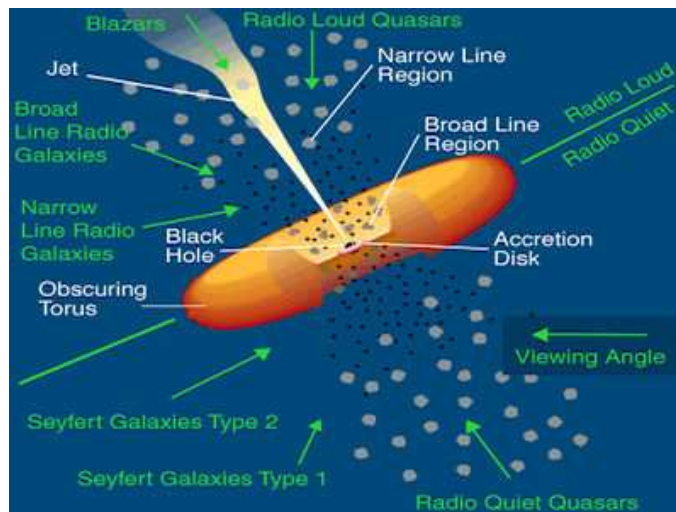


Figure 1.2: An illustration of the orientation-based unification scheme for AGNs (Section 1.2). The image is taken from the Scholarpedia website (<http://www.scholarpedia.org>).

the BLR, the NLR and the intense radiation from the central engine and thus observes a RLQ. Between these two regimes lies another regime, where the viewing angle permits a view of both the NLR and BLR but not the radiation from the central engine, and thus a broad-line radio galaxy is observed. In the extreme case, when an observer is looking straight down the axis of the radio jet, a blazar is observed. In the case of less powerful radio galaxies a BL Lac is seen.

Over recent years there has been an accumulation of evidence to support the unified scheme described here. The strongest evidence is the discovery of polarised broad lines in type 2 Seyfert galaxies (Antonucci & Miller 1985), which suggests that the BLR is present in both type 1 and type 2 Seyferts, but only directly visible in type 1 objects. In type 2 Seyferts the BLR is obscured, but reflected (and hence polarised) broad lines from the BLR are observed. McLure et al. (1999), followed by Dunlop et al. (2003) with a larger sample, found that the host galaxies of RQQs, RLQs and radio galaxies are all massive elliptical galaxies with scalelengths of  $\sim 10$  kpc. The presence of a supermassive black hole at the centre of AGNs is suggested by a combination of the minimum mass (derived from Eddington-limited accretion rates) and the maximum size (indicated by the

variability timescale and the light travel time). However, despite the evidence in support of this unified scheme, evidence also exists which suggests that the picture is more complicated than the basic one presented here. For example, it is thought that low excitation galaxies (LEGs) lack BLRs, obscuring tori and radiatively efficient accretion discs (e.g. Chiaberge, Capetti & Celotti 2002; Whysong & Antonucci 2004; Hardcastle, Evans & Croston 2006; Hardcastle, Evans & Croston 2009; see Section 1.3). They therefore do not fit the picture of AGN unification presented here. I therefore now turn to more sophisticated unification schemes.

### 1.2.2 The Receding Torus Model

Whilst the traditional unified scheme described above (Section 1.2.1) provides a good description of most of the observed properties of AGNs, attempts have been made over the past decades to explain some of the more subtle properties of AGNs. This has involved modifications to the simple orientation picture. One of the most popular of these is the so-called ‘receding torus model,’ first suggested by Lawrence (1991).

This model arises from the observation that the spectral energy distributions of quasars at wavelengths longer than  $1\mu\text{m}$  appear almost identical (e.g. Elvis et al. 1994). This consistency of spectral shapes into the near-infrared waveband implies that the location of the inner surface of the dusty torus (see Figure 1.2) is determined by the distance at which dust can survive without sublimating due to the heat emitted from the accretion disc. This idea is underscored by time-delay experiments in the optical and near-infrared wavebands (e.g. Clavel, Wamsteker & Glass 1989), where more luminous objects exhibit longer time delays between the optical and the near-infrared continua. The result of a receding torus model is that more luminous AGNs have larger torus opening angles, which in turn leads to the observed fraction of type 1 AGNs increasing with quasar luminosity.

Some of the strongest evidence in support of the receding torus model has been pro-

---

vided by low-frequency radio surveys. The selection of AGNs at low radio frequencies is possibly the most effective way of obtaining a sample free of orientation biases since the selection is based on the optically-thin extended lobe emission which should be the same in pole-on and edge-on radio sources. Using such samples, many studies have found evidence for a higher fraction of quasars with increasing luminosity when compared with the obscured type 2 radio galaxies (e.g. Hill, Goodrich & DePoy 1996; Simpson, Rawlings & Lacy 1999; Simpson & Rawlings 2000; Willott et al. 2000; Grimes, Rawlings & Willott 2004). In addition to the radio based surveys, similar evidence has been found using X-ray surveys (e.g. Steffen et al. 2003; Hasinger et al. 2004), which are also less influenced by orientation than optical surveys (e.g. Luo et al. 2011).

The Sloan Digital Sky Survey (SDSS) has allowed such studies to be taken further. In particular, large spectroscopic surveys from the SDSS allow narrow emission lines to be used as a tracer of the orientation of the AGNs. Simpson (2005) determined the luminosity function of the [OIII] emission line for both broad- and narrow-line AGNs (or type 1 and type 2 AGNs). He found that the fraction of the broad-line (type 1) AGNs increases with the luminosity of the [OIII] line, consistent with the receding torus model. However, this study does make the assumption that [OIII] is an isotropic tracer of the intrinsic AGN luminosity. It is worth noting that this assumption has recently been called into question (Fine, Jarvis & Mauch 2011).

More recent work using the *Spitzer Space Telescope* has also found evidence in support of the receding torus model. Treister et al. (2008) used  $24\mu\text{m}$  observations, which directly probe the torus emission, to show that the hot dust emission appears to decrease with increasing bolometric luminosity.

However, a critical review of the receding torus hypothesis was recently undertaken by Lawrence & Elvis (2010), who suggested that evidence that the fraction of type 1 objects increases with luminosity may be due simply to selection effects and to mis-classification

---

of genuine type 2 objects. It is still unclear, therefore, whether some of the evidence in support of the receding torus model may be due to obscuration in the host galaxy. This leads onto the picture of an evolutionary unified scheme (e.g. Sanders et al. 1988a), to which I now turn (Section 1.2.3).

### 1.2.3 Evolutionary Unification

Another alternative to the simple orientation-based unified scheme is one in which the galaxy hosting the AGN moves from an obscured system to an unobscured system over a period of time. This idea was first proposed by Sanders et al. (1988a; 1988b) who, using a sample of just 10 nearby infrared-luminous galaxies, found strong evidence of AGN activity in these highly disturbed systems. These systems are undergoing a major episode of obscured star formation, believed to be triggered via a galaxy-galaxy merger. In the scheme which Sanders et al. (1988a) propose, quasars are viewed as the end point of galaxy mergers, where the quasar is obscured by the dust produced in the star formation which has been triggered by the merger event. This dust eventually clears and the AGN thus appears to evolve from an obscured quasar to a naked quasar.

Since this early work, many groups have found evidence that an evolutionary scheme, in which galaxy mergers play a key role, may be needed to fully understand the wide variety of observed AGN phenomena (Sanders & Mirabel 1996; Surace et al. 1998; Surace & Sanders 1999; Canalizo & Stockton 2000; Surace, Sanders & Evans 2000; Canalizo & Stockton 2001). However, detailed studies of the host galaxies of AGNs find mixed evidence of merger-triggered AGN activity (e.g. Bahcall et al. 1997; Dunlop et al. 2003; see Section 1.5). In complementary work, Harvanek et al. (2001) found that, whilst both quasars and radio galaxies inhabit rich environments at  $z > 0.4$ , this is not true for  $0.15 < z < 0.4$  (where only the radio galaxies are found in rich clusters), supporting a hypothesis in which quasars fade into radio galaxies. Doubt has been cast on this result,

---

however, by Hardcastle (2004) who showed that this result arises as a result of including LEGs (which do not unify with quasars) in the  $0.15 < z < 0.4$  radio galaxy sample. Excluding the LEGs from this sample, Hardcastle (2004) showed that the environments of high excitation radio galaxies and quasars at  $0.15 < z < 0.4$  are statistically consistent, in agreement with a simple unified model (Section 1.2.1).

In the high redshift universe, where the majority of AGN activity occurs (see Section 1.4), work with (sub-)mm telescopes has enabled the study of ‘host-obscured’ AGNs. Alexander et al. (2005) used deep X-ray observations to determine the AGN component in far-infrared/sub-millimetre bright high redshift galaxies, believed to be undergoing a major burst of star formation. They find evidence for continual growth of the supermassive black hole during this intense star-burst phase.

More recently, Rafferty et al. (2011) used a large sample of AGNs at  $0.3 < z < 3$ , selected based on their  $70\mu\text{m}$  emission, to investigate how AGN activity may be linked to the strength of the star-burst phase. They find compelling evidence that the most intense bursts of star formation in galaxies are accompanied by an increasing probability of AGN activity, with around 30% of these far-infrared bright galaxies exhibiting X-ray emission due to an AGN. This is very similar to that found in the higher redshift sub-mm galaxies and suggests that the mergers which cause the most intense star-burst episodes in high redshift galaxies may also trigger the AGN activity. Using the opposite approach, Trichas et al. (2009) found that bright X-ray sources also tend to exhibit far-infrared emission consistent with a starburst. However, they suggest that these sources have relatively moderate star formation rates which is contrary to the study of Rafferty et al. (2011). This discrepancy is easily explained by the selection methods used in these studies, since a sub-mm selected sample is expected to have a much higher average star formation rate than an X-ray selected sample.

It is clear, therefore, that many studies suggest that some kind of evolutionary unifi-

---

cation is likely to be needed in order to account for some of the different properties of the population of AGNs. However, we still lack an understanding of when and how the evolutionary unification (rather than the more traditional orientation-based unification) dominates our selection of AGNs at various wavelengths. Deep imaging studies underway with the *Hubble Space Telescope* (e.g. Kocevski et al. 2011), combined with some of the deepest observations of AGNs at X-ray and far-infrared wavelengths using *Chandra* (e.g. Brandt & Alexander 2010) and *Herschel* (e.g. Mullaney et al. 2011) respectively, should shed light on this connection in the near future.

### 1.3 Classification of Radio Galaxies

This thesis is based on work using a sample of 41 radio galaxies (see Section 1.8), and in this section I outline relevant classification schemes. The most basic division of radio galaxies is into compact and extended sources. Compact sources contain only a core, whereas extended sources usually contain two lobes in addition to the core, with associated jets and hotspots.

Extended sources are most commonly classified morphologically into Fanaroff-Riley Class I (FRI) and Class II (FR II) objects. For their sample of radio galaxies, Fanaroff & Riley (1974) calculated the ratio of the distance between the brightest regions on either side of the central galaxy to the total size of the source. If this ratio was less than 0.5 the source was classified as an FRI type object; if the ratio was greater than 0.5 it was classified as an FR II. As noted by Fanaroff & Riley, this classification scheme draws a distinction between those objects whose brightest components are closer to the central galaxy than the diffuse radio emission (FRI type objects), and those objects where the hotspots are further away (FR IIs). Classified in this way, FRIs are weaker radio sources whose radio luminosity is highest in the centre and decreases towards the edges of the

---

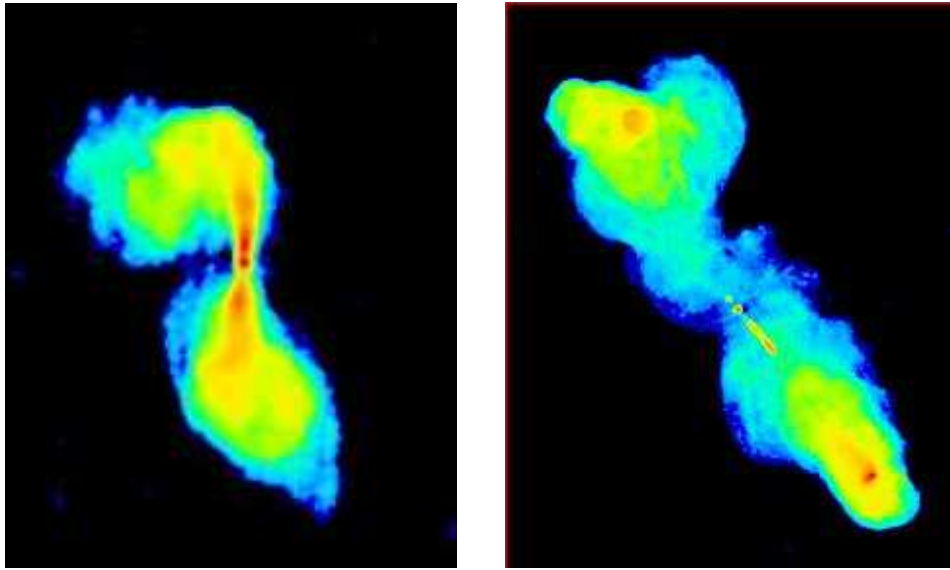


Figure 1.3: Examples of an FRI and an FRII type radio galaxy, taken from the DRAGN Atlas website (Section 1.3). Left: a 1414 MHz radio image of 3C272.1, an FRI type radio galaxy, obtained with the Very Large Array (VLA) by Laing & Bridle (1987). Right: a 1519 MHz radio image of 3C219, an FRII type radio galaxy, obtained with the VLA by Clarke et al. (1992).

radio structure. FRII type objects on the other hand are more powerful radio sources with the highest radio luminosities towards the edge of the lobes or in hotspots within the lobes. The difference between the structures of FRIs and FRIIs is shown in Figure 1.3. Fanaroff & Riley found that FRIs and FRIIs are well divided in radio luminosity. The division falls at  $L_{178} \approx 2 \times 10^{25} \text{ W Hz}^{-1} \text{ sr}^{-1}$  (where  $L_{178}$  is the radio luminosity at 178 MHz), with most FRIs lying below the divide and most FRIIs above.

An alternative classification scheme for extended radio sources is that of Owen & Laing (1989), who classified sources as Classical Doubles, Jetted sources or Fat Doubles. In their classification scheme, Classical Doubles are sources which have elongated, diffuse lobes extending from the nucleus out to compact outer hotspots. Jetted sources (or Twin Jet sources) have symmetric jets which extend out from the nucleus on both sides of the radio galaxy. Fat Doubles have diffuse radio lobes which are approximately round in shape and have bright outer rims. For a visual presentation of these classifications, in

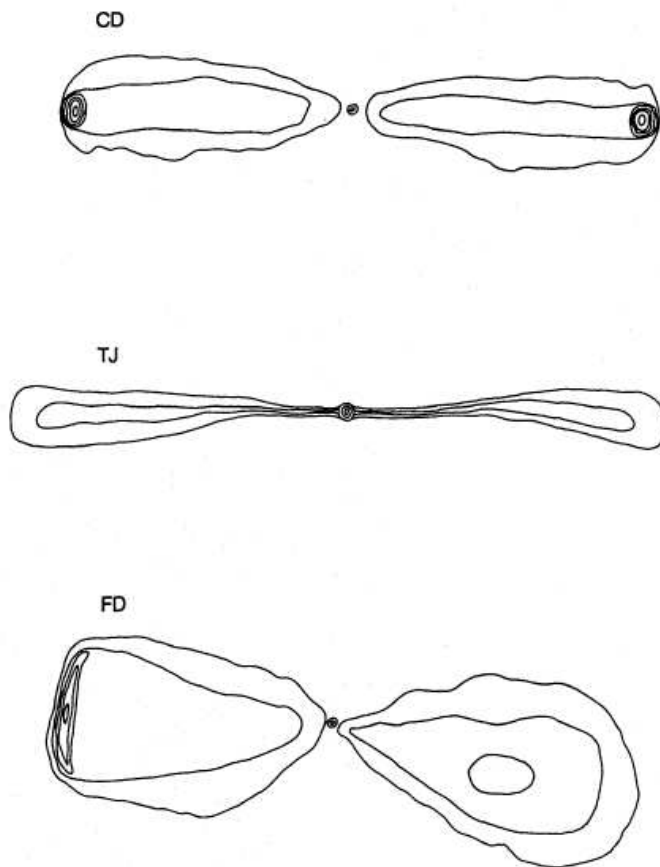


Figure 1.4: Example sketches illustrating the Owen & Laing (1989) classification of radio galaxies into Classical Doubles (CDs; top), Jetted sources (TJs; middle) and Fat Doubles (FDs; bottom), as discussed in Section 1.3. The lines illustrate contours in radio luminosity. These sketches are taken from figure 5 of Owen & Laing (1989).

Figure 1.4 I show Owen & Laing's illustration of these different object classes. In terms of their Fanaroff-Riley classification, Classical Doubles are always identified with FR II type sources whilst Fat Doubles are usually identified as FR II or FR I/II radio galaxies. Jetted sources are generally identified with FR I type sources.

In parallel with these morphological classification schemes is the division introduced by Hine & Longair (1979) based on optical spectra into high excitation galaxies (HEGs) and low excitation galaxies (LEGs). HEGs are objects whose spectra contain strong  $[\text{OII}]_{3727}$  emission lines. In addition, they often contain other strong high excitation lines such as  $[\text{OIII}]_{5007}$  and  $[\text{NeIII}]_{3869}$ . The spectra of LEGs do not show these fea-

tures; they instead resemble the spectra of giant elliptical galaxies, with at most very weak [OII]<sub>3727</sub> lines. This classification of Hine & Longair (1979) was further refined by Laing et al. (1994) and Jackson & Rawlings (1997) who classified 3CR radio galaxies on this basis. In the classification scheme of Jackson & Rawlings an object is classified as a LEG if it has an [OIII] rest frame equivalent width  $<10\text{\AA}$  or an [OII]/[OIII] ratio  $>1$  (or both). The lack of strong emission lines in LEGs (which does not seem to be an orientation-dependent effect) suggests that these objects do not possess BLRs and thus do not fit within the standard AGN unification scheme described in Section 1.2, in contrast to HEGs. Furthermore, studies at infrared and X-ray wavelengths have suggested that LEGs also lack the obscuring tori and radiatively efficient accretion discs which are essential ingredients of the standard unified scheme (e.g. Chiaberge et al. 2002; Whysong & Antonucci 2004; Hardcastle et al. 2006; Hardcastle et al. 2009).

There is increasing evidence that this emission line classification scheme, rather than the Fanaroff-Riley class, has a direct link to the accretion mode of the AGN. Hardcastle, Evans & Croston (2007) showed that Bondi accretion (Bondi 1952) of the hot phase of the inter-galactic medium (IGM) is sufficient to power all low excitation radio sources. Bondi accretion is spherically symmetric, which is a plausible assumption for hot, geometrically thick accreting material near to the central black hole. In this case the accretion rate,  $\dot{M}_{Bondi}$ , is given by the following equation (Allen et al. 2006):

$$\dot{M}_{Bondi} = \pi \lambda c_s \rho r_A^2, \quad (1.1)$$

where  $\lambda$  is a numeric coefficient dependent on the adiabatic index of the accreting gas,  $c_s$  is the adiabatic sound speed of the gas at the accretion radius,  $\rho$  is the density of the gas at the accretion radius and  $r_A$  is the accretion radius, calculated as follows:

$$r_A = \frac{2GM_{BH}}{c_s^2}, \quad (1.2)$$

where  $G$  is the Newtonian gravitational constant and  $M_{BH}$  the black hole mass. Whilst such a mode of accretion is shown by Hardcastle et al. (2007) to be sufficient for the LEGs studied, this is not the case for the HEGs. Hardcastle et al. (2007) propose that the HEGs are powered by the accretion of cold gas typically thought to be driven towards the central engine during a galaxy merger. In this case, the accretion occurs via a standard geometrically thin, radiatively efficient accretion disc (see Section 1.2.1). The merger scenario is not, however, the only possible source of cold gas in galaxies. For example, in the hydrodynamical model of Ciotti & Ostriker (2007), gas from dying stars can be recycled by cooling radiatively and falling to the nuclear region where a small fraction ( $\approx 1\%$  or less) is accreted onto the central black hole. Alternatively, various authors (Kereš et al. 2005; Dekel & Birnboim 2006; Ocvirk, Pichon & Teyssier 2008; Dekel et al. 2009; Brooks et al. 2009; Kereš et al. 2009) have used hydrodynamic simulations to show that cold mode accretion via streams or filaments of cold gas could be responsible for the majority of the gas supplied to massive galaxies at high redshifts. For lower mass galaxies this cold mode accretion could be the dominant source of cold gas right up to the present day.

## 1.4 The Evolution of AGNs

Although not directly addressed in this thesis, it is important to consider how the AGN population evolves with cosmic time, which has been a key element in establishing the link between AGNs and galaxies. Radio galaxies were central to the early work conducted in order to determine the evolution of the AGN population due to the fact that radio synchrotron radiation follows a simple power law, together with the fact that radio waves penetrate dust, resulting in relatively simple  $k$ -corrections and negating one of the selection effects inherent to optical surveys (e.g. Longair 1966).

---

It is now clearly established that powerful AGNs, regardless of selection wavelength, evolve strongly out to at least  $z \sim 2$ , with their space density increasing by a factor of 100–1000 (e.g. Dunlop & Peacock 1990; Shaver et al. 1996; Boyle & Terlevich 1998; Willott et al. 2001; Richards et al. 2006). More recently work at both radio and optical wavelengths has shown that this evolution may also be linked to the luminosity of the AGN (Croom et al. 2009; Rigby et al. 2011) in line with the idea of downsizing (Cowie et al. 1996), where the most luminous AGNs in this case peak at higher redshifts, whereas the lower luminosity AGNs are the dominant population at lower redshifts (see also Babić et al. 2007).

The strong evolution in the AGN population has important implications for our ability to construct samples that can be used to determine the key drivers in AGN activity. For example, the low space density of powerful AGNs at low redshift means that there is not enough cosmological volume in our universe to find many powerful AGNs at  $z < 0.2$ . On the other hand, extending to higher redshifts it becomes more difficult to study the host galaxy properties in detail due to the reduction in the angular diameter and the cosmological dimming. Furthermore, in any flux-density limited sample we are always dominated by sources at the flux-density limit, thus biasing such samples to the lowest luminosity sources. The sample under study in this thesis overcomes these issues as described in Section 1.8.

## 1.5 Host Galaxies of AGNs

The host galaxies of AGNs allow us to determine how the AGN activity may influence (or be influenced by) the stellar population in the immediate vicinity of the central engine. For many years the study of the host galaxies of AGNs was restricted to the obscured radio galaxies, where the lack of dominant quasar nuclei allows the hosts to be studied

---

in as much detail as any other type of ‘normal’ galaxy. Early work using the most luminous sources from the 3CR catalogue showed that powerful radio galaxies reside in massive elliptical galaxies (Lilly & Longair 1984). Subsequent work using the near-infrared  $K$ -band as a proxy for stellar mass have shown that the host galaxies of powerful radio galaxies at all redshifts lie towards the bright end of the luminosity function of elliptical galaxies (De Breuck et al. 2002, with typical luminosities of  $1 - 3 L^*$ ; Jarvis et al. 2001a; Willott et al. 2003; Bryant et al. 2009).

The high spatial resolution and, more importantly, the stability of the point spread function of the refurbished *Hubble Space Telescope* have enabled complementary studies of the host galaxies of the quasar population to be undertaken. The initial work on this subject suggested that RQQs generally resided in spiral hosts (e.g. Bahcall et al. 1997). However, more detailed studies which concentrated on more luminous quasars, with bolometric luminosities similar to the radio galaxies, showed that both powerful RQQs and powerful RLQs appear to reside in massive elliptical hosts (e.g. McLure et al. 1999; Kukula et al. 2001; Dunlop et al. 2003). This type of precise AGN imaging has been used already for the sample under investigation in this thesis (McLure et al. 2004). This showed that the host galaxy properties are linked to the radio luminosity; the more powerful radio sources generally reside in the more massive host galaxies, at least for the FRII type objects, whereas the FRIs all appear to reside in hosts of similar mass (McLure et al. 2004).

### **1.5.1 Star Formation Histories of AGNs**

Following on from earlier work by Lilly & Longair (1984), Baldi & Capetti (2008) studied a sample of nearby 3CR radio galaxies and compared optical and UV images in order to detect evidence of recent star formation. They found evidence of recent star formation in the HEGs in their sample, but not in the LEGs. They suggest that the HEGs have

---

undergone recent major mergers which both trigger star formation and power the AGN by providing a supply of cold gas for accretion. The LEGs, on the other hand, have experienced no such mergers. In this case no bursts of star formation are triggered and the AGN is powered by accretion of the hot interstellar medium (ISM). This picture supports the one put forward by Hardcastle, Evans & Croston (2007), as described in Section 1.3.

In complementary work, Emonts et al. (2008) find no evidence for large-scale HI structures in the host galaxies of FRI type sources, but find that the host galaxies of most of the FR II type sources in their sample contain significant amounts of HI. They suggest that this dichotomy is a result of different formation histories for FRI and FR II type radio sources. This is again consistent with the picture in which high- and low-luminosity radio galaxies have undergone different star formation histories, and this also influences the mode of accretion onto the central supermassive black hole.

In recent work using the vast data set available from the SDSS, Kauffmann, Heckman & Best (2008) study a sample of radio-loud AGNs with emission lines. They find a strong correlation between the presence of emission lines and the presence of a young stellar population, consistent with the findings of Baldi & Capetti (2008). They also find a correlation between the age of the stellar population and the radio luminosity normalised by the black hole mass. They note that strong optical AGNs have a significantly enhanced probability of hosting radio jets, and thus the radio and optical phenomena are not independent. However, although the SDSS is a wide-area survey, it does not probe the necessary volume to obtain a significant sample of the more luminous FR II type or HEG populations at  $z < 0.5$ . In order to study these effects further, a complete sample of radio sources selected by other methods is needed (see Section 1.8).

---

## 1.5.2 The Fundamental Plane

### An Introduction to the Fundamental Plane

The concept of the Fundamental Plane (Djorgovski & Davis 1987; Dressler et al. 1987) describes the observation that a three-dimensional representation of  $\log R_e$  versus  $\log \sigma$  versus  $\log I_e$  (where  $R_e$  is the effective radius,  $\sigma$  the velocity dispersion and  $I_e$  the effective surface brightness of the galaxy) for local elliptical and lenticular galaxies yields a plane. This is illustrated in Figure 1.5. The Fundamental Plane has a lower scatter than the Faber-Jackson  $L$ - $\sigma$  relation (Faber & Jackson 1976), and thus was initially of interest for its use as an alternative distance determination method. However, it was also realised that the Fundamental Plane scalings and small scatter were important for constraining models of elliptical galaxy formation. We may describe the Fundamental Plane as follows:

$$R_e \propto \sigma^\alpha I_e^{-\beta}. \quad (1.3)$$

Use of the virial theorem with constant mass-to-light ratio permits us to reproduce this relation with coefficients of  $\alpha = 2$  and  $\beta = 1$  (Faber et al. 1987). However, the observed Fundamental Plane does not follow this virial scaling. For example, Jørgensen, Franx & Kjærgaard (1996) find  $\alpha = 1.24 \pm 0.07$  and  $\beta = 0.82 \pm 0.02$  (see Figure 1.5). This ‘tilt’ in the Fundamental Plane suggests that the mass-to-light ratio ( $M/L$ ) varies as a function of galaxy mass (Robertson et al. 2006a). Faber et al. (1987) also note that deviations from the Fundamental Plane can be caused by other changes in  $M/L$ , for example due to stellar metallicity or age, or the distribution of dark and baryonic matter. Robertson et al. (2006a) comment that each of these effects could, in principle, introduce a systematic tilt into the Fundamental Plane if they vary as a function of galaxy mass. Jørgensen et al. (1996) also find that the slope of the Fundamental Plane is independent of cluster properties such as cluster velocity dispersion and gas temperature.

---

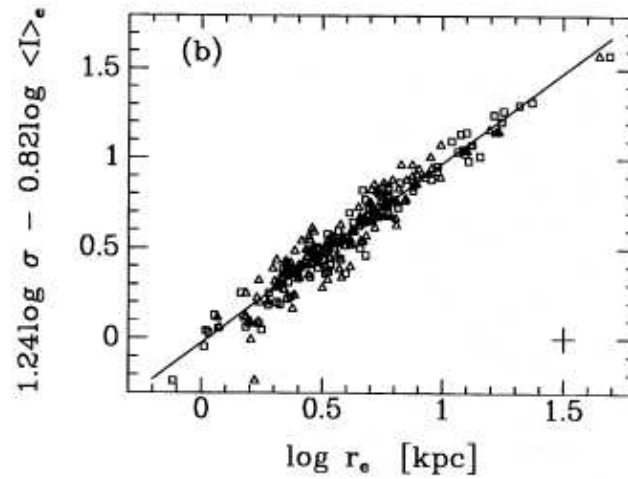


Figure 1.5: A graphical illustration of the Fundamental Plane (Section 1.5.2): a two dimensional representation of the Fundamental Plane of 226 local elliptical and lenticular S0-type galaxies (Jørgensen, Franx & Kjørgaard 1996). The plane equation is of the form  $\log(r_e) = 1.24 \log(\sigma) - 0.82 \log \langle I \rangle_e + \gamma$ , where  $r_e$  is the effective radius in kpc,  $\langle I \rangle_e$  the mean surface brightness within  $r_e$  in units of  $L_\odot/\text{pc}^2$  (where  $L_\odot$  is the solar luminosity) and  $\gamma$  is a constant. The figure is taken from figure 1b of Jørgensen et al. (1996). Elliptical galaxies are shown by boxes, S0 galaxies by triangles and the typical error is illustrated in the bottom right-hand corner of the figure.

### **The Fundamental Plane of Radio Galaxies & AGNs**

Bettoni et al. (2001) collected photometric and dynamical data for 73 low redshift ( $z < 0.2$ ) and predominantly low-luminosity, FRI-type radio galaxies from a variety of samples. They find that these local active galaxies lie on the same Fundamental Plane as the inactive population, with the implication that the gas accretion of the central black hole does not influence the global properties of early-type galaxies. In a complementary study, Wolf & Sheinis (2008) investigate the location on the Fundamental Plane of ten nearby ( $z < 0.3$ ) luminous quasars. They find that the radio-loud objects in their sample fall on the upper extreme region of the Fundamental Plane and have host galaxy properties similar to those of giant early-type galaxies, whilst their radio-quiet objects are located in the region of the Fundamental Plane occupied by normal early-type galaxies and have host galaxy properties more similar to intermediate-mass galaxies. Both of these therefore indicate that the properties of the AGN host galaxies are very similar to those of normal galaxies in the same luminosity and/or mass range.

### **Redshift Evolution of the Fundamental Plane**

Work has also been undertaken to examine the redshift evolution of the Fundamental Plane. The intermediate redshift Fundamental Plane ( $z \sim 0.3-0.4$ ) for cluster (van Dokkum & Franx 1996; Kelson et al. 2000) and field (Treu et al. 2001) early-type galaxies is found to be similar to that observed locally. Treu et al. (2001) find an offset (from the local relation) in their intermediate redshift Fundamental Plane of early-type field galaxies. This offset increases with redshift and is attributed to an increase in effective brightness of these galaxies with respect to a local sample. The use by Treu et al. of field, rather than cluster, galaxies may be the origin of their slightly different findings as compared with the previous authors. Moreover, each of these studies is limited by small number statistics and the accompanying large errors. Woo et al. (2004) study the Funda-

---

mental Plane of the host galaxies of 15 AGNs out to a redshift of  $z \sim 0.34$ . They find that the host galaxies of these intermediate redshift BL Lac objects and radio galaxies lie on the same Fundamental Plane as normal local early type galaxies and the local radio galaxy sample of Bettoni et al. (2001), although their higher redshift objects possess an offset in the same fashion as the one observed by Treu et al. (2001). Woo et al. (2004) also observe an increase in the mass-to-light ratio of their galaxies of approximately 40% since  $z \sim 0.3$ , also in agreement with the findings for normal early-type galaxies.

At higher redshifts ( $z \sim 0.8-1.3$ ) various authors (di Serego Alighieri et al. 2005; Treu et al. 2005a; Jørgensen et al. 2006; Jørgensen et al. 2007; Fritz & Ziegler 2009; Fritz et al. 2009; Fritz, Jørgensen & Schiavon 2010) find not only an offset but also a rotation in the Fundamental Plane when compared to the local relation. For example, Jørgensen et al. (2007) find a slope described by  $\alpha = 0.60 \pm 0.22$  and  $\beta = 0.70 \pm 0.06$  for galaxies in their two  $z \sim 0.8$  clusters whilst di Serego Alighieri et al. (2005) find a slope described by  $\alpha = 0.88 \pm 0.16$  and  $\beta = 0.63 \pm 0.04$  for their  $0.88 \leq z \leq 1.3$  early-type galaxies. The latter authors show at the 90% confidence level that the Fundamental Plane rotates with redshift. This is interpreted as a mass-dependent evolution of the mass-to-light ratio, where the evolution is faster for less massive galaxies. Fritz et al. (2010) study field-type early galaxies and demonstrate that the rotation of the Fundamental Plane appears to be independent of the environment of the galaxies. There is thus an emerging picture in which variation in the mass-to-light ratio causes a redshift-dependent offset in the Fundamental Plane (see also van Dokkum & Stanford 2003; van der Wel et al. 2005). This variation is mass-dependent, giving rise to the redshift-dependent rotation observed in the Fundamental Plane. In this picture it is galaxy mass, rather than environment, which plays the major role in determining galaxy evolution (Treu et al. 2005b), and less massive distant galaxies have much younger stellar populations than more massive galaxies [consistent with the downsizing scenario of Cowie et al. (1996) in which the most massive

---

galaxies form earliest]. It should, however, be noted that there is not universal agreement on this picture; Gebhardt et al. (2003) study the Fundamental Plane of 36 field galaxies (21 early-type and 15 disc galaxies) in the redshift range 0.3-1.0 (with a median redshift  $z = 0.8$ ) and find no difference in the slope of the plane when compared to the local relation. The reason for this discrepancy is not at this stage entirely clear, although the large redshift range studied, the relatively small number of objects (30), and the mixture of galaxy types used lead inevitably to large uncertainties in this result.

Robertson et al. (2006a) employ a multiphase interstellar medium model to investigate the contribution made by various different factors to the tilt of the Fundamental Plane. They find that merging gas-rich disc galaxy models (with gas fractions  $f_{gas} > 0.3$ ) including the effects of gas dissipation (cooling, star formation and supernova feedback) yields a scaling of the Fundamental Plane which is similar to the observed infrared Fundamental Plane of 251 local early-type galaxies found by Pahre, Djorgovski & de Carvalho (1998). Changing the redshift of the progenitor galaxies within the range  $z = 0-6$  has little effect on the plane produced. The inclusion of gas dissipation has the effect of decreasing the total-to-stellar mass ratio ( $M_{total}/M_*$ ) in the central regions of the galaxies. This decrease varies as a function of galaxy mass (with a greater decrease in lower mass systems) thus producing the required tilt in the Fundamental Plane. Re-merging the remnants of these gas-rich galaxy mergers leaves the Fundamental Plane largely intact. Including the effects of feedback from accreting supermassive black holes in their models makes little difference to the Fundamental Plane inhabited by the merger remnants. However, use of these full-model simulations allow Robertson et al. (2006b) to reproduce the power-law scaling of the  $M_{BH}-\sigma$  relation between  $z = 6$  and  $z = 0$ . The remnant re-mergers of Robertson et al. (2006a) preserve the  $M_{BH}-\sigma$  relation (albeit with increased scatter).

---

## 1.6 Environments of AGNs

In addition to studying the host galaxies of AGNs, it is also important to investigate their environments. There have been suggestions that radio jets may both trigger (Wiita 2004) and suppress (Rawlings & Jarvis 2004) star formation on the Mpc scale and thus have a profound influence on their environments. Alongside this, however, is the suggestion that the environment of an AGN may have an important impact on the AGN itself. For example, mergers with close companions is one plausible explanation for the suggested difference between the material accreted onto the central black hole in HEGs and LEGs, as discussed in Section 1.3. An important question with respect to AGN environments is therefore whether they are the product of nature or of nurture, that is to say, whether they have an influence on or are influenced by the AGN (or both).

### 1.6.1 Environmental Densities

It has become clear over recent years that the host galaxies of many AGNs lie in regions which have an overdensity of galaxies when compared to the background galaxy count (e.g. Hall & Green 1998; Best 2000; Best et al. 2003; Wold et al. 2003; Falder et al. 2010). However, the picture is less clear as regards the possible connection between cluster environment and radio luminosity. On the one hand, various authors have found a clear difference between the environments of radio-loud and radio-quiet AGNs, including Ellingson, Yee & Green (1991), who found that the radio-quiet objects in their sample of  $0.3 < z < 0.65$  quasars inhabited significantly poorer environments than RLQs, and Hutchings et al. (1999), who found a similar result for their  $0.85 < z < 4.16$  quasar sample, although in neither of these studies were the radio-loud and radio-quiet quasars matched in terms of their bolometric luminosity. More recently, Kauffmann, Heckman & Best (2008) found that their radio-loud AGNs were located in cluster environments

---

approximately twice as dense as a matched radio-quiet sample, and Falder et al. (2010) found a positive correlation between radio luminosity and environmental overdensity for their matched sample of quasars at the same high redshift ( $z \sim 1$ ). On the other hand, Wold et al. (2001) found that the mean environmental density of their  $0.5 < z < 0.8$  radio-quiet quasars was indistinguishable from that of a radio-loud sample matched in optical luminosity and redshift. Similarly, McLure & Dunlop (2001a) found no significant difference in the cluster richness between their matched  $z \sim 0.2$  radio-loud and radio-quiet quasars. Furthermore, McLure & Dunlop (2001a) found no correlation between radio luminosity and environmental density for the radio-loud quasars and radio galaxies in their sample. They did, however, note that an apparent positive correlation between the two quantities was driven by the radio galaxies on their own, and conceded that the limited dynamic range of the sample meant they could not rule out the existence of a weak correlation. The discrepancy between the findings of Wold et al. (2001) and McLure & Dunlop (2001a) and the findings of Ellingson, Yee & Green (1991) and Hutchings et al. (1999) may arise from the latter authors not using matched samples in terms of their optical and/or radio luminosities and therefore they may not have been comparing like with like. The radio-loud objects of Kauffmann, Heckman & Best (2008) are at much lower radio luminosity than those of either Wold et al. (2001) or McLure & Dunlop (2001a), which may account for the different findings of these studies at higher redshifts. Falder et al. (2010) studied the environments using massive, bright evolved galaxies whereas Wold et al. (2001) and McLure & Dunlop (2001a) were sensitive to a wider range of lower luminosity objects which may also have affected the results.

In terms of the radio morphology, at low redshifts, FRIs are found to inhabit moderately rich cluster environments whereas FRIIs are isolated or found in small groups (Longair & Seldner 1979; Prestage & Peacock 1988, 1989; Hill & Lilly 1991). This result suggests that the environments of radio galaxies and their radio structures are linked,

---

although Prestage & Peacock (1988) noted a substantial overlap between their two populations with the implication that cluster strength is not the sole factor which determines radio luminosity. Hill & Lilly (1991) found that the environments of their  $z \sim 0.5$  FRIs were similar to those of low redshift FRIs, but that their  $z \sim 0.5$  FRIIs were, on average, found in richer environments than local FRIIs. They therefore concluded that the environments of powerful radio galaxies undergo an epoch-dependent evolution, although their low redshift samples were not matched in radio luminosity. In contrast, with better and more recent data McLure & Dunlop (2001a) find no change in the environmental richness between their  $z \sim 0.2$  FRIIs and those of Hill & Lilly (1991). McLure & Dunlop matched their FRIIs in radio luminosity with those at higher redshift from Hill & Lilly, which may be the cause of the differing results.

### 1.6.2 Alignment Effects

Another aspect of the relation between galaxies and their environments is the alignment of galaxies within clusters. Sastry (1968) first discovered that the major axes of Brightest Cluster Galaxies (BCGs) are aligned with the major axes of their host clusters. Sastry used Palomar Sky Survey prints and measured the position angles (PAs) of the clusters surrounding five supergiant cD-type galaxies using a transparent celluloid. A transparent celluloid with two cross-lines drawn on was initially positioned with the cross-lines intersecting at the cD galaxy and with one of the lines aligned with the visually apparent major axis of the cluster. The position of the celluloid was then adjusted so as to find the position in which the cluster galaxy counts for each quadrant were most equal, and this was used to define both the cluster centre and the major axis of the cluster.

This alignment has since become known as the Binggeli effect, after the work of Binggeli (1982). Various studies have since confirmed the effect for both rich and poor clusters and have found that the alignment is only present for BCGs and not, in general,

---

other cluster members (e.g. Binggeli 1982; Trevese, Cirimele & Flin 1992; Fuller, West & Bridges 1999; Torlina, De Propris & West 2007). These subsequent studies have used a variety of means to determine the major axes of galaxies and clusters. For the cluster major axes, techniques have included finding the axis which minimises the sum of the perpendicular distances between the axis and each cluster member (Binggeli 1982) and using the moments of the galaxy distribution (e.g. Carter & Metcalfe 1980; Trevese et al. 1992). The galaxy PAs have been determined using the moments of the galaxy intensity distributions (Trevese et al. 1992) as well as in an automated fashion using tools in the Image Reduction and Analysis Facility (IRAF) package (Fuller et al. 1999) or the output from the SExtractor programme<sup>1</sup> (Torlina et al. 2007).

Donoso, Mill & Lambas (2006) found that the Binggeli alignments were already present by  $z \sim 0.5$  but only for the red galaxies in clusters, not the blue population. More recently, Niederste-Ostholt et al. (2010) found that the alignment is stronger at lower redshift ( $z < 0.26$ ) than at higher redshift ( $z > 0.26$ ), is stronger for rich clusters than poor clusters, and is stronger for clusters with dominant BCGs. They interpret the latter result as suggesting that the Binggeli effect arises from galaxy infall along primordial filaments, together with mergers during cluster formation. They therefore discount the other main possibility for the origin of the alignment, namely tidal interactions. It is therefore clear that if powerful radio galaxies are preferentially hosted by central dominant cluster galaxies (e.g. Burns, White & Hough 1981; Best et al. 2007) then they may also exhibit the Binggeli effect.

Work has also been undertaken to investigate the possible alignment of the radio jets in radio galaxies with features in their environments. For example, Mackay (1971) used a sample of 18 3C radio sources and found a strong correlation (at the 99.9% level) between the PAs of the host galaxy (determined from optical imaging) and the radio axis. The an-

---

<sup>1</sup><http://www.astromatic.net/software/sextractor>

---

gle between the radio and optical axes was not found to be correlated with the luminosity of the host galaxy. At lower radio luminosities, Birkinshaw & Davies (1985) used Very Large Array (VLA) observations of a sample of 47 nearby bright elliptical galaxies. They found a preference for the radio major axis to lie within  $0\text{--}50^\circ$  of the optical minor axis (with an 83% chance of finding an alignment within this range), although there was no single preferred alignment within this range. Using a far larger data set of 14,302 galaxies with data from the SDSS and Faint Images of the Radio Sky at Twenty centimetres (FIRST), Battye & Browne (2009) found similar results for the early-type galaxies in their sample: they found evidence of an alignment between the radio major axis and the optical minor axis, but only for objects with lower radio luminosities. For late-type galaxies, they found a strong alignment between the radio and optical major axes. Finally, considering the possibility of an alignment between radio axes and the distributions of neighbouring cluster galaxies, Roche & Eales (2000) found tentative evidence at the 97% ( $2.2\sigma$ ) level of such an alignment for the cD cluster galaxy 3C348, in agreement with the model of West (1994) for the high redshift formation of dominant cluster galaxies and powerful radio sources.

## 1.7 AGN-driven Feedback

There is increasing evidence that active galactic nuclei have an important role to play in the formation and evolution of galaxies via AGN-driven feedback. The first piece of evidence in support of this is the existence of various relationships between the central black hole of an AGN and the stellar population of the galaxy: for example, the relation between black hole mass and stellar velocity dispersion ( $M_{BH}\text{-}\sigma$ ) (Gebhardt et al. 2000; Ferrarese & Merritt 2000; Merritt & Ferrarese 2001; Gültekin et al. 2009) and the relation between black hole mass and bulge luminosity (e.g. McLure & Dunlop 2001b; McLure

---

& Dunlop 2002; Gültekin et al. 2009). The latter may also be expressed as the Magorrian relation between black hole mass and bulge stellar mass (Magorrian et al. 1998). These tight correlations provide compelling evidence for links between galaxy formation and evolution and the growth of black holes through AGN (accretion) activity. One suggested mechanism is that of quasar outflows limiting black hole masses, dependent on the depth of the potential wells of dark matter haloes (Silk & Rees 1998).

Secondly, a connection between AGNs and star formation is suggested by the cosmic star formation rate normalised by volume (e.g. Hopkins & Beacom 2006) and the comoving space density of quasars and luminous radio galaxies (e.g. Shaver et al. 1996; Jarvis et al. 2001b; Richards et al. 2006). These quantities exhibit a parallel increase out to a redshift of approximately two to three.

The third piece of evidence comes from the galaxy luminosity function, for which semi-analytic models of galaxy formation that do not incorporate feedback overproduce galaxies at both the faint and the bright ends of the luminosity function compared with what is observed (Figure 1.6). The models and the data can be reconciled by the inclusion in the models of supernova feedback (for the faint end of the luminosity function) and AGN-driven feedback (for the bright end of the luminosity function). For example, Croton et al. (2006) include AGN-driven feedback phenomena in their semi-analytic model, separated into ‘quasar mode’ (associated with the efficient accretion of cold gas) and ‘radio mode’ (associated with the less efficient accretion of warm gas) feedback. Sijacki et al. (2007) also include AGN-driven feedback in their full hydrodynamical model, once again separated into two modes: the ‘quasar regime’ (corresponding to central black holes with high accretion rates) and mechanical feedback (corresponding to central black holes with low accretion rates).

Despite the nomenclature, radio galaxies can exhibit either ‘quasar mode’ or ‘radio mode’/mechanical feedback, dependent on the accretion onto the central black hole. In

---

‘quasar mode,’ feedback occurs hydrodynamically and radiatively, with the effect that cold gas is expelled from the host galaxy. ‘Radio mode’ feedback, on the other hand, proceeds mechanically via the radio lobes, suppressing the cooling of hot gas so as to reduce or halt the cooling flow of material accreting onto the central black hole. Important evidence for the existence of the two different modes of AGN fuelling which lie behind these two feedback modes is the work of Hardcastle et al. (2007) on the energetics of AGN which showed that HEGs and LEGs may be powered by the efficient accretion of cold gas and the inefficient accretion of hot gas respectively (see Section 1.3). Furthermore, whilst the existence in some AGNs of the radio lobes necessary for ‘radio mode’ feedback has been accepted for many years (see Section 1.1), there now also exists evidence for highly energetic blueshifted outflows in AGNs (e.g. de Kool et al. 2001, using primarily the [MgII], [MgI] and [FeII] lines; Crenshaw, Kraemer & George 2003, using the [HI] Lyman- $\alpha$ , [CIV] and [NV] rest-frame UV lines together with X-ray lines including [AlXIII], [MgXI], [MgXII], [SXV], [SXVI], [SiXIII] and [SiXIV]; Reeves, O’Brien & Ward 2003, using highly ionised iron lines from [FeXVII] to [FeXXIV]; Alexander et al. 2010, using the [OIII]<sub>5007</sub> line). These outflows appear to be phenomena which are distinct from the radio jets and are thus evidence in support of the hydrodynamic and radiative feedback necessary for the postulated ‘quasar mode.’

## 1.8 This Thesis

In light of the essential role that AGNs are increasingly believed to play in the formation and evolution of galaxies, it is important that we strive to develop a better understanding of the nature of AGNs and of their interactions with their host galaxies. By studying the host galaxies of radio-loud AGNs spanning luminosities from the radio mode (typically lower radio luminosities) through to the quasar mode (typically higher radio luminosities) we

---

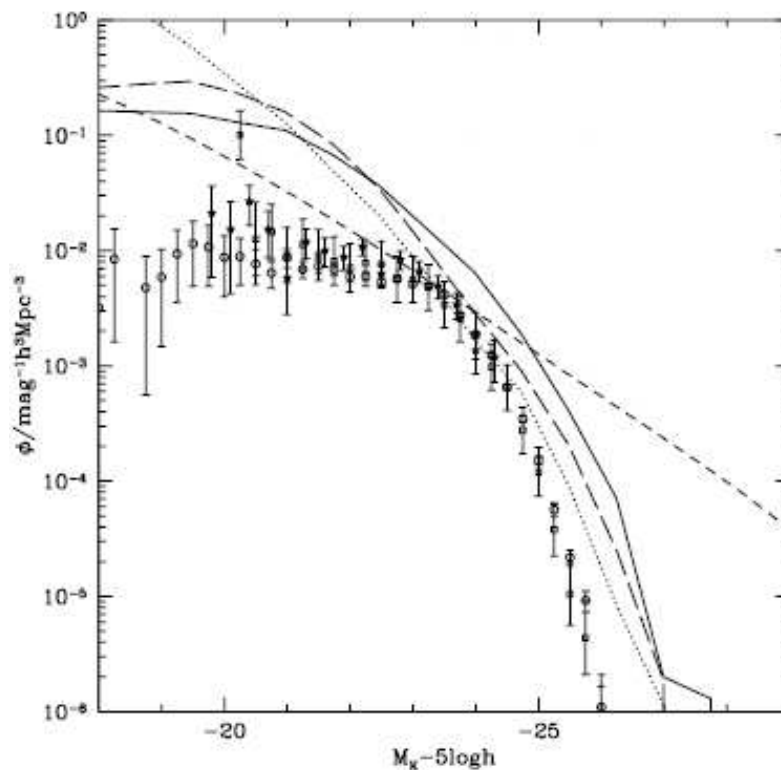


Figure 1.6: An example of the K-band galaxy luminosity function, taken from figure 1 of Benson et al. (2003).  $\phi$  is the number density in units of  $\text{mag}^{-1}h^3\text{Mpc}^{-3}$ , where  $h$  is the Hubble constant divided by 100, and  $M_K$  the absolute K-band magnitude. The data points show observational determinations of the luminosity function; circles show the data of Cole et al. (2001), squares the data of Kochanek et al. (2001), and stars the data of Huang et al. (2003). The short dashed line shows the luminosity function produced by a model in which the dark matter halo mass function is converted into the galaxy luminosity function via a fixed mass-to-light ratio. The dotted line shows the luminosity function produced by the GALFORM semi-analytic model (Cole et al. 2000) with no feedback, photoionization suppression, galaxy merging or conduction. The long dashed line shows the luminosity function when photoionization is added to the model, and the solid line shows the luminosity function when both photoionization and galaxy merging are included. As is clearly seen from the figure, models which do not incorporate feedback produce an overdensity of galaxies at both ends of the luminosity function when compared with observations (Section 1.7).

should be able to place important constraints on the validity of the feedback mechanisms in the models of galaxy formation and evolution. Furthermore, radio galaxies reside in the most massive galaxies at all epochs (e.g. Jarvis et al. 2001a; Willott et al. 2003) and as such allow us to trace the evolution of the most massive galaxies across virtually all of cosmic time. Alongside studying the host galaxies of AGNs, it is also important (as discussed in Section 1.6) to investigate their environments, in order to determine whether they are influenced by, or have an influence on, the AGNs (or both).

An effective way to select a sample of AGNs for the study of their host galaxies and environments is on the basis of their low-frequency radio emission. Selecting AGNs in this way enables the selection of type 2, or obscured AGNs, in the same way as RLQs. This is because the radio waves are unaffected by dust obscuration, and the radio emission from the extended lobes is optically thin and therefore orientation independent. Furthermore, selecting the radio galaxies allows the study of the stellar populations in the AGN host galaxy, as the central nuclear emission is obscured by the putative dusty torus invoked in unified schemes (Section 1.2). This obscuration-related optical faintness in powerful AGNs has enabled many authors to study the evolution of their host galaxies, with most work based on the near-infrared ( $K - z$ ) Hubble diagram (Lilly & Longair 1982; Jarvis et al. 2001a; Willott et al. 2003) and broad-band colours (e.g. Lilly 1989) suggesting that the hosts of powerful radio galaxies are comprised of an old stellar population which forms at high redshift ( $z > 2$ ) and then passively evolves.

In this thesis, therefore, I investigate the star formation histories and Fundamental Plane of the host galaxies of a sample of 41 radio galaxies at  $z \sim 0.5$  selected on the basis of their low-frequency radio emission (the ZP5 sample), as well as the overdensities and alignments found in their wider environments. The ZP5 sample is described in McLure et al. (2004) and contains all of the narrow-line radio galaxies in the redshift interval  $0.4 < z < 0.6$  from four complete, low-frequency selected radio surveys; 3CRR

---

(Laing, Riley & Longair 1983), 6CE (Eales et al. 1997; Rawlings, Eales & Lacy 2001), 7CRS (Lacy et al. 1999; Willott et al. 2003) and TexOx-1000 (Hill & Rawlings 2003; Vardoulaki et al. 2010). Details of the sample are provided in Table 1.1. In Figure 1.7 I show the location of the objects in the ZP5 sample in the radio luminosity – redshift plane. The sample selection was motivated by several factors, including the presence at  $z \sim 0.5$  of a three decade range in radio luminosity (extending towards the most radio luminous objects in existence), as well as sufficient numbers of objects to permit the construction of subsamples divided by radio luminosity in order to investigate possible correlations with radio luminosity. This choice of sample also has advantages for studies of the environments of the AGNs. Most previous studies in this area (Section 1.6) have used different parent surveys where matching in host and radio luminosity has been attempted. This matching is, however, difficult to achieve, possibly leading to contradictory conclusions as discussed in Section 1.6.1. The ZP5 sample, on the other hand, is a unique sample of objects at a single redshift taken from complete, radio selected samples. There is, therefore, no need for matching in radio or host luminosity and therefore avoids the difficulties and uncertainties inherent therein.

This dissertation is arranged as follows: in Chapter 2 I describe the reduction of my spectroscopic data for the sample, in Chapter 3 I use this spectroscopic data to investigate connections between the star formation histories of the host galaxies and the AGNs, and in Chapter 4 I use the spectroscopic data in order to study the Fundamental Plane of  $z \sim 0.5$  radio galaxies. In Chapter 5 I describe my reduction of wide field multi-band imaging data for the sample which I use in Chapter 6 to study the cluster environments of my sample. I summarise the thesis and outline possible future work in Chapter 7. Throughout this thesis I assume a standard cosmology in which  $H_0 = 70 \text{ km s}^{-1}$ ,  $\Omega_M = 0.3$  and  $\Omega_\Lambda = 0.7$ .

---

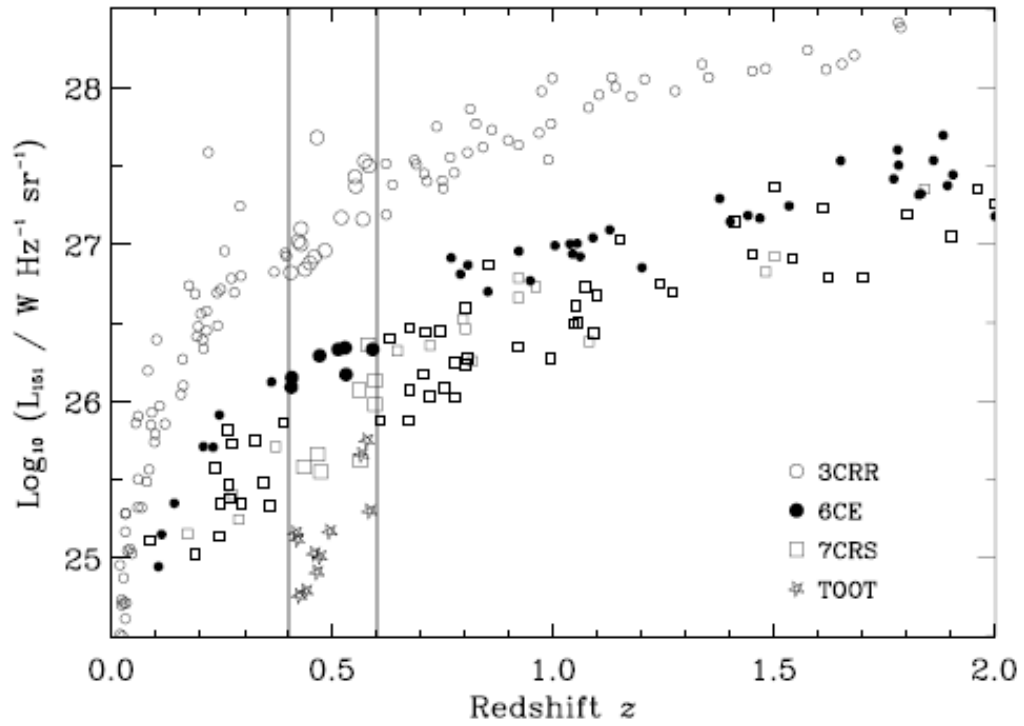


Figure 1.7: The location of the objects in the ZP5 sample (enlarged symbols in the redshift range  $0.4 < z < 0.6$ ) in the 151 MHz radio luminosity ( $L_{151}$ ) – redshift ( $z$ ) plane (taken from figure 1 of McLure et al. 2004). The vertical lines show the lower and upper redshift boundaries for the ZP5 sample.

Source (1)	R.A. (2)	Dec. (3)	$z$ (4)	$L_{151}$ (5)	$M_R$ (6)	$r_e$ (7)	FR Class (8)	Morph. (9)	Spec. Class (10)
3C16	00 37 45.39	13 20 09.6	0.405	26.82	-23.23	22.9	FRII	CD/FD	HEG
3C19	00 40 55.01	33 10 07.3	0.482	26.96	-23.81	30.9	FRII	CD	LEG
3C46	01 35 28.47	37 54 05.7	0.437	26.84	-23.49	15.8	FRII	CD	HEG
3C172	07 02 08.32	25 13 53.9	0.519	27.17	-23.25	12.6	FRII	CD	HEG
3C200	08 27 25.38	29 18 45.5	0.458	26.92	-23.48	13.2	FRII	CD	LEG
3C225B	09 42 15.41	13 45 51.0	0.582	27.50	-23.49	18.6	FRII	CD	HEG?
3C228	09 50 10.79	14 20 00.9	0.552	27.37	-22.64	13.2	FRII	CD	HEG
4C74.16	10 14 14.84	74 37 37.4	0.568	27.16	-23.04	18.6	FRII	CD	HEG
3C244.1	10 33 33.97	58 14 35.8	0.428	27.10	-23.45	15.8	FRII	CD	HEG
3C274.1	12 35 26.64	21 20 34.7	0.422	27.02	-23.18	9.5	FRII	CD	HEG
3C295	14 11 20.65	52 12 09.0	0.464	27.68	-24.52	29.5	FRII	CD	HEG
3C330	16 09 35.01	65 56 37.7	0.550	27.43	-23.71	20.9	FRII	CD	HEG
3C341	16 28 04.04	27 41 39.3	0.448	26.88	-23.45	16.6	FRII	CD	HEG
3C427.1	21 04 07.07	76 33 10.8	0.572	27.53	-23.81	18.2	FRII	CD	LEG
3C457	23 12 07.57	18 45 41.4	0.428	27.00	-23.67	14.1	FRII	CD	HEG
6C0825+3407	08 25 14.59	34 07 16.8	0.406	26.09	-23.14	14.5	FRII	FD	LEG
6C0850+3747	08 50 24.77	37 47 09.1	0.407	26.15	-23.35	12.6	FRII	CD	HEG
6C0857+3945	08 57 43.56	39 45 29.0	0.528	26.34	-23.42	11.7	FRII	CD	HEG
6C1111+3940	11 11 19.39	39 40 14.5	0.590	26.33	-22.78	6.7	FRII	CD	LEG
6C1132+3439	11 32 45.74	34 39 36.2	0.512	26.33	-22.96	10.5	FRII	CD	HEG
6C1200+3416	12 00 53.34	34 16 47.3	0.530	26.17	-23.35	20.0	FRII	CD	LEG
6C1303+3756	13 03 44.26	37 56 15.2	0.470	26.29	-23.28	12.3	FRII	CD	HEG
7C0213+3418	02 13 28.39	34 18 30.6	0.465	25.66	-22.99	6.3	FRII	FD	LEG
7C0219+3419	02 19 15.89	34 19 43.2	0.595	26.13	-22.87	10.9	FRII	FD	HEG?
7C0219+3423	02 19 37.83	34 23 11.2	0.595	25.98	-22.26	7.8	FRII	J	HEG?
7C0220+2952	02 20 34.26	29 52 19.5	0.560	26.07	-22.43	12.9	FRII	FD	LEG?
7C0223+3415	02 23 47.24	34 15 11.9	0.473	25.55	-22.62	9.8	FRII	CD	HEG
7C0810+2650	08 10 26.10	26 50 49.1	0.435	25.58	-23.22	14.8	FRII	CD	HEG
7C1731+6638	17 31 43.84	66 38 56.7	0.562	25.62	-21.67	6.0	FRII	FD	HEG
7C1806+6831	18 06 50.16	68 31 41.9	0.580	26.36	-23.68	14.8	FRII	FD	HEG
TOOT0009+3523	00 09 46.90	35 23 45.1	0.439	24.79	-22.87	12.6	FRI	FD	LEG
TOOT0013+3459	00 13 13.29	34 59 40.6	0.577	25.75	-24.14	15.5	FRII	FD	LEG
TOOT0018+3510	00 18 53.93	35 10 12.1	0.416	25.16	-23.51	19.5	FRI	FD	LEG
TOOT1255+3556	12 55 55.83	35 56 35.8	0.471	25.01	-22.53	7.8	FRI	J	LEG
TOOT1301+3658	13 01 25.03	36 58 9.40	0.424	24.76	-23.79	21.9	FRI	FD	LEG
TOOT1303+3334	13 03 10.29	33 34 7.00	0.565	25.66	-22.32	5.0	FRII	J	HEG
TOOT1307+3639	13 07 27.07	36 39 16.4	0.583	25.30	-23.51	12.0	FRI	J	LEG
TOOT1309+3359	13 09 53.95	33 59 28.2	0.464	24.91	-22.70	6.6	FRI	CM	HEG
TOOT1626+4523	16 26 48.50	45 23 42.6	0.458	25.03	-23.19	7.4	FRI	FD	LEG
TOOT1630+4534	16 30 32.80	45 34 26.0	0.493	25.17	-23.88	10.2	FRI	J	LEG
TOOT1648+5040	16 48 26.19	50 40 58.0	0.420	25.12	-22.97	9.5	FRI	CM	LEG

Table 1.1: Details of the  $z \sim 0.5$  (ZP5) sample as used in this thesis (see Section 1.8). With the exception of the morphological classifications, the data are taken from McLure et al. (2004) where the sample was first defined and described. The morphological classifications are taken from the more recent work of Mitchell (2005). Column 1 lists the radio galaxy names and columns 2 and 3 list the J2000 source coordinates. Column 4 lists the object redshifts, column 5 the logarithm of the 151 MHz radio luminosities in units of  $\text{W Hz}^{-1} \text{sr}^{-1}$  and column 6 the absolute R-band host luminosities. Column 7 gives the effective radii in kpc and column 8 the Fanaroff-Riley classifications (Fanaroff & Riley 1974) into Fanaroff-Riley Class I (FRI) and Class II (FRII) objects. Column 9 lists the morphological classifications into Classical Doubles (CD), Fat Doubles (FD), Jetted sources (J) and Compact (CM) sources and column 10 gives the emission line classifications into high-excitation galaxies (HEGs) and low-excitation galaxies (LEGs).

# Chapter 2

## GMOS Spectroscopy

Spectroscopic data for 15 of the objects in the  $z \sim 0.5$  (ZP5) sample were obtained in August 2002 (prior to the commencement of my Ph.D. studies) using the Intermediate dispersion Spectrograph and Imaging System (ISIS) on the 4.2-metre William Herschel Telescope (WHT). During the course of my Ph.D. studies, spectroscopic data for nine of the remaining ZP5 objects were obtained between August 2008 and June 2009 using the Gemini Multi-Object Spectrograph (GMOS) on the 8.1-metre Gemini North telescope. In this chapter I first provide details of the observations (Section 2.1) and data reduction (Section 2.2) for the Gemini data (these data being those acquired and reduced during the course of my Ph.D. studies). A similar reduction procedure was followed for the WHT data reduced by C. Willott and this I outline, together with the WHT observations, in Section 2.3.

### 2.1 Observations

As discussed above, spectroscopic data for 15 ZP5 objects was already available from earlier observations using the WHT. Objects observed in our Band 3 Gemini time in semesters 2008B and 2009A were chosen at random from the ZP5 objects left unobserved

Source (1)	R.A. (2)	Dec. (3)	z (4)	Semester (5)	Time (s) (6)
3C172	07 02 08.32	+25 13 53.9	0.519	2008B	2400
3C200	08 27 25.38	+29 18 45.5	0.458	2008B	2400
3C295	14 11 20.65	+52 12 09.0	0.464	2009A	2400
3C427.1	21 04 07.07	+76 33 10.8	0.572	2008B	4800
6C0857+3945	08 57 43.56	+39 45 29.0	0.528	2008B	4200
6C1303+3756	13 03 44.26	+37 56 15.2	0.470	2009A	8400
7C0219+3423	02 19 37.83	+34 23 11.2	0.595	2008B	10200
7C1731+6638	17 31 43.84	+66 38 56.7	0.562	2008B	9600
7C1806+6831	18 06 50.16	+68 31 41.9	0.580	2008B	9600

Table 2.1: Objects observed in semesters 2008B and 2009A using the Gemini Multi-Object Spectrograph (GMOS) on Gemini North. Column 1 lists the radio galaxy names and columns 2 and 3 list the J2000 source coordinates. Column 4 lists the object redshifts, column 5 lists the semester of observation and column 6 lists the total integration time (in seconds) of the useable frames.

from previous observing runs. The objects observed are listed in Table 2.1. For the observations I used the B600\_G5303 grating (and subsequently the new B600\_G5307 grating) together with a 0.75 arcsec slit. This gives a spectral resolution of 0.40 nm. I used 2 (spectral) by 4 (spatial) binning in 2008B, and 4 (spectral) by 2 (spatial) binning in 2009A. The binning regimes were different due to an error in the setup, although the final signal-to-noise ratios (dependent on the number of pixels binned) and the resolution (dependent on the slit width) are unaffected by this. I also used slow readout, low gain and three amplifiers. The GMOS On-Instrument Wavefront Sensor (OIWFS) was used for guiding. As far as possible (within the constraint of locating a suitable guide star within the OIWFS field of view) I adopted a slit position angle that matched the position angle of the optical galaxy from McLure et al. (2004).

For each object, I split up the exposures into several observation blocks. This increased the likelihood of the programme being executed in queue-mode observing. It also allowed the removal from the final spectrum of cosmic rays and any other transient

noise present in just one observation. Within each observation block, two 600s observations were made with a central wavelength of 610nm, and a further two 600s observations were made using a central wavelength of 605nm. Between observations with the same central wavelength I applied an offset of 10 arcsec in the spatial direction. The use of two different central wavelengths allowed the gaps between the Charge-coupled Devices (CCDs) to be covered (see Section 2.2.7), whilst the offset allowed for the removal of CCD artefacts when frames with different offsets were combined (Section 2.2.4). Each observation block was repeated four times per source, thus giving a total integration time of 9600s per object. However, not all observation blocks were completed for all objects. Whilst many of the final spectra in these cases are still useable, the total integration time (listed in Table 2.1) is less than 9600s.

Within each observation block I also took one flat for each central wavelength, using the Quartz Halogen lamp and a 2s exposure each time. A flat is a spectrum of a uniformly illuminated source used to correct for the non-uniform response of pixels in the CCDs (Section 2.2.1). I obtained a CuAr arc at each central wavelength each night that science data was acquired (apart from 07/09/2008, 12/09/2008, 14/09/2008, 19/10/2008, 06/11/2008 and, in the case of the arc centred on 605nm, 13/06/2009). I used the same setup as above (with the exception of fast, rather than slow, readout) and a 25s exposure. This arc, whose spectrum is accurately known, is used for the purposes of wavelength calibration (Section 2.2.2). A standard star spectrum for use in the flux calibration (Section 2.2.5) was obtained using exactly the same instrumental setup as for the science observations, a central wavelength of 610nm, and an exposure time of 120s. In order that I could correct for the bias (Section 2.2.1), I was supplied with a bias frame obtained on 22/08/2008 (generated by reading out unexposed CCDs).

---

## 2.2 Data Reduction

Before the observed data can be used they need to be reduced in order to remove the effects of the background and the instrument on the data insofar as it is possible, as well as to calibrate the wavelength and flux information in the spectra. The motivation for each stage of the data reduction process is explained in the relevant section below.

For my data, I performed the initial data reduction (bias subtraction, cosmic ray removal, flat field correction, wavelength calibration, background subtraction, flux calibration and spectrum extraction) using the *gmoss* tools in the *gemini* Image Reduction and Analysis Facility (IRAF) package. This is described below in Sections 2.2.1 to 2.2.6. I use data from the object 7C1731+6638 to illustrate the stages in the data reduction. Since my objects are extended in the spatial direction on the CCDs (due both to their physical extent and to the effects of seeing) it is possible to extract the spectrum for each object using a variety of different apertures, with a wider aperture selecting more of the light from the object but also including more noise from the sky. I extracted my spectra using a range of apertures for each object, as described in Sections 2.2.6, 4.2.1 and 4.4.4. Following this I was left with two reduced spectra per aperture extracted for each object; one with a central wavelength of 610nm and one with a central wavelength of 605nm (see Section 2.1). I then used the Interactive Data Language (IDL) to shift and combine the two spectra for each object and produce the noise spectra, as described in Section 2.2.7.

### 2.2.1 Flatfielding, Bias Subtraction & Cosmic Ray Removal

The first effect that needs to be accounted for is the bias, which is a combination of the unique offset voltage inherent to every pixel in the CCD together with a fixed voltage which is intentionally applied to all the pixels in order to prevent the analogue-to-digital converter receiving a negative voltage due to negative fluctuations from the noise. The

---

use of a bias frame (obtained by reading out unexposed CCDs) allows this to be removed. Secondly, the flat fields (exposures of a uniform source) allow the non-uniform response of the CCDs to be taken into account.

The first step in the data reduction process was therefore to combine the flat fields into master flats for use in the flat field correction. I split the 2008B observations into two groups: one containing all the observations in the date range 05/08/2008 to 04/09/2008, and the second containing all the observations in the date range 07/09/2008 to 26/11/2008. I treated the 2009A observations (where all of the science data was taken on 13/06/2009 and the standard star on 10/08/2009) as one group. Within each group I used *gsflat* to combine all the Quartz Halogen flats at each central wavelength into one master flat, thus creating a master flat centred on 610nm and a master flat centred on 605nm for each group. The bias frame taken on 22/08/2008 was used for the bias subtraction for each group.

Figure 2.1 shows the two master flats produced for the first 2008B observation group. This group contains all the observations for 7C1731+6638, which I will use below to illustrate the data reduction. In order to produce master flats for the standard stars I repeated this procedure, using only the flat taken on the night of each standard star observation (14/09/2008 in 2008B, 10/08/2009 in 2009A).

Using the *splot* task in the *onedspec* IRAF package I determined the full width at half maximum (FWHM) of the lines in my arc spectra to be  $4.0\text{\AA}$  for the 2008B arcs and  $3.7\text{\AA}$  for the 2009A arcs. Since the arc lines are unresolved these are a good measurement of the spectral resolution of the data. I set the *gscrrej.datares* parameter equal to this in readiness for the cosmic ray subtraction. I also used *gscut* on each of the incombined flat files produced by *gsflat* to determine the chip edge locations (required by the reduction software).

I then used the *gsreduce* task to reduce the standard star and all of the science frames

---

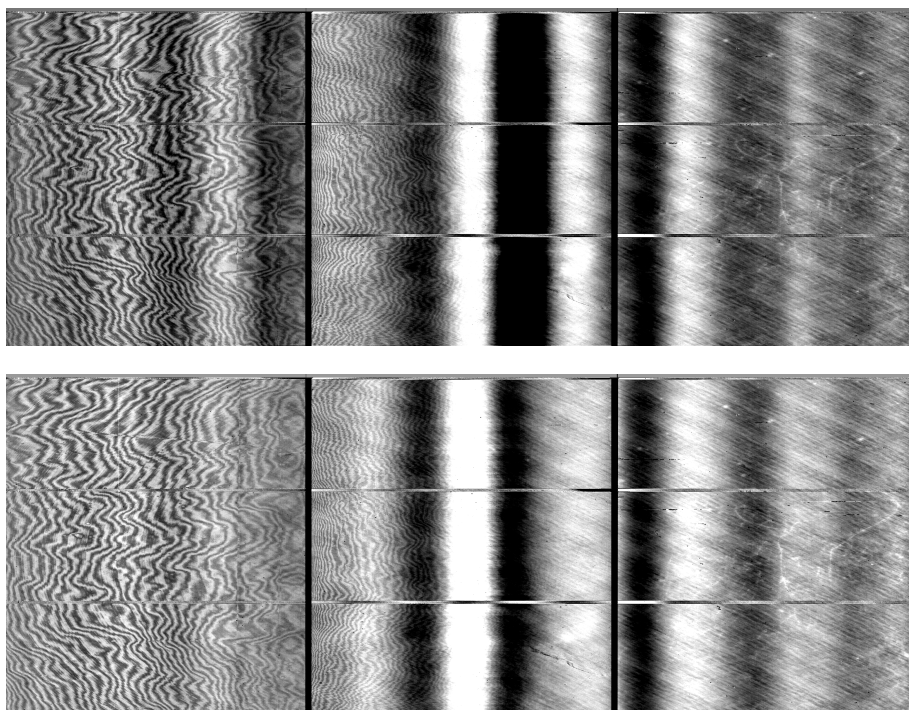


Figure 2.1: The master flats for the first 2008B observation group (see Section 2.2.1), with central wavelengths of 610nm (top) and 605nm (bottom).

(subtracting the bias, cleaning for cosmic rays, and applying the flat field correction). The 22/08/2008 bias frame was used for the bias subtraction. For each science frame I used the master flat (with the correct central wavelength) made from the group whose dates contained the science observation date. The standard star flat was used for the standard star reduction. Finally, I repeated the *gsreduce* step for all my arc images but with no cosmic ray subtraction or flat field correction. This is because in this case only the position of the bright lines is of interest, for which correcting for the flat field is unnecessary. In addition, cosmic ray hits are negligible since the integration time is short.

In Figure 2.2 I show four of the unreduced science frames for 7C1731+6638 (with a central wavelength of 610nm), followed by the same frames after the *gsreduce* step in Figure 2.3.

---

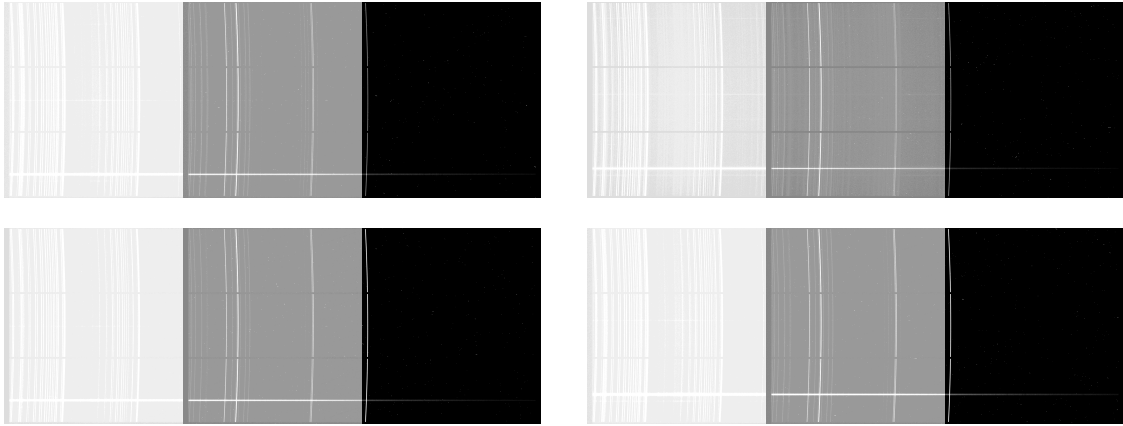


Figure 2.2: Four of the unreduced science frames for the object 7C1731+6638, centred on a wavelength of 610nm (see Section 2.2.1).

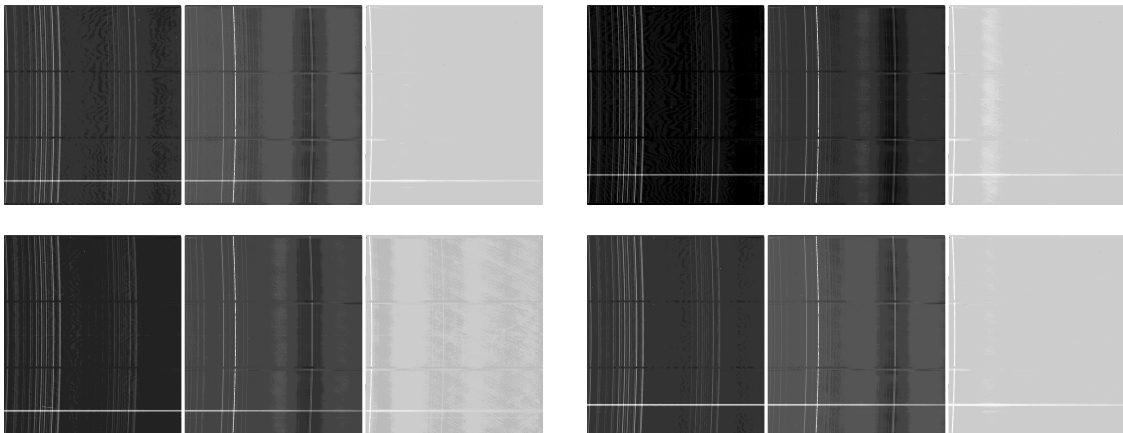


Figure 2.3: Four of the science frames with a central wavelength of 610nm following the *gsreduce* task for the object 7C1731+6638 (see Section 2.2.1).

### 2.2.2 Wavelength Calibration

The next step in the data reduction process is to calibrate the wavelength information to ensure that the correct wavelengths are determined for features in the spectra. This calibration was achieved using the CuAr arcs, whose spectra are accurately known, and I used *gswavelength* to find a wavelength solution for each of my arcs. Each time I checked and accepted the wavelength solution using the interactive fit.

Next I applied the wavelength solutions to the science data and standard stars using the *gstransform* task. In each case I used the arc taken on the night of observation at the correct central wavelength, with the following exceptions:

- Four frames of 7C1806+6831 were observed on 07/09/2008, but no arcs. Arcs from 08/09/2008 were used instead.
- 12 frames of 7C0219+3423 were observed on 12/09/2008, but no arcs. Arcs from 10/09/2008 were used instead.
- The 2008B standard star was observed on 14/09/2008, but no arcs. An arc from 16/09/2008 was used instead.
- Four frames of 3C427.1 were observed on 19/10/2008, but no arcs. Arcs from 21/10/2008 were used instead.
- Four frames of 7C0219+3423 and four frames of 3C172 were observed on 06/11/2008, but no arcs. Arcs from 03/11/2008 were used instead.
- All of the 2009A science data was observed on 13/06/2009, along with the arc centred on 610nm. The arc centred on 605nm was taken on 01/10/2009.

I then checked that the wavelength calibration for all of these was correct using the position of the sky lines in the spectra.

---

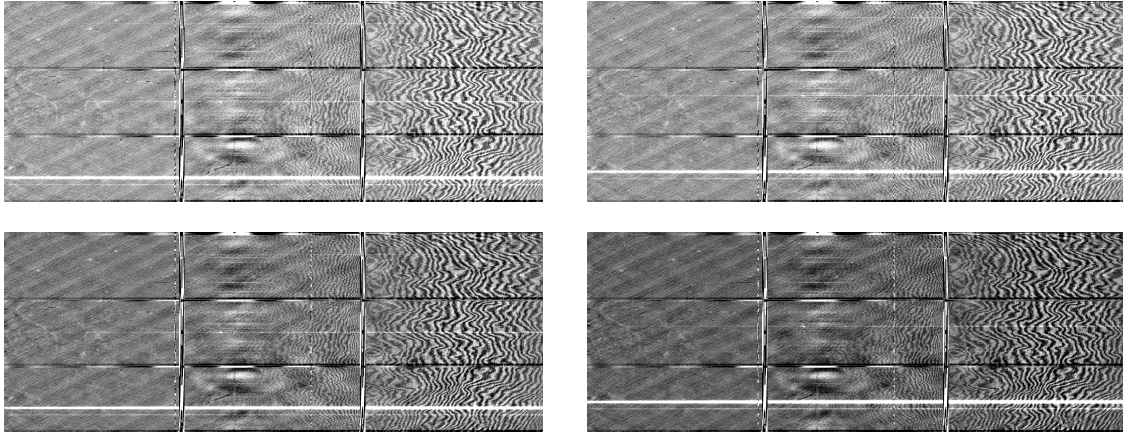


Figure 2.4: Four of the science frames with a central wavelength of 610nm following the background subtraction for the object 7C1731+6638 (see Section 2.2.3). Note the heavy fringing at the red (right) end of the spectra.

### 2.2.3 Background Subtraction

As the next stage in the data reduction, the contribution to the spectrum from the sky background is determined using a fit to object-free regions of the spectrum and subtracted in order to ensure the signal in the spectrum is, as far as possible, from the source rather than from the sky background. Background subtraction removes the variability between columns in the spectra, particularly the variation in intensity at different wavelengths due to emission from sky lines. To perform the background subtraction, the *gsskysub* task was used to fit a polynomial of order four to each of the columns in order to remove large scale variations in the spatial direction. For each image I used a central column for the interactive fit and only fitted over rows free of objects. If I did not mask out the rows with objects in, the polynomial would try to fit these peaks and lead to the subtraction of flux from real objects, which is obviously undesirable. Figure 2.4 shows four of the 7C1731+6638 frames (with a central wavelength of 610nm) after background subtraction.

---

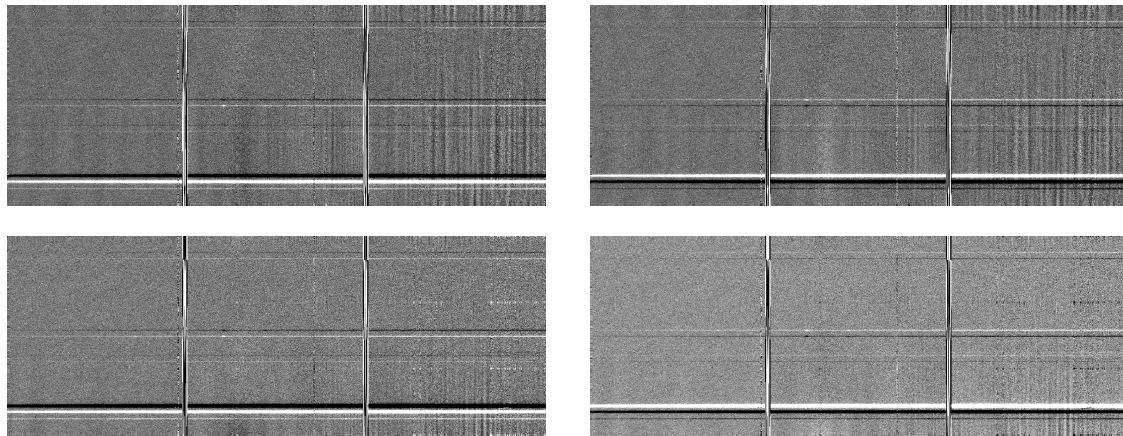


Figure 2.5: Four of the de-fringed science frames with a central wavelength of 610nm for the object 7C1731+6638 (see Section 2.2.4).

### 2.2.4 De-fringing and Frame Combination

At this stage in the data reduction process, the spectra exhibit notable fringes, particularly at the red ends. This is caused by the interference of incoming photons (with a wavelength comparable to the depth of the CCD) with reflected photons. Before combining the individual frames it was therefore necessary to remove fringing in the data.

To remove the fringing from any given frame I used the companion frame taken in the same observation block at the same central wavelength but with a 10 arcsec spatial offset (Section 2.1). I used the IRAF *imarith* task to subtract this companion frame from the data frame in question. Where an observing block was incomplete, leaving an unpaired frame, I instead used the nearest possible frame for that object with a complementary offset and the correct central wavelength. In Figure 2.5 I show four of the de-fringed frames for 7C1731+6638 (with a central wavelength of 610nm).

Since *imarith* does not preserve the ‘EXPTIME’ exposure time header keyword it was necessary to manually extract the value of EXPTIME (using *hselect*) from the header of each given frame and add it to the header of the corresponding de-fringed frame (using *hedit*) in order to prevent problems with the flux calibration (Section 2.2.5).

Once all of the data were de-fringed I was able, for each object, to combine all the data

---

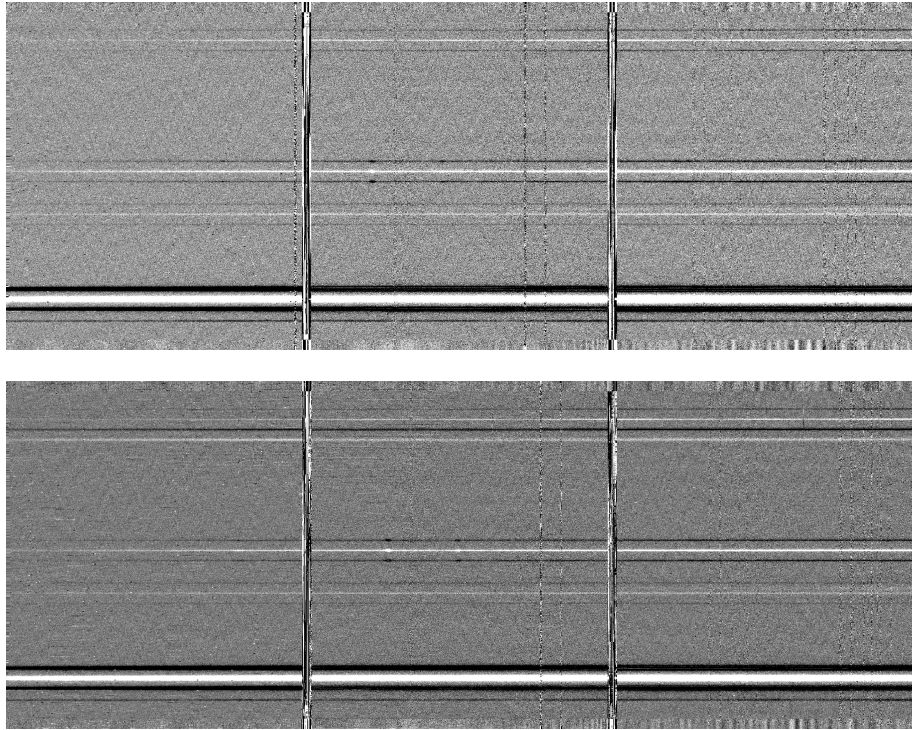


Figure 2.6: The combined science frames for 7C1731+6638 (see Section 2.2.4), with central wavelengths of 610nm (top) and 605nm (bottom).

that shared a central wavelength into one frame, thus creating two master frames for each object (one with a central wavelength of 610nm, the other with a central wavelength of 605nm). This was accomplished using the *imcombine* task with appropriate spatial offsets (measured directly from the spectra in each case). Figure 2.6 shows the 7C1731+6638 summed images for each central wavelength.

### 2.2.5 Flux Calibration

Once the frames have been combined their flux data must be calibrated to ensure that they are correct for the subsequent analysis. This calibration is performed using the observed spectrum of the standard star, whose true spectrum (including the flux data) is accurately known. In order to do this it was necessary to extract the standard star spectrum using the IRAF *apsum* task in interactive mode. The ‘line’ parameter was set to the central line

---

of the spectrum continuum and the ‘nsum’ parameter to 200, which sums the flux over 200 columns (in order to ensure a high enough signal-to-noise ratio). I used a full width at zero intensity (FWZI) aperture for the extraction, to enclose all of the flux from the standard star.

I next used the IRAF *standard* task (with default parameters, except for the required observation information) and an interactive fit (avoiding telluric absorption features) to compare my standard star observation with the calibration data. The *standard* task integrates the observed standard star flux over calibration bandpasses and writes these integrated fluxes, along with the corresponding calibration fluxes (taken from IRAF’s standard star calibration files), to a file. This file is then used by the IRAF *sensfunc* task to generate a sensitivity function (a fitted polynomial of order six) which was applied to the spectra using the *fluxcalib* task.

### 2.2.6 Aperture Extraction

Once the frames are flux calibrated, the spectrum in the correct aperture must be extracted from these frames (which contain many rows of spectral data, corresponding to different spatial positions along the spectrograph slit). In other words, the correct row(s) in the spatial direction must be extracted for the object of interest to produce a single spectrum.

The IRAF *apsum* task was once again used, as before, but this time on the science frames in order to extract the spectra of my objects. The spectra were extracted over a variety of apertures (see Sections 2.2, 4.2.1 and 4.4.4): full width at three-quarters intensity (FWTQI), FWHM, FWZI, and over the aperture corresponding to the effective radius ( $r_e$ ). For the latter, the effective radius (from McLure et al. 2004) was used along with the angular diameter distance ( $d_A$ ) to calculate the angle subtended by  $r_e$  ( $\theta_{rad}$ ):

$$\theta_{rad} = \frac{r_e}{d_A}. \quad (2.1)$$

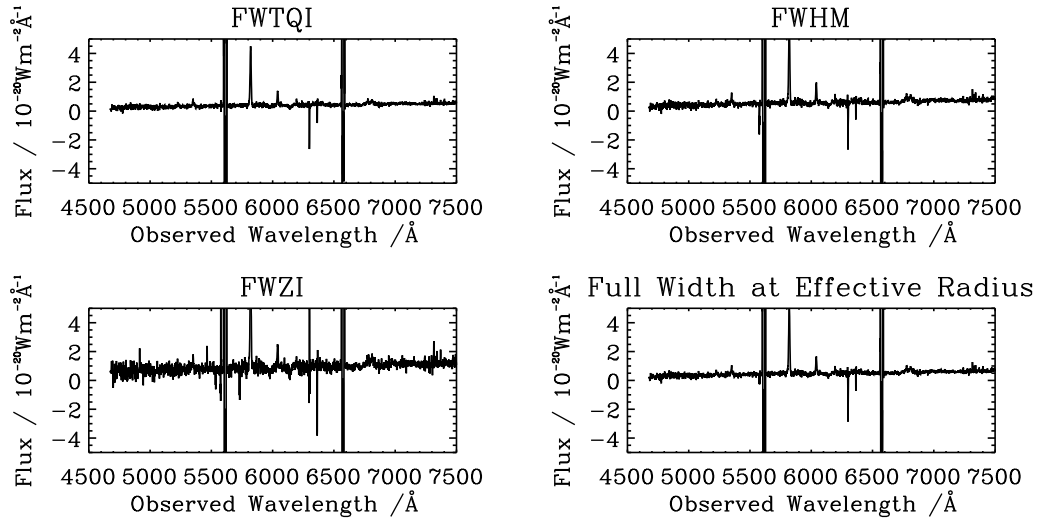


Figure 2.7: The one-dimensional spectra for 7C1731+6638 with a central wavelength of 610nm, extracted using the four apertures discussed in the text (see Section 2.2.6): full width at three-quarters intensity (FWTQI), full width at half maximum (FWHM), full width at zero intensity (FWZI), and the aperture corresponding to the effective radius,  $r_e$ . The large spikes in the spectra are due to the chip gaps at approximately 5595–5635Å and 6555–6595Å.

This, converted into arcseconds ( $\theta_{arcsec}$ ), was used along with the detector pixel scale ( $P$ ) to determine the aperture to extract in pixels:

$$Aperture = \frac{\theta_{arcsec}}{P} \quad (2.2)$$

I show the extracted spectra for 7C1731+6638 in Figures 2.7 (central wavelength of 610nm) and 2.8 (central wavelength of 605nm).

### 2.2.7 Spectrum Combination and Noise

The final step in the data reduction is to combine the spectra produced at each central wavelength (610nm and 605nm) for each aperture and each object into a single spectrum for each aperture and each object, along with the corresponding noise spectrum, ready for the subsequent analysis. Since there are two gaps between the CCDs in the spectral

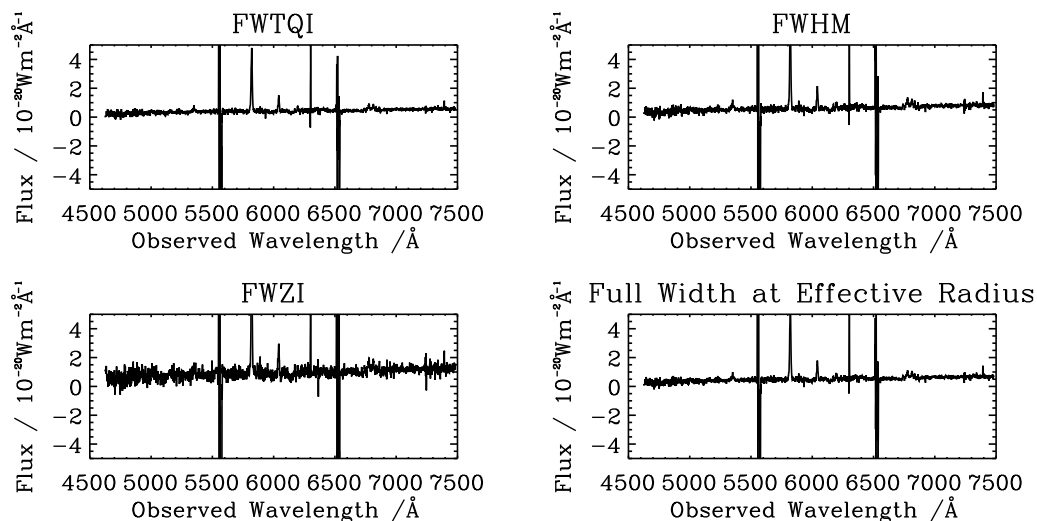


Figure 2.8: The extracted spectra for 7C1731+6638 with a central wavelength of 605nm, extracted using the four apertures discussed in the text (see Section 2.2.6): full width at three-quarters intensity (FWTQI), full width at half maximum (FWHM), full width at zero intensity (FWZI), and the aperture corresponding to the effective radius,  $r_e$ . The large spikes in the spectra are due to the chip gaps at approximately 5545–5585Å and 6505–6545Å.

direction, each of the two individual spectra for any object will have corresponding regions without any data. However, since each of the two spectra have a different central wavelength, the wavelength ranges of these empty regions are different for each of the spectra. Combining the two individual spectra for each object thus produces a final spectrum without any gaps. For wavelengths which do not correspond to a CCD gap in either the 610nm centred or the 605nm centred spectra (the majority of the spectrum), the final signal-to-noise ratio is increased by combining the two individual spectra in this way.

Firstly, I used cubic convolution interpolation in IDL to transform the spectrum centred on 605nm into one with data points at wavelengths identical to the spectrum centred on 610nm. The two spectra were then median combined, where for each data point the final flux was taken to be the midpoint between the flux values of the two constituent spectra. I then normalised the resulting single spectrum to a mean flux of one (in preparation for the spectral fitting in Section 4.2.1). Chip edges in the constituent spectra were

removed by using only the alternative spectrum in these regions.

The noise was calculated from the reduced two-dimensional frames (Section 2.2.5), using regions of the image free from spectra or other artefacts. For each column, I calculated the flux in a series of apertures (of the same size as the spectrum extraction in Section 2.2.6) from these blank regions and calculated the standard deviation of the flux measurements to yield the noise in that column. The noise spectrum centred on a wavelength of 605nm was interpolated to give data points at wavelengths identical to the spectrum centred on 610nm. For each object and aperture I then median combined the two noise spectra (corresponding to the two different central wavelengths) and divided by a factor of  $\sqrt{2}$  in order to produce the single noise spectrum. I divided this by the correct galaxy spectrum normalisation factor before converting to a signal-to-noise spectrum. I note that, using this method, the noise in the chip edge regions will be too low by a factor of  $\sqrt{2}$ . Upon testing this, however, it is found to have a negligible effect on the results presented in Chapters 3 and 4.

Regions of the spectra known to contain emission-line features common to radio galaxies [rest frame 3718–3740Å ([OII]<sub>3727</sub>), 3859–3880Å ([NeIII]<sub>3869</sub>), 3963–3978Å ([NeIII]<sub>3967</sub>), 4095–4112Å ([Hδ]<sub>4102</sub>), 4332–4378Å ([Hγ]<sub>4341</sub>), 4674–4698Å ([HeII]<sub>4686</sub>), 4854–4875Å ([Hβ]<sub>4861</sub>) and 4945–5021Å ([OIII]<sub>4959</sub> and [OIII]<sub>5007</sub>)] or telluric absorption features (5570–5585Å, 6864–6911Å and 7166–7323Å) were masked (in preparation for the 4000Å break calculation in Section 3.2.1 and the spectral fitting in Section 4.2.1) by setting the signal-to-noise to zero. Additional masks were also used for any remaining chip artefacts.

Figures 2.9 to 2.12 show the final galaxy and signal-to-noise spectra for each aperture, as used in Chapters 3 and 4.

---

## 2.3 WHT Observations & Data Reduction

The objects observed in August 2002 using the ISIS spectrograph on the WHT were chosen to have  $z < 0.5$  so that satisfactory signal-to-noise ratios could be obtained without excessively long integration times. This constraint aside, the objects were chosen at random from the objects in the full sample that were visible on the dates of observation. Details of the objects observed with the WHT can be found in Table 2.2. The R316R grating on the red arm was used together with a 1.0 arcsec slit resulting in a resolution of 3.7 Å full width at half maximum (FWHM). The central wavelength used was dependent on the redshift such that the spectra contained the *Mgb* complex to determine the velocity dispersion (see Section 4.2.1). Each object was observed for a total integration time of 7200s, split into three 2400s observations to allow the removal of cosmic rays.

As for the Gemini data described in Sections 2.1 and 2.2, the data were reduced in order to remove the effects of the instrument as far as possible. This was done using standard Image Reduction and Analysis Facility (IRAF) routines following the same procedure (bias subtraction, flat-fielding, wavelength-calibration and flux-calibration) as described in Section 2.2 for the GMOS data. Coaddition (the combining of the individual frames for each object into one final frame) was done using an average sigma-clipping routine, in which the final pixel value is calculated as the mean of the constituent pixel values, discarding for each pixel any values which fall more than two standard deviations away from the initial mean pixel value.

The WHT observations and data reduction had been performed by C. Willott prior to the start of my Ph.D. studies. I used the reduced data, along with the apertures and the procedure described in Section 2.2.6, to extract the one-dimensional spectra of my objects. I also calculated the noise spectra, and masked emission lines ionised by the central engine and telluric absorption features, using the procedure described in Section 2.2.7. I show the final galaxy and signal-to-noise spectra for each aperture in Appendix A.

---

Source (1)	R.A. (2)	Dec. (3)	$z$ (4)
3C16	00 37 45.39	13 20 09.6	0.405
3C19	00 40 55.01	33 10 07.3	0.482
3C46	01 35 28.47	37 54 05.7	0.437
3C244.1	10 33 33.97	58 14 35.8	0.428
3C341	16 28 04.04	27 41 39.3	0.448
3C457	23 12 07.57	18 45 41.4	0.428
6C0825+3407	08 25 14.59	34 07 16.8	0.406
6C0850+3747	08 50 24.77	37 47 09.1	0.407
7C0213+3418	02 13 28.39	34 18 30.6	0.465
7C0810+2650	08 10 26.10	26 50 49.1	0.435
TOOT0009+3523	00 09 46.90	35 23 45.1	0.439
TOOT0018+3510	00 18 53.93	35 10 12.1	0.416
TOOT1626+4523	16 26 48.50	45 23 42.6	0.458
TOOT1630+4534	16 30 32.80	45 34 26.0	0.493
TOOT1648+5040	16 48 26.19	50 40 58.0	0.420

Table 2.2: Objects observed in August 2002 using the Intermediate dispersion Spectrograph and Imaging System (ISIS) on the William Herschel Telescope (WHT). Column 1 lists the radio galaxy names, columns 2 and 3 list the J2000 source coordinates and column 4 lists the object redshifts.

## 2.4 Summary

In this chapter, I have described the observations and data reduction used to obtain spectroscopic data of nine of the ZP5 objects. The observations were made between August 2008 and June 2009 using the GMOS spectrograph on the Gemini North telescope. I have used standard tools in the *gemini* IRAF package to reduce the data before combining individual frames and calculating noise spectra using a program written in IDL. I have also outlined the observations and data reduction performed by C. Willott to obtain spectroscopic data of a further 15 of the ZP5 objects using the ISIS spectrograph on the WHT.

---

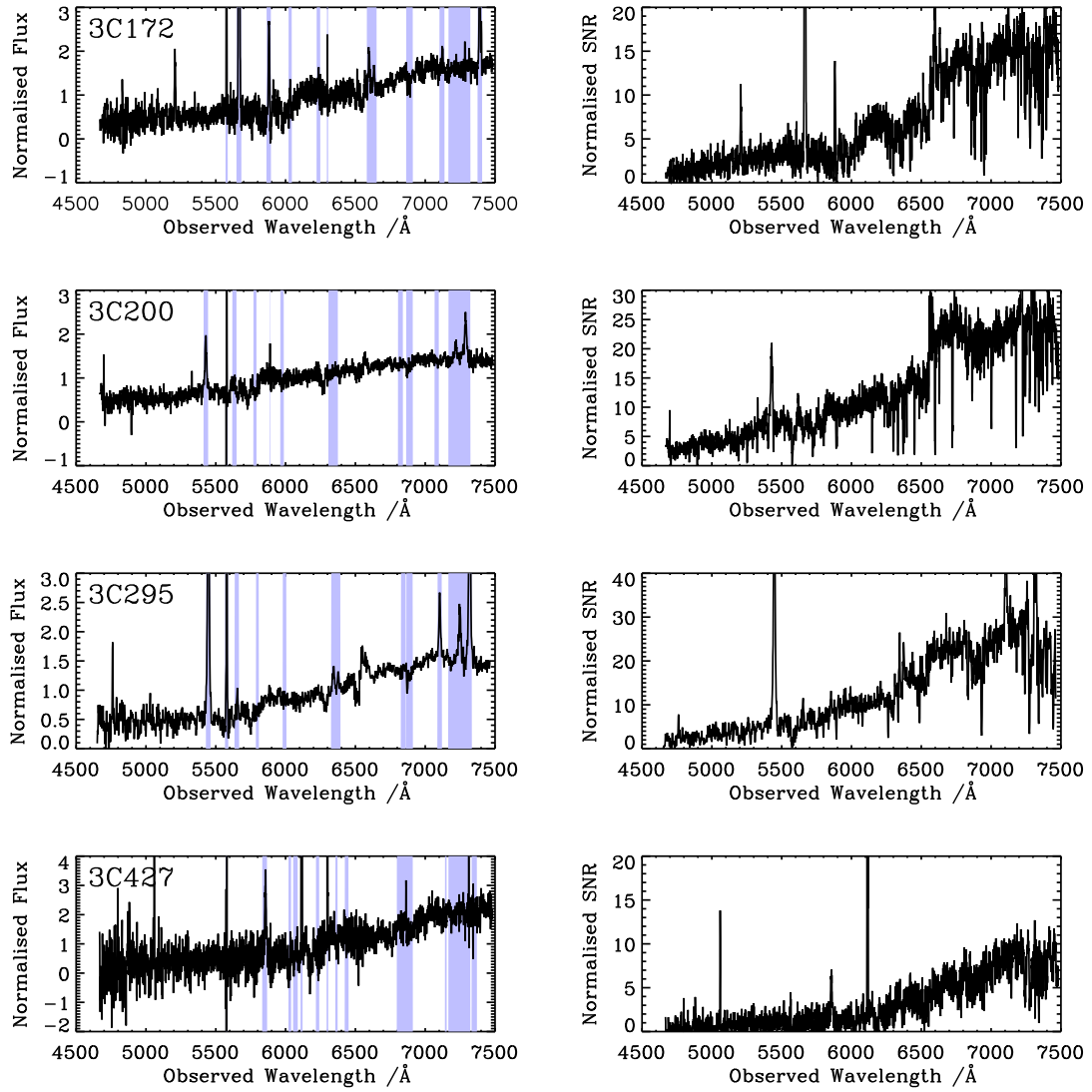


Figure 2.9: The final galaxy (left panels) and signal-to-noise (right panels) spectra for the full width at three-quarters intensity (FWTQI) aperture. Each galaxy spectrum is normalised to a mean flux of one, and the corresponding noise spectrum is divided by the same normalisation factor before conversion to a signal-to-noise spectrum (Section 2.2.7). The shaded areas indicate regions which are masked due to the presence of emission or telluric absorption features or chip artefacts, as discussed in the text (Section 2.2.7).

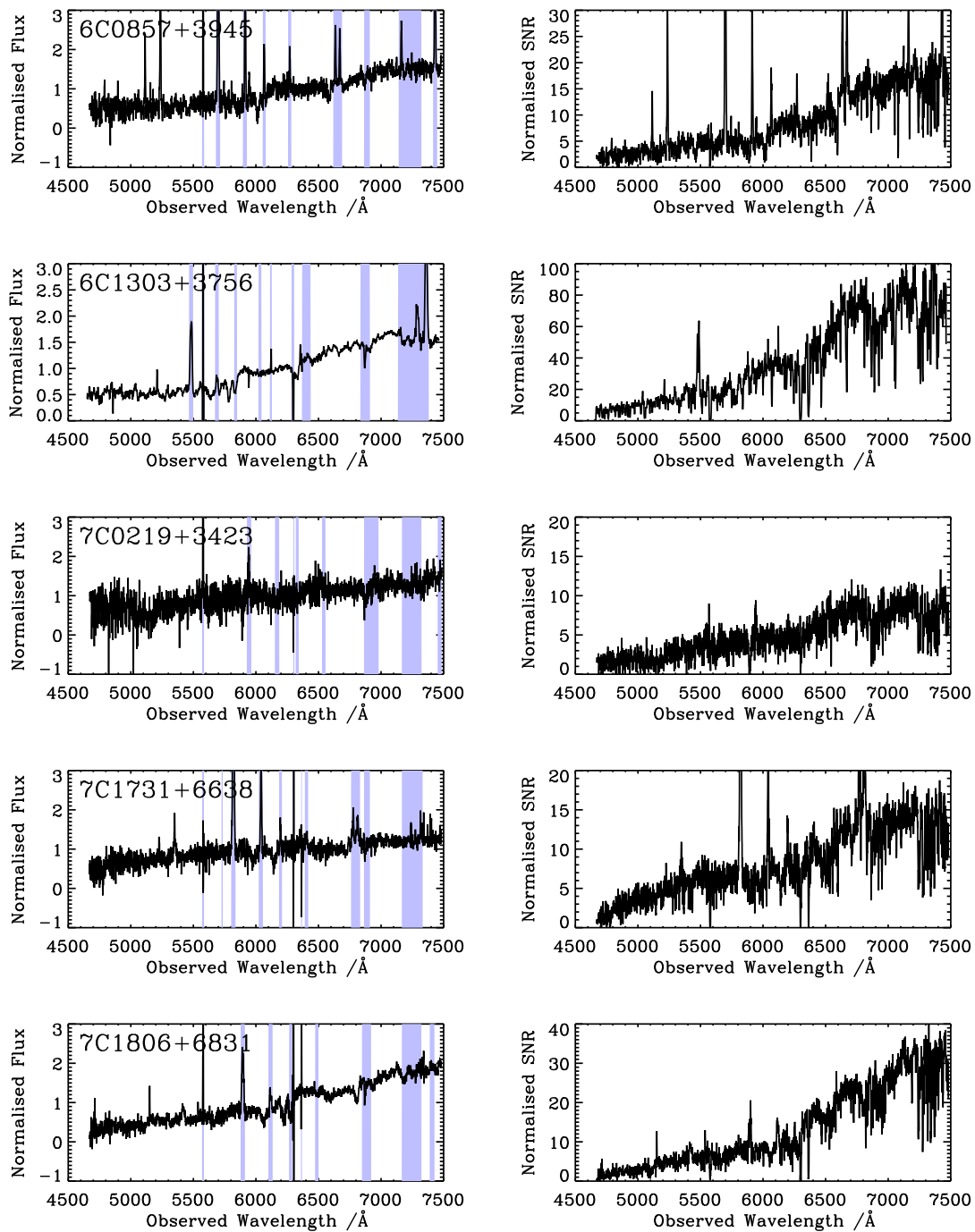


Figure 2.9 continued.

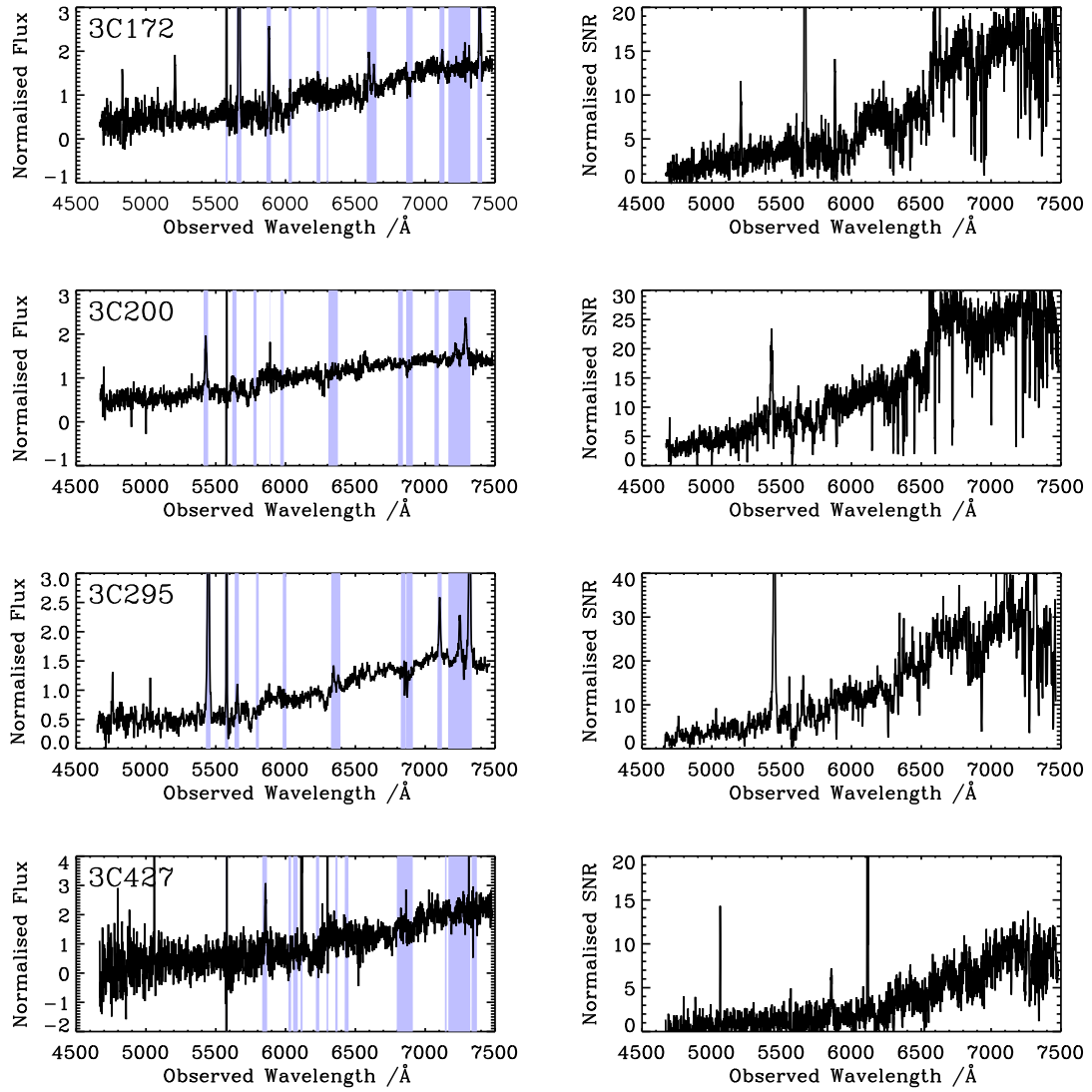


Figure 2.10: The final galaxy (left panels) and signal-to-noise (right panels) spectra for the full width at half maximum (FWHM) aperture. Each galaxy spectrum is normalised to a mean flux of one, and the corresponding noise spectrum is divided by the same normalisation factor before conversion to a signal-to-noise spectrum (Section 2.2.7). The shaded areas indicate regions which are masked due to the presence of emission or telluric absorption features or chip artefacts, as discussed in the text (Section 2.2.7).

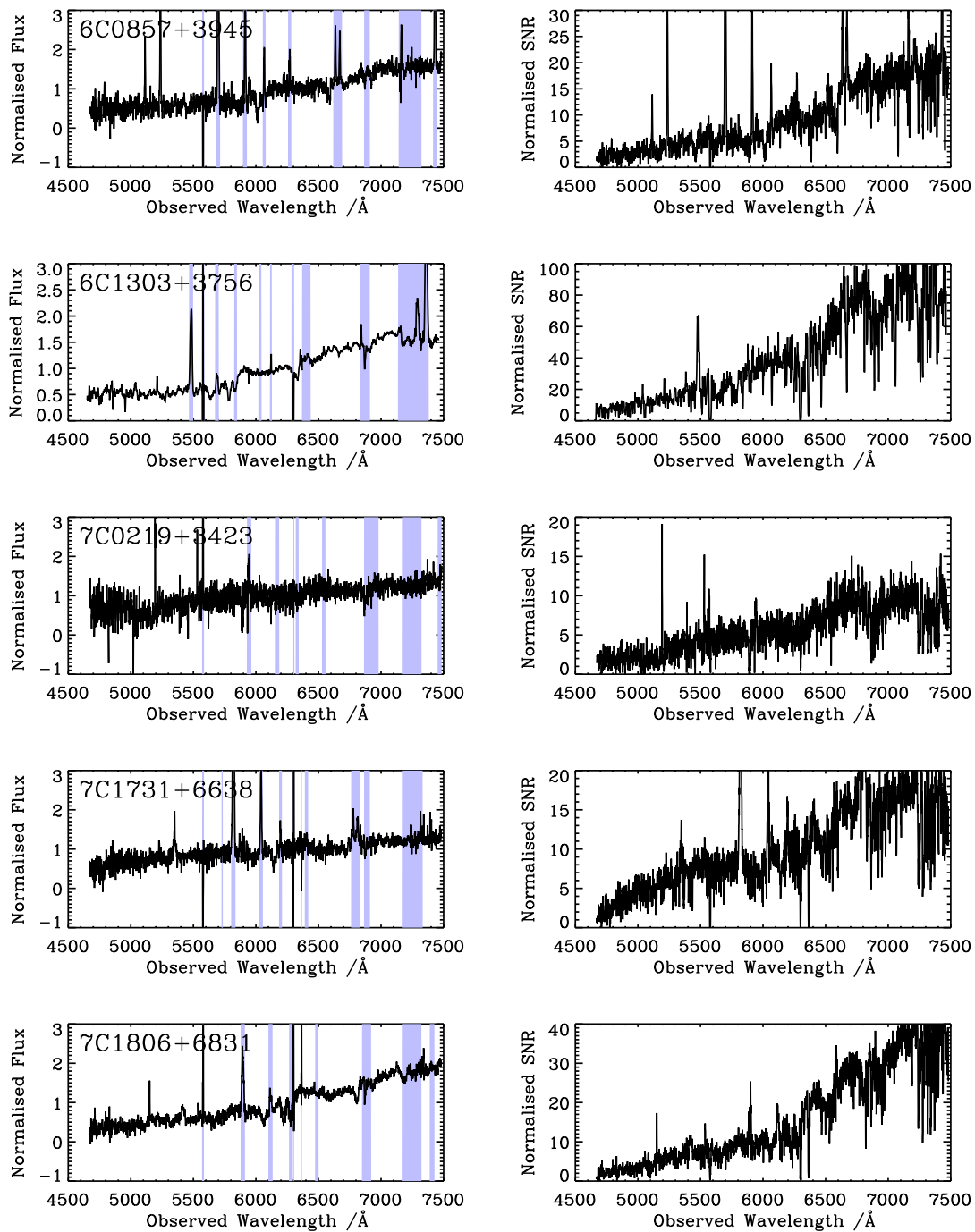


Figure 2.10 continued.

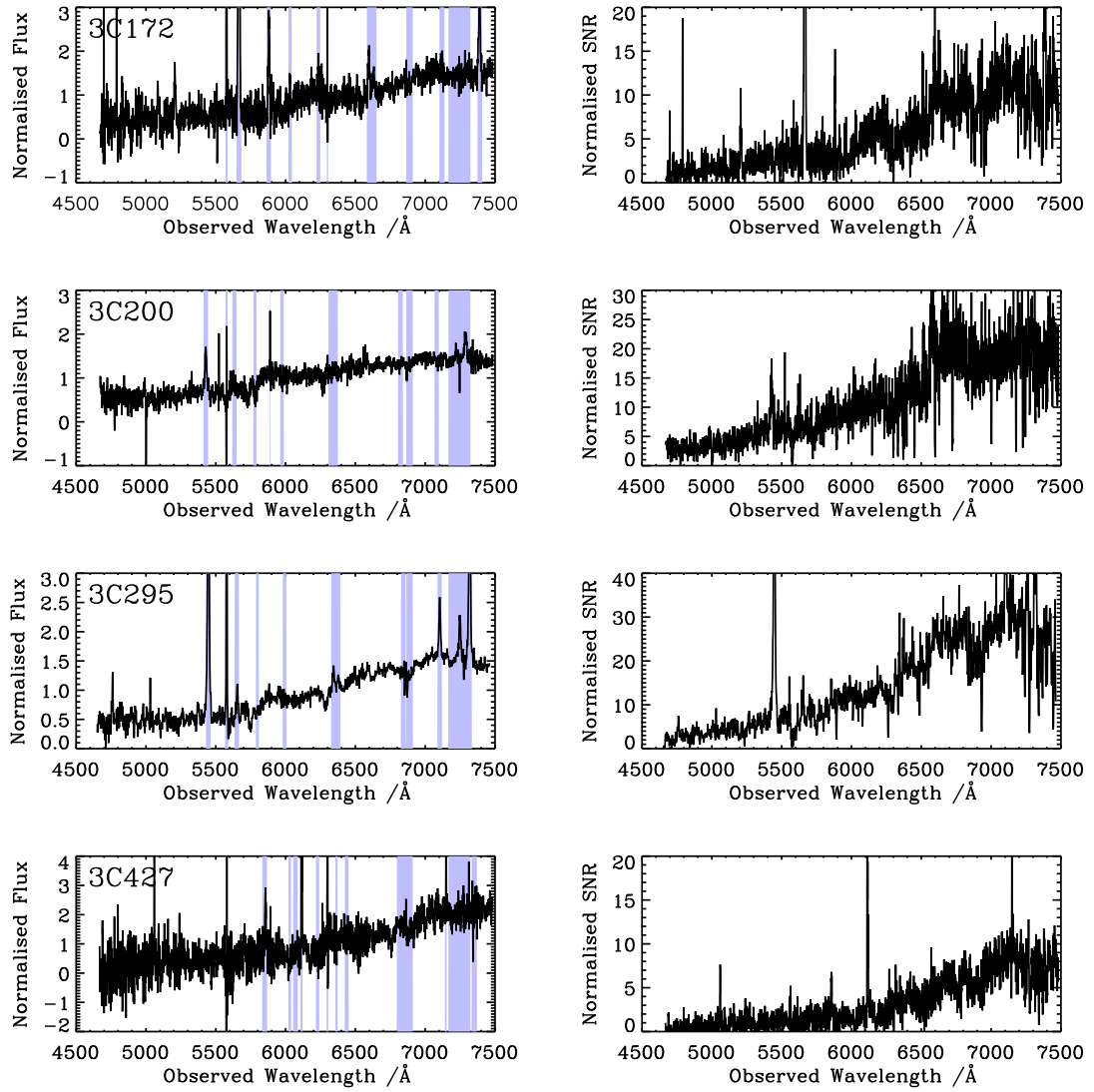


Figure 2.11: The final galaxy (left panels) and signal-to-noise (right panels) spectra for the full width at zero intensity (FWZI) aperture. Each galaxy spectrum is normalised to a mean flux of one, and the corresponding noise spectrum is divided by the same normalisation factor before conversion to a signal-to-noise spectrum (Section 2.2.7). The shaded areas indicate regions which are masked due to the presence of emission or telluric absorption features or chip artefacts, as discussed in the text (Section 2.2.7).

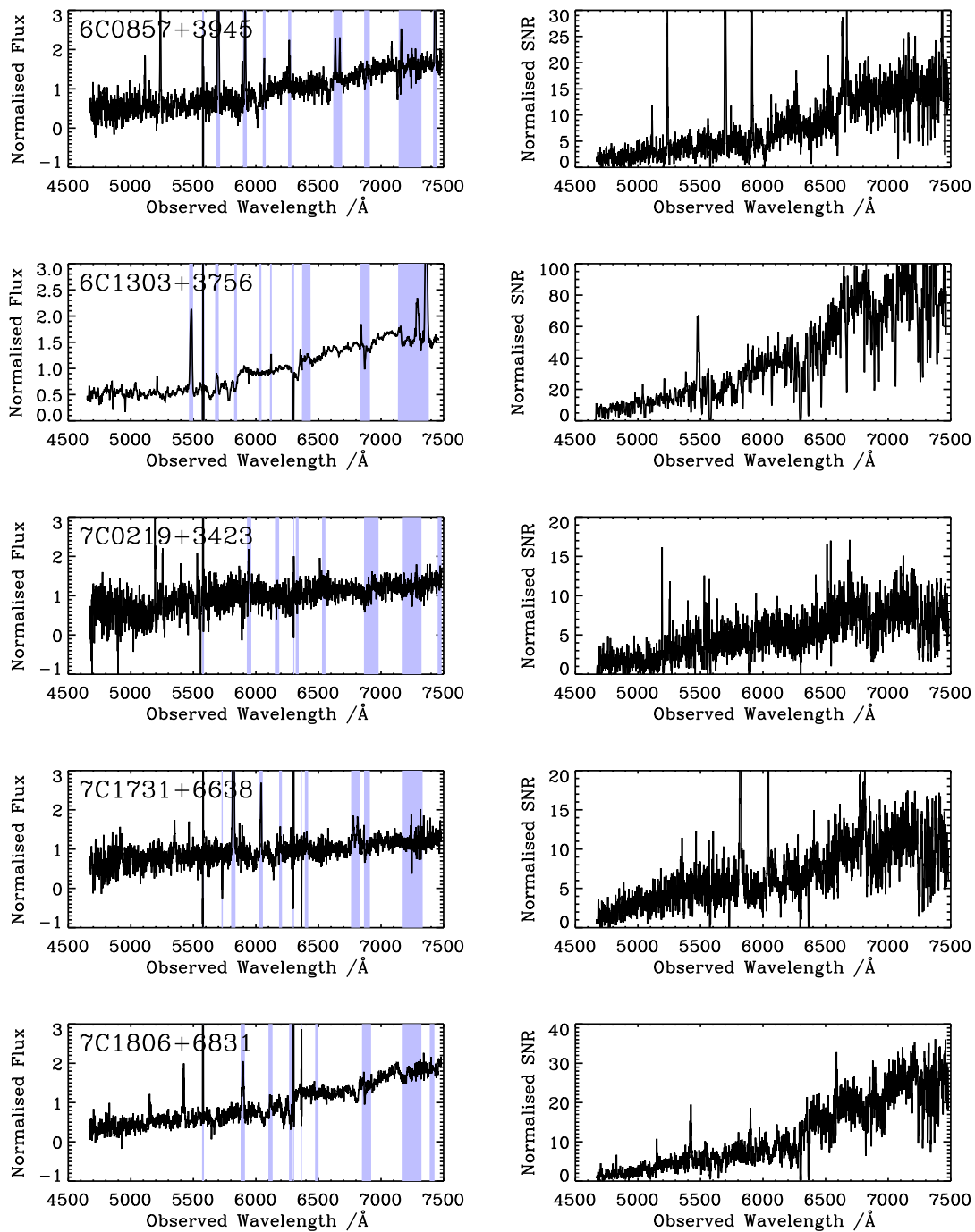


Figure 2.11 continued.

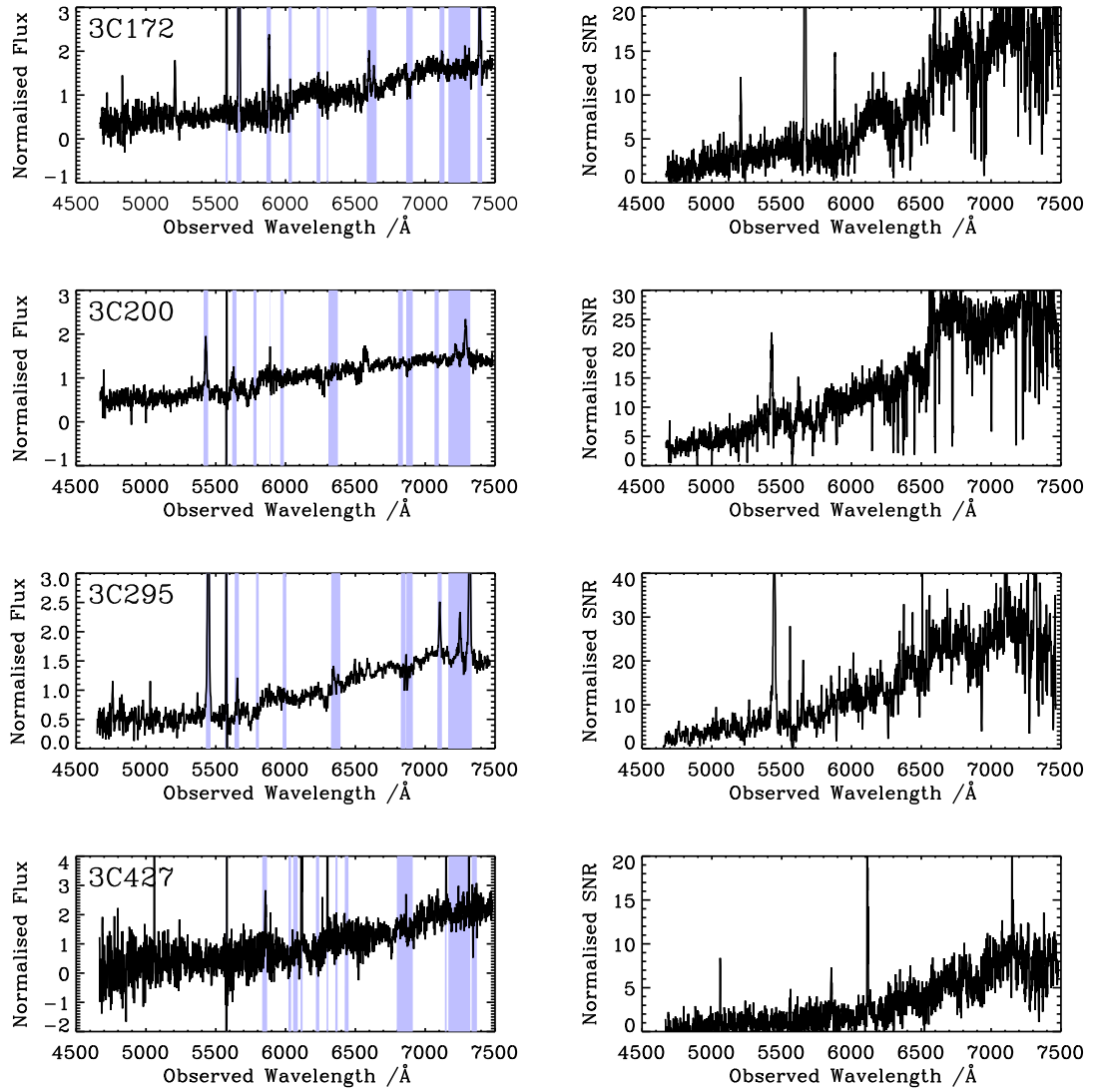


Figure 2.12: The final galaxy (left panels) and signal-to-noise (right panels) spectra for the apertures corresponding to the effective radii of the objects. Each galaxy spectrum is normalised to a mean flux of one, and the corresponding noise spectrum is divided by the same normalisation factor before conversion to a signal-to-noise spectrum (Section 2.2.7). The shaded areas indicate regions which are masked due to the presence of emission or telluric absorption features or chip artefacts, as discussed in the text (Section 2.2.7).

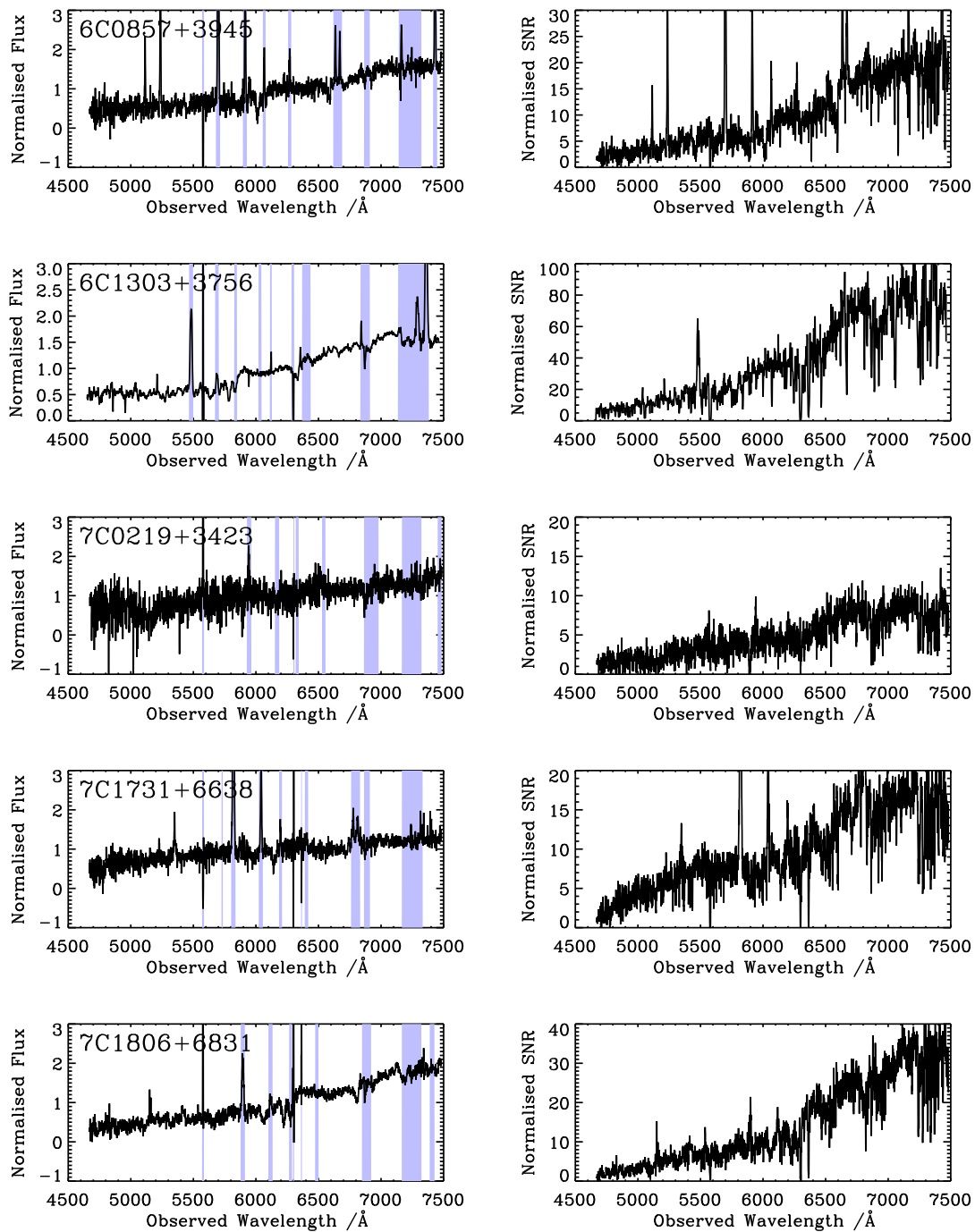


Figure 2.12 continued.

# Chapter 3

## Star Formation Histories

In this chapter I study the 24 galaxies from my full  $z \sim 0.5$  (ZP5) sample for which I have spectroscopic data (see Chapter 2) and use the strength of the  $4000\text{\AA}$  break as an indicator of recent star formation. I compare this with radio luminosity, optical spectral classification and morphological classification. I describe the data in Section 3.1, followed by my analysis in Section 3.2. I present my results in Section 3.3 before concluding in Section 3.4. The content of this chapter has been published in Herbert et al. (2010).

### 3.1 Spectroscopic Data

In this chapter and in Chapter 4 I use a subsample of the full  $z \sim 0.5$  radio galaxy sample, namely the 24 objects for which spectroscopic data has been obtained. These objects are listed in Table 3.1. Nine of the objects were observed using the 8.1-metre Gemini North telescope, and the observations and data reduction have been described in Chapter 2. The remaining objects were observed in August 2002 using the Intermediate dispersion Spectrograph and Imaging System (ISIS) on the 4.2-metre William Herschel Telescope (WHT), and the observations and data reduction have been outlined in Section 2.3.

The objects comprising the subsample were selected randomly from those visible on

the dates of observation (with the constraint that  $z < 0.5$  for those objects observed using the WHT), rather than on the basis of their radio or host galaxy luminosity. That the subsample is representative of the whole  $z \sim 0.5$  sample is highlighted by a two-sample Kolmogorov-Smirnov (K-S) test on the logarithms of the 151 MHz radio luminosities of the objects in the full sample and in the subsample, which gives a probability of  $>99.9\%$  that they are drawn from the same underlying distribution and thus the null hypothesis cannot be rejected. Furthermore, a two-sample K-S test on the host magnitudes of the objects in the full sample and in the subsample gives a probability of 75% that they are drawn from the same underlying distribution and thus once again the null hypothesis cannot be rejected.

## 3.2 Analysis

### 3.2.1 4000Å Break Strength

The strength of the 4000Å break can be used as a measure of recent star formation, as outlined by Kauffmann et al. (2003). Younger stellar populations contain hotter stars which have multiply ionised elements. This leads to a decrease in opacity and consequently a smaller 4000Å break. Conversely, the 4000Å break is larger for older populations.

In order to measure the strength of the 4000Å break, I adopt the band definitions of Balogh et al. (1999) as used by Kauffmann et al. (2003); the break strength  $[D_n(4000)]$  is calculated as the mean flux in the 4000–4100Å band divided by the mean flux in the 3850–3950Å band (see Figure 3.1). I calculate  $D_n(4000)$  for each object directly from the spectra, masking out regions affected by emission lines from the central radio source. For each object the spectrum used was that extracted using either the full width half maximum aperture (ensuring a high signal-to-noise ratio) or the full width at zero intensity aperture (giving the total object light), depending on which was fit with the lowest reduced- $\chi^2$  by

---

Source (1)	$L_{151}$ (2)	Telescope (3)	$D_n(4000)$ (4)	Spec. Class (5)	Morph. Class (6)
3C16	26.82	WHT	$1.54 \pm 0.10$	HEG	CD/FD
3C19	26.96	WHT	$1.59 \pm 0.04$	LEG	CD
3C46	26.84	WHT	$1.47 \pm 0.04$	HEG	CD
3C172	27.17	Gemini	$1.63 \pm 0.05$	HEG	CD
3C200	26.92	Gemini	$1.55 \pm 0.03$	LEG	CD
3C244.1	27.10	WHT	$1.30 \pm 0.03$	HEG	CD
3C295	27.68	Gemini	$1.58 \pm 0.04$	HEG	CD
3C341	26.88	WHT	$1.34 \pm 0.04$	HEG	CD
3C427.1	27.53	Gemini	$1.52 \pm 0.08$	LEG	CD
3C457	27.00	WHT	$1.24 \pm 0.03$	HEG	CD
6C0825+3407	26.09	WHT	$1.65 \pm 0.10$	LEG	FD
6C0850+3747	26.15	WHT	$1.25 \pm 0.04$	HEG	CD
6C0857+3945	26.34	Gemini	$1.46 \pm 0.03$	HEG	CD
6C1303+3756	26.29	Gemini	$1.56 \pm 0.01$	HEG	CD
7C0213+3418	25.66	WHT	$1.82 \pm 0.06$	LEG	FD
7C0219+3423	25.98	Gemini	$1.17 \pm 0.02$	HEG	J
7C0810+2650	25.58	WHT	$1.40 \pm 0.04$	HEG	CD
7C1731+6638	25.52	Gemini	$1.21 \pm 0.03$	HEG	FD
7C1806+6831	26.36	Gemini	$1.58 \pm 0.02$	HEG	FD
TOOT0009+3523	24.79	WHT	$1.68 \pm 0.06$	LEG	FD
TOOT0018+3510	25.16	WHT	$1.69 \pm 0.04$	LEG	FD
TOOT1626+4523	25.03	WHT	$1.76 \pm 0.05$	LEG	FD
TOOT1630+4534	25.17	WHT	$1.74 \pm 0.03$	LEG	J
TOOT1648+5040	25.12	WHT	$1.90 \pm 0.07$	LEG	-

Table 3.1: The  $z \sim 0.5$  subsample used to study the star formation histories of the host galaxies. Column 1 lists the radio galaxy names and column 2 the logarithm of the 151 MHz luminosities in units of  $\text{W Hz}^{-1} \text{sr}^{-1}$ . Column 3 lists the telescope used for the spectroscopic observations; either the Gemini North telescope (Gemini) or the William Herschel Telescope (WHT). Column 4 lists the calculated  $4000\text{\AA}$  break strengths [ $D_n(4000)$ ] and column 5 the emission line classification into high-excitation galaxies (HEGs) and low-excitation galaxies (LEGs). Column 6 lists the morphological classification into Classical Doubles (CD), Jetted sources (J) and Fat Doubles (FD). TOOT1648+5040 was too compact to be classified.

a simple stellar spectrum (see Section 4.2.1).

The subsample used in this chapter along with my calculated  $D_n(4000)$  indices can be found in Table 3.1. The  $D_n(4000)$  indices lie in the range 1.17–1.90. From figure 6 of Kauffmann et al. (2003) I note that the galaxies at the upper end of this range correspond to old galaxies with no recent star formation. Those galaxies at the lower end of the range are consistent with galaxies where a small fraction of the stellar mass has been formed 0.1–2 Gyr ago.

The  $D_n(4000)$  index can be contaminated by dust and/or scattered quasar light: dust increases the value of  $D_n(4000)$  since it extinguishes more in the blue than in the red (e.g. Calzetti et al. 2000) whereas scattered quasar light decreases  $D_n(4000)$  since the scattered quasar light is brighter in the blue than in the red (e.g. Vanden Berk 2001). There are thus potential limitations in using  $D_n(4000)$  in isolation as an indicator of star formation histories. An additional indicator is the  $H\delta$  index, which is based upon the strength of the 4102Å  $H\delta$  Balmer absorption line (see Worthey & Ottaviani 1997; Kauffmann et al. 2003). However, I am unable to measure  $H\delta$  for my galaxies due to the presence of emission lines from the Active Galactic Nuclei (AGNs). I therefore use  $D_n(4000)$  by itself, noting that there is no evidence for dust in any of the objects, i.e. they are all adequately fit by simple stellar populations without dust obscuration (see Section 4.2.1) and include the Ca H+K lines, giving confidence that the contribution to the blue light is stellar in origin. The effect of scattered quasar light on my results is discussed in Section 3.3.

### 3.2.2 Spectral and Morphological Classifications

I classify the radio galaxies as high-excitation (HEGs) or low-excitation (LEGs) according to the classification scheme of Jackson & Rawlings (1997). An object is classified as a LEG if it has an [OIII] rest frame equivalent width  $< 10\text{\AA}$  or an [OII]/[OIII] ratio

---

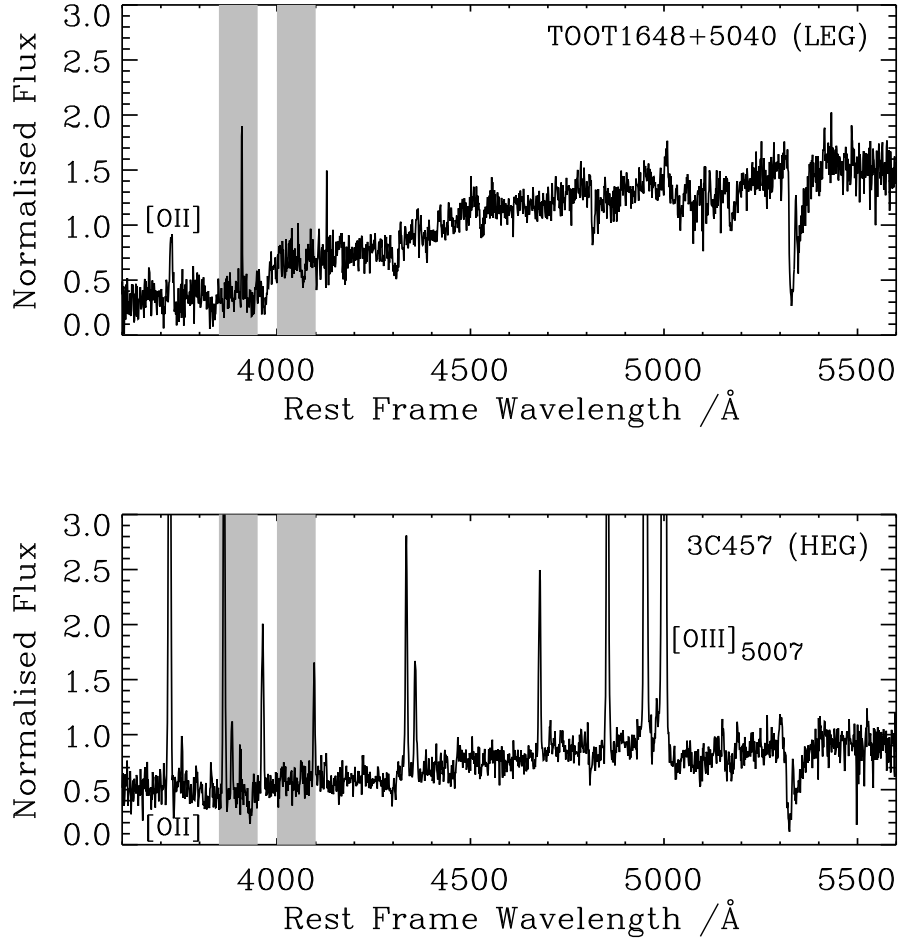


Figure 3.1: The spectra of two of the objects: TOOT1648+5040 [a low-excitation galaxy (LEG) with a large 4000Å break] and 3C457 [a high-excitation galaxy (HEG) with a smaller 4000Å break]. The shaded regions indicate the bands used for the 4000Å break strength  $[D_n(4000)]$  calculation (Section 3.2.1). The emission lines used for the spectral classification (Section 3.2.2), [OII] and [OIII], are labelled on the spectra ([OIII] is not detected in the case of TOOT1648+5040).

$> 1$  (or both). The classifications can be found in Table 3.1<sup>1</sup>. Figure 3.1 illustrates the difference in the spectra between high-excitation and low-excitation objects.

Morphological classifications of the radio sources are taken from Mitchell (2005) and can be found in Table 3.1. Mitchell used the classification scheme of Owen & Laing (1989), where sources are classified as Classical Doubles (CD), Jetted sources (J) or Fat Doubles (FD), as described in Section 1.3. In terms of their Fanaroff-Riley classification (Fanaroff & Riley 1974), Classical Doubles are always identified with Fanaroff-Riley Class II (FR II) sources whilst Jetted sources are generally identified with Fanaroff-Riley Class I (FR I) radio galaxies and Fat Doubles are identified as FR II or FR I/II sources.

### 3.3 Discussion

#### 3.3.1 $D_n(4000)$ versus Radio Luminosity

In Figure 3.2 I show  $D_n(4000)$  versus the low-frequency radio luminosity at 151 MHz,  $L_{151}$ , for the galaxies, with symbols corresponding to their spectral classification. Motivated by figure 6 of Kauffmann et al. (2003), I include a dashed line at  $D_n(4000) = 1.6$  in order to illustrate differences in star formation. Objects with  $D_n(4000) < 1.6$  may have formed a noticeable fraction (5% or greater) of their stellar mass in recent star bursts in the models of Kauffmann et al. (2003). On the other hand, objects with  $D_n(4000) > 1.6$  show little or no evidence for recent star formation. This division at  $D_n(4000) = 1.6$  therefore represents a conservative division between objects which have evidence of recent star formation, and those which do not. I reiterate that since I am unable to measure  $H\delta$  for the objects I am unable to be more specific as regards the star formation histories of the galaxies.

---

<sup>1</sup>For objects where the wavelength range does not extend to the [OIII] emission line I use data from <http://www.science.uottawa.ca/~cwillott/3crr/3crr.html>

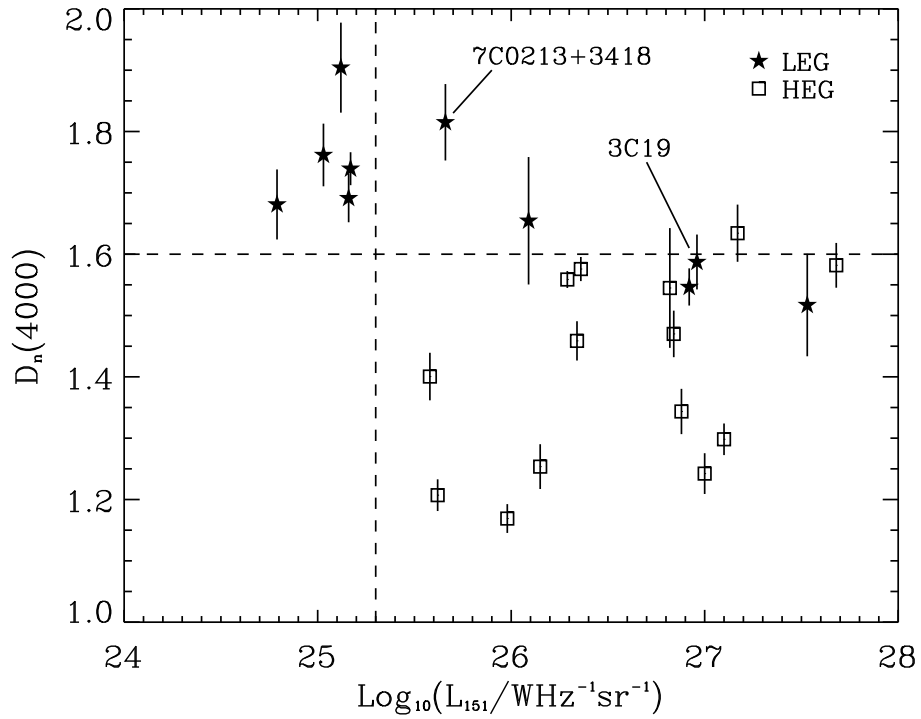


Figure 3.2: The strength of the 4000Å break,  $D_n(4000)$ , versus the logarithm of the 151 MHz luminosity,  $L_{151}$ , split by spectral classification (Section 3.3.1). Low-excitation galaxies (LEGs) are shown as filled stars and high-excitation galaxies (HEGs) as open squares. The vertical dashed line is included to highlight the division between the two populations discussed in the text. The horizontal dashed line highlights the dichotomy in  $D_n(4000)$  for the two populations. The two objects labelled (3C19 and 7C0213+3418) have characteristics of both LEGs and HEGs, as discussed in Section 3.3.2.

Mindful of this note of caution, it is still readily apparent that the galaxies form two distinct populations. One population, with lower radio luminosities ( $L_{151} < 10^{25.3} \text{ W Hz}^{-1} \text{ sr}^{-1}$ ), is composed exclusively of LEGs. The galaxies in this population have systematically higher  $D_n(4000)$  indices and thus older stellar populations. The second population, at higher radio luminosities ( $L_{151} > 10^{25.3} \text{ W Hz}^{-1} \text{ sr}^{-1}$ ) and smaller  $D_n(4000)$  indices (younger stellar populations), consists mainly of HEGs, although a few LEGs are also present in this population. 6C0825+3407 and 7C0213+3418 could belong to either population (as discussed in Section 3.3.2). I illustrate the division between the two populations by the vertical dashed line in Figure 3.2. The traditional division between FRI type and FR II type radio galaxies falls at  $L_{151} = 10^{25.3} \text{ W Hz}^{-1} \text{ sr}^{-1}$  and motivates my population division at this value. This is also the radio luminosity at which there is an apparent divergence in the redshift evolution of the comoving space density, with the higher luminosity radio sources tending to evolve more strongly than the lower luminosity sources, see e.g. Clewley & Jarvis (2004) using data from the Westerbork Northern Sky Survey (WENSS), Faint Images of the Radio Sky at Twenty-centimetres (FIRST) and the National Radio Astronomy Observatory Very Large Array Sky Survey (NVSS), together with data from the Sloan Digital Sky Survey (SDSS). Sadler et al. (2007) also found similar results using data from FIRST and NVSS together with data from the Two Degree Field SDSS Luminous Red Galaxy and Quasi-stellar Object (2SLAQ) survey. More recently, McAlpine & Jarvis (2011) used radio observations of the X-ray Multi-mirror Mission Large Scale Structure (XMM-LSS) field, as described by Tasse et al. (2007), together with data from the UK Infrared Telescope Infrared Deep Sky Survey (UKIDSS), to push to higher redshifts and found consistent results.

Performing a two sided K-S test on the  $D_n(4000)$  indices for the two populations enables me to reject at a significance of 99.96% ( $3.5\sigma$ ) that the two populations are drawn from the same distribution. I also perform a Mann-Whitney-Wilcoxon (MWW) test on

---

the two populations and reject at a significance of  $>99.9\%$  ( $>3.3\sigma$ ) the null hypothesis that they are drawn from the same distribution. I thus find evidence for different star formation histories for high- and low-luminosity radio galaxies. The transition occurs around  $L_{151} \simeq 10^{25.3} \text{ W Hz}^{-1} \text{ sr}^{-1}$ , although it is not possible to make a clean division at a single value of  $L_{151}$ .

### 3.3.2 $D_n(4000)$ versus Emission-line Classification

I also split my objects according to their optical classification (i.e. LEGs and HEGs) and perform another two sided K-S test on the  $D_n(4000)$  indices. In this case I reject the null hypothesis that the  $D_n(4000)$  indices are drawn from the same distribution at a significance of  $99.4\%$  ( $2.8\sigma$ ). An MWW test in this case rejects the null hypothesis at a significance of  $99.8\%$  ( $3.1\sigma$ ). The difference in  $D_n(4000)$  between a LEG and an HEG is illustrated in Figure 3.1, and Figure 3.3 shows clearly that the HEGs and LEGs are divided into two separate populations on the basis of their  $D_n(4000)$  indices. I thus find evidence in support of the work of Kauffmann et al. (2008) and Baldi & Capetti (2008). The latter authors used near ultraviolet (UV) data from the *Hubble Space Telescope* Space Telescope Imaging Spectrograph (STIS) to probe the star formation and found evidence of recent star formation in HEGs but not in LEGs. They suggest that HEGs have undergone a recent major merger that triggered star formation and also provided the fuel to power the AGNs via cold gas accretion. In their picture, LEGs on the other hand have had no such recent merger, and thus are fuelled by the hot interstellar medium (ISM) and show no evidence of recent star formation. However, whilst mergers seem a likely explanation of the origin of the influx of cold gas in HEGs, I note that there are alternative explanations of this influx, as discussed in Chapter 1. I also note that the population that shows evidence of more recent star formation contains three (or possibly four) LEGs. Thus a spectral line classification system may not be a clean method with which to study the history of the

---

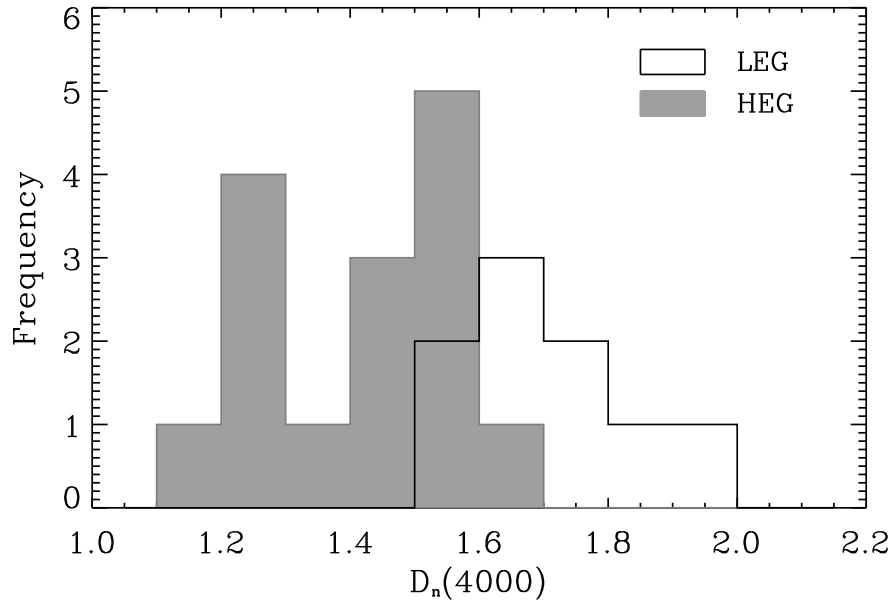


Figure 3.3: A histogram of the 4000Å break strengths [ $D_n(4000)$ ] of my objects, with high-excitation galaxies (HEGs; shaded) and low-excitation galaxies (LEGs; clear) shown separately (see Section 3.3.2).

influx of cold gas into AGN hosts – rather the star formation history measured by studying the host galaxies may offer a better indication of the past influx of cold gas by mergers or other processes.

However it is possible that, even when the principal accretion mechanism is through the hot-mode, minor mergers and interactions could stimulate some star-formation activity which would result in smaller  $D_n(4000)$  values. Furthermore, the timescale on which a merger influences the AGN fuelling could be different from the timescale on which it triggers star formation which would also cause mixing of the populations. It is also interesting to note that the LEGs still have amongst the oldest stellar populations in the higher radio luminosity population. I also observe that some of the LEGs belonging to the higher radio luminosity population possess HEG-like features. 3C19 (labelled in Figure 3.2) would be classed as a HEG on the basis of its [OIII] rest frame equivalent width,

but is classified as a LEG due to its [OII]/[OIII] ratio. Conversely 7C0213+3418 (also labelled in Figure 3.2) would be a HEG on the basis of its [OII]/[OIII] ratio, but is classified as a LEG because of its [OIII] rest frame equivalent width.

An important question is whether the dichotomy observed in  $D_n(4000)$  is primarily related to the radio luminosity (Section 3.3.1) or to the excitation state (this section). Given my current data I am unable to provide a conclusive answer to this question. However, given that the excitation state appears to be a better indicator of the accretion rate than the radio luminosity (Hardcastle et al. 2007), and thus is more closely linked to the state of the gas, I suggest that it is the excitation state, rather than the radio emission, which is primarily related to the strength of the 4000Å break (and thus the star formation history of the galaxy).

In Figure 3.4 I again show  $D_n(4000)$  versus  $L_{151}$ , this time with symbols corresponding to the radio morphology of the galaxy. I find that the lower radio luminosity population is composed mainly of Fat Doubles and the higher radio luminosity population contains predominantly Classical Doubles. However, there is a great deal of mixing of the radio morphology types, and I find no clear difference between the two populations on the basis of radio morphology alone due to the strong relation between radio morphology classification and the high- and low-excitation populations (Hine & Longair 1979).

### 3.3.3 Contamination by Scattered Quasar Light?

Scattered quasar light has, in the past, been posited as an explanation for the alignment effect in radio galaxies where the optical emission from the galaxy is observed as being aligned with the radio emission (e.g. Tadhunter et al. 1992, Cimatti et al. 1993) and could possibly lead to uncertainties in the inferred properties of quasar host galaxies (e.g. Young et al. 2009). In this chapter I use the strength of the 4000Å break as an indicator of recent star formation. Care must therefore be taken to consider whether the dilution in the

---

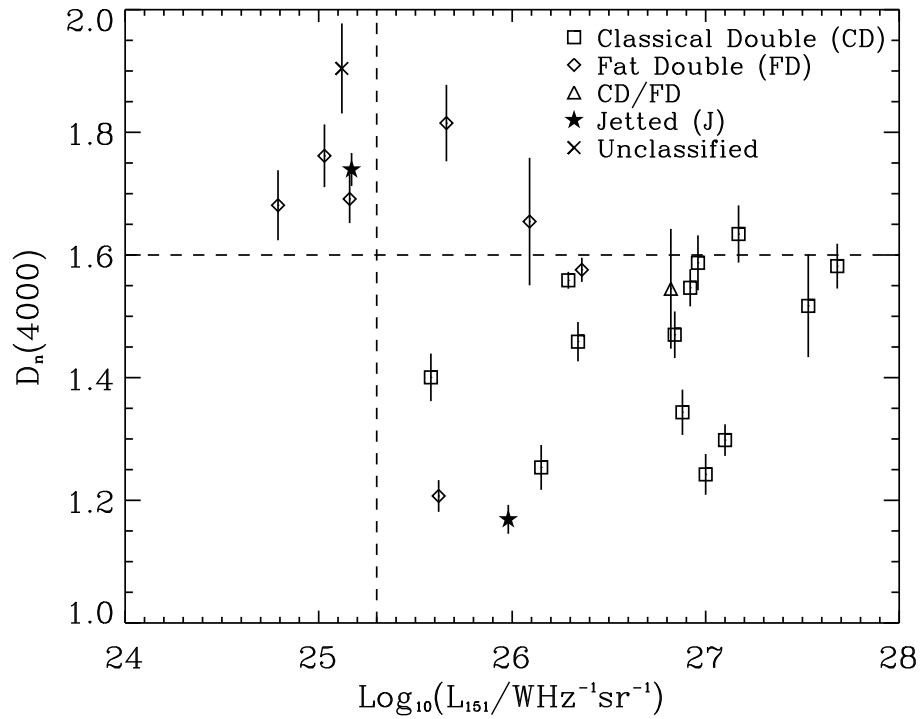


Figure 3.4: The strength of the 4000Å break,  $D_n(4000)$ , versus the logarithm of the 151 MHz luminosity,  $L_{151}$ , split by radio morphology (Section 3.3.2). Classical Doubles are represented by open squares and Fat Doubles by open diamonds. Classical Double/Fat Doubles are shown as open triangles. Jetted sources are represented by filled stars and unclassified objects are marked with a cross. The vertical dashed line is included to highlight the division between the two populations discussed in the text. The horizontal dashed line highlights the dichotomy in  $D_n(4000)$  for the two populations.

4000Å break arises as a result of a young stellar population or from other sources. Lilly & Longair (1984) and Lilly, Longair & Allington-Smith (1985) used the 3CR and ‘1-Jansky’ samples of radio galaxies to establish the trend for bluer galaxies to have stronger [OII]3727 line emission (from the AGN). More recent work (e.g. Tadhunter, Dickson & Shaw 1996; Aretxaga et al. 2001; Tadhunter et al. 2002; Holt et al. 2007) has emphasized the contribution of both young stellar populations and AGN-related components (e.g. nebular continuum, scattered and direct quasar light, emission lines) to the optical and UV continua in powerful radio galaxies.

As found by Lilly et al. (1985), we would expect the contamination by scattered quasar light to be highly correlated with the ionizing power of the central engine and thus the emission-line luminosity, assuming emission-line luminosity is a good proxy for ionizing power (see e.g. Rawlings & Saunders 1991). However, I find no evidence for a correlation between the [OII] luminosity and  $D_n(4000)$  with a Spearman Rank test giving only a 25% probability that the relation deviates from the null hypothesis of no correlation.

Furthermore, for scattered quasar light to have a large effect on my results would require a very strong dependence on wavelength, i.e. over the range where I calculate  $D_n(4000)$ . Using the most pronounced examples of scattered quasar light in the literature, i.e. in broad-line radio galaxies (see e.g. Tran et al. 1998) I find, by using the total polarized emission spectrum from these sources, that the spectrum of the scattered light gives a value of  $D_n(4000) \approx 0.9$ . Assuming that at 3900Å up to 10% of the total emission in my radio galaxies could be contributed by the scattered nuclear emission (e.g. figure 3 of Tran et al. 1998) I calculate that this would reduce my  $D_n(4000)$  by a maximum value of 0.1. Given that none of my radio galaxy spectra show any evidence for any scattered contribution, that they have pronounced absorption-line spectra and that they are all well fit by a simple stellar population, along with the lack of a correlation between [OII] emission-line luminosity and  $D_n(4000)$ , I am confident that the dichotomy in  $D_n(4000)$

---

between the HEGs and LEGs is due to different star-formation histories rather than scattered quasar light.

### 3.4 Conclusions

In this chapter I have used deep spectroscopic observations to determine how the age of the stellar populations in the host galaxies of powerful radio sources is related to the structure of the radio emission and the ionizing power of the AGN.

- I have shown that the spectroscopic subsample of  $z \sim 0.5$  radio galaxies forms two distinct populations in the  $D_n(4000) - L_{151}$  plane. The population at lower radio luminosity is composed entirely of LEGs, the one at higher radio luminosity predominantly of HEGs (although a few LEGs fall within this population).
  - The lower radio luminosity population has systematically higher  $D_n(4000)$  indices than the higher radio luminosity population. I find that this is most likely due to the presence of a younger stellar population in the higher radio luminosity (or HEG) population after considering the possibility that scattered quasar light may significantly alter the  $D_n(4000)$ . I find that scattered quasar light could only decrease  $D_n(4000)$  by a maximum value of 0.1, which is not sufficient to explain the dichotomy that I observe. However, I am unable to measure the  $H\delta$  index for the objects, which does leave some uncertainty in determining the actual extent of the star formation in my galaxies.
  - I find that there is a preference for Fat Double sources to have older stellar populations than the Classical Double sources. However, this may simply reflect the underlying links between radio morphology and excitation state; the latter appearing to be more strongly correlated with  $D_n(4000)$  than is the morphology.
-

- 
- My results are consistent with the hypothesis that HEGs are powered by the accretion of cold gas, the influx of which could be due to mergers – which would also trigger star formation – or other processes, such as cooled, recycled gas from dying stars or cold mode accretion. On the other hand, I suggest that LEGs are powered by the accretion of the hot phase of the inter-stellar medium (as they have undergone no recent influx of cold gas).
-



# Chapter 4

## The Fundamental Plane

In this chapter I once more use the spectroscopic data, studied in Chapter 3, for 24 of the galaxies in the  $z \sim 0.5$  (ZP5) sample. I use a direct spectral fitting procedure to obtain the velocity dispersions of the galaxies. Combining these with the (previously published) effective radii and surface brightnesses (see McLure et al. 2004) I study the Fundamental Plane at  $z \sim 0.5$  and draw comparisons with the well documented local relation. The work of McLure et al. (2004) used only Hubble Space Telescope imaging of the sample, not spectroscopic data (which was unavailable at the time). The measurements of the velocity dispersions of the ZP5 galaxies are therefore new to my work, allowing me to study the Fundamental Plane of the ZP5 sample which McLure et al. (2004) were unable to do.

My spectral fits also allow me to investigate any possible correlation between the low-frequency radio luminosity at 151 MHz ( $L_{151}$ ) and the velocity dispersion ( $\sigma$ ). This enables me to investigate (via the black hole mass-sigma, or  $M_{BH}-\sigma$ , relation) the possible link between radio luminosity and black hole mass in radio-loud AGNs (e.g. Nelson & Whittle 1996; McLure & Jarvis 2004; Jarvis & McLure 2006).

After describing the data in Section 4.1, I describe my spectral fitting and aperture

correction techniques in Section 4.2, followed by a description of my Fundamental Plane fitting in Section 4.3. I present and discuss my findings in Section 4.4, before concluding in Section 4.5. The content of this chapter has been published in Herbert et al. (2011).

## 4.1 The ZP5 Sub-sample

In this chapter I once again use the spectroscopic data, as in Chapter 3, for the 24-object subsample of the full ZP5 sample (see Table 4.1). In Figure 4.1 I show the radio luminosity–redshift plane for these objects. The observations and data reduction are as described in Chapter 2.

The WHT observations were performed using the R316R grating on the red arm together with a 1.0 arcsec slit resulting in a resolution of  $3.7 \text{ \AA}$  FWHM. This corresponds to a velocity resolution of  $\text{FWHM} = 185 \text{ km s}^{-1}$  at  $6000 \text{ \AA}$  which results in a minimum measurable velocity dispersion of  $\sigma \sim 80 \text{ km s}^{-1}$ . Moreover, since the absorption lines are broadened by a factor of  $(1+z)$  in the observed spectra, the rest-frame velocity resolution is, in fact, slightly higher.

For the Gemini observations, the B600\_G5303 grating (and subsequently the new B600\_G5307 grating) was used together with a 0.75 arcsec slit resulting in a spectral resolution of  $4.0 \text{ \AA}$  FWHM. This corresponds to a velocity resolution of  $\text{FWHM} = 190 \text{ km s}^{-1}$  at  $6200 \text{ \AA}$  which results in a minimum measurable velocity dispersion of  $\sigma \sim 80 \text{ km s}^{-1}$ . Once again a slightly higher rest-frame velocity resolution is actually attainable due to the broadening of the absorption lines by a factor of  $(1+z)$ .

---

Source (1)	R.A. (2)	Dec. (3)	$z$ (4)	$L_{151}$ (5)	$r_e$ (6)	$\langle\mu\rangle_e$ (7)	$\sigma$ (8)	Reduced $\chi^2$ (9)	Telescope (10)
3C16	00 37 45.39	+13 20 09.6	0.405	26.82	22.9	21.75	-	-	WHT
3C19	00 40 55.01	+33 10 07.3	0.482	26.96	30.9	21.86	$359^{+52}_{-44}$	1.16	WHT
3C46	01 35 28.47	+37 54 05.7	0.437	26.84	15.8	20.78	$345^{+39}_{-33}$	1.34	WHT
3C172	07 02 08.32	+25 13 53.9	0.519	27.17	12.6	20.65	$328^{+34}_{-29}$	1.10	Gemini
3C200	08 27 25.38	+29 18 45.5	0.458	26.92	13.2	20.15	$343^{+42}_{-37}$	1.39	Gemini
3C244.1	10 33 33.97	+58 14 35.8	0.428	27.10	15.8	20.76	$234^{+21}_{-19}$	1.31	WHT
3C295	14 11 20.65	+52 12 09.0	0.464	27.68	29.5	21.03	$337^{+22}_{-21}$	0.99	Gemini
3C341	16 28 04.04	+27 41 39.3	0.448	26.88	16.6	21.08	$468^{+42}_{-39}$	1.78	WHT
3C427.1	21 04 07.07	+76 33 10.8	0.572	27.53	18.2	20.68	-	-	Gemini
3C457	23 12 07.57	+18 45 41.4	0.428	27.00	14.1	20.40	-	-	WHT
6C0825+3407	08 25 14.59	+34 07 16.8	0.406	26.09	14.5	21.12	-	-	WHT
6C0850+3747	08 50 24.77	+37 47 09.1	0.407	26.15	12.6	20.41	-	-	WHT
6C0857+3945	08 57 43.56	+39 45 29.0	0.528	26.34	11.7	20.15	$272^{+23}_{-20}$	1.13	Gemini
6C1303+3756	13 03 44.26	+37 56 15.2	0.470	26.29	12.3	20.65	$390^{+18}_{-18}$	3.24	Gemini
7C0213+3418	02 13 28.39	+34 18 30.6	0.465	25.66	6.3	19.47	$267^{+24}_{-21}$	1.26	WHT
7C0219+3423	02 19 37.83	+34 23 11.2	0.595	25.98	10.9	20.45	-	-	Gemini
7C0810+2650	08 10 26.10	+26 50 49.1	0.435	25.58	14.8	21.16	$121^{+19}_{-17}$	1.27	WHT
7C1731+6638	17 31 43.84	+66 38 56.7	0.562	25.52	6.0	20.47	$114^{+27}_{-24}$	1.12	Gemini
7C1806+6831	18 06 50.16	+68 31 41.9	0.580	26.36	14.8	20.54	$302^{+18}_{-15}$	1.15	Gemini
TOOT0009+3523	00 09 46.90	+35 23 45.1	0.439	24.79	12.6	20.48	$272^{+23}_{-20}$	1.35	WHT
TOOT0018+3510	00 18 53.93	+35 10 12.1	0.416	25.16	19.5	21.21	$232^{+17}_{-16}$	1.29	WHT
TOOT1626+4523	16 26 48.50	+45 23 42.6	0.458	25.03	7.4	19.54	$241^{+23}_{-20}$	1.24	WHT
TOOT1630+4534	16 30 32.80	+45 34 26.0	0.493	25.17	10.2	19.71	$257^{+9}_{-9}$	2.10	WHT
TOOT1648+5040	16 48 26.19	+50 40 58.0	0.420	25.12	9.5	19.71	$270^{+18}_{-17}$	1.18	WHT

Table 4.1: The  $z \sim 0.5$  sample. Column 1 lists the radio galaxy names and columns 2 and 3 list the J2000 source coordinates. Column 4 lists the object redshifts, column 5 the logarithm of the 151 MHz luminosities in units of  $\text{W Hz}^{-1} \text{sr}^{-1}$  and column 6 the effective radii in kiloparsecs from McLure et al. (2004). The effective radii are derived from fits in which the Sérsic parameter is allowed to vary. Column 7 lists the mean  $R$ -band surface brightness within the effective radii in  $\text{mag arcsec}^{-2}$ , also from McLure et al. (2004). Column 8 lists the aperture-corrected velocity dispersion of my best fit and column 9 the reduced  $\chi^2$  of this fit, whilst column 10 gives the telescope used for the spectroscopic observations.

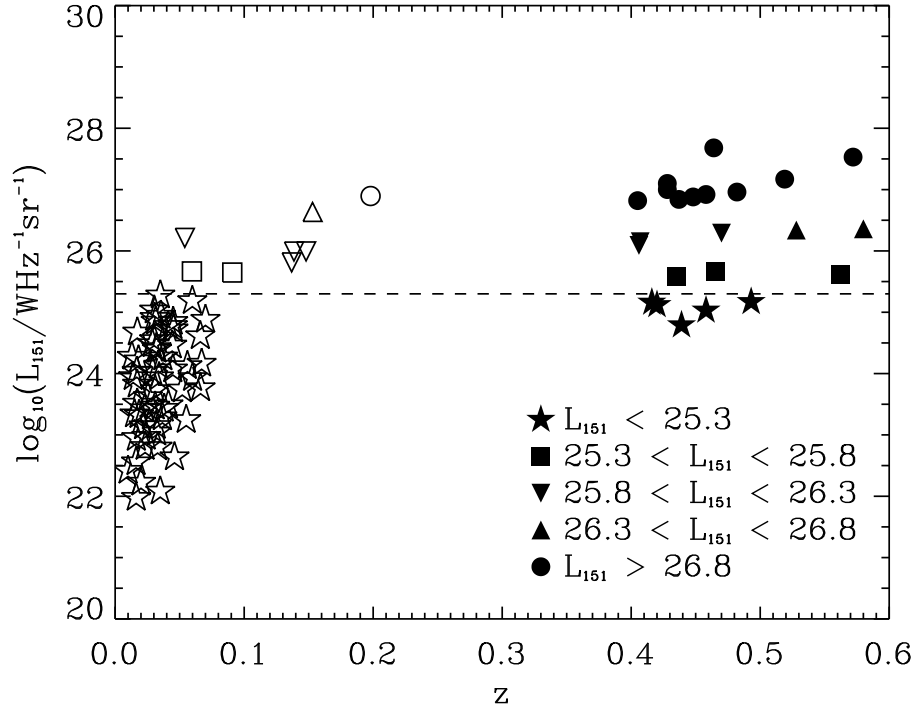


Figure 4.1: The logarithm of the 151 MHz radio luminosity,  $L_{151}$ , versus redshift for the ZP5 ( $z \sim 0.5$ ) objects in this chapter (filled symbols; see Section 4.1). I use open symbols to show the local radio galaxies from Bettoni et al. (2001;  $z \sim 0.03$ ), as also used in this chapter (see Section 4.3.3). In each case the symbols correspond to the 151 MHz radio luminosities. Objects with  $L_{151} < 10^{25.3} \text{ W Hz}^{-1} \text{ sr}^{-1}$  are shown as stars. Objects with  $L_{151}$  between  $10^{25.3}$  and  $10^{25.8} \text{ W Hz}^{-1} \text{ sr}^{-1}$  are shown as squares whilst objects with  $L_{151}$  between  $10^{25.8}$  and  $10^{26.3} \text{ W Hz}^{-1} \text{ sr}^{-1}$  are shown as inverted triangles. Objects with  $L_{151}$  between  $10^{26.3}$  and  $10^{26.8} \text{ W Hz}^{-1} \text{ sr}^{-1}$  are shown as triangles, and objects with  $L_{151} > 10^{26.8} \text{ W Hz}^{-1} \text{ sr}^{-1}$  are shown as circles. I do not show five of the objects of Bettoni et al. (0131-360, 0325+024, PKS 2322-122, 0112+084 and gin116) for which I have been unable to locate published radio luminosity data.

## 4.2 Spectral Fitting

### 4.2.1 The Fitting Procedure

In order to determine the velocity dispersion of each galaxy I perform a  $\chi^2$  minimisation, fitting each galaxy spectrum to a set of templates. The template set comprises 23 Elodie stellar templates<sup>1</sup> and (following Greene & Ho 2006) 34 G and K stars from the old open cluster M67 observed with the Sloan Digital Sky Survey. The templates are broadened using a series of Gaussians whose width depends on the velocity dispersion ( $\sigma$ ) and wavelength. A spectral feature at wavelength  $\lambda$  is broadened by a convolution of the feature with a Gaussian of width:

$$\frac{\lambda\sigma}{c}, \quad (4.1)$$

where  $c$  is the speed of light. For each wavelength in my initial template I create a Gaussian centred on this wavelength, with a width as given by Equation 4.1 and a peak value equal to the template flux at this wavelength. I sum all of these Gaussians together to produce my broadened template. I exclude from the fit regions of the galaxy spectra that feature emission lines ionised by the central engine, as well as skylines. The effect of broadening due to the instrumental resolution is typically within the uncertainties of the fitted velocity dispersions.

To implement the fitting I fit each (de-redshifted) galaxy in turn, using all 57 templates and with the velocity dispersion incrementing in steps of  $1 \text{ km s}^{-1}$ . At each step I minimise the reduced  $\chi^2$  of the fit using the Amoeba routine in IDL. I then inspect the resulting matrix of reduced  $\chi^2$  values in order to find the minimum reduced  $\chi^2$  and thus the best fitting template and velocity dispersion. For each galaxy I perform this fitting on both a spectrum extracted using an aperture defined at the full-width at half maximum

---

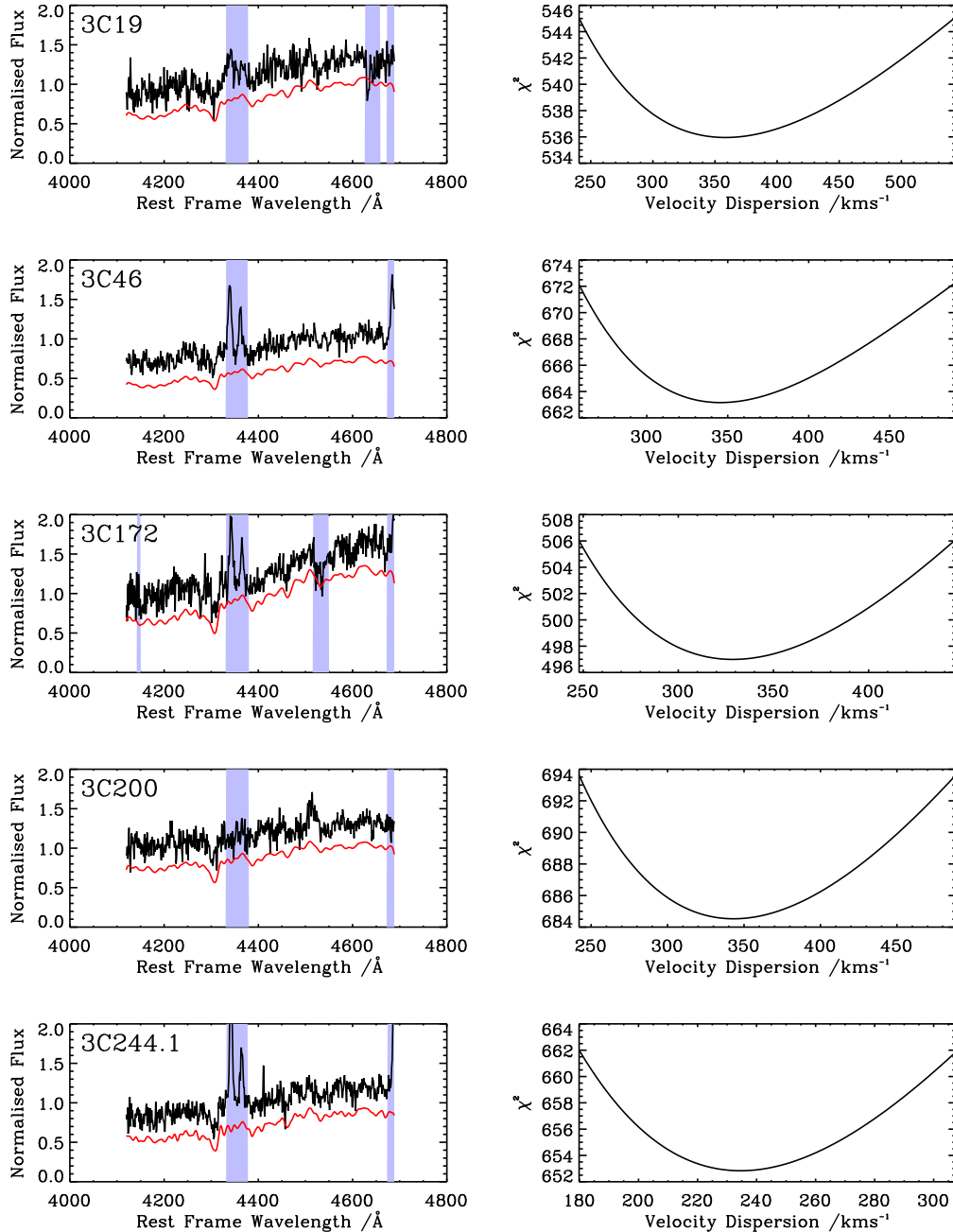
<sup>1</sup><http://atlas.obs-hp.fr/elodie/>

(FWHM) of the galaxy light profile and a spectrum extracted at the full-width at zero intensity (FWZI), ensuring both a high signal-to-noise ratio in the former and the total light spectrum for the latter. I then use whichever best fit has the lowest reduced  $\chi^2$ . Of the 18 final fits, 11 were best fitted by FWHM spectra whilst the remaining seven were best fitted by FWZI spectra.

I am unable to determine reliable measurements of the velocity dispersion for the cases where the mean signal-to-noise ratio per resolution element (measured between rest frame 4400Å and 4600Å where spectral features, in particular the *Mgb* complex, dominate the fitting) is less than  $\sim 10$ . On this basis I exclude the fits to 3C16, 3C427.1, 6C0825+3407, 6C0850+3747 and 7C0219+3423. Since this is based merely on the quality of the data, and not the host luminosity, I do not expect this to introduce any notable selection effects. In addition, I am unable to obtain a sensible fit in the case of 3C457 due to a combination of the signal-to-noise ratio and emission lines from the AGN. Given that this is the only object lacking a fit due to the AGN, I am confident that this has a negligible effect on my results. My final fits to the remaining objects are shown in Figure 4.2.

---

Figure 4.2: My final fits to the galaxy spectra to obtain measurements of the velocity dispersions (Section 4.2). The left hand panels show the galaxy spectrum (top, black) and the fitted template (bottom, red). A downward shift of 0.3 has been applied to the template spectra. The shaded areas indicate regions of the spectra removed from the fitting due to the presence of emission (rest frame 3859–3880Å, 3963–3978Å, 4095–4112Å, 4332–4378Å, 4674–4698Å and 4854–4875Å) or telluric absorption (5570–5585Å, 6864–6911Å, 7166–7323Å and 7590–7694Å) features. The additional masked regions in 3C172, 6C1303+3756 and 7C1731+6638 were due to artefacts on the chip. The right hand panels show the  $\chi^2$  minimisation as a function of velocity dispersion. Aperture corrections have been applied as described in Section 4.2.2.



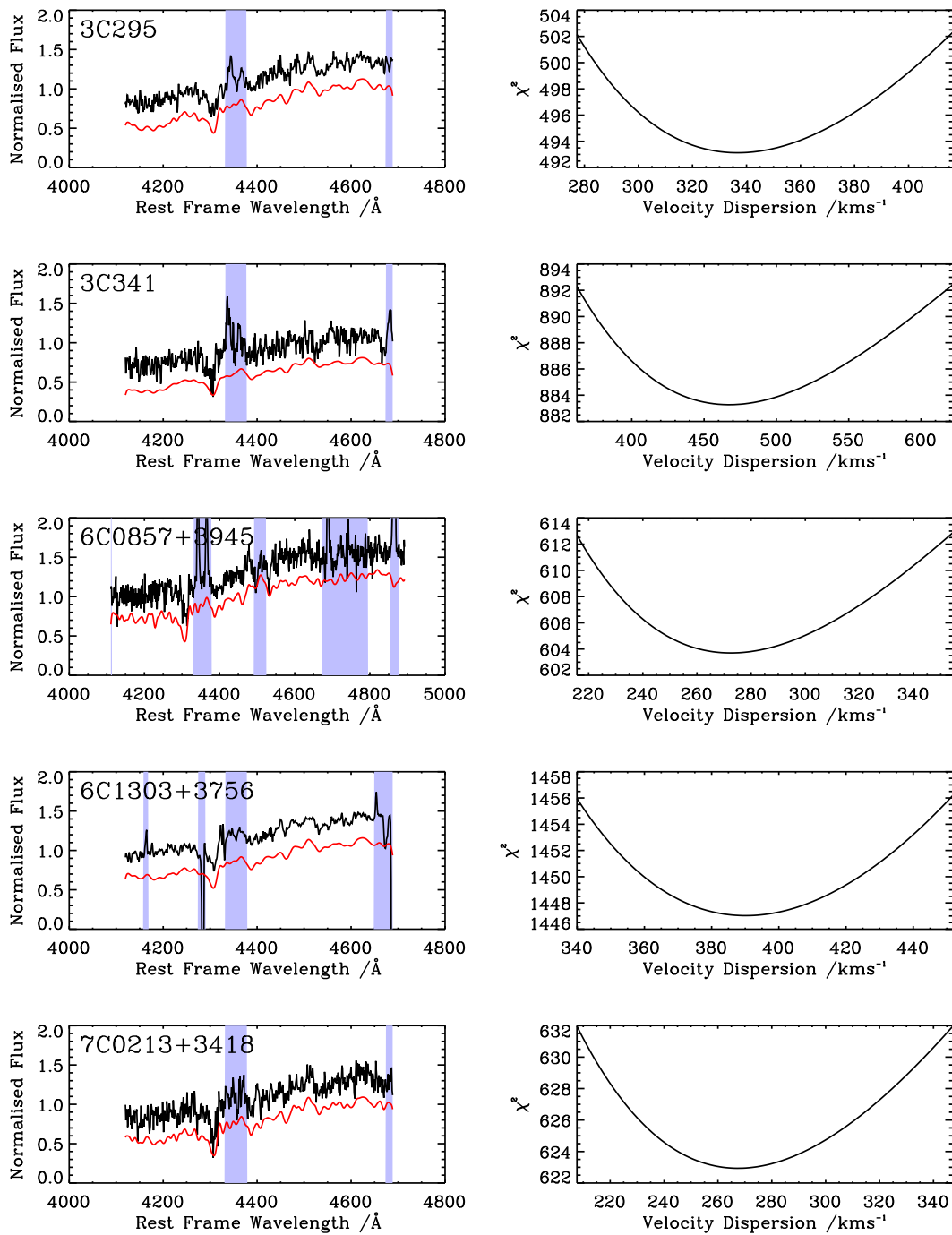


Figure 4.2 continued.

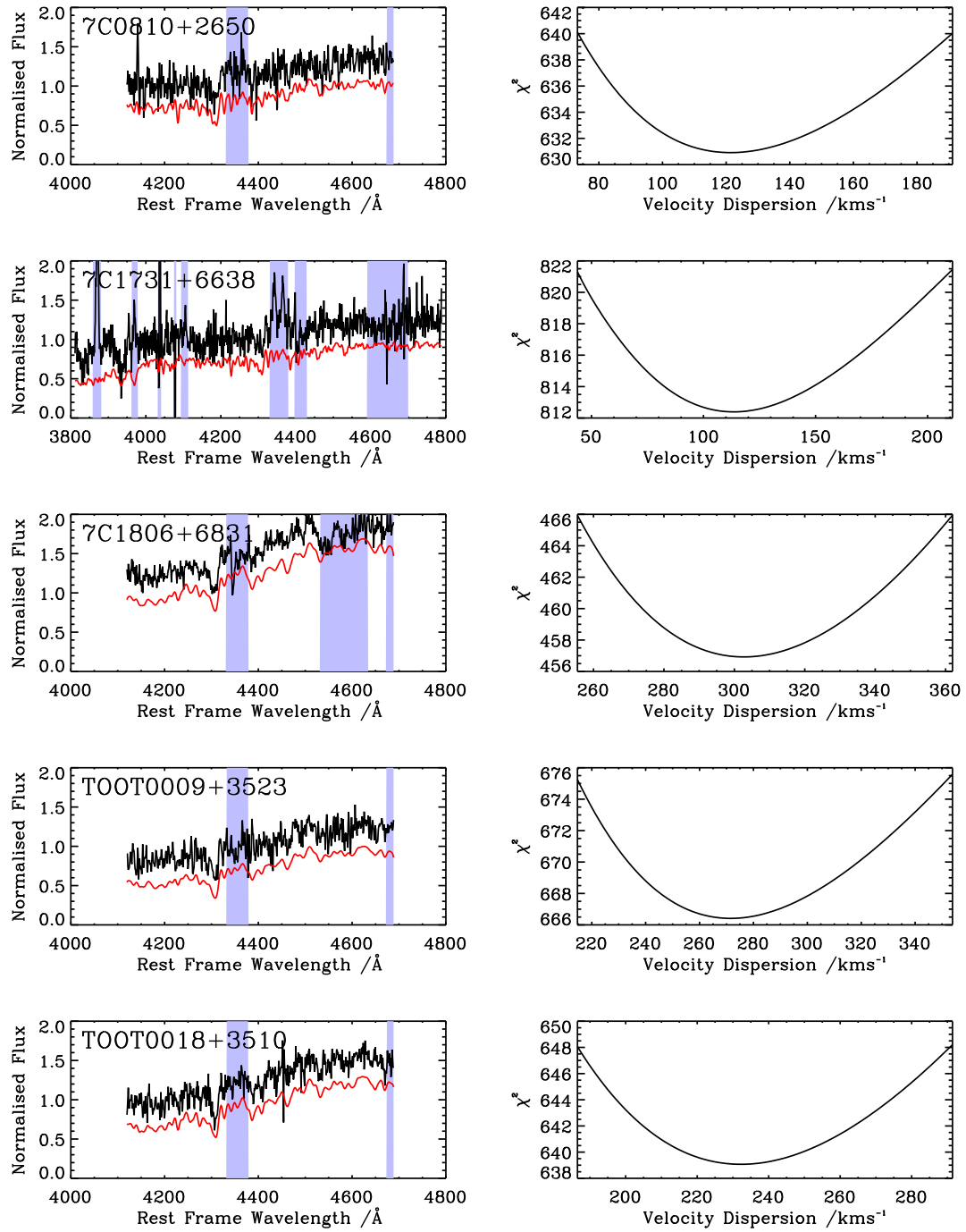


Figure 4.2 continued.

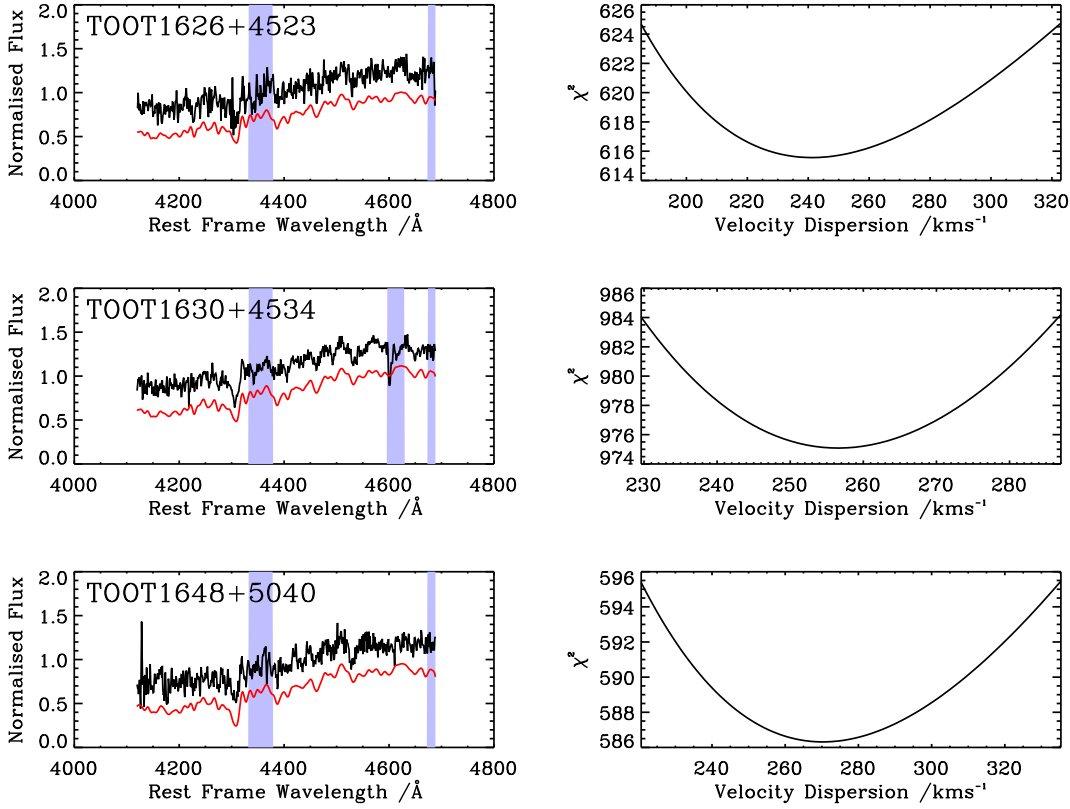


Figure 4.2 continued.

An advantage of explicitly looping over the velocity dispersion is that it allows me to obtain the standard errors on  $\sigma$  from the  $\chi^2$  distribution. I convert the  $\chi^2$  matrix ( $\chi_i^2$ ) (corresponding to the variation of  $\chi^2$  with  $\sigma$  for the best-fitting template for each galaxy) into a probability distribution matrix ( $P_i$ ) using

$$P_i \propto e^{\frac{(\chi_{min}^2 - \chi_i^2)}{2}}, \quad (4.2)$$

before normalising the sum of the matrix to one. I then inspect the probability distribution function in order to determine the range in velocity dispersion which contains 68.27% of the probability distribution function and thus obtain the standard errors on  $\sigma$ . As a check I note that this procedure results in the same standard errors as produced by

$\Delta\chi^2 = 1$ . I also note that three objects (3C341, 6C1303+3756 and TOOT1630+4534) have reduced  $\chi^2$  values  $> 1.5$ . The errors on these objects are therefore undoubtedly underestimated (see Table 4.1).

### 4.2.2 Aperture Correction

The galaxies in my  $z \sim 0.5$  sample are smaller on the sky than those of a local sample. Consequently the aperture size for my sample is of order 20 times greater than the aperture size for a local sample. This has the effect of including more of the galaxy in the slit, resulting in a lower determined velocity dispersion than would be the case for a local sample. Therefore, in order to be able to compare my results with existing results for local samples, I perform an aperture correction on my derived velocity dispersion values and their errors. I perform the aperture correction using the procedure described by Jørgensen, Franx & Kjørgaard (1995), where my values of  $\sigma$  are corrected to a circular aperture with an aperture diameter of  $1.19h^{-1}$  kpc (equivalent to 3.4 arcsec projected onto a galaxy in the Coma cluster). The average correction is 7.1%.

My derived velocity dispersion values, including aperture correction, can be found in Table 4.1. Table 4.1 also contains the McLure et al. (2004) values for the major-axis effective radii,  $r_e$ , and the mean  $R$ -band surface brightnesses within  $r_e$ ,  $\langle\mu\rangle_e$ , of the galaxies in the sample. The values of  $\langle\mu\rangle_e$  have been corrected for passive evolution as described in McLure et al. (2004).

### 4.2.3 Resolution Tests & Fitting Corrections

In order to determine the minimum resolution attainable by my fitting procedure I convolve my templates with a range of velocity dispersion values, degrade these convolved templates to the resolution of my data, and fit using my fitting procedure. The results (at the resolution of the Gemini spectra) are shown in Figure 4.3, from which it is readily

---

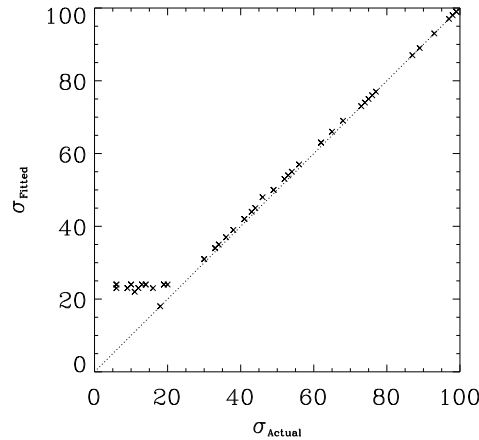


Figure 4.3: The input velocity dispersion ( $\sigma_{Actual}$ ) against the fitted velocity dispersion ( $\sigma_{Fitted}$ ) for noiseless convolved templates reduced to the resolution of my Gemini spectra and fitted using my fitting procedure (Section 4.2.3).

apparent that I achieve a minimum measurable velocity dispersion of  $\sigma_{min} < 50 \text{ km s}^{-1}$ .

Repeating with the WHT spectra yields  $\sigma_{min} < 50 \text{ km s}^{-1}$  also.

I repeat this procedure, adding Gaussian noise into the templates (according to the real noise spectra of my galaxies), in order to test the reliability of my fitting procedure at extracting values of  $\sigma$  from noisy spectra. An example of this is shown in Figure 4.4. I find that the extraction errors are within the uncertainties on my values of  $\sigma$  and therefore do not perform any further corrections.

## 4.3 Fundamental Plane Fitting

### 4.3.1 Initial Plane Fitting

In order to fit a plane to my data I adopt the formulation of the Fundamental Plane used by Robertson et al. (2006a), namely

$$R_e \propto \sigma^\alpha I_e^{-\beta}, \quad (4.3)$$

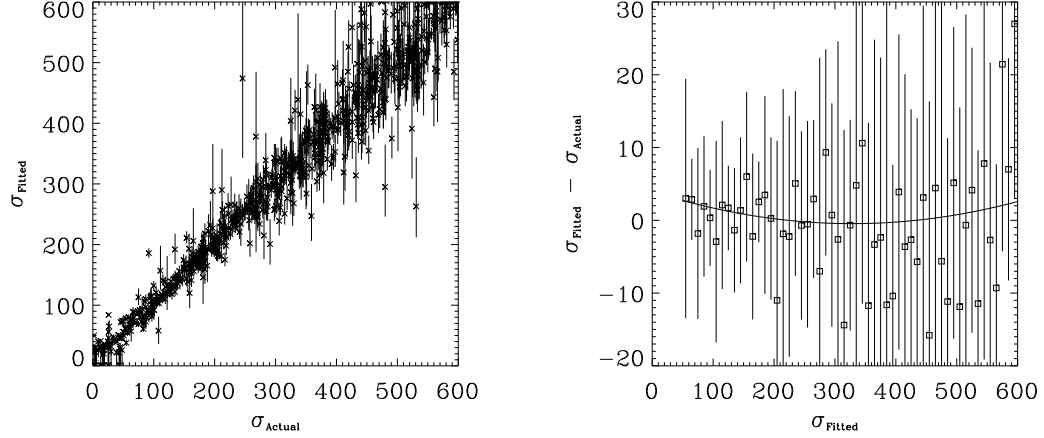


Figure 4.4: Left panel: The input velocity dispersion ( $\sigma_{Actual}$ ) against the fitted velocity dispersion ( $\sigma_{Fitted}$ ) for convolved templates reduced to the resolution of my William Herschel Telescope (WHT) spectra and fitted using my fitting procedure (Section 4.2.3). Noise has been added to the templates according to the actual WHT noise spectra. Right panel:  $\sigma_{Fitted}$  versus ( $\sigma_{Fitted} - \sigma_{Actual}$ ) for convolved noisy templates reduced to the resolution of the WHT spectra. The extraction errors are within the uncertainties on my values of the velocity dispersion.

where  $R_e$  is the effective radius and  $\sigma$  the velocity dispersion as before.  $I_e$  is the mean surface brightness within  $R_e$ , in units of  $L_{\odot}/\text{pc}^2$ , and is related to the previous quantity  $\langle \mu \rangle_e$ :

$$\log I_e = -0.4 (\langle \mu \rangle_e - k), \quad (4.4)$$

where for the  $R$ -band  $k = 26.4$  (see Jørgensen et al. 1996). In order to fit the Fundamental Plane I rewrite Equation 4.3 in the following form:

$$\log R_e = \alpha \log \sigma - \beta \log I_e - \gamma, \quad (4.5)$$

where  $\gamma$  is a constant. For a plane described by Equation 4.5 using coordinates  $(\log \mathbf{r}_e, \log \sigma, \log I_e)$  the residual  $\mathcal{R}$  of point  $(p_1, p_2, p_3)$  perpendicular to the plane is given by:

$$\mathcal{R} = \frac{1}{\delta} (-p_1 + \alpha p_2 - \beta p_3 - \gamma), \quad (4.6)$$

where

$$\delta = \sqrt{1 + \alpha^2 + \beta^2}. \quad (4.7)$$

I note that 12 of the 18 fitted objects have symmetric errors on  $\log \sigma$ . To fit a plane I therefore initially adopt symmetric errors in  $\log r_e$ ,  $\log \sigma$ , and  $\log I_e$ . For the six sources which do not have a symmetric error on  $\log \sigma$  I use the mean of  $(\log(\sigma + \sigma_{upper}) - \log \sigma)$  and  $(\log \sigma - \log(\sigma - \sigma_{lower}))$ , where  $\sigma_{upper}$  and  $\sigma_{lower}$  correspond to the upper and lower errors on  $\sigma$  listed in Table 4.1. The values of  $r_e$  and  $I_e$  taken from McLure et al. (2004) and used here have linear errors of 10%. I use the same procedure as above to estimate symmetric errors in log space for these quantities. In order to fit a plane to my results I use a technique similar to the one used by di Serego Alighieri et al. (2005), where I use a finely sampled grid over  $\alpha$ ,  $\beta$  and  $\gamma$ . At each point I use Equations 4.6 and 4.7 to calculate the residual perpendicular to the plane for each of my objects. I use the symmetric errors in log space in order to determine the error on each residual. I define a  $\chi^2$  statistic thus:

$$\chi^2 = \sum_i \frac{\mathcal{R}_i^2}{\sigma_{\mathcal{R}_i}^2}, \quad (4.8)$$

where the summation is over the objects I am fitting the plane to,  $\mathcal{R}_i$  is the residual of object  $i$  perpendicular to the plane, and  $\sigma_{\mathcal{R}_i}$  is the standard error on the residual. Finally I find the values of  $\alpha$ ,  $\beta$  and  $\gamma$  which minimise this statistic and thus determine the best fitting plane. My best fitting Fundamental Plane can be found in Table 4.2.

Jørgensen et al. (1996) and Bettoni et al. (2001) fit a plane by minimising the sum of the absolute residuals. However, by using my  $\chi^2$ -based technique, it is possible to determine the standard errors on  $\alpha$ ,  $\beta$  and  $\gamma$  in a similar fashion to that employed in Section

---

	$\alpha$	$\beta$	$\gamma$
Symmetric log errors	$0.47^{+0.16}_{-0.15}$	$0.61^{+0.12}_{-0.08}$	$-1.3 \pm 0.4$
MC, squared residuals	$0.52 \pm 0.13$	$0.63 \pm 0.06$	$-1.2 \pm 0.4$
MC, weighted	$0.45 \pm 0.09$	$0.63 \pm 0.06$	$-1.4 \pm 0.3$
Squared residuals	0.53	0.626	-1.3
Absolute residuals	0.32	0.617	-1.8

Table 4.2: Values of  $\alpha$ ,  $\beta$  and  $\gamma$  for a Fundamental Plane fitting the ZP5 data and described by the equation  $\log r_e = \alpha \log \sigma - \beta \log I_e - \gamma$ . The first row gives the results in the case where I assume symmetric errors in log space (Section 4.3.1). The second row gives the results from the full Monte Carlo (MC) fitting using squared residuals (Section 4.3.2). The same procedure, except weighting the minimised residuals by the error, produces the results listed in the third row (Section 4.3.2). The results obtained by minimising the sum of the square residuals and the sum of the absolute residuals without the Monte Carlo technique are given in the fourth and fifth rows respectively (Section 4.3.2).

4.2.1. I convert my three-dimensional  $\chi^2$  matrix into a probability distribution matrix and normalise. I then determine the region of parameter space that contains 68.27% of the probability distribution function and from this the standard errors on  $\alpha$ ,  $\beta$  and  $\gamma$ . The reduced- $\chi^2$  also provides me with a measure of the goodness of the fit. Alongside these advantages I do, however, emphasize that this technique does not make use of the exact errors on  $r_e$ ,  $\sigma$  and  $I_e$  and that small approximations are required. However, I show in Section 4.3.2 that the plane I obtain using this method is consistent with the plane produced using a method which involves no approximations.

### 4.3.2 Monte Carlo Simulations

In order to fit a plane (with errors) to my data, using the actual error distributions on  $\sigma$ , I employ a Monte Carlo technique. For each of my objects I randomly sample 12,000 values from each of the  $r_e$ ,  $I_e$  and  $\sigma$  probability distribution functions (PDFs). I use sufficient samples to produce smooth final distributions in  $\alpha$ ,  $\beta$  and  $\gamma$ . The procedure outlined in section 4.2.1 provides the  $\sigma$  PDF. For each sample set I grid over a range of  $\alpha$ ,  $\beta$  and  $\gamma$  and obtain the best fitting values of these parameters for each of the 12,000

simulations by minimising the sum of the squared residuals according to equation 4.6. I obtain the standard errors by finding the range containing 68.27% of the PDF for each parameter. Table 4.2 lists my fitting results.

Next I repeat this procedure but, rather than minimise just the sum of the squared residuals, I minimise the sum of the squared residuals weighted by the square of the error on the residual (where I estimate the residual error using the procedure described in Section 4.3.1). Finally, I fit a plane to the data by minimising the sum of the squared residuals, and another by minimising the sum of the absolute residuals (as per Jørgensen et al. 1996; Bettoni et al. 2001), but without any Monte Carlo sampling in either case. The results from all of these plane fittings can be found in Table 4.2, and in all cases my Fundamental Plane parameters are consistent.

### 4.3.3 Local Plane Fitting

In order to compare my  $z \sim 0.5$  plane with results for local active galaxies I use the data presented in Bettoni et al. (2001). This comprises both new data and data from the literature on their sample of low redshift radio galaxies. The median redshift of their sample is 0.03. I note that I use the same procedure as Bettoni et al. to apply the aperture corrections and thus the results can be compared directly. The first row of Table 4.3 contains the published plane fitting of Bettoni et al. (2001), converted from their plane parameterisation to mine using Equation 4.4. The second row of Table 4.3 gives my fit to the data of Bettoni et al. (2001) using their fitting procedure (minimising the sum of the absolute residuals perpendicular to the plane). I exclude from my data set the objects 0053-016 and 0431-134 from Ledlow & Owen (1995), for which I have been unable to locate published redshifts.

In order to compare my plane fitting with the data of Bettoni et al. (2001) I correct the scalelengths in the data from their cosmology ( $H_0 = 50 \text{ km s}^{-1}$ ,  $\Omega_M = 1$  and  $\Omega_\Lambda =$

---

	$\alpha$	$\beta$	$\gamma$
Published	$1.92 \pm 0.15$	$0.64 \pm 0.03$	$1.93 \pm 0.37$
Uncorrected absolute residuals	1.73	0.709	1.3
Absolute residuals	1.76	0.713	1.5
Squared residuals	1.33	0.655	0.6
Symmetric log errors	$2.11^{+0.42}_{-0.37}$	$0.60 \pm 0.05$	$2.6^{+1.0}_{-0.9}$

Table 4.3: Values of  $\alpha$ ,  $\beta$  and  $\gamma$  for a Fundamental Plane fitting the data of Bettoni et al. (2001) and described by the equation  $\log r_e = \alpha \log \sigma - \beta \log I_e - \gamma$  (Section 4.3.3). The first row lists the plane fitting results published by Bettoni et al. (2001), where I convert from their plane parameterisation to mine using Equation 4.4. The second row lists my fit to their data obtained by minimising the sum of the absolute residuals (excluding the two objects discussed in Section 4.3.3, and the fitting described in the third row is the same but using the data of Bettoni et al. (2001) corrected into my cosmology. Row four gives the results of my fit to the corrected data by minimising the sum of the squared residuals, and the fifth row gives the results where I assume symmetric errors in log space and minimise the  $\chi^2$  statistic.

0) to mine. Once again I exclude the objects 0053-016 and 0431-134 from Ledlow & Owen (1995) due to the lack of redshift information. I fit the Fundamental Plane to the corrected data by minimising the sum of the absolute residuals and then repeat, this time minimising the sum of the squared residuals (see Table 4.3). Finally, I use the procedure described in Section 4.3.1 to fit the Fundamental Plane to the corrected data of Bettoni et al. (2001) using a  $\chi^2$  fitting statistic, yielding uncertainties on the plane fitting as well as an indication of the goodness of fit. Uncertainties on  $\sigma$  have been published for the data presented by Bettoni et al. (2001) and Smith, Heckman & Illingworth (1990). For the remainder of the data I use a typical linear error of 10%. I also assume linear errors of 10% on  $r_e$  and  $I_e$ . The fitting results can be found in Table 4.3, from which it can be seen that my plane fittings are consistent for all but the squared residuals fit.

## 4.4 Discussion

### 4.4.1 The Local Fundamental Plane

In Figure 4.5 I show a two-dimensional projection of the Fundamental Plane that I fit to the cosmologically corrected data of Bettoni et al. (2001) using their fitting procedure (row three of Table 4.3). As well as showing the data of Bettoni et al. in this projection I also show my ZP5 objects with symbols corresponding to their radio luminosities. The y-axis uncertainties for the ZP5 objects were determined by assuming errors as in Section 4.3.1 and combining in quadrature according to the equation of the plane. It can be seen in Figure 4.5 that my objects with radio luminosity  $L_{151} < 10^{25.3} \text{ W Hz}^{-1} \text{ sr}^{-1}$  appear to lie on the local Fundamental Plane. The traditional division between lower radio luminosity Fanaroff-Riley type I (FRI) and higher radio luminosity Fanaroff-Riley type II (FR II) radio galaxies falls at  $L_{151} = 10^{25.3} \text{ W Hz}^{-1} \text{ sr}^{-1}$  (Fanaroff & Riley 1974), and this is also where there appears to be a difference in the evolution (Clewley & Jarvis 2004; Sadler et al. 2007), and thus these objects are probably FRI type radio galaxies, although some overlap in the populations is inevitable (see Chapter 3). I note that the majority of the sample of Bettoni et al. ( $\sim 90\%$  of the objects which have published radio luminosities) also have  $L_{151} < 10^{25.3} \text{ W Hz}^{-1} \text{ sr}^{-1}$  and are thus classified as FRI type radio galaxies. I therefore find evidence that the FRI type objects in my sample can inhabit the local Fundamental Plane of similar objects simply by passively evolving from  $z \sim 0.5$  to the present day.

Many of the remaining (FR II type,  $L_{151} > 10^{25.3} \text{ W Hz}^{-1} \text{ sr}^{-1}$ ) objects also lie close to the plane and within the scatter displayed by the data of Bettoni et al. (2001). However, I note that my FR II type radio galaxies exhibit a tendency to lie above the local Fundamental Plane, some by a reasonable distance (although there are also objects lying a reasonable distance below the plane). Passive evolution is not sufficient to explain how

---

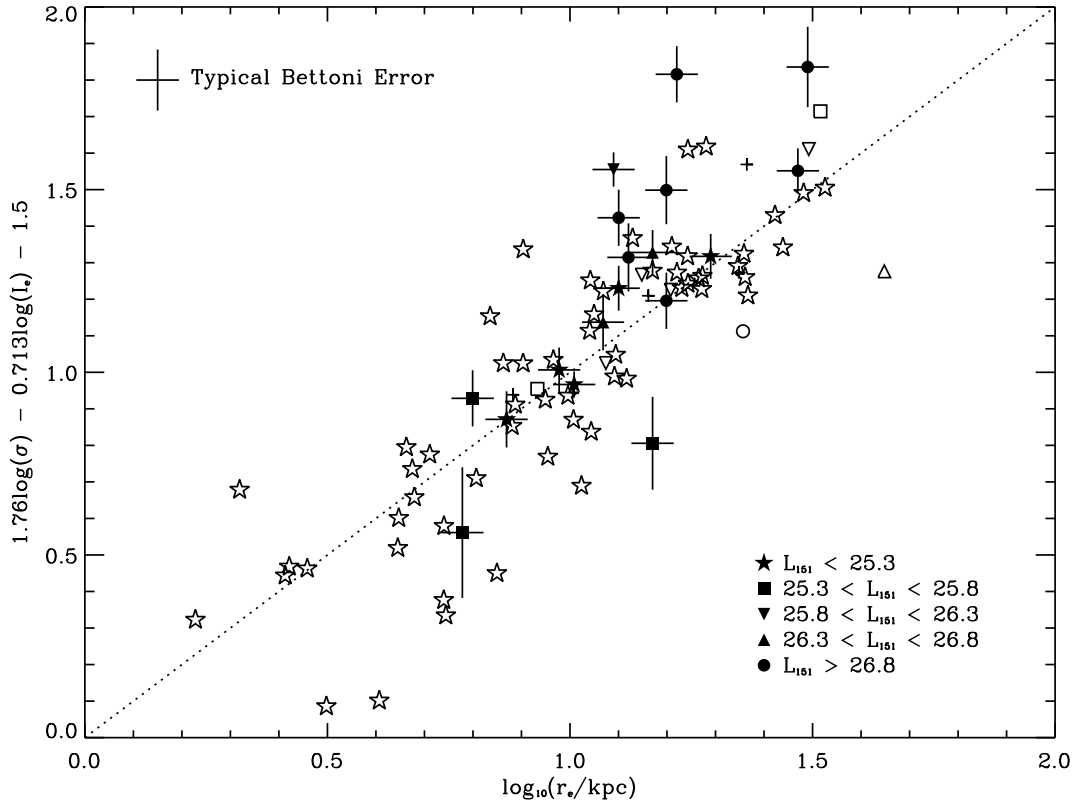


Figure 4.5: A 2D projection of the Fundamental Plane as fitted to the cosmologically corrected data of Bettoni et al. (2001;  $z \sim 0.03$ ) by minimising the sum of the absolute residuals perpendicular to the plane (Section 4.4.1). The data of Bettoni et al. is shown by open symbols. I use filled symbols to show the ZP5 data ( $z \sim 0.5$ ), corrected for passive evolution and aperture-corrected as described in Section 4.2.2. In each case the symbols correspond to the 151 MHz radio luminosities. Objects with  $L_{151} < 10^{25.3} \text{ W Hz}^{-1} \text{ sr}^{-1}$  are shown as stars. Objects with  $L_{151}$  between  $10^{25.3}$  and  $10^{25.8} \text{ W Hz}^{-1} \text{ sr}^{-1}$  are shown as squares whilst objects with  $L_{151}$  between  $10^{25.8}$  and  $10^{26.3} \text{ W Hz}^{-1} \text{ sr}^{-1}$  are shown as inverted triangles. Objects with  $L_{151}$  between  $10^{26.3}$  and  $10^{26.8} \text{ W Hz}^{-1} \text{ sr}^{-1}$  are shown as triangles, and objects with  $L_{151} > 10^{26.8} \text{ W Hz}^{-1} \text{ sr}^{-1}$  are shown as circles. Objects from Bettoni et al. for which I have been unable to locate a published radio luminosity are shown as crosses. I show the typical assumed error on the data of Bettoni et al. in the top left-hand corner (see Section 4.3.3).

these objects would move from their position at  $z \sim 0.5$  onto the  $z = 0$  Fundamental Plane. The FR II type objects of Bettoni et al. are consistent with the plane occupied by the rest of the  $z \sim 0$  sample, although there are insufficient objects with high radio luminosity to study this properly. Therefore, in contrast to my FRI type objects, I find evidence that the host galaxies of my  $z \sim 0.5$  FR II type objects must undergo evolution above and beyond their passive evolution to move them onto the local Fundamental Plane (Section 4.4.3). I find no clear correlation within the FR II type group between radio luminosity and the offset from the local Fundamental Plane, suggesting that this is indeed an evolutionary effect (rather than one related to the radio luminosity).

I also study the offsets of my ZP5 objects from the local Fundamental Plane of Figure 4.5 as a function of radio morphology and spectral classification (as used in Chapter 3). I find that those objects with large offsets are predominantly Classical Double (FR II) High Excitation Galaxies (HEGs), consistent with the above result based on radio luminosity and with a similar strength of trend. It is also worth emphasizing that I find no link between disturbed morphology from a recent merger (see McLure et al. 2004) and the size of the offset.

#### 4.4.2 The ZP5 Fundamental Plane

In Figure 4.6 I show a two-dimensional projection of the Fundamental Plane fitting the ZP5 data assuming symmetric errors in log space (row one of Table 4.2). It is apparent that my ZP5 objects do inhabit a  $z \sim 0.5$  Fundamental Plane, which is common to both the FRI type and the FR II type objects in the sample.

The reduced- $\chi^2$  of the ZP5 plane fitting shown in Figure 4.6 is 2.9 (tabulated, along with other reduced- $\chi^2$  values, in Table 4.4). The reduced- $\chi^2$  obtained when I compare the ZP5 data to the local Fundamental Plane of Figure 4.5 ( $\alpha = 1.76$ ,  $\beta = 0.713$ ,  $\gamma = 1.5$ ) is 10.2 (whereas comparing this local plane to the data of Bettoni et al. (2001) yields a

---

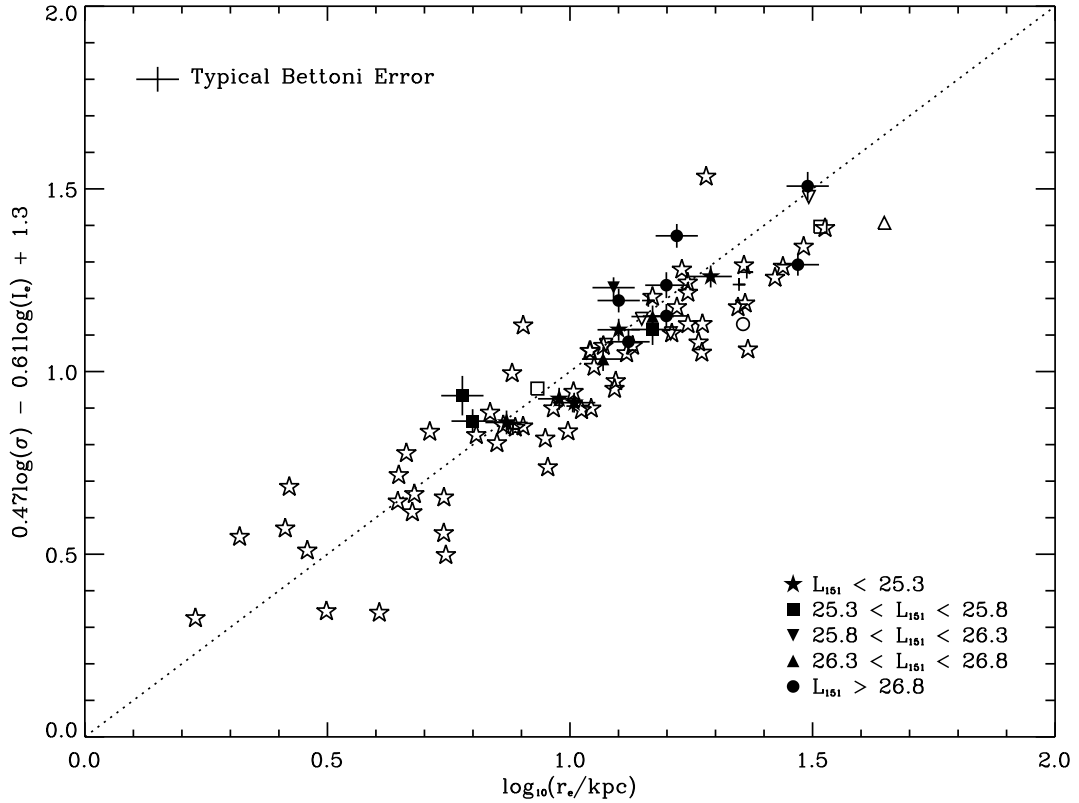


Figure 4.6: A 2D projection of the Fundamental Plane as fitted to the ZP5 data ( $z \sim 0.5$ ), assuming symmetric errors in log space (Section 4.4.2). I show the ZP5 data using filled symbols, corrected for passive evolution and aperture-corrected as described in Section 4.2.2, and the data of Bettoni et al. (2001;  $z \sim 0.03$ ) with open symbols. In each case the symbols correspond to the 151 MHz radio luminosities. Objects with  $L_{151} < 10^{25.3} \text{ W Hz}^{-1} \text{ sr}^{-1}$  are shown as stars. Objects with  $L_{151}$  between  $10^{25.3}$  and  $10^{25.8} \text{ W Hz}^{-1} \text{ sr}^{-1}$  are shown as squares whilst objects with  $L_{151}$  between  $10^{25.8}$  and  $10^{26.3} \text{ W Hz}^{-1} \text{ sr}^{-1}$  are shown as inverted triangles. Objects with  $L_{151}$  between  $10^{26.3}$  and  $10^{26.8} \text{ W Hz}^{-1} \text{ sr}^{-1}$  are shown as triangles, and objects with  $L_{151} > 10^{26.8} \text{ W Hz}^{-1} \text{ sr}^{-1}$  are shown as circles. Objects from Bettoni et al. for which I have been unable to locate a published radio luminosity are shown as crosses. I show the typical assumed error on the data of Bettoni et al. in the top left-hand corner (see Section 4.3.3).

reduced- $\chi^2$  of 3.4). For comparison I also fit a plane to the ZP5 data that follows the Kormendy ( $\mu_e - r_e$ ) relation (Kormendy 1977) by setting  $\alpha = 0$  and fitting for  $\beta$  and  $\gamma$ . My best fit in this case ( $\beta = 0.73$ ,  $\gamma = -2.7$ ) has a reduced- $\chi^2$  of 5.1. I find that my ZP5 fit is a significantly better fit to the ZP5 data than the local Fundamental Plane is. It is interesting to note from row one of Table 4.2 and row three of Table 4.3 that this ZP5 fit is significantly different from the fit to the local data. The most prominent difference between the local Fundamental Plane and the  $z \sim 0.5$  Fundamental Plane is that the  $\sigma$  exponent is much smaller for the  $z \sim 0.5$  plane. That is to say, the power law index that relates the effective radius and the surface brightness to the velocity dispersion is far smaller at  $z \sim 0.5$  than in the local universe. The velocity dispersion is related to the mass ( $M$ ) of the galaxy, and thus I infer that at  $z \sim 0.5$  the mass and size of these powerful radio galaxies are less closely related than in the local universe. However, despite the smaller  $\sigma$  exponent in the ZP5 relation, a comparison of the the reduced- $\chi^2$  values for the normal ZP5 fit and the Kormendy fit suggests that the  $z \sim 0.5$  Fundamental Plane is indeed a plane involving  $\sigma$  rather than merely a  $\mu_e - r_e$  relation; a fit with  $\alpha = 0$  is significantly worse than one where a dependence on  $\sigma$  is allowed.

Inspecting Figure 4.6 I find that, whilst the objects of Bettoni et al. are offset with regard to the ZP5 Fundamental Plane, there nevertheless appears to be a good agreement between the two data sets. I therefore perform a plane fitting (assuming symmetric errors in log space) to the two data sets combined. However, the resulting plane ( $\alpha = 1.23$ ,  $\beta = 0.61$ ,  $\gamma = 0.5$ ) yields reduced- $\chi^2$  values of 4.8, 6.1 and 3.5 when compared to the combined data, the ZP5 data and the data of Bettoni et al. respectively. I therefore find that a plane fitted to the combined data is not acceptable.

In Section 4.2.1 I noted that the errors on  $\sigma$  for some of my objects are undoubtedly underestimated. This contributes in part to the large reduced- $\chi^2$  values of the fits. In order to test whether these underestimated errors are leading me to reject acceptable plane

---

	Data of Bettoni et al.	ZP5 Data
Local Plane	3.4	10.2
ZP5 Plane	5.4	2.9
Size-evolved ZP5 Plane	4.8	2.9

Table 4.4: Reduced- $\chi^2$  values for fits to the Fundamental Plane. The first row contains the reduced- $\chi^2$  values yielded by a comparison of the local Fundamental Plane ( $\alpha = 1.76$ ,  $\beta = 0.713$ ,  $\gamma = 1.5$ ) to my data and that of Bettoni et al. (2001), whilst the second row shows the reduced- $\chi^2$  values from comparing the ZP5 plane (row one of Table 4.2) to the two data sets. The third row contains the reduced- $\chi^2$  values obtained by comparing the size-evolved ZP5 plane to the two data sets (Section 4.4.3), where the ZP5 data is also adjusted to account for size-evolution.

fittings I repeat my fittings and comparisons, but requiring a minimum error of 15% on  $r_e$ ,  $\sigma$ , and  $I_e$ . The reduced- $\chi^2$  values I obtain from comparing the data to the various plane fittings are shown in Table 4.5. I find, with a reduced- $\chi^2$  of 1.3, that the local plane (Figure 4.5) is an acceptable fit to the data of Bettoni et al.. I also find that the ZP5 plane (Figure 4.6) is an acceptable fit to the ZP5 data (reduced- $\chi^2$  of 1.2). However, I find that the local plane is not an acceptable fit to the ZP5 data (with a reduced- $\chi^2$  of 3.5), and nor is the ZP5 plane an acceptable fit to the local data (with a reduced- $\chi^2$  of 2.4). Finally, a plane fitted to the two data sets combined is also still rejected (reduced- $\chi^2$  values of 1.9, 2.6 and 1.3 when compared to the combined data, the ZP5 data and the data of Bettoni et al. respectively).

Taken altogether, my results therefore suggest that radio galaxies with lower and higher radio luminosities may share the same Fundamental Plane, but that there is substantial evolution in this plane between  $z = 0$  and  $z \sim 0.5$ .

### 4.4.3 Evolution of the Host Galaxies?

One explanation for the difference between the local Fundamental Plane of Bettoni et al. (2001) and the  $z \sim 0.5$  Fundamental Plane is evolution of the host galaxies. I have already shown in Sections 4.4.1 and 4.4.2 that passive evolution is not sufficient to explain

the difference between the planes, at least for the high radio luminosity population. Other possibilities include an evolution in the mass-to-light ratio or a size evolution of the host galaxies. I discuss each of these in turn.

Various authors have found evidence for a mass-dependent evolution of the mass-to-light ratio (e.g. Jørgensen et al. 2007; Fritz, Jørgensen & Schiavon 2010; see Chapter 1), and this in principle could explain the observed rotation between the ZP5 Fundamental Plane and the local one. I use my two plane fittings (row one of Table 4.2 and row three of Table 4.3) to calculate the mass-dependent evolution of the mass-to-light ratio that would be required to transform my  $z \sim 0.5$  plane into the local one (assuming  $r_e$  and  $\sigma$  remain constant and expressing  $\sigma$  in terms of  $r_e$  and  $M$ ). However, I find an implausibly large dependence on the  $z \sim 0.5$  luminosity would be required (greater than 10 orders of magnitude, with a correspondingly small dependence on the mass), and I therefore discount the possibility that this, by itself, could explain the difference between the two planes.

In Figure 4.7 I show histograms of the mass-to-light ratio distributions for the ZP5 and Bettoni samples. I use  $r_e$  and  $\sigma$  to calculate the mass of each object, according to the following equation (van der Wel et al. 2008):

	Data of Bettoni et al.	ZP5 Data
Local Plane	1.3	3.5
ZP5 Plane	2.4	1.2
Size-evolved ZP5 Plane	1.9	1.2

Table 4.5: Reduced- $\chi^2$  values for fits to the Fundamental Plane where the data used in the plane fittings and for the comparisons have errors  $\geq 15\%$ . The first row contains the reduced- $\chi^2$  values yielded by a comparison of the local Fundamental Plane to my data and that of Bettoni et al. (2001), whilst the second row shows the reduced- $\chi^2$  values from comparing the ZP5 plane to the two data sets. The third row contains the reduced- $\chi^2$  values obtained by comparing the size-evolved ZP5 plane to the two data sets (Section 4.4.3), where the ZP5 data is also adjusted to account for size-evolution.

$$M = \frac{5r_e\sigma^2}{G}, \quad (4.9)$$

where  $G$  is the Newtonian gravitational constant. I calculate the luminosity ( $L$ ) of each object from  $I_e$  and  $r_e$  as follows:

$$\frac{L}{L_\odot} = 4\pi I_e r_e^2. \quad (4.10)$$

A two-dimensional K-S test on the two distributions rejects at the 96% ( $2.0\sigma$ ) level the null hypothesis that the samples are drawn from the same distribution. I therefore find tentative evidence of an evolution in the mass-to-light ratio which, whilst not explaining the observed rotation between the  $z = 0$  and the  $z \sim 0.5$  planes by itself, may make some contribution to the tilt. Considering only the FR II type objects in my sample I reject the null hypothesis that this sample and that of Bettoni et al. are drawn from the same distribution at the 98% ( $2.3\sigma$ ) level. However, I find no clear evidence that the distribution of mass-to-light ratios is different for the FRI type objects and the sample of Bettoni et al. (rejecting the null hypothesis at only the 86% or  $1.1\sigma$  level), consistent with these objects lying on the local Fundamental Plane of Figure 4.5.

I next turn to consider the possibility of size evolution of the host galaxies. There exists evidence for the growth of early-type galaxies from higher redshifts to the present day: for example, the observational work of van der Wel et al. (2008) and the model of Hopkins et al. (2010), but see also Mancini et al. (2010). I use the size evolution model of van der Wel et al. (2009), where mergers cause the mass and effective radius to increase by the same factor. Thus  $\sigma$  remains constant (since  $\sigma \propto \sqrt{M/R}$ ), along with the mass-to-light ratio, whilst  $r_e$  and  $I_e$  vary. I characterise the size evolution using a factor  $\delta r_e$  where  $r_e(z = 0.5) = \delta r_e \cdot r_e(z = 0)$ . I investigate what value of  $\delta r_e$  gives the smallest offset between the ZP5 plane and the local data by varying  $\delta r_e$  (and adjusting

---

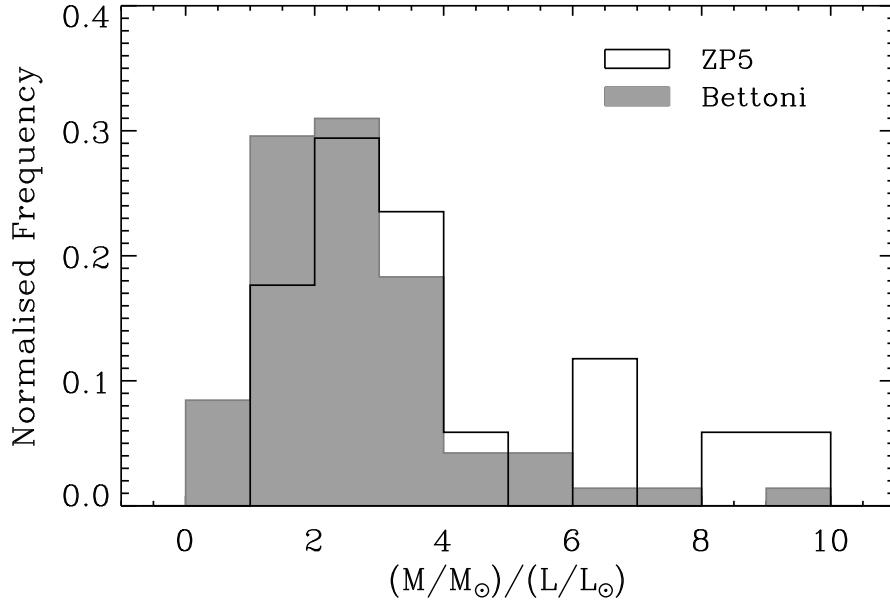


Figure 4.7: Histograms of the mass-to-light ratio distributions for the ZP5 ( $z \sim 0.5$ ) and Bettoni et al. (2001;  $z \sim 0.03$ ) samples (Section 4.4.3). The Bettoni et al. sample is shown by a shaded histogram and the ZP5 sample by an unshaded histogram.

$r_e$  and  $I_e$  accordingly), refitting a plane using the procedure described in Section 4.3.1, and minimising the reduced- $\chi^2$  of the fit of the local data of Bettoni et al. (2001) to this plane. For each value of  $\delta r_e$  I adjust the amount of passive evolution such that the ZP5 objects still satisfy the Kormendy relation of the bottom panel of figure 5 in McLure et al. (2004). I note that using the same  $\delta r_e$  factor for all galaxies simply produces a uniform translation of the objects with respect to the  $\log r_e$  and  $\log I_e$  axes and thus affects the offset but not the slope of the corresponding ZP5 plane. However, for each value of  $\delta r_e$  I re-fit a plane (rather than simply adjust the  $\gamma$  plane parameter) in order to account for the uncertainties in the  $\alpha$  and  $\beta$  plane parameters. The best fit is obtained with  $\delta r_e = 0.39$  (although the reduced- $\chi^2$  is fairly constant between 0.3 and 0.6) and is shown in Figure 4.8. This is in contrast to a value of  $\sim 0.91$  expected from the model of van der Wel et al. (2009; considering only the effects of mergers and excluding the effects of late-type

galaxies turning into early-types) but the upper end of the range is in good agreement with the model of Khochfar & Silk (2006) who predict a value of  $\delta r_e \sim 0.63\text{--}0.64$  for the most massive galaxies. The size evolution implied by  $\delta r_e = 0.39$  would result in a mean scalelength for my objects of 37.7 kpc. This is similar to the size of Brightest Cluster Galaxies (BCGs) in the local universe (Graham et al. 1996; McLure et al. 2004), which suggests that the host galaxies of powerful radio galaxies may evolve into BCGs.

However, as discussed above, whilst applying a uniform size evolution factor to the ZP5 objects can reduce the offset to the local galaxies, it does not affect the rotation. This is seen in Figure 4.8 where the tilt of the plane is still not consistent with the local data of Bettoni et al. (2001). Indeed, whilst the reduced- $\chi^2$  obtained by comparing the size-evolved ZP5 data to the plane of Figure 4.8 is 2.9 (Table 4.4), or 1.2 when I use errors  $\geq 15\%$ , when I compare the data of Bettoni et al. to this plane the reduced- $\chi^2$  is 4.8 (or 1.9 with  $\geq 15\%$  errors). Similarly, fitting a plane to the combined data of Bettoni et al. and the size-evolved ZP5 data yields a plane ( $\alpha = 1.32$ ,  $\beta = 0.61$ ,  $\gamma = 0.7$ ) whose reduced- $\chi^2$  values are 4.5, 5.3 and 3.4 when compared to the combined data, the ZP5 data and the data of Bettoni et al. respectively. Using errors  $\geq 15\%$  these values reduce to 1.8, 2.3 and 1.3 respectively. I therefore find that size evolution of the host galaxies by a uniform factor is not sufficient, in and of itself, to explain the difference between the  $z = 0$  and the  $z \sim 0.5$  Fundamental Planes, since it does not address the difference in rotation between these two planes.

In order for the tilt to be explained by size evolution we would require a mass (and size) dependent evolution of the host galaxies. Once more comparing the ZP5 plane fitting in row one of Table 4.2 with the local fitting in row three of Table 4.3, and taking  $\delta r_e$  (as defined above) to be a function of mass, I find  $\delta r_e \propto r_e^{1.52} M^{-2.11}$  (neglecting any other forms of evolution). This seems more plausible than the mass-dependent mass-to-light ratio evolution, although the actual evolutionary factors required for my objects (0.09–

---

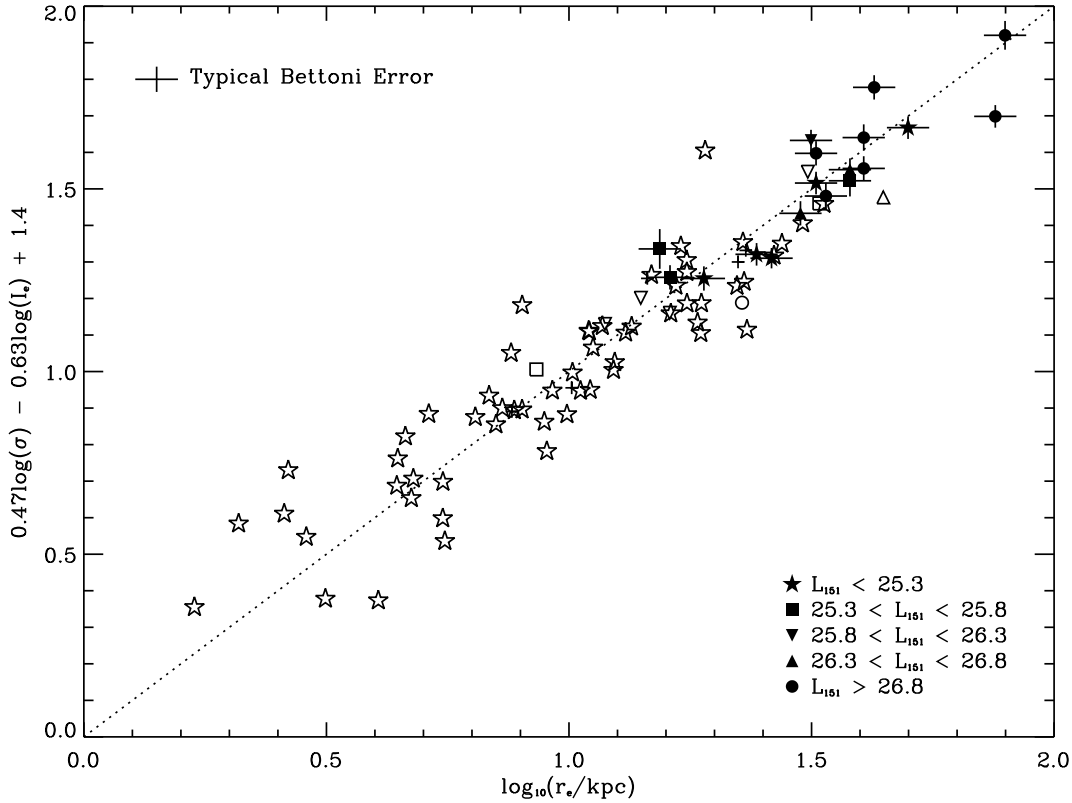


Figure 4.8: A 2D projection of the Fundamental Plane as fitted to the ZP5 data ( $z \sim 0.5$ ), size-evolved by a factor  $\delta r_e = 0.39$  (Section 4.4.3). I show the size-evolved ZP5 data using filled symbols, corrected for passive evolution and aperture-corrected as described in Section 4.2.2, and the data of Bettoni et al. (2001;  $z \sim 0.03$ ) with open symbols. In each case the symbols correspond to the 151 MHz radio luminosities. Objects with  $L_{151} < 10^{25.3} \text{ W Hz}^{-1} \text{ sr}^{-1}$  are shown as stars. Objects with  $L_{151}$  between  $10^{25.3}$  and  $10^{25.8} \text{ W Hz}^{-1} \text{ sr}^{-1}$  are shown as squares whilst objects with  $L_{151}$  between  $10^{25.8}$  and  $10^{26.3} \text{ W Hz}^{-1} \text{ sr}^{-1}$  are shown as inverted triangles. Objects with  $L_{151}$  between  $10^{26.3}$  and  $10^{26.8} \text{ W Hz}^{-1} \text{ sr}^{-1}$  are shown as triangles, and objects with  $L_{151} > 10^{26.8} \text{ W Hz}^{-1} \text{ sr}^{-1}$  are shown as circles. Objects from Bettoni et al. for which I have been unable to locate a published radio luminosity are shown as crosses. I show the typical assumed error on the data of Bettoni et al. in the top left-hand corner (see Section 4.3.3).

86.7, calculated using the same method) are not. A mass-dependent size evolution could be driven by environmental effects (where the most massive galaxies are found only in virialized clusters where mergers are suppressed), which I investigate in Chapter 6 using deep multi-band imaging data.

I therefore find that, whilst a mass-dependent size evolution may be the dominant effect behind the evolution of the Fundamental Plane, it is not sufficient in and of itself to explain the observed rotation between the  $z \sim 0.5$  and  $z = 0$  planes. I suggest that size evolution may combine with passive evolution and a mass-dependent evolution of the mass-to-light ratio to produce the observed rotation.

#### 4.4.4 A Link with Recent Star Formation?

I next consider the possibility that my powerful ZP5 radio galaxies already inhabit the local Fundamental Plane, but that the effects of recent star formation make them appear to lie off it. In other words, is it possible that my objects that lie below the local Fundamental Plane could have a bright extended disc of recent star formation that would increase the observed effective radius? Conversely, is it possible that my objects that lie above the local plane could have a bright nucleocentric region of recent star formation that would decrease the observed effective radius? If the star formation terminates by  $z = 0$  then the observed effective radius would be altered in both cases, possibly moving the objects back on to the local relation.

I test this hypothesis using the strength of the 4000Å break for my objects; the  $D_n(4000)$  indices (see Chapter 3) can be used as a measure of recent star formation, where younger populations have smaller 4000Å breaks, as discussed in Chapter 3. In Figure 4.9 I show the residual perpendicular to the plane of Figure 4.5 versus  $D_n(4000)$  for the ZP5 objects. It is seen that those objects that fall significantly below the local Fundamental Plane, as well as the two furthest above it, all have lower  $D_n(4000)$  indices

---

and thus younger stellar populations. This lends a degree of support to the recent star formation hypothesis, although I note that some of the objects that fall furthest from the plane have no evidence of recent star formation whilst some falling on or near the plane do have evidence for younger stellar populations.

In order to test the hypothesis further I extract the spectra for my objects using a range of apertures across the galaxy: in addition to the FWHM and FWZI apertures used above, I also use an aperture corresponding to the full-width at three-quarters intensity, and a further aperture corresponding to the effective radius,  $r_e$ , of the galaxy. I calculate  $D_n(4000)$  indices in each case and look for any trends between  $D_n(4000)$  and extraction radius for each object. However, I find no such trends within the uncertainties on  $D_n(4000)$  and the amount of possible contamination discussed in Chapter 3. I cannot therefore, with my current data, prove star formation in extended discs and nucleocentric regions as an explanation for why some of my objects lie away from the local Fundamental Plane.

#### 4.4.5 Correlations with Radio Luminosity

Evidence of a correlation between black hole mass and radio luminosity was first presented by Franceschini, Vercellone & Fabian (1998), who showed that both the nuclear and the total radio fluxes of their sample of nearby radio galaxies displayed a remarkably tight dependence on black hole mass. This result has been confirmed by more recent work (e.g. McLure et al. 1999; Lacy et al. 2001; McLure & Jarvis 2004) whilst evidence has also emerged of a connection between black hole mass and radio-loudness (e.g. Laor 2000; McLure & Dunlop 2001b; McLure & Jarvis 2004), although other studies have found no evidence of such connections (e.g. Ho 2002; Woo & Urry 2002).

In order to investigate the possible link between radio luminosity and black hole mass for the objects in this sample I calculate the black hole mass from  $\sigma$  using the  $M_{BH}-\sigma$  relation for elliptical galaxies published by Gültekin et al. (2009) and propagate errors

---

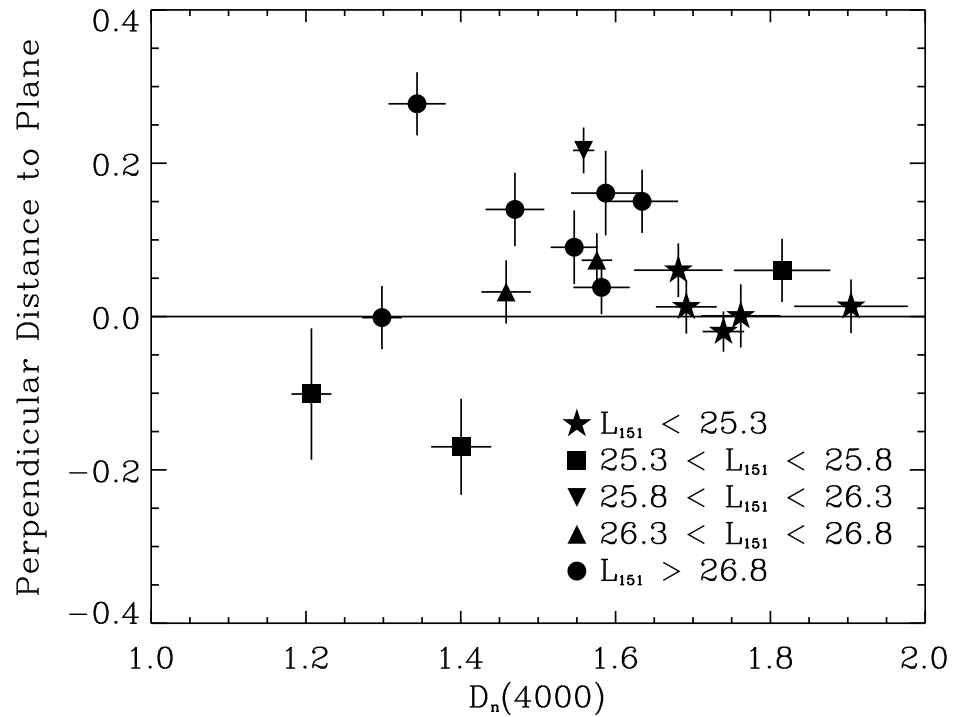


Figure 4.9: The residual of the data perpendicular to the plane of Figure 4.5 versus  $D_n(4000)$  for the ZP5 ( $z \sim 0.5$ ) objects (Section 4.4.4). Objects with  $L_{151} < 10^{25.3} \text{ W Hz}^{-1} \text{ sr}^{-1}$  are shown as stars. Objects with  $L_{151}$  between  $10^{25.3}$  and  $10^{25.8} \text{ W Hz}^{-1} \text{ sr}^{-1}$  are shown as squares whilst objects with  $L_{151}$  between  $10^{25.8}$  and  $10^{26.3} \text{ W Hz}^{-1} \text{ sr}^{-1}$  are shown as inverted triangles. Objects with  $L_{151}$  between  $10^{26.3}$  and  $10^{26.8} \text{ W Hz}^{-1} \text{ sr}^{-1}$  are shown as triangles, and objects with  $L_{151} > 10^{26.8} \text{ W Hz}^{-1} \text{ sr}^{-1}$  are shown as circles.

in the standard fashion by assuming symmetric errors on  $\log \sigma$  as above. It is important to note that, whilst the majority of the previous studies have used the high-frequency (5-GHz) radio luminosity, I use the extended low-frequency (151 MHz) radio luminosity. This may be significant, since the 151 MHz radio luminosity is closely connected with the time-averaged kinetic energy of the jets (e.g. Rawlings & Saunders 1991) and the effects of beaming are smaller on the 151 MHz radio luminosity than on the 5-GHz radio luminosity (e.g. Jarvis & McLure 2002).

In Figure 4.10 I show  $L_{151}$  versus black hole mass. Figure 4.10 provides evidence in support of a link between radio luminosity and black hole mass: using the Spearman rank correlation coefficient I find a positive correlation between the  $L_{151}$  radio luminosity and  $M_{BH}$  at a significance level of 97% ( $2.2\sigma$ ). This is in good agreement with the  $L_{151}$ - $M_{BH}$  relation for the whole ZP5 sample found at a significance level of 97% ( $2.2\sigma$ ) by McLure et al. (2004) where the black hole masses were estimated via the  $M_{BH}$ - $M_{Bulge}$  relation of McLure & Dunlop (2002). However, in contrast to McLure et al. (2004), who find that the significance of the correlation is increased to 99.5% ( $2.8\sigma$ ) by excluding the TOOT objects, I find that excluding the TOOT objects decreases the correlation significance to 84% ( $1.4\sigma$ ). However, this could be purely due to the decrease in the number of objects used for the analysis: 18 compared to the full sample of 41 used in the work of McLure et al. (2004). Additional spectroscopy on the remaining radio galaxies would be needed to confirm this.

I also find a positive correlation between  $L_{151}$  and  $r_e$  (Figure 4.11). Applying the Spearman rank correlation coefficient yields a significance of 98% ( $2.3\sigma$ ). It is interesting to note that the TOOT objects (triangles) — FRI type objects with  $L_{151} < 10^{25.3}$  W Hz<sup>-1</sup> sr<sup>-1</sup> — do not appear to follow this relation; for the TOOT objects  $r_e$  appears to be largely independent of  $L_{151}$ . This is consistent with the above findings for the Fundamental Plane, where the low-luminosity radio sources are consistent with being able to

---

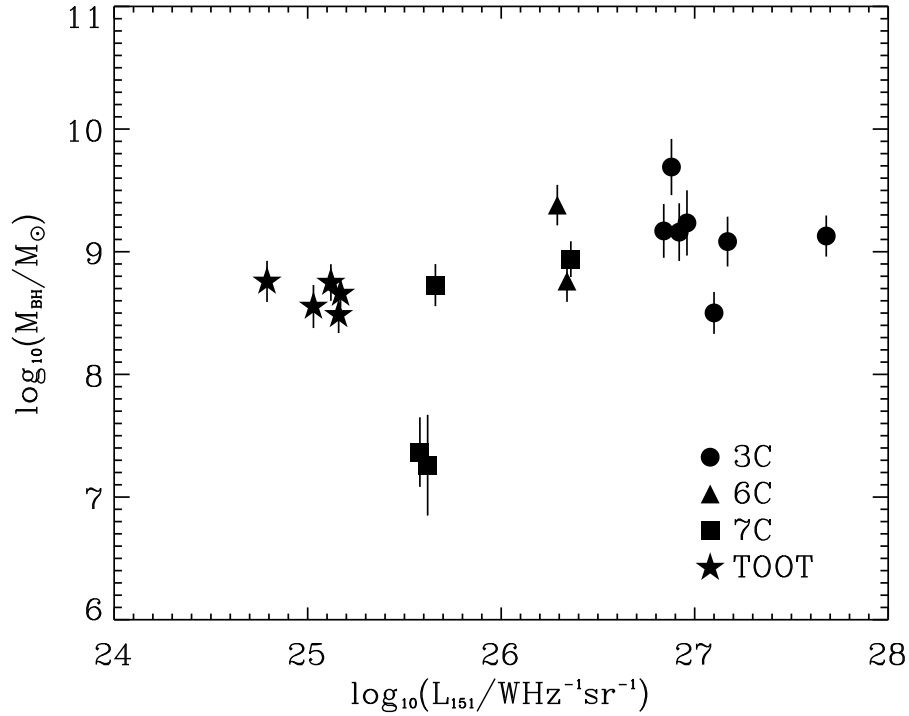


Figure 4.10: The variation of the logarithm of the 151 MHz radio luminosity,  $L_{151}$ , with black hole mass for the ZP5 ( $z \sim 0.5$ ) objects (Section 4.4.5). Circles represent 3C galaxies, 6C galaxies are represented by triangles, 7C galaxies by squares, and TOOT objects by stars.

passively evolve onto the local relation.

## 4.5 Conclusions

In this chapter I have presented deep spectroscopic observations of 24 powerful radio galaxies at  $z \sim 0.5$ . I have used a direct fitting procedure to determine the velocity dispersions of the objects and combined these with the host galaxy data from McLure et al. (2004) to study the Fundamental Plane.

- I have shown that the FRI type objects in the sample, once corrected for passive evolution, lie on the Fundamental Plane inhabited by the local radio galaxies of

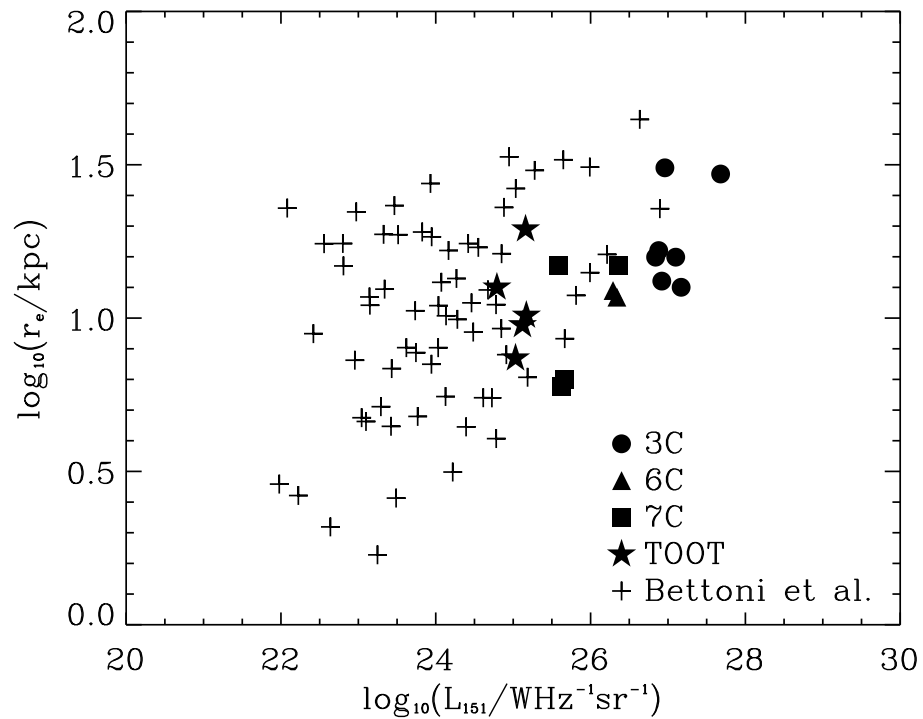


Figure 4.11: The variation of the logarithm of the 151 MHz radio luminosity,  $L_{151}$ , with effective radius,  $r_e$ , for the ZP5 ( $z \sim 0.5$ ) objects (Section 4.4.5). Circles represent 3C galaxies, 6C galaxies are represented by triangles, 7C galaxies by squares, and TOOT objects by stars. The data of Bettoni et al. (2001;  $z \sim 0.03$ ) are shown by crosses.

Bettoni et al. (2001). The FR II type objects in the sample do not lie on the local plane. However, whilst the majority of the sample of Bettoni et al. are lower radio luminosity (FRI type) objects, the FR II type objects in their sample are consistent with the local plane. Furthermore, my FRI type objects and my FR II type objects appear able to share the same plane at  $z \sim 0.5$ . I therefore suggest that radio galaxies with lower and higher radio luminosities may share the same Fundamental Plane, but that there is substantial evolution in this plane between  $z = 0$  and  $z \sim 0.5$ .

- One explanation for the tilt observed between the  $z = 0$  and the  $z \sim 0.5$  Fundamental Planes is evolution of the host galaxies. I consider passive evolution, a mass-dependent evolution in the mass-to-light ratio and an evolution in the size of the host galaxy, but find that none of these effects can, by themselves, plausibly explain the observed rotation. I suggest, however, that some combination of all three effects, with size evolution as the dominant factor, may be sufficient to explain the difference between the planes. Indeed, indirect evidence for size evolution for the high-luminosity sources comes from the significant correlation (98%,  $2.3\sigma$ ) between the effective radius and the radio luminosity for these sources, whereas the FRI sources do not appear to align with such a relation.
  - I also consider the possibility that my radio galaxies do, in fact, lie on the local Fundamental Plane (once passive evolution has been corrected for), but that a bright extended disc or nucleocentric region of recent star formation alters the observed effective radius, thus causing some of the objects to appear to lie off the local relation. Using the  $D_n(4000)$  index as an indicator of recent star formation, I see some hints that this may be having an effect, but the evidence is far from conclusive.
  - I find evidence at the 97% ( $2.2\sigma$ ) level of a correlation between galaxy velocity
-

dispersion and the radio luminosity, suggesting that radio luminosity scales with black-hole mass. This is in line with previous work on this sample using the host galaxy luminosity as a proxy for black-hole mass (McLure et al. 2004). Unlike McLure et al., however, I do not find that this correlation becomes stronger in the absence of the low-luminosity (FRI type) radio sources. I attribute this to the lack of objects in the present study (18) compared with the analysis of the full sample of 41 in McLure et al..

---

# Chapter 5

## Imaging Data

Deep multi-band imaging data were obtained, using the Wide Field Camera (WFC) on the Isaac Newton Telescope (INT), between November 2000 and May 2008 for the entire  $z \sim 0.5$  (ZP5) sample, with the exception of TOOT0009+3523 and TOOT0013+3459. Data for these objects were obtained using the William Herschel Telescope (WHT) in January 2009. In this chapter I describe the acquisition of the INT data (Section 5.1) and its data reduction (Section 5.2). I then describe the processing of all of the imaging data (Section 5.3) in preparation for my study of the large-scale environments of the ZP5 sample in Chapter 6.

### 5.1 INT Observations

The INT data were obtained between November 2000 and May 2008. Each object was observed with the Sloan Digital Sky Survey (SDSS)  $g'$ ,  $r'$  and  $i'$  filters. In most cases, objects were observed for a total of 2700 seconds in the  $g'$  band and 1800 seconds in the  $r'$  and  $i'$  bands, split into three separate observations with appropriate offsets in each case. The offsets moved bad pixels around on the sky, whilst the separate observations allowed for the removal of cosmic rays and other transients (Section 5.2). Details for each object

can be found in Table 5.1. A suitable guide star was used for each observation, and slow readout was used. Bias frames, twilight flat fields and standard stars were also observed on each night.

## 5.2 INT Data Reduction

The raw data produced by the telescope need reducing in order to remove, as far as possible, the effects of the instrument on the data. These effects are removed in three ways: bias frames, flat field frames, and fringe frames. The bias is caused by the readout noise of the Charge-coupled Devices (CCDs), and a bias frame is generated by reading out the unexposed CCDs. Flat fields account for distortions in the optical path, as well as the non-uniform response of pixels in the CCDs, and are obtained by exposures of the (approximately uniform) twilight sky. Fringing is caused at longer wavelengths by the interference of incoming photons (whose wavelength is comparable to the depth of the CCD) with reflected photons. A fringe frame can be generated from a set of unique pointings in the relevant filter, and this can be used to substantially reduce the presence of the fringes in the final images.

I used the INT pipeline at the Cambridge Astronomical Survey Unit (Irwin & Lewis 2001) in order to reduce my data (bias, flat field and fringe frame correct, as well as astrometric and photometric calibrations and stacking of individual frames), as described below.<sup>1</sup>

A master bias frame is created by the pipeline for each observing run. A maximum of 12 bias frames, forming consecutive runs and omitting the first bias of each night, are median combined into twelve or fewer combined bias frames. These combined bias frames are then median combined a further time into the master bias frame for that observing

---

<sup>1</sup>I am grateful to Eduardo Gonzalez-Solares of the Institute of Astronomy, Cambridge, for performing the initial data reduction (bias, flat field and fringe frame corrections and the astrometric and photometric calibrations) on the observations of the object 6C1111+3940.

---

Object	$g'$		$r'$		$i'$	
	Frames	Exp. Time	Frames	Exp. Time	Frames	Exp. Time
3C16	3	2700	3	1800	3	1800
3C19	8	7200	6	4500	3	1800
3C46	3	2700	3	1800	3	1800
3C172	4	3600	3	1800	3	1800
3C200	3	2700	3	1800	6	3600
3C225B	3	2700	3	1800	3	1800
3C228	3	2700	3	1800	3	1800
4C74.16	3	2700	3	1800	3	1800
3C244.1	7	6000	3	1800	6	3600
3C274.1	3	2700	3	1800	3	1800
3C295	3	2700	3	1800	3	1800
3C330	6	4500	6	4500	6	4500
3C341	4	2700	3	1800	3	1800
3C427.1	3	2700	3	1800	3	1800
3C457	6	4500	5	3000	6	3600
6C0825+3407	5	3000	4	2400	3	1800
6C0850+3747	3	1800	3	1800	3	1800
6C0857+3945	6	5400	3	1800	10	6000
6C1111+3940	6	2700	3	1800	3	1800
6C1132+3439	6	4500	6	3600	6	3600
6C1200+3416	3	2700	3	1820	3	1800
6C1303+3756	2	1800	3	1800	4	2700
7C0213+3418	3	2700	3	1800	3	1800
7C0219+3419	6	5400	3	1800	3	1800
7C0219+3423	3	2700	3	1800	3	1800
7C0220+2952	3	2700	3	1800	3	1800
7C0223+3415	3	2700	3	1800	3	1800
7C0810+2650	4	3600	3	1800	3	1800
7C1731+6638	3	2700	3	1800	3	1800
7C1806+6831	4	2700	3	1800	3	1800

Table 5.1: The number of frames and total exposure time (in seconds) making up the final stack in the  $g'$ ,  $r'$  and  $i'$  bands for the  $z \sim 0.5$  objects observed using the Isaac Newton Telescope (INT). TOOT0009+3523 and TOOT0013+3459, which were observed using the William Herschel Telescope (WHT), are also included (see Section 5.3.1).

Object	$g'$		$r'$		$i'$	
	Frames	Exp. Time	Frames	Exp. Time	Frames	Exp. Time
TOOT0009+3523	3	1200	3	750	3	750
TOOT0013+3459	3	1200	3	750	3	750
TOOT0018+3510	3	2700	3	1800	3	1800
TOOT1255+3556	3	2400	3	2400	3	2400
TOOT1301+3658	6	5400	3	1800	3	1800
TOOT1303+3334	3	2700	3	1800	3	1800
TOOT1307+3639	5	4500	3	1800	3	1800
TOOT1309+3359	3	2700	3	1800	3	1800
TOOT1626+4523	4	2700	3	1800	3	1800
TOOT1630+4534	5	4500	4	3600	4	3600
TOOT1648+5040	6	5400	3	1800	4	2400

Table 5.1 continued.

run. An example of a master bias frame is shown in Figure 5.1.

A master flat is created for each band observed in each observing run. For this purpose, twilight flats with counts in the range 17,000 – 30,000 are used. Ideally, when sufficient acceptable flat fields are available from an observing run, this range is restricted to 20,000 – 30,000. The lower constraint is imposed since too few counts results in too low a signal-to-noise ratio. The upper constraint is a result of the highly non-linear behaviour of the CCDs as they near saturation. The acceptable flat fields are bias subtracted and median combined to produce the master flat for each band. The pipeline also uses a look-up table at this stage to correct for non-linearities in the CCDs. CCDs 2 and 4 exhibit significant non-linearities and share one Analogue-to-Digital Converter (ADC). This ADC is believed to be the source of the non-linearities which are thus expected to be stable with time (Irwin & Lewis 2001). Examples of the master flats from the January 2008 observing run can be found in Figure 5.2. The pipeline is then used to bias-subtract and flat-field the science data, once again using the look-up table to correct for CCD non-linearities. The pipeline also corrects the gain for each CCD in order to place all of the CCDs on the same zeropoint system.

At this stage, significant fringing is still present in  $i'$  band images (and also, whilst

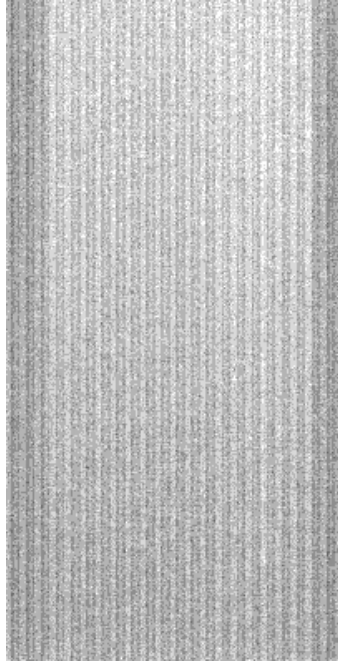


Figure 5.1: An example of a master bias frame for CCD 4, taken from the January 2008 observing run (Section 5.2).

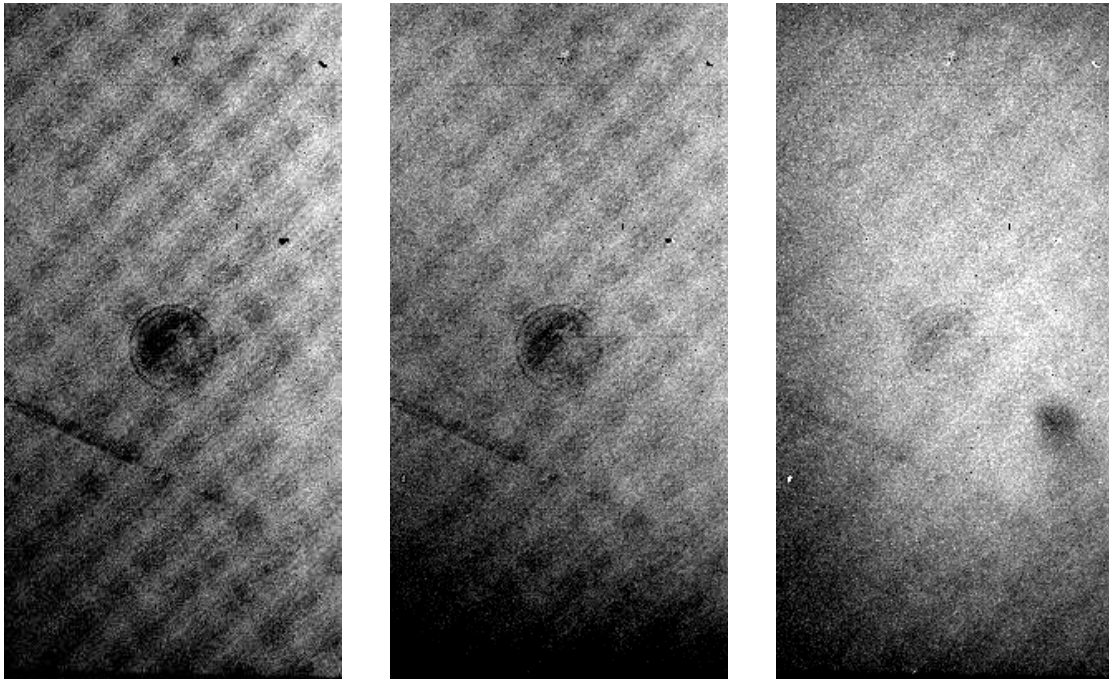


Figure 5.2: Examples of the master flat frames produced by the pipeline for CCD 4, taken from the January 2008 observing run (Section 5.2). Left to right the images show the  $g'$ ,  $r'$  and  $i'$  bands.

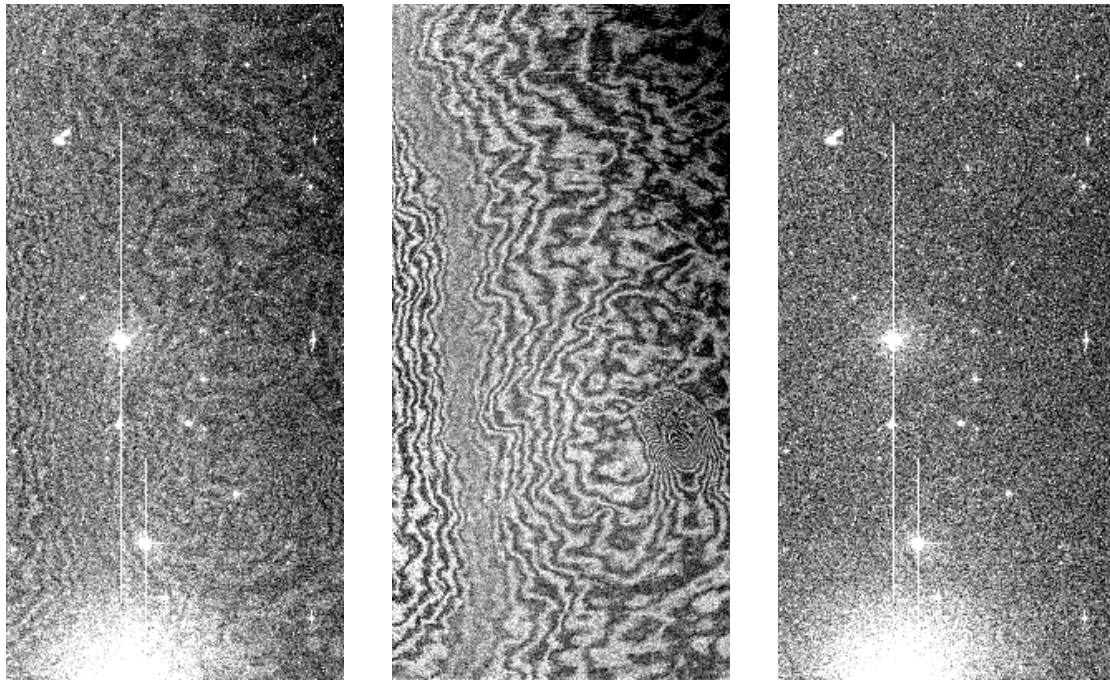


Figure 5.3: An example of fringe removal for CCD 4 in the  $i'$  band, taken from the August 2003 observing run (Section 5.2). The left-hand panel shows one of the bias-subtracted and flat-fielded  $i'$  images of TOOT1630+4534. The middle panel shows the master  $i'$  band fringe frame for this run, and the right-hand panel shows the de-fringed science image.

not used in this thesis, I and Z band images). The pipeline uses a selection of 10-12 unique pointings in these bands to create a master fringe frame for each observing run. After manual inspection to ensure that no residual star images are present, this is used to de-fringe the science data in the  $i'$ , I and Z bands. An example is shown in Figure 5.3.

Confidence maps are generated from the master flats for each run and the pipeline's own directory of bad pixels. The confidence maps are used by the pipeline to generate an object catalogue for each image. An initial astrometric solution for each frame is derived from the telescope pointing, rotator angle, and array geometry. This solution is improved by comparing the object catalogues with Hubble Space Telescope Guide Star Catalogue objects present in the reduced frames, and the new solution is written to the image headers. Photometric calibrations are automatically performed by the pipeline, using Landolt standard fields (where observed) from each night.

---

Finally, the pipeline is used to stack the individual frames for each object and band into a single, deeper, image. The pipeline uses the astrometric solutions in order to align the (offset) individual frames, producing an image with an increased signal-to-noise ratio which lacks CCD artefacts (due to the offset between the constituent frames), cosmic rays and other transients. The pipeline also produces a confidence map accompanying each stack. The total exposure time and number of observations making up each stacked image can be found in Table 5.1.

### 5.2.1 Further Photometric Calibrations

The photometry in the stacked images was not always correct, for one or both of the following reasons:

1. The constituent frames are median combined into the stacked image by the stacking routine. Thus the counts are not properly combined in those cases where constituent frames had different zeropoints or different exposure times.
2. Some of the constituent frames were observed in non-photometric conditions.

26 of the objects lie in Sloan Digital Sky Survey (SDSS) fields. For these objects I therefore used the photometry of bright stars taken from the SDSS catalogue<sup>2</sup> in order to manually calibrate the zeropoints in the final stacked images. For the remaining objects, I used the reduced nightly standard stars (and, where appropriate, an individual frame observed in photometric conditions) to manually calibrate the zeropoints.

The  $i'$  band data for 3C172 was obtained on the night of 27/01/2003, which suffered from particularly bad weather. As well as non-photometric data, no suitable standard star was obtained on this night, and 3C172 does not lie within the SDSS regions. The  $i'$  band photometry for 3C172 can not, therefore, be relied upon, and I exclude this object from

---

<sup>2</sup><http://cas.sdss.org/astrodr7/en/>

the analysis in Chapter 6. Examples of the multi-colour images of the central CCD for each object, created from the final reduced images, are shown in Figure 5.4.

## 5.3 Data Processing

### 5.3.1 Source Extraction

Following the reduction of the INT data, I further processed the data so they could be used to investigate the large scale environments surrounding the radio galaxies (Chapter 6). Similar data for two further ZP5 objects (TOOT0009+3523 and TOOT0013+3459), obtained using the WHT and already reduced, were processed in the same way.<sup>3</sup>

To begin with, the data from the central chips was copied into single-extension FITS files. For each object, the central chip (CCD 4 for the INT data and CCD 2 for the WHT data) images the ZP5 radio galaxy and its environment. The second most sensitive chips (CCD 1 for both the INT and the WHT) were also copied into single-extension FITS files to act as reference images. The confidence maps accompanying the object and reference chips were copied in the same way.

Each of the images was then normalised by the exposure time (taken from the image header). The Image Reduction and Analysis Facility (IRAF) *wregister* task was used to register the  $g'$  and  $r'$  band images to the (deeper)  $i'$  band images. Finally, the SExtractor programme<sup>4</sup> was used to extract a catalogue of sources for each image, ready for use in Chapter 6.

---

<sup>3</sup>The data for TOOT0009+3523 and TOOT0013+3459, obtained using the WHT, were reduced by my principal supervisor, Dr Matt Jarvis.

<sup>4</sup><http://www.astromatic.net/software/sextractor>

---



Figure 5.4: Examples of the *gri* multi-colour images of the environments of the  $z \sim 0.5$  objects (Section 5.2.1). Top row (left to right): 3C16, 3C295, 6C0857+3945. Bottom row (left to right): 7C0213+3418, 7C0219+3419, TOOT1648+5040.

### 5.3.2 Completeness

In order to investigate the completeness of each of my images, I began by adding fake galaxies to the single-extension image files normalised by the exposure time. For each image, the fake galaxy was constructed as a point spread function with Gaussian profiles. The vertical dimension had a full-width at half-maximum (FWHM) of  $0.9''$  convolved with the seeing of the image. The horizontal dimension had a FWHM of  $1.2''$  convolved with the seeing. The galaxies were given a magnitude between 11 and 33, with 200 fake galaxies per 0.1 magnitude bin, and the magnitudes were randomly generated within each bin. The fake galaxies were split between 20 fake images in order to prevent overly dense fields. I also required that each fake galaxy was at least 20 pixels from any other fake galaxy.

The sources in the fake images were then extracted using SExtractor and compared to the catalogue of inserted fake galaxies in order to determine the fraction recovered at each magnitude for each image. I show examples of the completeness curves for the objects in Figure 5.5. Based on the completeness curves, I impose a conservative cut of  $i' < 21.5$  and correct my data for completeness. This cut is based on the completeness curves rather than the sensitivities since my determination of the sensitivities is affected by the presence of bright stars in some of the fields. For  $i' < 21.5$  the completeness fractions range from 1.0 down to 0.76.

For the completeness correction I fit a third order polynomial to each completeness curve for  $i' < 21.5$  (also shown in Figure 5.5). A satisfactory fit is achieved for all of the images except for the 6C1111+3940  $i'$  band image, for which I use two polynomials (for  $i' < 21$  and  $i' > 21$ ).

---

## 5.4 Summary

In this Chapter I have described the observations and data reduction used to obtain wide field multi-band imaging of the ZP5 sample. The observations were made between November 2000 and May 2008 using the WFC on the INT and in January 2009 using the WHT. In each case the  $g'$ ,  $r'$  and  $i'$  filters were used. The INT data were reduced using the Cambridge Astronomical Survey Unit pipeline, and photometric calibrations were performed manually using the nightly standard stars as well as data from the SDSS. Sources were extracted using SExtractor and completeness fractions were calculated for each image by inserting fake galaxies into them before re-extracting.

---

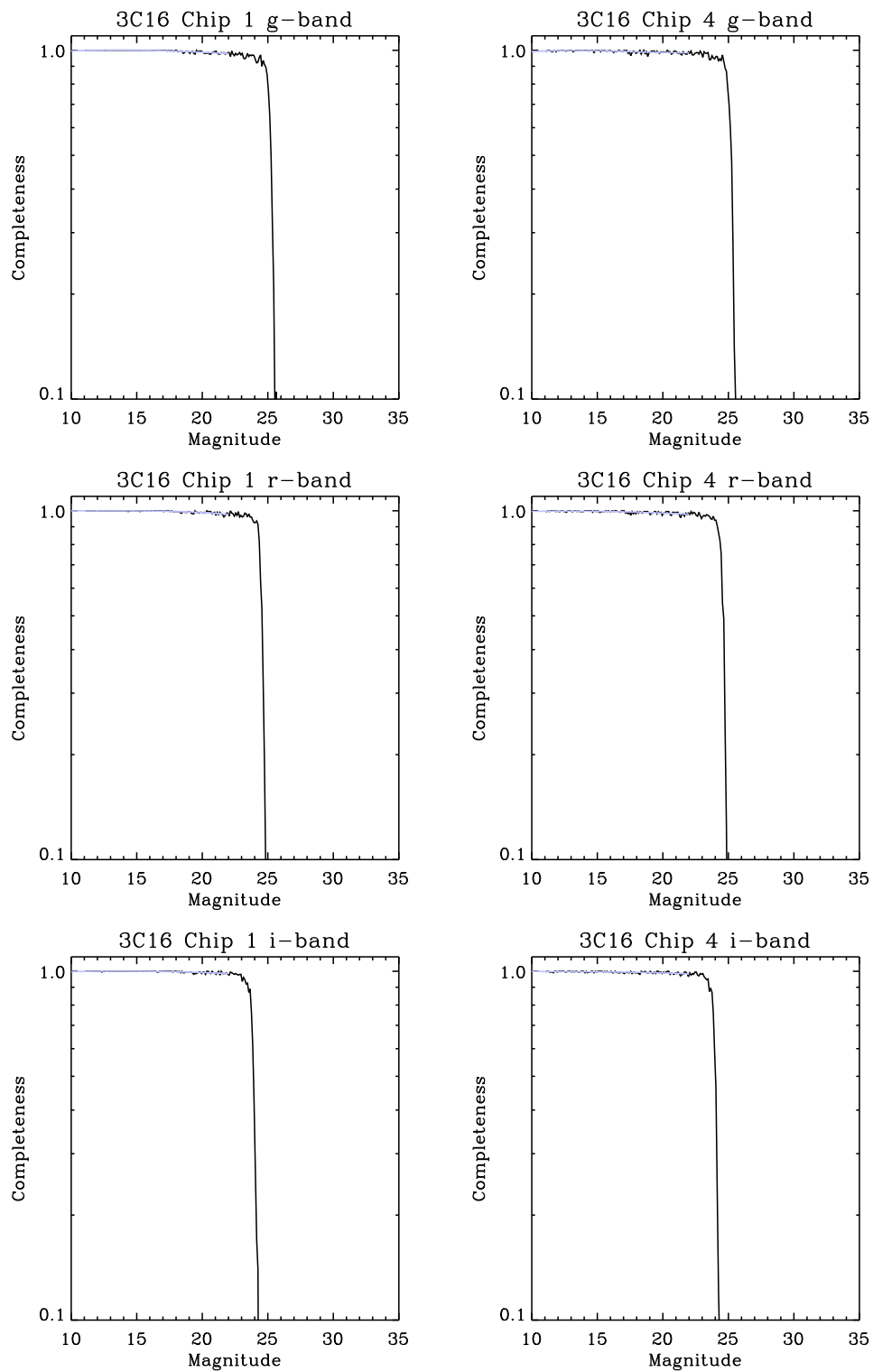


Figure 5.5: Examples of completeness curves (black) for the ZP5 objects, overlaid with the fitted polynomial (blue) as described in Section 5.3.2.

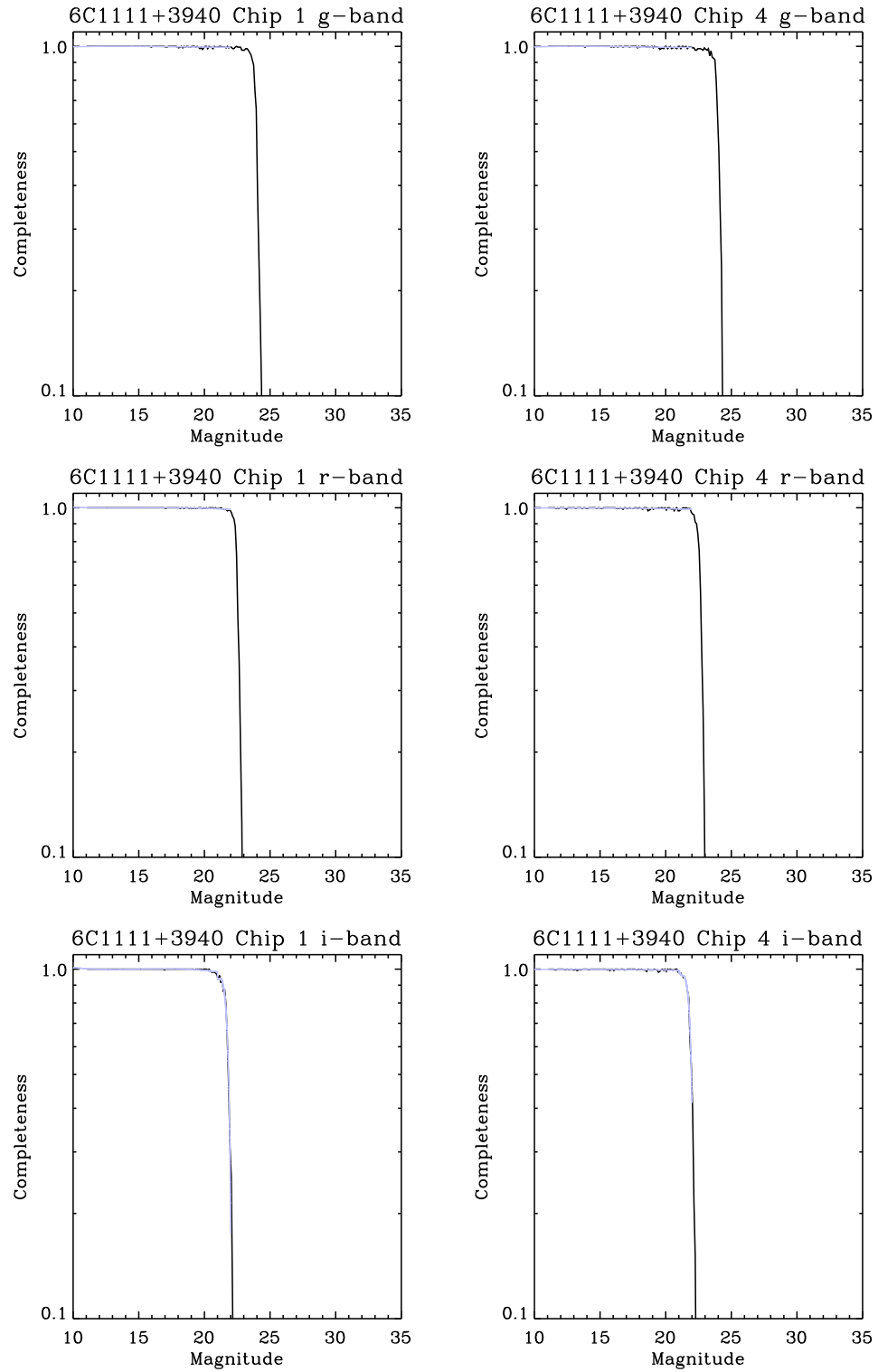


Figure 5.5 continued.

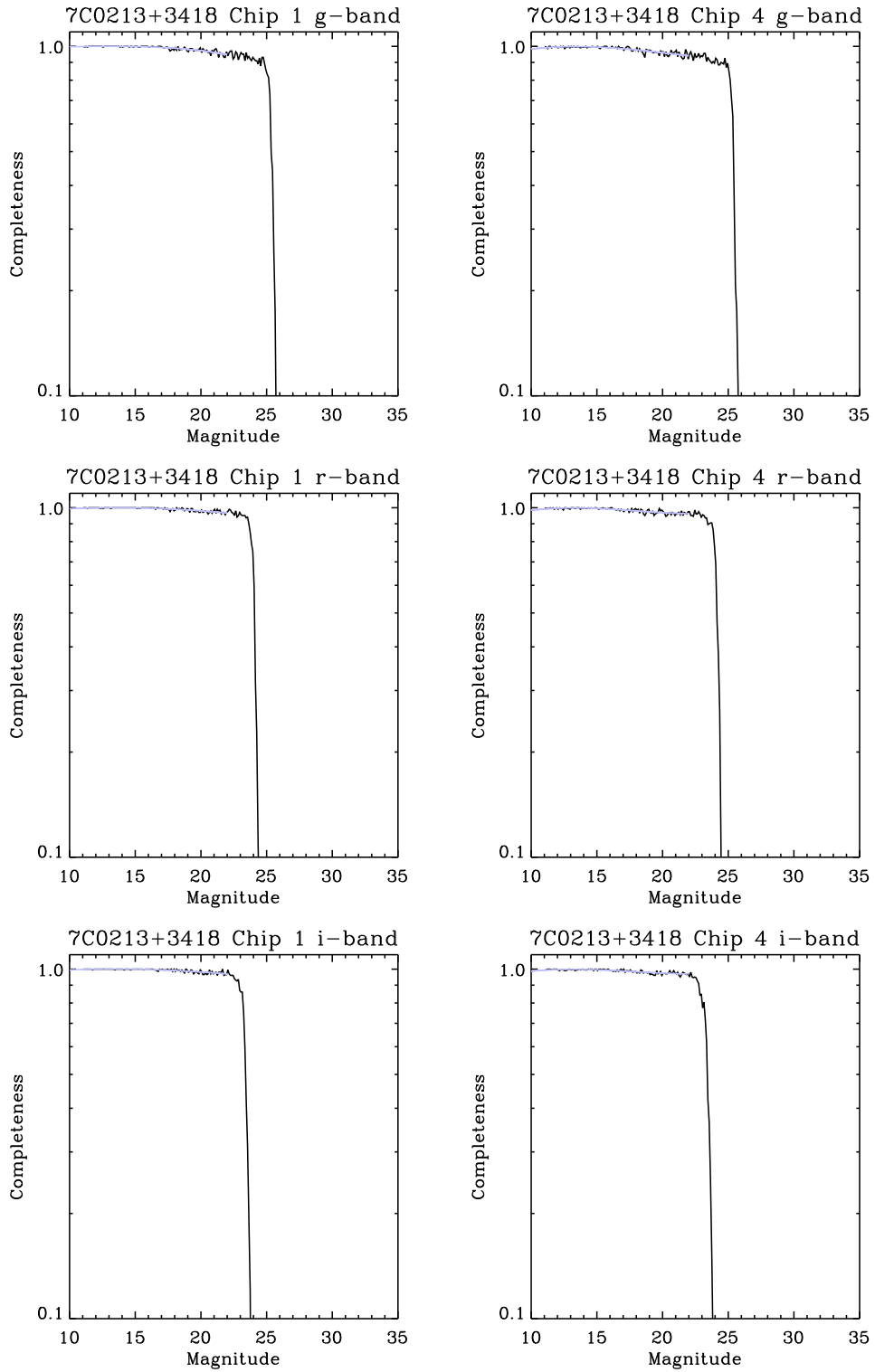


Figure 5.5 continued.

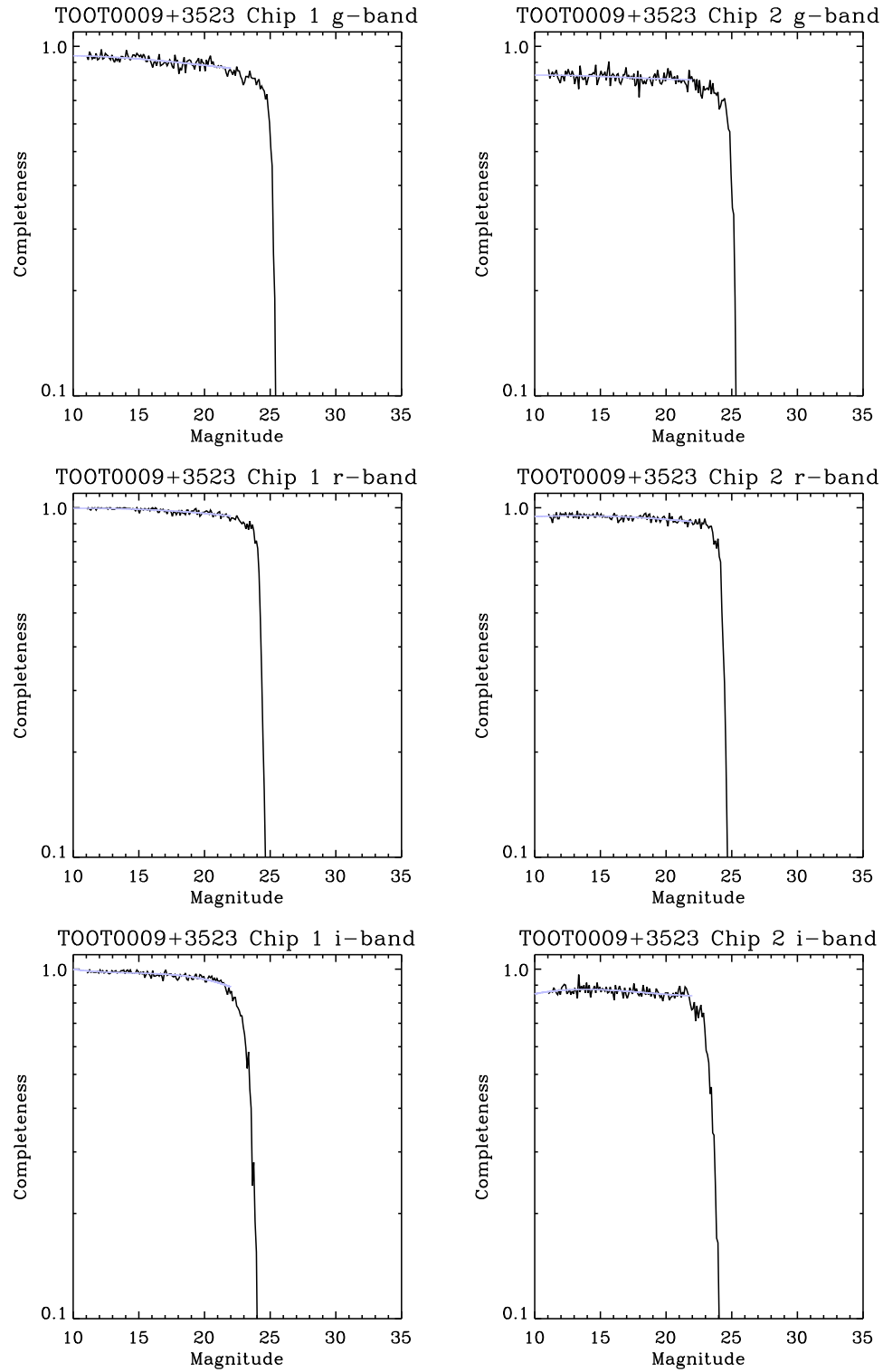


Figure 5.5 continued.



# Chapter 6

## The Radio Galaxy Environments

In this chapter I use the wide field imaging data from the Isaac Newton Telescope (INT), as described in Chapter 5, to study the environments of the  $z \sim 0.5$  (ZP5) sample in order to investigate the connection between the radio properties, the host properties and the environments of the ZP5 galaxies. In Section 6.1 I describe the data and colour selections used for my overdensity calculations, together with my calculation of the background density. I investigate the annular overdensities as a function of radio luminosity, host luminosity, radio morphology and spectral classification in Section 6.2 and in Section 6.3 I use an alternative measure of the overdensity to further investigate the relationships between environment and radio luminosity and between environment and host luminosity. In Section 6.4 I investigate the possible link between environment and orientation of the radio jet and in Section 6.5 I consider alignments between the environments and the ZP5 host galaxies before concluding in Section 6.6.

## 6.1 Environmental Densities

### 6.1.1 INT Wide Field Imaging Data

In order to study the environments of the ZP5 radio galaxies I used the INT wide field imaging data, the observations and data reduction for which have been described in Chapter 5. Each chip on the INT covers a large sky area of  $22.8 \times 11.4$  arcmin (Irwin & Lewis 2001), which corresponds to  $8.4 \times 4.2$  Mpc at  $z = 0.5$ , thus providing a sufficiently large field of view to study typical clusters ( $\sim 1$  Mpc in size; e.g. Hansen et al. 2005).

The data processing described in Chapter 5 produced a catalogue for each of the final INT images; one catalogue for the central Charge-coupled Device (CCD) and one catalogue for the reference CCD for each band and each ZP5 object. These catalogues listed all of the sources extracted from each of the final images, together with their magnitudes in the  $g'$ ,  $r'$  and  $i'$  bands.

### 6.1.2 Colour Selection

Using the catalogues described in Chapter 5 and Section 6.1.1, I next imposed a colour selection on the sources in each of these catalogues so as to target a specific redshift range (surrounding the redshift of the objects) and therefore make my investigations less prone to issues associated with the foreground and background populations which dominate the number counts. I used Hyperz<sup>1</sup> to generate SDSS  $g'$ ,  $r'$  and  $i'$  band magnitudes for 10,000 elliptical galaxies in the redshift range  $z = 0$  to  $z = 6$ . For this I used the appropriate filter transmission functions and elliptical galaxy templates as defined in Hyperz. I assumed a formation redshift of  $z_{form} = 4$ , although I note that the actual choice of  $z_{form}$  makes no difference to the colour cuts imposed in this chapter when  $z_{form} > 2$ , and made no corrections for reddening due to dust. The resulting colour-redshift and colour-colour

---

<sup>1</sup><http://webast.ast.obs-mip.fr/hyperz/>

diagrams are shown in Figure 6.1. I then used the colour-redshift diagrams to determine manually the colour cuts needed to select elliptical galaxies in the redshift range  $z = 0.3$  to  $z = 0.7$ . The colour cuts imposed on the sources were as follows:

- $1.54 < (g' - r') < 1.95$
- $0.83 < (r' - i') < 1.40$
- $2.62 < (g' - i') < 3.01$

The effect of these colour cuts on the galaxy templates generated by Hyperz is shown in Figure 6.1. I note that imposing these colour cuts will have the effect of excluding blue star forming objects in the vicinity of my sources as well as sources which are highly reddened due to the effects of dust. However, the ranges are relatively broad, and should still provide an accurate measure of the overdensity since the objects for both the background count (Section 6.1.3) and the cluster investigations (Sections 6.2 and 6.3) are filtered in the same way.

### 6.1.3 Background Density

To investigate the environmental densities surrounding the ZP5 objects it was necessary to calculate the background galaxy density as a point of reference. To do this I used the extracted catalogue for each of the final stacked reference images (Section 6.1.1) and imposed the same colour cuts as used for the sources falling on the central chips (Section 6.1.2). Using the same colour cuts ensures that the same types of objects are selected for both the cluster density and background density calculations.

In addition, when calculating the background density I only used the half of each reference chip that observed the sky furthest from the associated ZP5 object. This was to minimise the effects on the background count of any large-scale structure surrounding the

---

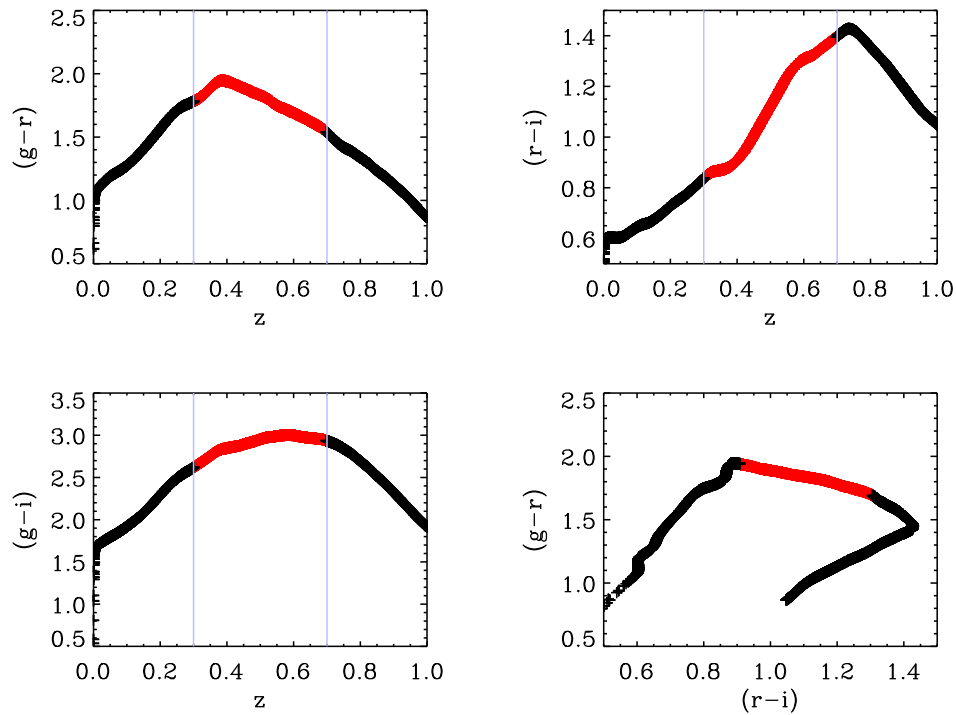


Figure 6.1: Colour-redshift and colour-colour diagrams for the elliptical galaxy templates generated using Hyperz (Section 6.1.2). Red symbols denote sources retained by the colour cuts described in Section 6.1.2, whilst black symbols denote those sources which are excluded.

radio galaxies. Using only the furthest halves of the reference chips removes the effects of structures smaller than  $\sim 4$  Mpc since the distance on the  $z = 0.5$  sky between the centre of the central chip and the centre of the reference chip on the INT is 4.2 Mpc (Section 6.1.1 and Irwin & Lewis 2001). This is sufficient to remove the effects of the clusters on the calculated background density in normal cases (since a typical cluster is  $\sim 1$  Mpc in size; e.g. Hansen et al. 2005), although very large clusters may still have a small effect on the calculated value by raising it slightly from the true value. However, this offset will not affect any trends present in the data and their significances, since the same offset will be present for all of the objects. Nevertheless, this potential drawback is later addressed in Section 6.3 by using a background count estimated over a wide area from the Canada-France-Hawaii Telescope Legacy Survey (CFHTLS) D1 field.<sup>2</sup>

Finally, from the sources on the furthest half of each chip which remained in the reference catalogues after the colour cuts, I calculated the average density of sources per unit area, along with the Poisson uncertainty. I corrected the number counts for completeness according to Section 5.3.2. My final calculated background source density was  $(2.1 \pm 0.1) \times 10^{-6} \text{ kpc}^{-2}$ .

## 6.2 Annular Overdensities

The first set of overdensity measurements that I consider are the environmental overdensities surrounding the ZP5 radio galaxies relative to the background source count, measured in concentric annuli (centred in each case on the relevant ZP5 object). To calculate these overdensities I used sources from the central chips (chip two for TOOT0009+3523 and TOOT0013+3459, obtained using the William Herschel Telescope, and chip four for the remainder of the objects, observed using the INT) which matched the colour cuts of Sec-

---

<sup>2</sup>Details of the CFHTLS, the Deep Survey and the D1 field can be found at <http://www.cfht.hawaii.edu/Science/CFHLS/>, <http://www.ast.obs-mip.fr/article204.html> and <http://www.ast.obs-mip.fr/article212.html> respectively.

tion 6.1.2. I excluded the ZP5 radio galaxy from the source list in each case and sorted the remaining objects into ten concentric annuli of equal area ( $10^6 \text{ kpc}^2$ ). The number counts in each annulus were corrected for completeness as described in Section 5.3.2 and converted into a source density per unit area. Finally, I subtracted the background density from the density of sources per unit area to determine the overdensity around each ZP5 object in each annulus. In addition, the Poisson uncertainties on the source densities were combined in quadrature with the uncertainty on the background density in order to determine the uncertainties on the final overdensities. The overdensity calculated in each annulus for each object is listed in Table 6.1.

### 6.2.1 Overdensity and Radio Luminosity

Investigating the existence of a relationship between the radio luminosity of the ZP5 objects and their environmental overdensities is of interest in light of the suggestion (e.g. Barthel & Arnaud 1996; Kauffmann, Heckman & Best 2008; Falder et al. 2010) that radio jets are enhanced in denser environments, since a denser environment would give rise to a denser inter-galactic medium (IGM) through tidal stripping. This leads to an increased amount of material on which the radio jets can work, which would in turn increase the radio jet synchrotron losses and hence the radio luminosity. If this hypothesis is correct then we would expect the radio luminosity of the ZP5 objects to be positively correlated with their environmental overdensities. However, as discussed in Chapter 4, we know that radio luminosity is correlated with black-hole mass and so (via the relation between black hole mass and bulge luminosity, e.g. McLure & Dunlop 2001b; McLure & Dunlop 2002; Gültekin et al. 2009) host galaxy magnitude. Thus in Section 6.2.2 I also investigate whether there is a link between the environmental density and the host galaxy magnitude.

To investigate whether such a relationship exists, I first examine the annular overden-

---

Object	Overdensity / $10^5 \text{ kpc}^2$									
	$r < 564$	$564 < r < 798$	$798 < r < 977$	$977 < r < 1128$	$1128 < r < 1262$	$1262 < r < 1382$	$1382 < r < 1493$	$1493 < r < 1596$	$1596 < r < 1693$	$1693 < r < 1784$
3C16	-0.21 ± 0.01	-0.21 ± 0.01	-0.21 ± 0.01	-0.21 ± 0.01	-0.21 ± 0.01	-0.21 ± 0.01	-0.21 ± 0.01	-0.11 ± 0.10	-0.21 ± 0.01	-0.21 ± 0.01
3C19	0.40 ± 0.25	0.20 ± 0.20	0.40 ± 0.25	-0.21 ± 0.01	0.50 ± 0.27	-0.11 ± 0.10	0.10 ± 0.18	-0.01 ± 0.14	0.20 ± 0.20	-0.11 ± 0.10
3C46	-0.10 ± 0.11	-0.10 ± 0.11	-0.21 ± 0.01	-0.21 ± 0.01	-0.10 ± 0.11	0.01 ± 0.15	-0.21 ± 0.01	0.01 ± 0.15	-0.10 ± 0.11	-0.10 ± 0.11
3C200	0.40 ± 0.25	0.10 ± 0.18	-0.11 ± 0.10	0.50 ± 0.27	-0.21 ± 0.01	0.10 ± 0.18	-0.01 ± 0.14	-0.21 ± 0.01	-0.01 ± 0.14	-0.11 ± 0.10
3C225B	0.00 ± 0.15	-0.11 ± 0.10	0.30 ± 0.23	0.10 ± 0.18	-0.11 ± 0.10	0.10 ± 0.18	0.20 ± 0.21	-0.11 ± 0.10	0.10 ± 0.18	-0.21 ± 0.01
3C228	0.40 ± 0.25	0.20 ± 0.20	0.20 ± 0.20	-0.01 ± 0.14	-0.21 ± 0.01	0.10 ± 0.18	-0.21 ± 0.01	0.30 ± 0.23	-0.11 ± 0.10	-0.21 ± 0.01
4C74.16	0.21 ± 0.21	0.00 ± 0.15	-0.10 ± 0.11	0.21 ± 0.21	0.00 ± 0.15	-0.10 ± 0.10	-0.21 ± 0.01	0.00 ± 0.15	0.00 ± 0.15	0.10 ± 0.18
3C244.1	0.81 ± 0.32	0.10 ± 0.18	0.30 ± 0.23	0.51 ± 0.27	0.30 ± 0.23	0.20 ± 0.20	0.40 ± 0.25	0.10 ± 0.18	0.20 ± 0.20	0.30 ± 0.23
3C274.1	0.60 ± 0.29	-0.01 ± 0.14	0.19 ± 0.20	-0.11 ± 0.10	-0.01 ± 0.14	0.09 ± 0.17	0.09 ± 0.17	-0.01 ± 0.14	-0.01 ± 0.14	-0.21 ± 0.01
3C295	2.54 ± 0.53	1.01 ± 0.35	0.30 ± 0.23	0.20 ± 0.20	0.20 ± 0.20	0.40 ± 0.25	-0.11 ± 0.10	0.40 ± 0.25	0.40 ± 0.25	0.00 ± 0.14
3C330	0.20 ± 0.21	-0.11 ± 0.10	-0.11 ± 0.10	-0.21 ± 0.01	0.00 ± 0.15	0.10 ± 0.18	0.00 ± 0.15	0.20 ± 0.21	-0.11 ± 0.10	0.82 ± 0.32
3C341	0.50 ± 0.27	-0.01 ± 0.14	0.10 ± 0.18	-0.01 ± 0.14	-0.11 ± 0.10	0.30 ± 0.23	0.30 ± 0.23	-0.11 ± 0.10	-0.11 ± 0.10	-0.01 ± 0.14
3C427.1	0.30 ± 0.23	0.20 ± 0.20	0.71 ± 0.31	0.00 ± 0.15	0.71 ± 0.31	0.40 ± 0.25	0.40 ± 0.25	0.61 ± 0.29	0.61 ± 0.29	0.10 ± 0.18
3C457	0.71 ± 0.31	0.10 ± 0.18	0.41 ± 0.25	0.30 ± 0.23	0.51 ± 0.27	0.51 ± 0.27	0.40 ± 0.25	0.41 ± 0.25	0.61 ± 0.29	0.41 ± 0.25
6C0825+3407	0.00 ± 0.14	-0.11 ± 0.10	0.20 ± 0.20	0.20 ± 0.20	0.00 ± 0.14	0.20 ± 0.20	0.40 ± 0.25	0.20 ± 0.20	0.10 ± 0.18	0.20 ± 0.20
6C0850+3747	0.42 ± 0.26	1.15 ± 0.38	0.73 ± 0.31	0.21 ± 0.21	0.21 ± 0.21	0.84 ± 0.33	0.32 ± 0.23	0.32 ± 0.23	0.21 ± 0.21	0.11 ± 0.18
6C0857+3945	0.20 ± 0.20	0.00 ± 0.15	0.60 ± 0.29	-0.01 ± 0.14	-0.01 ± 0.14	0.40 ± 0.25	0.20 ± 0.21	0.10 ± 0.18	-0.01 ± 0.14	-0.11 ± 0.10
6C1111+3940	-0.11 ± 0.10	-0.11 ± 0.10	-0.21 ± 0.01	-0.21 ± 0.01	-0.11 ± 0.10	-0.01 ± 0.14	-0.21 ± 0.01	-0.01 ± 0.14	-0.11 ± 0.10	-0.21 ± 0.01
6C1132+3439	0.40 ± 0.25	0.50 ± 0.27	-0.01 ± 0.14	0.20 ± 0.20	-0.01 ± 0.14	0.20 ± 0.20	0.20 ± 0.20	-0.11 ± 0.10	0.09 ± 0.18	-0.01 ± 0.14
6C1200+3416	0.40 ± 0.25	-0.11 ± 0.10	-0.21 ± 0.01	-0.11 ± 0.10	-0.21 ± 0.01	0.09 ± 0.17	0.19 ± 0.20	0.09 ± 0.17	-0.21 ± 0.01	-0.11 ± 0.10
6C1303+3756	0.09 ± 0.18	0.20 ± 0.20	0.80 ± 0.32	-0.21 ± 0.01	0.20 ± 0.20	-0.01 ± 0.14	-0.01 ± 0.14	-0.11 ± 0.10	-0.11 ± 0.10	-0.01 ± 0.14
7C0213+3418	0.51 ± 0.27	0.61 ± 0.29	0.61 ± 0.29	0.31 ± 0.23	0.30 ± 0.23	0.51 ± 0.27	0.10 ± 0.18	0.51 ± 0.27	-0.01 ± 0.14	0.41 ± 0.25
7C0219+3419	-0.11 ± 0.10	0.10 ± 0.18	-0.11 ± 0.10	-0.11 ± 0.10	-0.21 ± 0.01	0.10 ± 0.18	0.00 ± 0.15	-0.21 ± 0.01	0.00 ± 0.15	0.00 ± 0.15
7C0219+3423	0.00 ± 0.15	-0.21 ± 0.01	-0.21 ± 0.01	-0.21 ± 0.01	-0.10 ± 0.11	-0.10 ± 0.11	-0.10 ± 0.11	-0.21 ± 0.01	-0.21 ± 0.01	0.00 ± 0.15
7C0220+2952	0.01 ± 0.15	0.12 ± 0.19	-0.21 ± 0.01	0.33 ± 0.24	0.12 ± 0.19	-0.10 ± 0.11	-0.10 ± 0.11	0.01 ± 0.15	0.01 ± 0.15	-0.10 ± 0.11
7C0223+3415	-0.11 ± 0.10	-0.21 ± 0.01	-0.01 ± 0.14	-0.21 ± 0.01	0.20 ± 0.20	0.00 ± 0.14	-0.21 ± 0.01	-0.11 ± 0.10	-0.21 ± 0.01	-0.11 ± 0.10
7C0810+2650	0.41 ± 0.25	0.51 ± 0.27	0.10 ± 0.18	0.10 ± 0.18	0.00 ± 0.15	0.10 ± 0.18	-0.11 ± 0.10	0.20 ± 0.20	0.10 ± 0.18	0.00 ± 0.15
7C1731+6638	-0.11 ± 0.10	0.20 ± 0.21	-0.11 ± 0.10	0.00 ± 0.15	-0.11 ± 0.10	-0.11 ± 0.10	0.10 ± 0.18	0.10 ± 0.18	-0.11 ± 0.10	-0.21 ± 0.01
7C1806+6831	-0.11 ± 0.10	0.10 ± 0.18	0.21 ± 0.21	-0.21 ± 0.01	-0.11 ± 0.10	-0.11 ± 0.10	-0.21 ± 0.01	-0.21 ± 0.01	0.10 ± 0.18	-0.11 ± 0.10

Table 6.1: The final environmental overdensity calculated around each  $z \sim 0.5$  (ZP5) object and for each of the ten annuli described in Section 6.2. In each case  $r$  is the distance from the central ZP5 object in kpc.

Object	Overdensity / $10^5 \text{ kpc}^2$									
	$r < 564$	$564 < r < 798$	$798 < r < 977$	$977 < r < 1128$	$1128 < r < 1262$	$1262 < r < 1382$	$1382 < r < 1493$	$1493 < r < 1596$	$1596 < r < 1693$	$1693 < r < 1784$
TOOT0009+3523	$0.03 \pm 0.24$	$0.03 \pm 0.24$	$-0.21 \pm 0.01$	$-0.21 \pm 0.01$	$-0.21 \pm 0.01$	$-0.21 \pm 0.01$	$0.03 \pm 0.24$	$-0.21 \pm 0.01$	$0.03 \pm 0.24$	$-0.21 \pm 0.01$
TOOT0013+3459	$0.05 \pm 0.26$	$-0.21 \pm 0.01$	$0.05 \pm 0.26$	$0.05 \pm 0.26$	$-0.21 \pm 0.01$					
TOOT0018+3510	$-0.21 \pm 0.01$	$-0.21 \pm 0.01$	$-0.21 \pm 0.01$	$-0.11 \pm 0.10$	$-0.21 \pm 0.01$					
TOOT1255+3556	$0.10 \pm 0.18$	$-0.21 \pm 0.01$	$0.20 \pm 0.20$	$0.10 \pm 0.18$	$0.10 \pm 0.18$	$-0.01 \pm 0.14$	$-0.01 \pm 0.14$	$-0.21 \pm 0.01$	$-0.01 \pm 0.14$	$-0.01 \pm 0.14$
TOOT1301+3658	$0.51 \pm 0.27$	$0.10 \pm 0.18$	$0.00 \pm 0.14$	$0.00 \pm 0.15$	$-0.21 \pm 0.01$	$0.00 \pm 0.14$	$0.00 \pm 0.15$	$-0.21 \pm 0.01$	$0.10 \pm 0.18$	$0.10 \pm 0.18$
TOOT1303+3334	$0.09 \pm 0.17$	$-0.11 \pm 0.10$	$-0.01 \pm 0.14$	$-0.01 \pm 0.14$	$-0.11 \pm 0.10$	$0.19 \pm 0.20$	$-0.01 \pm 0.14$	$-0.01 \pm 0.14$	$-0.11 \pm 0.10$	$-0.21 \pm 0.01$
TOOT1307+3639	$0.29 \pm 0.22$	$-0.01 \pm 0.14$	$-0.11 \pm 0.10$	$-0.01 \pm 0.14$	$0.09 \pm 0.17$	$-0.11 \pm 0.10$	$-0.01 \pm 0.14$	$-0.01 \pm 0.14$	$-0.11 \pm 0.10$	$-0.01 \pm 0.14$
TOOT1309+3359	$-0.01 \pm 0.14$	$0.10 \pm 0.18$	$-0.11 \pm 0.10$	$-0.11 \pm 0.10$	$-0.11 \pm 0.10$	$-0.11 \pm 0.10$	$-0.11 \pm 0.10$	$-0.11 \pm 0.10$	$-0.21 \pm 0.01$	$-0.21 \pm 0.01$
TOOT1626+4523	$-0.21 \pm 0.01$	$-0.21 \pm 0.01$	$-0.21 \pm 0.01$	$-0.21 \pm 0.01$	$-0.21 \pm 0.01$	$-0.21 \pm 0.01$	$-0.21 \pm 0.01$	$-0.21 \pm 0.01$	$-0.21 \pm 0.01$	$-0.21 \pm 0.01$
TOOT1630+4534	$0.10 \pm 0.18$	$-0.21 \pm 0.01$	$0.20 \pm 0.21$	$-0.11 \pm 0.10$	$0.00 \pm 0.15$	$-0.21 \pm 0.01$	$0.30 \pm 0.23$	$0.00 \pm 0.15$	$0.00 \pm 0.15$	$0.00 \pm 0.15$
TOOT1648+5040	$0.00 \pm 0.15$	$-0.10 \pm 0.11$	$0.10 \pm 0.18$	$0.00 \pm 0.15$	$-0.10 \pm 0.11$	$-0.10 \pm 0.11$	$0.00 \pm 0.15$	$0.10 \pm 0.18$	$0.00 \pm 0.15$	$-0.21 \pm 0.01$

Table 6.1 continued.

sities of the ZP5 objects, binned according to their 151 MHz radio luminosity ( $L_{151}$ ). I adopt the same radio luminosity bins as used in Chapter 4, namely  $L_{151} < 10^{25.3} \text{ W Hz}^{-1} \text{ sr}^{-1}$ ,  $L_{151}$  from  $10^{25.3}$  to  $10^{25.8} \text{ W Hz}^{-1} \text{ sr}^{-1}$ ,  $L_{151}$  from  $10^{25.8}$  to  $10^{26.3} \text{ W Hz}^{-1} \text{ sr}^{-1}$ ,  $L_{151}$  from  $10^{26.3}$  to  $10^{26.8} \text{ W Hz}^{-1} \text{ sr}^{-1}$  and  $L_{151} > 10^{26.8} \text{ W Hz}^{-1} \text{ sr}^{-1}$ . I show the resulting binned overdensities in Figure 6.2.

Figure 6.2 shows a significant overdensity [ $(4.8 \pm 0.7) \times 10^{-6} \text{ kpc}^{-2}$ ; significant at the  $6.9 \sigma$  level] in the first annulus of the bin with the greatest radio luminosity [that is to say,  $\log_{10}(L_{151}/\text{W Hz}^{-1} \text{ sr}^{-1}) > 26.8$ ] and some level of overdensity extending out to the outer radii. This not seen in the other bins, in which a modest and insignificant overdensity is found in the inner annulus in each case. The bin with the lowest radio luminosity [ $\log_{10}(L_{151}/\text{W Hz}^{-1} \text{ sr}^{-1}) < 25.3$ ] is seen to exhibit an underdensity in the outer annuli, although the uncertainties preclude definitive statements.

These results suggest the presence of some link between the radio luminosity of the ZP5 objects and the richness of their environments. However, I note that the bin with the greatest radio luminosity [ $\log_{10}(L_{151}/\text{W Hz}^{-1} \text{ sr}^{-1}) > 26.8$ ] contains within it the object 3C295, which is known to reside in an extremely dense cluster (e.g. Hill & Lilly 1991). Care must therefore be taken to consider whether the overdensities exhibited in this bin are due solely to the inclusion of 3C295 or whether they indicate a wider trend. I therefore recalculate the binned overdensities for the  $\log_{10}(L_{151}/\text{W Hz}^{-1} \text{ sr}^{-1}) > 26.8$  bin, excluding 3C295 from the analysis. The resulting overdensities are shown by the grey dashed line in the final subfigure of Figure 6.2. Even without 3C295, it can be seen that the most radio luminous objects still exhibit a significant overdensity (at the  $5.0\sigma$  level) in the inner annulus. Whilst not as large as when 3C295 is included, this overdensity is still significantly greater than those found in the other bins, with the next most significant overdensity in the first annulus being at the  $1.8\sigma$  level in the second ( $L_{151}$  from  $10^{25.3}$  to  $10^{25.8} \text{ W Hz}^{-1} \text{ sr}^{-1}$ ) bin. The outer annuli also continue to show evidence of overdensi-

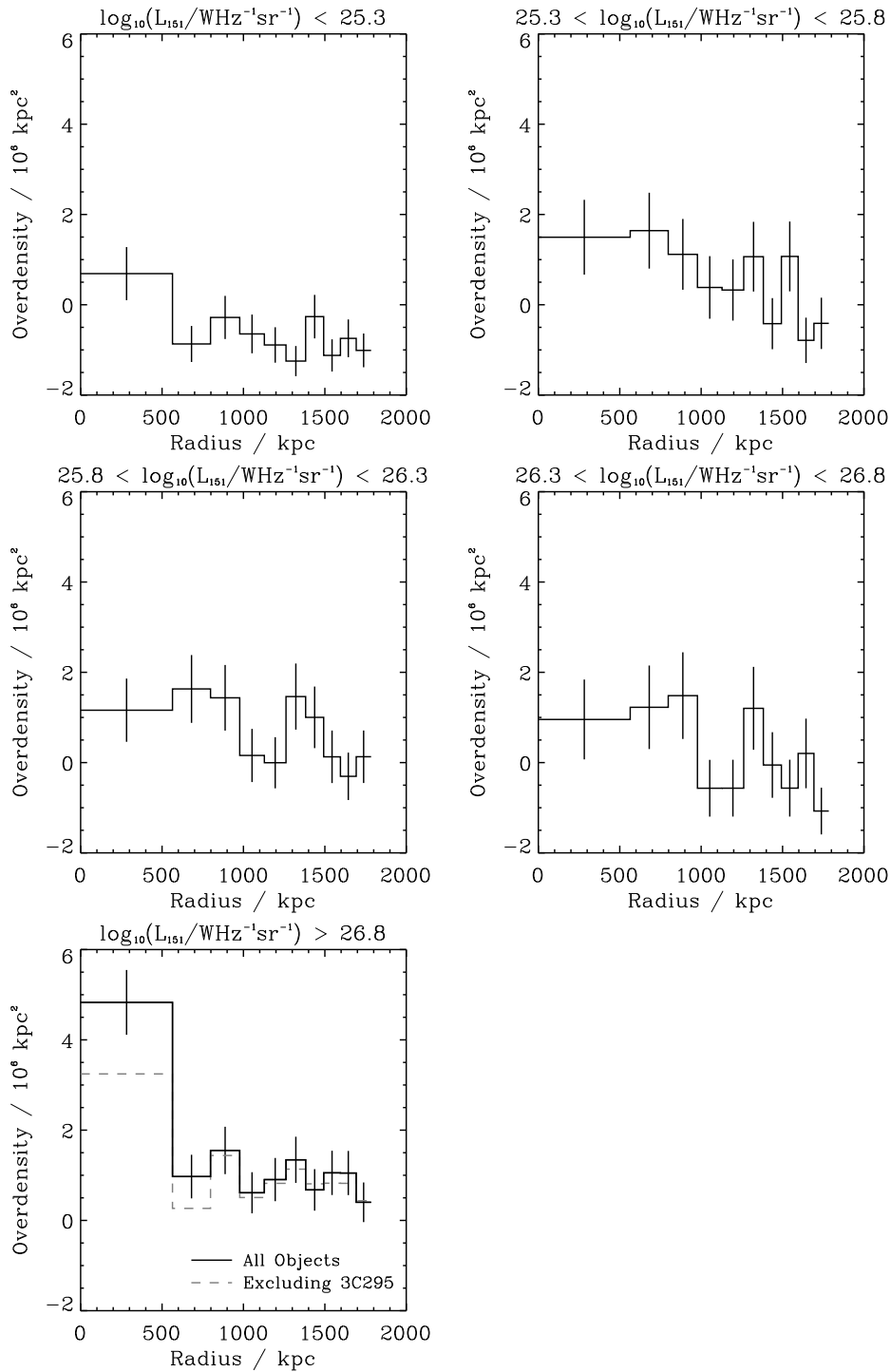


Figure 6.2: The environmental overdensity in each of the annuli for the ZP5 galaxies, binned according to their 151 MHz radio luminosity,  $L_{151}$  (Section 6.2.1). The black line in each subfigure shows the binned overdensity for all of the objects contained within the bin. The grey dashed line in the final bin ( $L_{151} > 10^{26.8} \text{ W Hz}^{-1} \text{ sr}^{-1}$ ) shows the binned annular overdensity when the object 3C295 is excluded from the results.

Annulus ( $r/\text{kpc}$ )	All Objects		3C295 Excluded	
	$\rho$	Significance	$\rho$	Significance
$r < 564$	0.38	98%	0.33	96%
$564 < r < 977$	0.34	97%	0.29	93%
$r < 977$	0.43	99%	0.39	98%

Table 6.2: The Spearman’s rank correlation coefficients ( $\rho$ ) for correlations between the 151 MHz radio luminosities of the ZP5 objects and their environmental overdensities, together with their associated significances that they deviate from the null hypothesis of no correlation (Section 6.2.1 and Figures 6.3, 6.4 and 6.5). The coefficients and their significances are listed for the three annuli used in Figures 6.3 to 6.5, namely  $r < 564$  kpc,  $564 \text{ kpc} < r < 977$  kpc and  $r < 977$  kpc (where  $r$  is the distance from the central ZP5 galaxy). I also show the coefficients and their significances when 3C295 is excluded from the analysis (see Section 6.2.1).

ties. Therefore, even without 3C295, my data suggest that the environmental density and the radio luminosity of the ZP5 objects may be linked in some way.

To investigate this possible link further, in Figures 6.3, 6.4 and 6.5 I show the 151 MHz radio luminosities of each of the ZP5 objects versus their environmental overdensities for three annuli:  $r < 564$  kpc,  $564 \text{ kpc} < r < 977$  kpc and  $r < 977$  kpc respectively (where  $r$  is the distance from the central ZP5 galaxy). I also test each of these three data sets for correlations using Spearman’s rank correlation coefficient, and the resulting coefficients and their significances are listed in Table 6.2. These correlations are tested using the full ZP5 sample (40 objects, or 39 when 3C295 is excluded) over a large range in radio luminosity, ensuring that the resulting statistics are robust.

Figure 6.3 shows hints of a relationship between 151 MHz radio luminosity and environmental overdensity in the  $r < 564$  kpc annulus, with some (but not all) of the objects with higher radio luminosities exhibiting greater overdensities than objects at lower radio luminosity. This can be seen slightly more clearly in the weighted means of Figure 6.3. Calculating Spearman’s rank correlation coefficient for the data I find a positive correlation, with the null hypothesis of no correlation being rejected at 98% ( $2.3\sigma$ ) significance (see Table 6.2), although this drops to 96% ( $2.0\sigma$ ) when 3C295 is excluded (as discussed

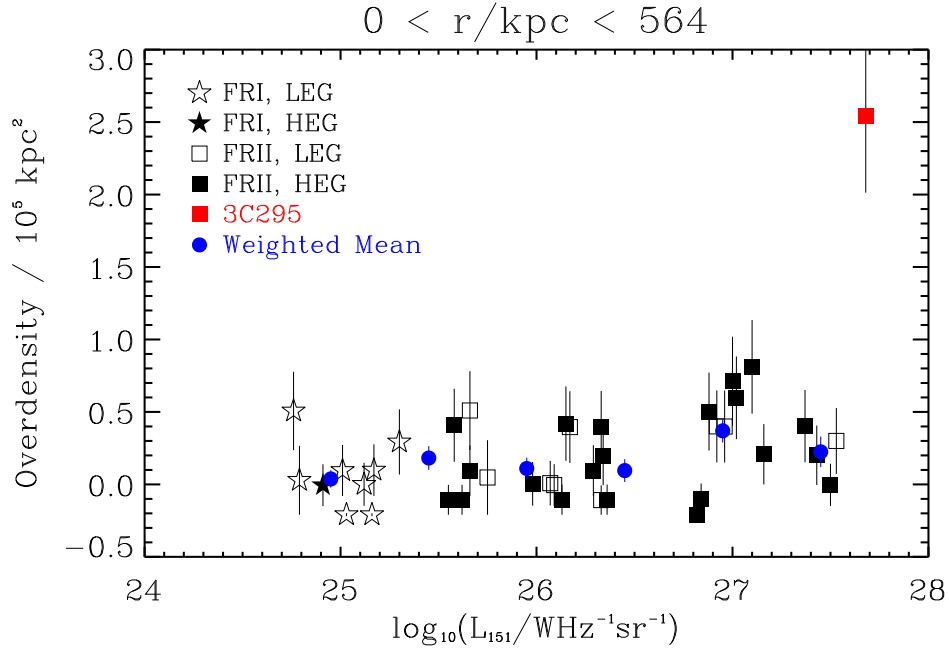


Figure 6.3: The environmental overdensity per  $10^5 \text{ kpc}^2$  versus the logarithm of the 151 MHz radio luminosity ( $L_{151}$ ) for the  $r < 564 \text{ kpc}$  annulus, where  $r$  is the distance from the central ZP5 galaxy (Section 6.2.1). Fanaroff-Riley Class I (FRI) objects are shown as stars whilst Fanaroff-Riley Class II (FRII) objects are shown as squares. Simultaneously, Low Excitation Galaxies (LEGs) are shown using open symbols whilst High Excitation Galaxies (HEGs) are shown using filled symbols. 3C295 is highlighted with a red symbol. I also calculate the weighted mean overdensity in six bins of equal size in  $\log_{10}(L_{151}/\text{WHz}^{-1}\text{sr}^{-1})$ , between  $\log_{10}(L_{151}/\text{WHz}^{-1}\text{sr}^{-1}) = 24.7$  and  $\log_{10}(L_{151}/\text{WHz}^{-1}\text{sr}^{-1}) = 27.7$  (excluding 3C295). These weighted means are shown by the blue circles.

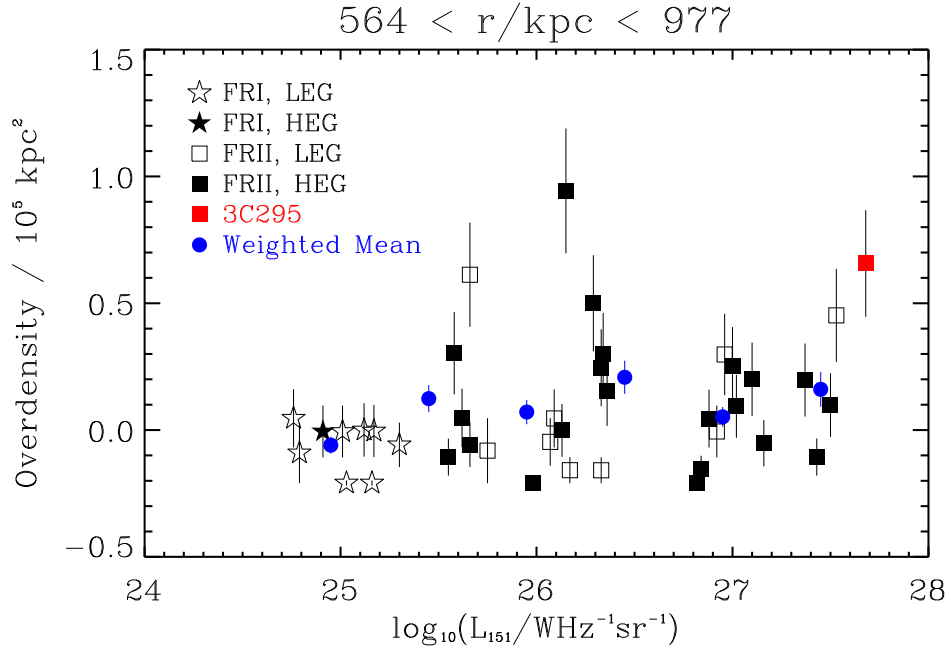


Figure 6.4: The environmental overdensity per  $10^5 \text{ kpc}^2$  versus the logarithm of the 151 MHz radio luminosity ( $L_{151}$ ) for the  $564 \text{ kpc} < r < 977 \text{ kpc}$  annulus, where  $r$  is the distance from the central ZP5 galaxy (Section 6.2.1). Fanaroff-Riley Class I (FRI) objects are shown as stars whilst Fanaroff-Riley Class II (FRII) objects are shown as squares. Simultaneously, Low Excitation Galaxies (LEGs) are shown using open symbols whilst High Excitation Galaxies (HEGs) are shown using filled symbols. 3C295 is highlighted with a red symbol. I also calculate the weighted mean overdensity in six bins of equal size in  $\log_{10}(L_{151}/\text{WHz}^{-1}\text{sr}^{-1})$ , between  $\log_{10}(L_{151}/\text{WHz}^{-1}\text{sr}^{-1}) = 24.7$  and  $\log_{10}(L_{151}/\text{WHz}^{-1}\text{sr}^{-1}) = 27.7$  (excluding 3C295). These weighted means are shown by the blue circles.

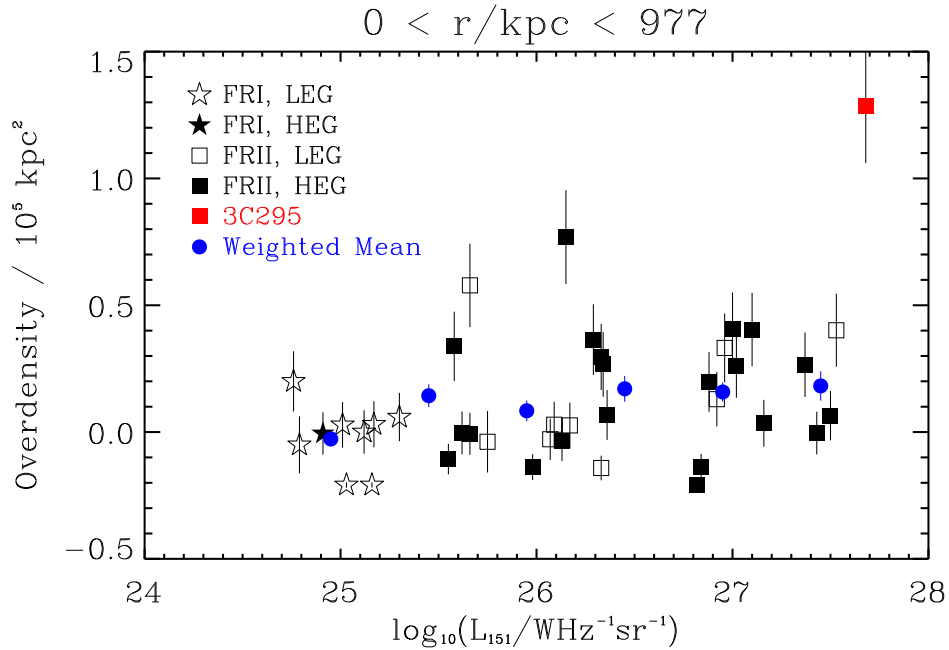


Figure 6.5: The environmental overdensity per  $10^5 \text{ kpc}^2$  versus the logarithm of the 151 MHz radio luminosity ( $L_{151}$ ) for the  $r < 977 \text{ kpc}$  annulus, where  $r$  is the distance from the central ZP5 galaxy (Section 6.2.1). Fanaroff-Riley Class I (FRI) objects are shown as stars whilst Fanaroff-Riley Class II (FRII) objects are shown as squares. Simultaneously, Low Excitation Galaxies (LEGs) are shown using open symbols whilst High Excitation Galaxies (HEGs) are shown using filled symbols. 3C295 is highlighted with a red symbol. I also calculate the weighted mean overdensity in six bins of equal size in  $\log_{10}(L_{151}/\text{WHz}^{-1}\text{sr}^{-1})$ , between  $\log_{10}(L_{151}/\text{WHz}^{-1}\text{sr}^{-1}) = 24.7$  and  $\log_{10}(L_{151}/\text{WHz}^{-1}\text{sr}^{-1}) = 27.7$  (excluding 3C295). These weighted means are shown by the blue circles.

above). Further from the radio galaxy this relationship is less discernible, as illustrated by the  $564 \text{ kpc} < r < 977 \text{ kpc}$  annulus, with a correspondingly lower significance for the Spearman's rank correlation coefficient (Table 6.2). This, however, is unsurprising since for any cluster we would expect the environmental density to tend towards the background count as the edge of the cluster is approached. The combined ( $r < 977 \text{ kpc}$ ) annulus shows some evidence for the correlation again in both the individual data points and the weighted means, and the null hypothesis is here rejected at the higher significance of 99% or  $2.6\sigma$  (falling to 98% or  $2.3\sigma$  when 3C295 is excluded).

I therefore find tentative evidence of a relationship between 151 MHz radio luminosity and environmental overdensity in the centres of the ZP5 clusters, in agreement with the suggestion that radio jets are enhanced in denser environments. This finding is in contrast to the work of Wold et al. (2001) and McLure & Dunlop (2001a) described in Chapter 1, who find no significant difference in environment between radio-loud and radio-quiet quasars (although in agreement with other studies described in Chapter 1). However, the radio-loud objects used by both Wold et al. (2001) and McLure & Dunlop (2001a) do not span the range of radio luminosities encompassed by the ZP5 sample. Most of their objects have  $\log_{10}(L_{151}/\text{WHz}^{-1}\text{sr}^{-1}) < 26.5$ , which is below the range in luminosity where the positive correlation in my data is particularly noticeable. Furthermore, although McLure & Dunlop (2001a) found no correlation between radio luminosity and environmental density for the radio-loud quasars and radio galaxies in their sample taken together, they did note that an apparent positive correlation between the two quantities was driven by the radio galaxies on their own, which is consistent with my findings here. I also emphasise the unique qualities of the ZP5 sample; using objects from complete, radio selected samples at a single redshift as I do here removes the need to attempt to construct samples adequately matched in radio luminosity and host luminosity from different parent surveys as has been the case with previous studies. This enables the analysis

---

presented here to be performed without the difficulties and uncertainties inherent in these previous approaches.

Finally, I note that the tentative correlation found in my data is not a tight relationship; several of the objects with higher radio luminosities do not reside in particularly dense clusters. Clearly there are more variables at work, and so I continue in the remainder of this chapter to investigate the environmental densities and any possible link with the host magnitude, radio morphology or spectral classification, as well as direction-dependent variations in the environmental densities.

## 6.2.2 Overdensity and Host Magnitude

Under hierarchical galaxy formation and evolution, the largest and most massive galaxies reside in the densest regions of the universe (e.g. Davis et al. 1988; Hamilton 1988; Croton et al. 2005; Deng, He & Jiang 2007; Zandivarez & Martínez 2011). This being the case, we would expect the optical luminosities of the ZP5 galaxies to be linked to their environmental densities, with the brightest and most massive objects residing in the densest environments. In order to investigate such a link, I examine the annular overdensities of the ZP5 objects, binned according to their R-band host magnitude ( $M_R$ ). I use the following host magnitude bins:  $M_R > -22.98$ ,  $-23.46 < M_R < -22.98$  and  $M_R < -23.46$ . These bins ensure approximately equal numbers of objects in each bin (13, 13 and 14 respectively). In Figure 6.6 I show the resulting binned overdensities.

Figure 6.6 shows that the bin with the lowest host luminosity ( $M_R > -22.98$ ) does not show an environmental overdensity, even in the innermost annuli. Furthermore, there is some suggestion of an underdensity in the outermost bins. The middle bin ( $-23.46 < M_R < -22.98$ ) shows a modest overdensity in the inner three annuli, reducing to the background density by the outer edge of my annuli. The brightest bin ( $M_R < -23.46$ ) displays an overdensity in the innermost annulus, although this overden-

---

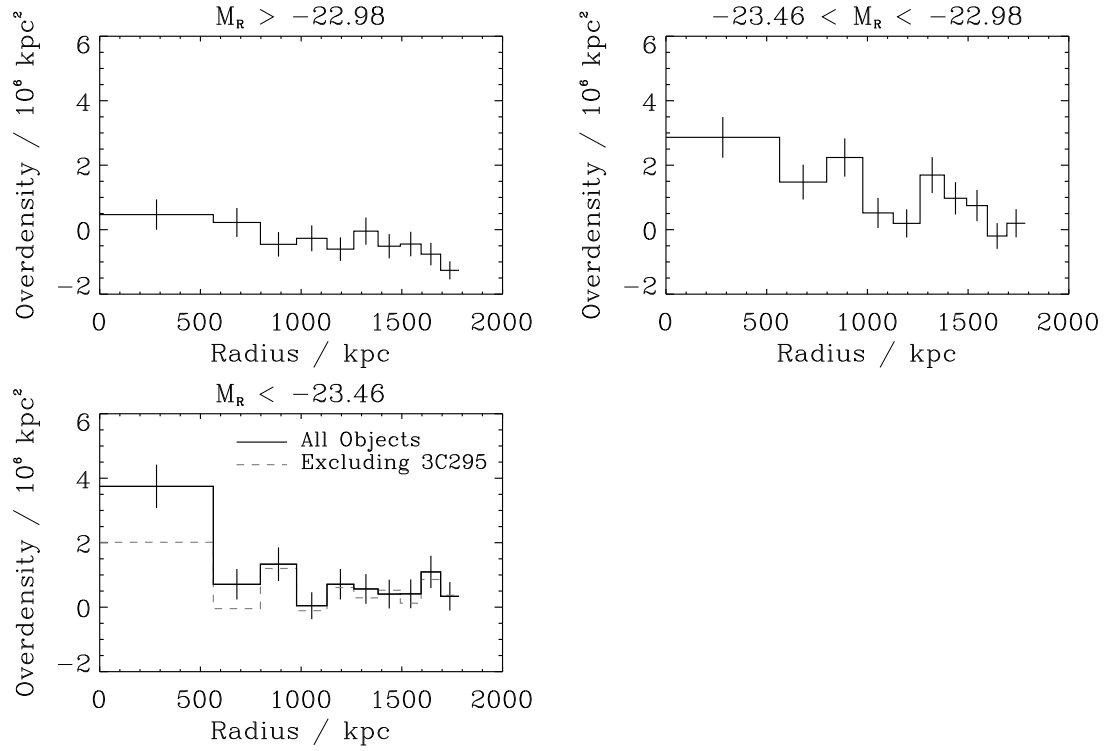


Figure 6.6: The environmental overdensity in each of the annuli for the ZP5 galaxies, binned according to their host magnitude,  $M_R$  (Section 6.2.2). The black line in each subfigure shows the binned overdensity for all of the objects contained within the bin. The grey dashed line in the final bin ( $M_R < -23.46$ ) shows the binned annular overdensity when the object 3C295 is excluded from the results.

Annulus ( $r/\text{kpc}$ )	All Objects		3C295 Excluded	
	$\rho$	Significance	$\rho$	Significance
$r < 564$	-0.34	97%	-0.29	92%
$564 < r < 977$	-0.23	85%	-0.18	72%
$r < 977$	-0.36	98%	-0.31	95%

Table 6.3: The Spearman’s rank correlation coefficients ( $\rho$ ) for correlations between the host magnitudes of the ZP5 objects and their environmental overdensities, together with their associated significances that they deviate from the null hypothesis of no correlation (Section 6.2.2 and Figures 6.7, 6.8 and 6.9). The coefficients and their significances are listed for the three annuli used in Figures 6.7 to 6.9, namely  $r < 564$  kpc,  $564 < r < 977$  kpc and  $r < 977$  kpc (where  $r$  is the distance from the central ZP5 galaxy). I also show the coefficients and their significances when 3C295 is excluded from the analysis (see Section 6.2.1). Note that the coefficients are negative since a more luminous object has a smaller magnitude, and the horizontal axes of Figures 6.7 to 6.9 are correspondingly reversed.

sity is not significantly greater than the overdensity found in the innermost annulus of the  $-23.46 < M_R < -22.98$  bin, and indeed is actually less when 3C295 with its populous cluster is excluded from the analysis (see Section 6.2.1). Furthermore, the overdensities in the next two annuli out are not as significant for the  $M_R < -23.46$  bin as for the  $-23.46 < M_R < -22.98$  bin.

Therefore, comparing the faintest bin with the other two I see hints of a connection between the host magnitudes of the ZP5 objects and their overdensities. However, the similarities between the  $-23.46 < M_R < -22.98$  and  $M_R < -23.46$  bins (particularly when 3C295 is excluded from the analysis) suggest that the connection may not be a strong one. In a similar fashion to Section 6.2.1, I investigate this possible link further in Figures 6.7, 6.8 and 6.9, in which I show the host magnitudes of the ZP5 objects versus their environmental overdensities for the three annuli used in Section 6.2.1:  $r < 564$  kpc,  $564 < r < 977$  kpc and  $r < 977$  kpc respectively. Once again I test each of these three data sets for correlations using Spearman’s rank correlation coefficient. I list the resulting coefficients and their significances in Table 6.3. Again, the statistics are robust given the use of a large number of objects and a wide range in host luminosity ( $\sim 2$  mag).

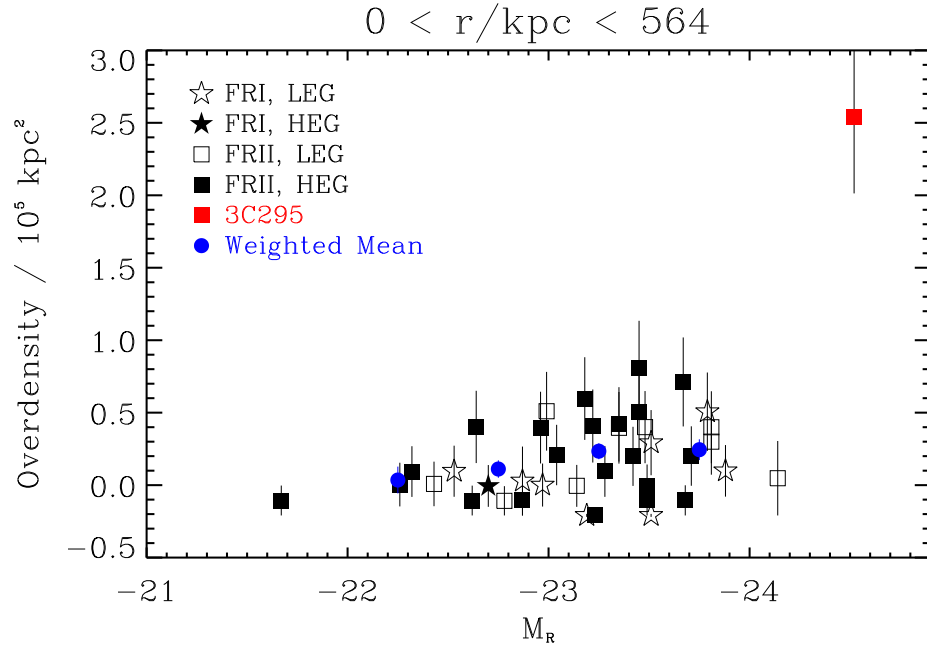


Figure 6.7: The environmental overdensity per  $10^5 \text{ kpc}^2$  versus host magnitude ( $M_R$ ) for the  $r < 564 \text{ kpc}$  annulus, where  $r$  is the distance from the central ZP5 galaxy (Section 6.2.2). Fanaroff-Riley Class I (FRI) objects are shown as stars whilst Fanaroff-Riley Class II (FRII) objects are shown as squares. Simultaneously, Low Excitation Galaxies (LEGs) are shown using open symbols whilst High Excitation Galaxies (HEGs) are shown using filled symbols. 3C295 is highlighted with a red symbol. I also calculate the weighted mean overdensity in four bins of equal size in  $M_R$ , between  $M_R = -22$  and  $M_R = -24$ . These weighted means are shown by blue circles. 3C295 is outside of these bins, as are two other objects (7C1731+6638 and TOOT0013+3459) which would, without the use of excessively large bins, be the sole object in their respective bins.

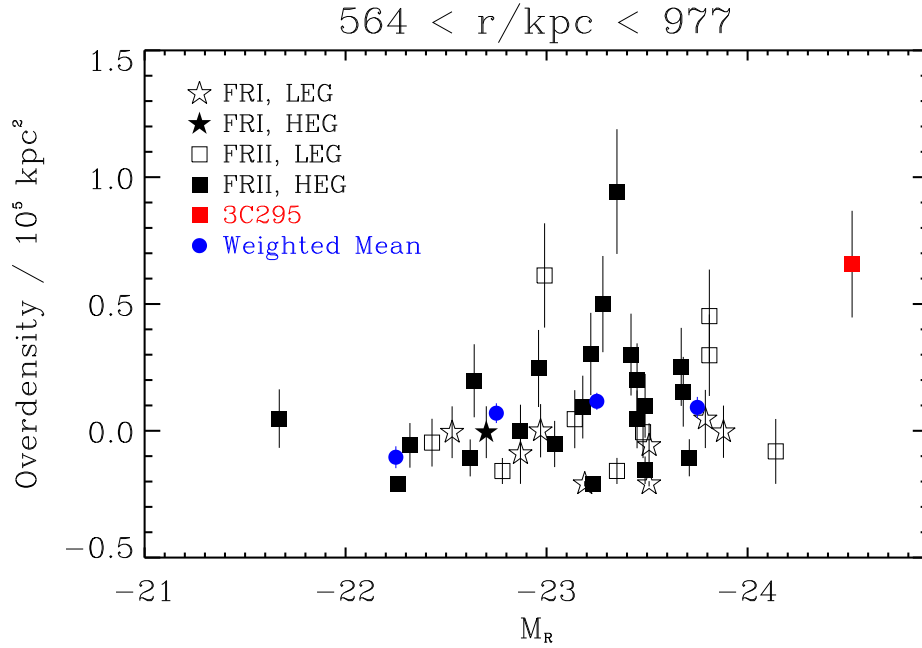


Figure 6.8: The environmental overdensity per  $10^5 \text{ kpc}^2$  versus host magnitude ( $M_R$ ) for the  $564 \text{ kpc} < r < 977 \text{ kpc}$  annulus, where  $r$  is the distance from the central ZP5 galaxy (Section 6.2.2). Fanaroff-Riley Class I (FRI) objects are shown as stars whilst Fanaroff-Riley Class II (FRII) objects are shown as squares. Simultaneously, Low Excitation Galaxies (LEGs) are shown using open symbols whilst High Excitation Galaxies (HEGs) are shown using filled symbols. 3C295 is highlighted with a red symbol. I also calculate the weighted mean overdensity in four bins of equal size in  $M_R$ , between  $M_R = -22$  and  $M_R = -24$ . These weighted means are shown by blue circles. 3C295 is outside of these bins, as are two other objects (7C1731+6638 and TOOT0013+3459) which would, without the use of excessively large bins, be the sole object in their respective bins.

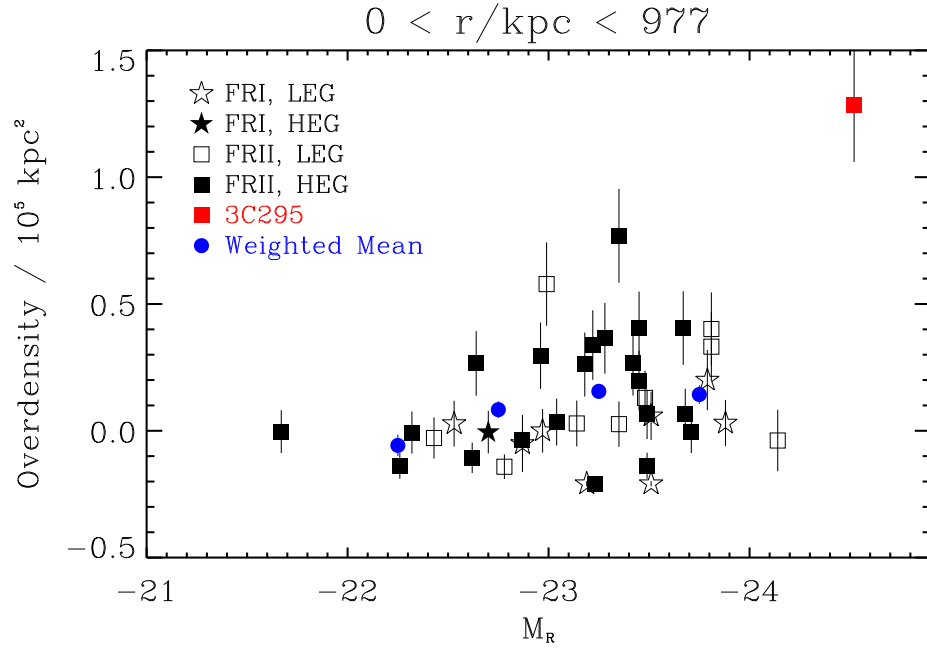


Figure 6.9: The environmental overdensity per  $10^5 \text{ kpc}^2$  versus host magnitude ( $M_R$ ) for the  $r < 977 \text{ kpc}$  annulus, where  $r$  is the distance from the central ZP5 galaxy (Section 6.2.2). Fanaroff-Riley Class I (FRI) objects are shown as stars whilst Fanaroff-Riley Class II (FRII) objects are shown as squares. Simultaneously, Low Excitation Galaxies (LEGs) are shown using open symbols whilst High Excitation Galaxies (HEGs) are shown using filled symbols. 3C295 is highlighted with a red symbol. I also calculate the weighted mean overdensity in four bins of equal size in  $M_R$ , between  $M_R = -22$  and  $M_R = -24$ . These weighted means are shown by blue circles. 3C295 is outside of these bins, as are two other objects (7C1731+6638 and TOOT0013+3459) which would, without the use of excessively large bins, be the sole object in their respective bins.

Hints of a trend for more luminous objects (i.e. those with larger negative values of  $M_R$ ) to reside in denser clusters can be seen in Figure 6.7, and the significance with which the Spearman's rank correlation coefficient deviates from the null hypothesis of no correlation is 97% or  $2.2\sigma$  (Table 6.3), although this drops to an insignificant 92% or  $1.8\sigma$  when 3C295 is excluded. These hints can also be seen in the weighted means of Figure 6.7. The annulus of Figure 6.8 ( $564 \text{ kpc} < r < 977 \text{ kpc}$ ) shows little evidence for a correlation between host magnitude and overdensity, and whilst the correlation is again hinted at by the summed annulus of Figure 6.7. 6.9 ( $r < 977 \text{ kpc}$ ), without 3C295 the correlation is still not significant (see Table 6.3).

Therefore my results hint at a link between host luminosity and overdensity in the centres of the ZP5 clusters. They are, however, far from conclusive (particularly when 3C295 is excluded from the analysis), and a larger sample (particularly at higher luminosities) would be required to investigate this further.

### 6.2.3 Overdensity and Radio Morphology

In Chapter 4 I showed that the Fanaroff-Riley Class I (FRI) objects in my subsample, once corrected for passive evolution, lie on the Fundamental Plane of local radio galaxies (Bettoni et al. 2001) but the Fanaroff-Riley Class II (FR II) objects do not. Rather they occupy an alternative plane, rotated with respect to the local plane. I suggested that merger-induced size evolution may be the dominant factor behind the rotation of the FR II Fundamental Plane between  $z \sim 0.5$  and  $z = 0$ . If this is indeed the case we might therefore expect to observe a greater number of close companions around the FR IIs in the sample (as potential objects for mergers, thus causing the plane rotation) than the FR Is. In order to investigate whether this is indeed the case, in Figure 6.10 I show the annular overdensities of the ZP5 objects, binned according to their radio morphology (FRI or FR II).

---

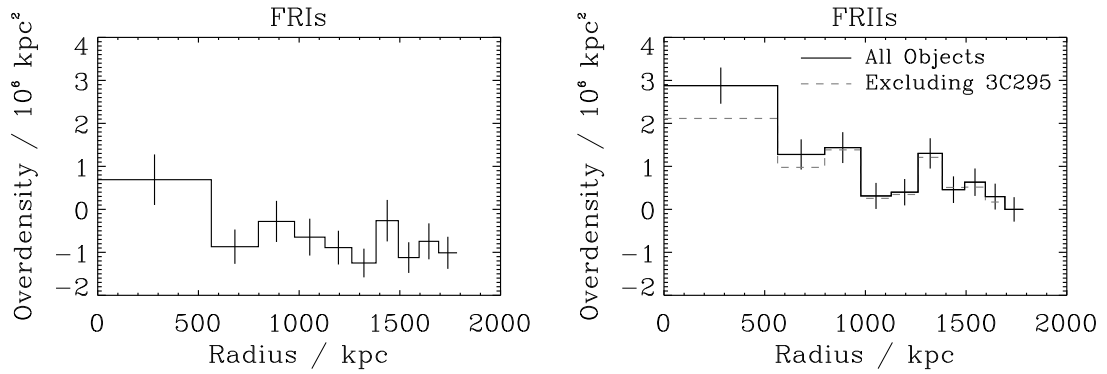


Figure 6.10: The environmental overdensity in each of the annuli for the ZP5 galaxies, binned into Fanaroff-Riley Class I (FRI) objects and Fanaroff-Riley Class II (FR II) objects. The grey dashed line in the FR II bin shows the binned annular overdensity when the object 3C295 is excluded from the results.

From the left hand panel of Figure 6.10 it can be seen that there is no significant evidence for environmental overdensities in the inner annuli of the FRI type objects, while there are hints of an underdensity in their outer annuli. In contrast, the right hand panel of Figure 6.10 shows a rather different overdensity distribution for the FR II type objects, with large overdensities being seen in the inner three annuli (and hints continuing to the sixth annulus) before the environmental density approaches the background density in the outer annuli. The FR II overdensities, and the consequent difference in distribution to the FRIs, remains when 3C295 is excluded from the analysis. A Mann-Whitney-Wilcoxon (MWW) test on the number counts in the first annulus, split into FRIs and FR IIs matched in  $M_R$ , rejects at a significance level of  $>99.9\%$  ( $>3.3\sigma$ ) the null hypothesis that the two distributions have the same mean. The null hypothesis is still rejected at a significance level of  $>99.9\%$  ( $>3.3\sigma$ ) when 3C295 is excluded from the calculation. However, I note that only nine of my objects (from 40 in the full sample) are classified as FRIs, and therefore a larger sample of FRIs at  $z \sim 0.5$  would enable the uncertainties in the left hand panel of Figure 6.10 to be reduced. Unlike for powerful FRIs, which are very rare, this should be possible with existing and forthcoming deep radio surveys, coupled with

multi-wavelength photometry and optical spectroscopy.

Nevertheless, these results as they currently stand are consistent with with my findings in Chapter 4, where I found that the FRI type objects in my subsample lie on the local Fundamental Plane (after correction for passive evolution) but the FRII type objects do not. The host galaxies of the FRII type galaxies must therefore undergo further evolution between  $z \sim 0.5$  and  $z = 0$ , with merger-induced size evolution a plausible candidate for the dominant process behind this. The presence of a greater overdensity of close companions for the FRII type objects than for the FRI type objects, as found here, would allow for such an evolution in the FRII host galaxies but possibly not as strong an evolution for the host galaxies of the FRI type objects.

#### 6.2.4 Overdensity and Spectral Classification

It has been suggested (Hardcastle, Evans & Croston 2007) that Low Excitation Galaxies (LEGs) are powered by the accretion of the hot phase of the IGM but High Excitation Galaxies (HEGs) are powered by the accretion of cold gas. One explanation for the supply of cold gas in HEGs is that it is driven towards the Active Galactic Nucleus (AGN) during a galaxy merger (see Chapter 1). Support for this was given in Chapter 3, in which I found that the HEGs in my subsample show evidence for the presence of younger stellar populations (possibly as a result of merger-induced star formation) but the LEGs do not. If this scenario is correct then it is possible that there exists a difference in the environmental density of LEGs and HEGs, with HEGs residing in denser environments (giving rise to the proposed recent merger). A difference is not, however, demanded by this theory since a recent merger in and of itself does not demand the presence of other close companions. I use my data to investigate any such difference in environmental density by binning the annular overdensities of the ZP5 objects according to their spectral classification (LEG or HEG). The resulting binned overdensities are shown in Figure 6.11.

---

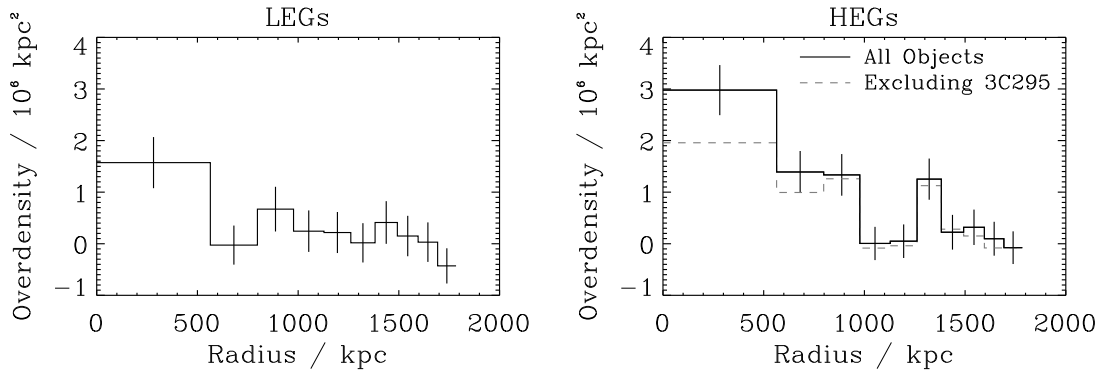


Figure 6.11: The environmental overdensity in each of the annuli for the ZP5 galaxies, binned according to their spectral classification into Low Excitation Galaxies (LEGs) and High Excitation Galaxies (HEGs). The grey dashed line in the HEG bin shows the binned annular overdensity when the object 3C295 is excluded from the results.

Figure 6.11 shows a greater overdensity in the first three annuli for the HEGs than for the LEGs. However, even for the innermost annulus, the difference in the number counts for LEGs and HEGs matched in  $M_R$  is statistically insignificant using an MWW test, and the difference in the distributions may arise as a result of the apparent links between radio morphology and excitation state. Furthermore, the apparent difference in the overdensity distribution for the LEGs and the HEGs vanishes when 3C295 is excluded. I therefore find no evidence of differences in environment for LEGs when compared with HEGs, thus the largest effect appears to be with radio morphology rather than excitation state and/or accretion mode (Hardcastle et al. 2007).

### 6.3 An Alternative Overdensity Measurement

The method used to investigate the overdensities in Section 6.2 has a number of drawbacks. First, objects within the sample at lower redshift will tend to bias the results since on average more objects will be detected around these sources (since their apparent magnitude is smaller, i.e. they appear brighter). Second, the method of using the reference chips to calculate the background count allows the calculation to be affected by extremely

large clusters, as discussed in Section 6.1.3. Third, it is not easy to compare my results with others in the literature.

An alternative measure of overdensity is the spatial clustering amplitude  $B_{gq}$  as devised by Longair & Seldner (1979) and subsequently used by numerous authors to study the environments of different types of active and inactive galaxies (e.g. Yee & Green 1987; Ellingson, Yee & Green 1991; Wold et al. 2000; McLure & Dunlop 2001a; Wold et al. 2001; Farrah et al. 2004; Geach et al. 2007). Working in terms of  $B_{gq}$  allows one to compare results with others in the literature calculated in the same way. Furthermore, the inclusion of the integrated luminosity function in the denominator of the calculation (see Section 6.3.1) allows us to compare the environments of objects at different redshifts on an equal footing, since the results are in effect normalised by the expected number of objects at each redshift given the magnitude cut of the data.

In this section I therefore re-analyse the overdensities around the ZP5 objects as a function of radio luminosity and as a function of host luminosity, this time using  $B_{gq}$  as my measure of the overdensity in order to take advantage of these desirable attributes. Furthermore, rather than use the background count as calculated from my reference chips, I now use a background count and the luminosity function determined from a large survey (see Section 6.3.1) in order to avoid the potential problems with the previous method discussed above.

### 6.3.1 Calculating $B_{gq}$

I followed the standard procedure (e.g. Longair & Seldner 1979; McLure & Dunlop 2001a) in calculating  $B_{gq}$  values for the ZP5 clusters as follows. First I calculated the quantity  $A_{gq}$ , which measures the excess in the number of objects surrounding the central source compared to the expected background count:

---

$$A_{gq} = \left[ \frac{N_t}{N_b} - 1 \right] \left( \frac{3 - \gamma}{2} \right) \theta^{\gamma-1}, \quad (6.1)$$

where  $N_t$  is the number of galaxies contained within a radius of  $\theta$  from the central source, excluding the central source itself, and  $N_b$  is the expected background count in the same aperture. The constant  $\gamma$  arises from the angular correlation function (see e.g. Longair & Seldner 1979; Wold et al. 2000) and I here adopt the usual value of  $\gamma = 1.77$  (e.g. Groth & Peebles 1977; Geach et al. 2007). However, I note that Prestage & Peacock (1988) and Prestage & Peacock (1989) showed that  $B_{gq}$  is insensitive to the choice of  $\gamma$ , providing  $\gamma \simeq 2$ . From  $A_{gq}$ , the spatial clustering amplitude  $B_{gq}$  is calculated as follows:

$$B_{gq} = \frac{A_{gq} N_g}{I_\gamma \phi(z)} \left[ \frac{D}{1+z} \right]^{\gamma-3}, \quad (6.2)$$

where  $I_\gamma$  is a constant whose value is 3.78 when  $\gamma = 1.77$  (e.g. McLure & Dunlop 2001a).  $N_g$  is the expected background count per square radian,  $D$  is the angular diameter distance of the central source and  $z$  is its redshift. The quantity  $\phi(z)$  is calculated as the galaxy luminosity function at the redshift of the target, integrated from the bright end of the luminosity function up to the absolute magnitude which corresponds to the apparent magnitude limit of the data at the redshift of the central source. In this case, the magnitude cut is  $i' < 21.5$  (Chapter 5), and appropriate k-corrections are used to convert from the apparent magnitude to the absolute magnitude in each case. The k-corrections were generated using Hyperz<sup>3</sup> in a similar fashion to the colour cuts in Section 6.1.2; at each redshift Hyperz was used to generate the absolute  $i'$  band magnitude of an elliptical galaxy corresponding to the magnitude limit of the data ( $i' = 21.5$ ). The assumptions and caveats are as described in Section 6.1.2.

For each of the ZP5 objects I calculated a value of  $B_{gq}$  using two different apertures:

---

<sup>3</sup><http://webast.ast.obs-mip.fr/hyperz/>

$r < 564$  kpc and  $r < 977$  kpc. The calculated  $B_{gq}$  values can be found in Table 6.4. The first was designed to probe the immediate vicinity of the central galaxy in each case, the second to investigate a greater area of the cluster. Number counts for each annulus ( $N_t$ ) were taken from the catalogues of objects detected on the central chips (Section 6.1.1 and Chapter 5) using the colour cuts described in Section 6.1.2 in order to limit my investigations to elliptical galaxies of comparable redshift to the central source. The background count per square degree was estimated from the CFHTLS D1 field, using the same colour cuts (with a conversion from Vega to AB magnitudes) as used for the INT data (Section 6.1.2).<sup>4</sup> The CFHTLS has a depth of  $i' = 27.3$ , which is significantly deeper than my data and thus suitable for use in this way. Using the average background count from a large survey removes the potential problem, discussed in Section 6.1.3, of a large cluster having an effect on the background count calculated using my reference chips.

The luminosity function used was the  $I$ -band luminosity function for the redshift range 0.40–0.60 from Ilbert et al. (2005). This yields parameters of  $\phi^* = 8.37 \times 10^{-4}$ ,  $\alpha = -1.47$  and  $M^* = -23.52$  for the Schechter luminosity function (Schechter 1976):

$$\phi(M, z) = \frac{\ln 10}{2.5} \phi^* 10^{0.4(\alpha+1)(M^*-M)} e^{-10^{0.4(M^*-M)}}. \quad (6.3)$$

I note that this luminosity function is for all galaxies, not just for ellipticals. Since my colour selection produces values of  $N_t$ ,  $N_b$  and  $N_g$  which are dominated by ellipticals, my resulting  $B_{gq}$  values will not be strictly correct and, as they currently stand, cannot be compared directly with other values of  $B_{gq}$  in the literature. However, I do not expect the discrepancy to be large since at the bright end of the luminosity function we are dominated by elliptical galaxies (figure 4 of Zucca et al. 2006). I test this assumption

---

<sup>4</sup>Details of the CFHTLS, the Deep Survey and the D1 field can be found at <http://www.cfht.hawaii.edu/Science/CFHLS/>, <http://www.ast.obs-mip.fr/article204.html> and <http://www.ast.obs-mip.fr/article212.html> respectively. The conversion from Vega to AB magnitudes was done using the equations at <http://www.ast.cam.ac.uk/wfcsur/technical/photom/colours/>.

Object	$B_{gq} / \text{Mpc}^{1.77}$	
	$r < 564 \text{ kpc}$	$r < 977 \text{ kpc}$
3C16	$-61 \pm 38$	$-94 \pm 33$
3C19	$261 \pm 153$	$340 \pm 128$
3C46	$-25 \pm 62$	$-61 \pm 50$
3C200	$216 \pm 129$	$131 \pm 90$
3C225B	$105 \pm 221$	$295 \pm 217$
3C228	$478 \pm 264$	$522 \pm 209$
4C74.16	$331 \pm 257$	$203 \pm 183$
3C244.1	$330 \pm 131$	$261 \pm 93$
3C274.1	$236 \pm 114$	$168 \pm 80$
3C295	$1300 \pm 268$	$1023 \pm 177$
3C330	$273 \pm 219$	$110 \pm 148$
3C341	$245 \pm 128$	$166 \pm 90$
3C427.1	$453 \pm 289$	$875 \pm 276$
3C457	$291 \pm 125$	$262 \pm 93$
6C0825+3407	$7 \pm 61$	$28 \pm 56$
6C0850+3747	$150 \pm 93$	$409 \pm 99$
6C0857+3945	$221 \pm 183$	$422 \pm 172$
6C1111+3940	$-31 \pm 190$	$-119 \pm 152$
6C1132+3439	$334 \pm 191$	$399 \pm 155$
6C1200+3416	$388 \pm 219$	$125 \pm 133$
6C1303+3756	$78 \pm 106$	$334 \pm 120$
7C0213+3418	$283 \pm 145$	$485 \pm 133$
7C0219+3419	$-26 \pm 201$	$114 \pm 207$
7C0219+3423	$133 \pm 252$	$-114 \pm 161$
7C0220+2952	$94 \pm 187$	$84 \pm 154$
7C0223+3415	$-28 \pm 77$	$-42 \pm 68$
7C0810+2650	$183 \pm 111$	$235 \pm 93$
7C1731+6638	$-28 \pm 150$	$127 \pm 164$
7C1806+6831	$-27 \pm 175$	$295 \pm 214$
TOOT0009+3523	$22 \pm 85$	$-5 \pm 66$
TOOT0013+3459	$125 \pm 249$	$66 \pm 190$
TOOT0018+3510	$-64 \pm 40$	$-98 \pm 35$
TOOT1255+3556	$79 \pm 107$	$66 \pm 86$
TOOT1301+3658	$205 \pm 109$	$135 \pm 77$
TOOT1303+3334	$194 \pm 220$	$125 \pm 167$
TOOT1307+3639	$495 \pm 317$	$287 \pm 217$
TOOT1309+3359	$23 \pm 88$	$35 \pm 78$
TOOT1626+4523	$-77 \pm 50$	$-117 \pm 44$
TOOT1630+4534	$100 \pm 126$	$87 \pm 101$
TOOT1648+5040	$12 \pm 67$	$18 \pm 59$

Table 6.4: The value of  $B_{gq}$  calculated for each  $z \sim 0.5$  (ZP5) object using two annuli:  $r < 564 \text{ kpc}$  and  $r < 977 \text{ kpc}$  (Section 6.3.1).

Annulus ( $r/\text{kpc}$ )	All Objects		3C295 Excluded	
	$\rho$	Significance	$\rho$	Significance
$r < 564$	0.50	99.8%	0.46	99.6%
$r < 977$	0.52	99.9%	0.48	99.7%

Table 6.5: The Spearman’s rank correlation coefficients ( $\rho$ ) for correlations between the 151 MHz radio luminosities of the ZP5 objects and their  $B_{gg}$  values, together with their associated significances that they deviate from the null hypothesis of no correlation (Section 6.3.2 and Figures 6.12 and 6.13). The coefficients and their significances are listed for the two annuli used in Figures 6.12 and 6.13, namely  $r < 564$  kpc and  $r < 977$  kpc (where  $r$  is the distance from the central ZP5 galaxy). I also show the coefficients and their significances when 3C295 is excluded from the analysis (see Section 6.2.1).

further in Sections 6.3.2 and 6.3.3, and show that whilst the exact  $B_{gg}$  values cannot be compared directly with other values in the literature, any trends or correlations found using them can be relied upon.

### 6.3.2 $B_{gg}$ and Radio Luminosity

Following on from Section 6.2.2, in Figures 6.12 and 6.13 I show the 151 MHz radio luminosities of each of the ZP5 objects versus their  $B_{gg}$  values for two annuli:  $r < 564$  kpc and  $r < 977$  kpc respectively (where  $r$  is the distance from the central ZP5 galaxy). I test these data sets for correlations using Spearman’s rank correlation coefficient, and the resulting coefficients and their significances are listed in Table 6.5. Since I once again test for correlations using the entire sample and over a large range in radio luminosity, these results are statistically robust.

Figure 6.12 shows evidence of a positive correlation between  $B_{gg}$  and radio luminosity, and the Spearman’s rank correlation coefficient is significant at the 99.8% ( $3.1\sigma$ ) level (see Table 6.5), dropping to 99.6% ( $2.9\sigma$ ) when 3C295 is excluded from the analysis. Considering the larger ( $r < 977$  kpc) annulus in Figure 6.13, a positive correlation is once again visible. Here the Spearman’s rank correlation coefficient is significant at the 99.9% ( $3.3\sigma$ ) level, falling to 99.7% ( $3.0\sigma$ ) with the exclusion of 3C295. As in Section

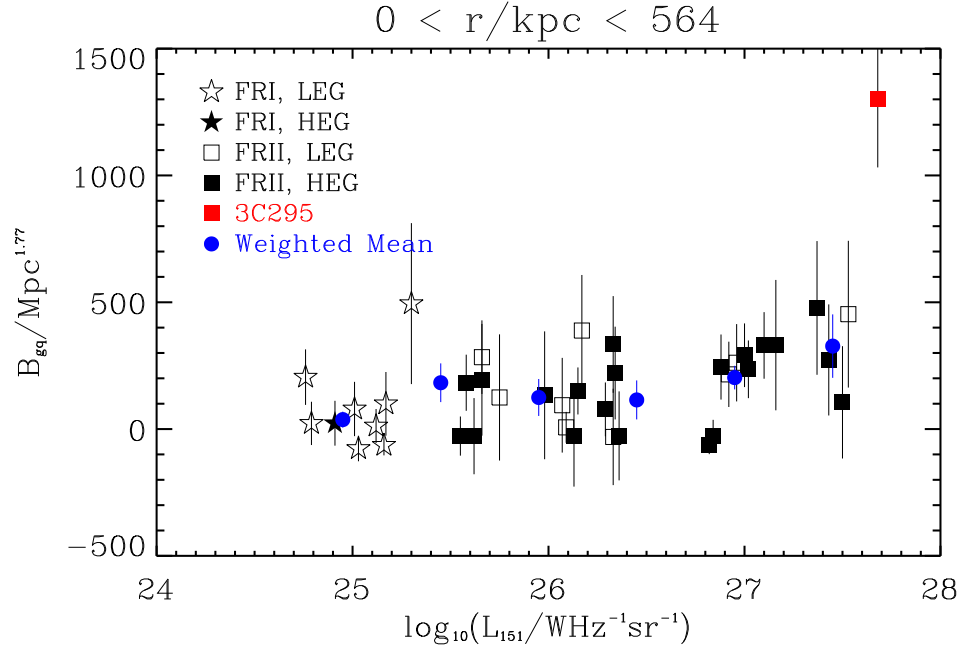


Figure 6.12:  $B_{gq}$  versus the logarithm of the 151 MHz radio luminosity ( $L_{151}$ ) for the  $r < 564$  kpc annulus, where  $r$  is the distance from the central ZP5 galaxy (Section 6.3.2). Fanaroff-Riley Class I (FRI) objects are shown as stars whilst Fanaroff-Riley Class II (FRII) objects are shown as squares. Simultaneously, Low Excitation Galaxies (LEGs) are shown using open symbols whilst High Excitation Galaxies (HEGs) are shown using filled symbols. 3C295 is highlighted with a red symbol. I also calculate the weighted mean overdensity in six bins of equal size in  $\log_{10}(L_{151}/\text{WHz}^{-1}\text{sr}^{-1})$ , between  $\log_{10}(L_{151}/\text{WHz}^{-1}\text{sr}^{-1}) = 24.7$  and  $\log_{10}(L_{151}/\text{WHz}^{-1}\text{sr}^{-1}) = 27.7$  (excluding 3C295). These weighted means are shown by the blue circles.

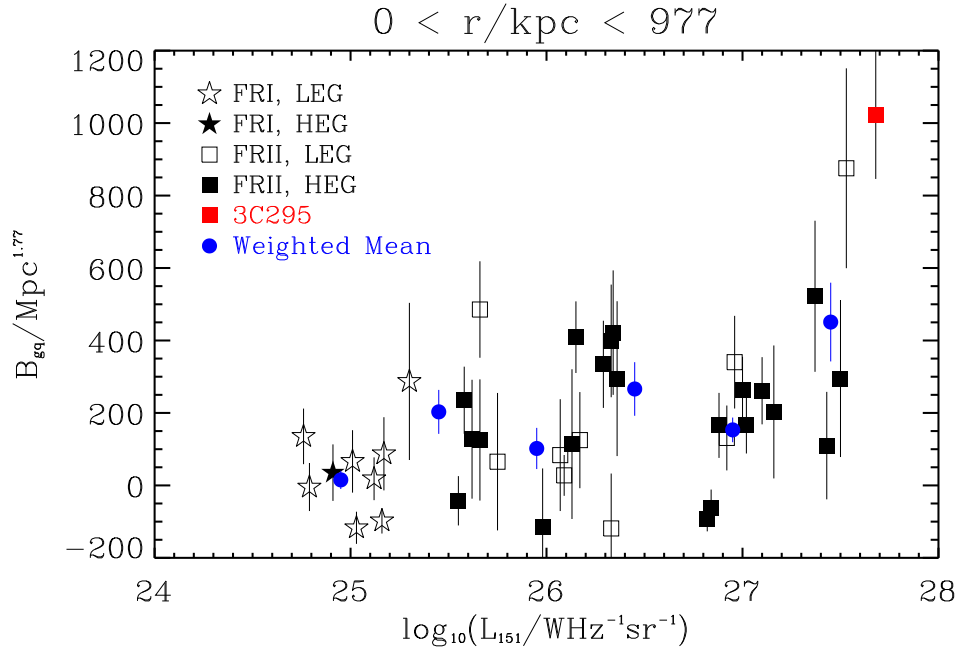


Figure 6.13:  $B_{gq}$  versus the logarithm of the 151 MHz radio luminosity ( $L_{151}$ ) for the  $r < 977$  kpc annulus, where  $r$  is the distance from the central ZP5 galaxy (Section 6.3.2). Fanaroff-Riley Class I (FRI) objects are shown as stars whilst Fanaroff-Riley Class II (FRII) objects are shown as squares. Simultaneously, Low Excitation Galaxies (LEGs) are shown using open symbols whilst High Excitation Galaxies (HEGs) are shown using filled symbols. 3C295 is highlighted with a red symbol. I also calculate the weighted mean overdensity in six bins of equal size in  $\log_{10}(L_{151}/\text{WHz}^{-1}\text{sr}^{-1})$ , between  $\log_{10}(L_{151}/\text{WHz}^{-1}\text{sr}^{-1}) = 24.7$  and  $\log_{10}(L_{151}/\text{WHz}^{-1}\text{sr}^{-1}) = 27.7$  (excluding 3C295). These weighted means are shown by the blue circles.

Annulus ( $r/\text{kpc}$ )	All Objects		3C295 Excluded	
	$\rho$	Significance	$\rho$	Significance
$r < 564$	0.45	99.5%	0.41	99%
$r < 977$	0.51	99.9%	0.47	99.6%

Table 6.6: The Spearman’s rank correlation coefficients ( $\rho$ ) for correlations between the 151 MHz radio luminosities of the ZP5 objects and their  $B_{gq}$  values, when  $B_{gq}$  is calculated using the elliptical galaxy luminosity function of Zucca et al. (2006) for  $0.4 < z < 0.9$  (Section 6.3.2). Also listed are the significances with which these coefficients deviate from the null hypothesis of no correlation. The coefficients and their significances are listed for the two annuli used in Figures 6.12 and 6.13, namely  $r < 564$  kpc and  $r < 977$  kpc (where  $r$  is the distance from the central ZP5 galaxy). I also show the coefficients and their significances when 3C295 is excluded from the analysis (see Section 6.2.1).

6.2.1, both of these correlations are more evident when the weighted means of Figures 6.12 and 6.13 are considered.

As discussed in Section 6.3.1, my standard  $B_{gq}$  calculation makes the assumption that the global luminosity function in the regime we are probing here is dominated by elliptical galaxies, and therefore that any trends identified using the  $B_{gq}$  values can be relied upon. To test this further, I re-calculate my  $B_{gq}$  values, this time using the  $I$ -band luminosity function for elliptical galaxies in the redshift range 0.4–0.9 from Zucca et al. (2006). Note that I do not use this luminosity function in the first instance due to its less precise redshift range. With this luminosity function the calculated values of  $B_{gq}$  are slightly higher, as expected from Equation 6.2 since  $\phi(z)$  is lower for the elliptical-only luminosity function. I then re-test the positive correlations identified in the data using the Spearman’s rank correlation coefficient. The coefficients, along with their significances, are listed in Table 6.6. Whilst the significances of the correlations (99% or  $2.6\sigma$  and 99.6% or  $2.9\sigma$  when 3C295 is excluded from the analysis for the  $r < 564$  kpc and  $r < 977$  kpc annuli respectively) are slightly lower than in the initial calculation, it is clear that significant correlations are still detected and that the trends identified in Figures 6.12 and 6.13 can be relied upon, as assumed.

Annulus ( $r/\text{kpc}$ )	All Objects		3C295 Excluded	
	$\rho$	Significance	$\rho$	Significance
$r < 564$	-0.32	95%	-0.26	89%
$r < 977$	-0.33	96%	-0.28	92%

Table 6.7: The Spearman’s rank correlation coefficients ( $\rho$ ) for correlations between the host magnitudes of the ZP5 objects and their  $B_{gq}$  values, together with their associated significances that they deviate from the null hypothesis of no correlation (Section 6.3.3 and Figures 6.14 and 6.15). The coefficients and their significances are listed for the two annuli used in Figures 6.14 and 6.15, namely  $r < 564$  kpc and  $r < 977$  kpc (where  $r$  is the distance from the central ZP5 galaxy). I also show the coefficients and their significances when 3C295 is excluded from the analysis (see Section 6.2.1). As in Figures 6.7 to 6.9, the coefficients are negative since a more luminous object has a smaller magnitude. The horizontal axes of Figures 6.14 and 6.15 are correspondingly reversed.

These correlations are therefore both clearer and statistically more significant than those based on the simple overdensity calculations presented in Section 6.2.2, and provide stronger evidence for the existence of a relationship between radio luminosity and environmental density, consistent with the suggestion that radio luminosity is enhanced in denser environments. However, I note that some of the objects with high radio luminosities still have lower  $B_{gq}$  values in both Figures 6.12 and 6.13, once again indicating that the picture is more complicated than a simple dependence of radio luminosity on environmental density or vice versa.

### 6.3.3 $B_{gq}$ and Host Magnitude

Following on from Section 6.2.2, in Figures 6.14 and 6.15 I show the host magnitudes of each of the ZP5 objects versus their  $B_{gq}$  values for the two annuli used in Section 6.3.2:  $r < 564$  kpc and  $r < 977$  kpc respectively (where  $r$  is the distance from the central ZP5 galaxy). I again test each of these three data sets for correlations using Spearman’s rank correlation coefficient. I list the resulting coefficients and their significances in Table 6.7. The use of the whole sample, and the consequent range in host luminosity this entails, once again ensures the robustness of the statistics.

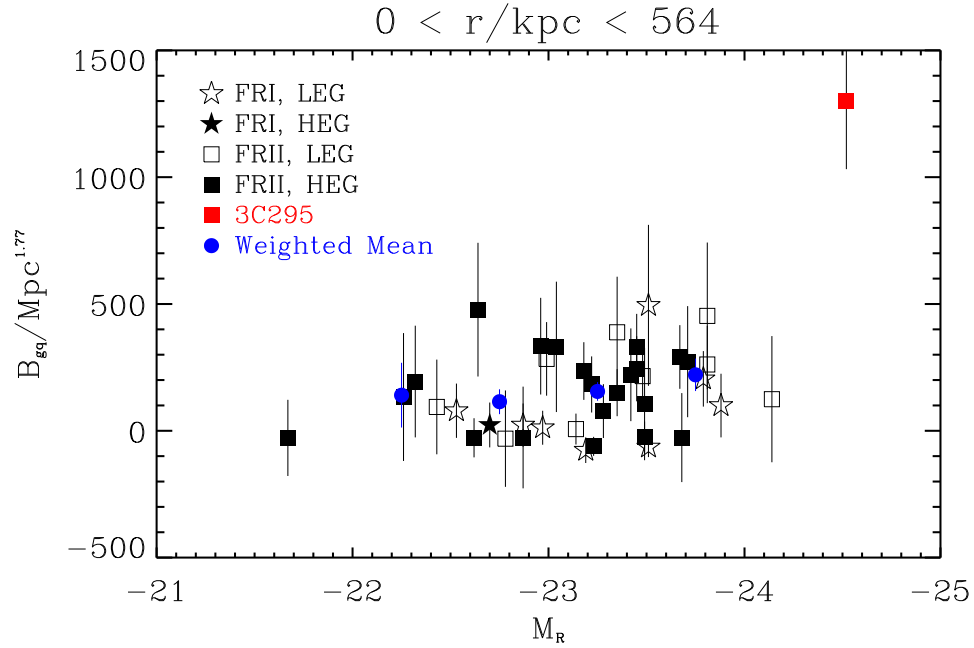


Figure 6.14:  $B_{gg}$  versus host magnitude ( $M_R$ ) for the  $r < 564$  kpc annulus, where  $r$  is the distance from the central ZP5 galaxy (Section 6.3.3). Fanaroff-Riley Class I (FRI) objects are shown as stars whilst Fanaroff-Riley Class II (FRII) objects are shown as squares. Simultaneously, Low Excitation Galaxies (LEGs) are shown using open symbols whilst High Excitation Galaxies (HEGs) are shown using filled symbols. 3C295 is highlighted with a red symbol. I also calculate the weighted mean overdensity in four bins of equal size in  $M_R$ , between  $M_R = -22$  and  $M_R = -24$ . These weighted means are shown by blue circles. 3C295 is outside of these bins, as are two other objects (7C1731+6638 and TOOT0013+3459) which would, without the use of excessively large bins, be the sole object in their respective bins.

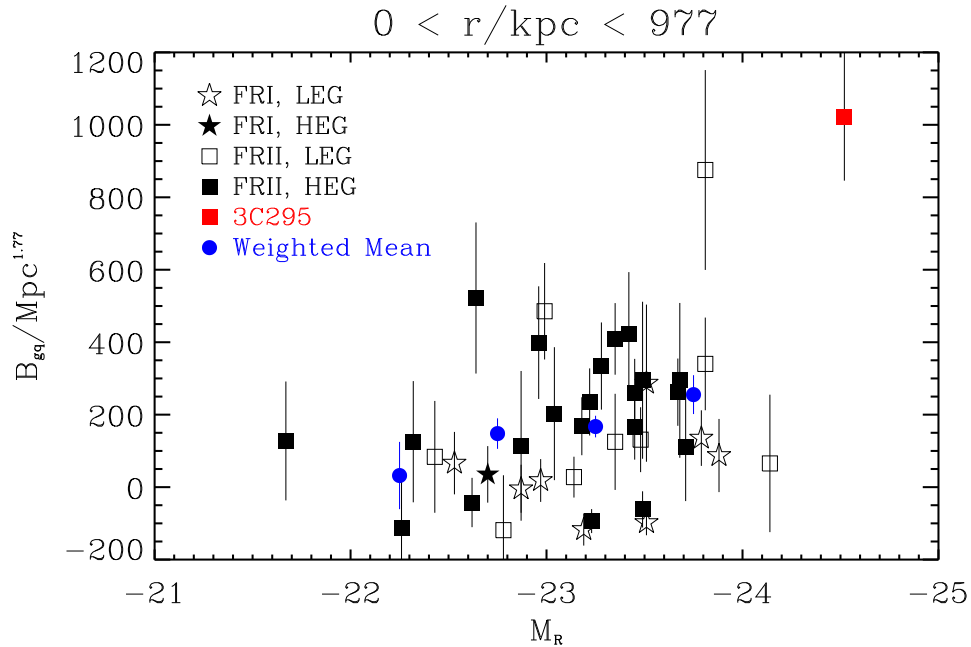


Figure 6.15:  $B_{gg}$  versus host magnitude ( $M_R$ ) for the  $r < 977$  kpc annulus, where  $r$  is the distance from the central ZP5 galaxy (Section 6.3.3). Fanaroff-Riley Class I (FRI) objects are shown as stars whilst Fanaroff-Riley Class II (FRII) objects are shown as squares. Simultaneously, Low Excitation Galaxies (LEGs) are shown using open symbols whilst High Excitation Galaxies (HEGs) are shown using filled symbols. 3C295 is highlighted with a red symbol. I also calculate the weighted mean overdensity in four bins of equal size in  $M_R$ , between  $M_R = -22$  and  $M_R = -24$ . These weighted means are shown by blue circles. 3C295 is outside of these bins, as are two other objects (7C1731+6638 and TOOT0013+3459) which would, without the use of excessively large bins, be the sole object in their respective bins.

Annulus ( $r/\text{kpc}$ )	All Objects		3C295 Excluded	
	$\rho$	Significance	$\rho$	Significance
$r < 564$	-0.32	96%	-0.27	90%
$r < 977$	-0.33	96%	-0.27	91%

Table 6.8: The Spearman’s rank correlation coefficients ( $\rho$ ) for correlations between the host magnitudes of the ZP5 objects and their  $B_{gq}$  values, when  $B_{gq}$  is calculated using the elliptical galaxy luminosity function of Zucca et al. (2006) for  $0.4 < z < 0.9$  (Section 6.3.3). Also listed are the significances with which these coefficients deviate from the null hypothesis of no correlation. The coefficients and their significances are listed for the two annuli used in Figures 6.14 and 6.15, namely  $r < 564$  kpc and  $r < 977$  kpc (where  $r$  is the distance from the central ZP5 galaxy). I also show the coefficients and their significances when 3C295 is excluded from the analysis (see Section 6.2.1). Note that the coefficients are once again negative since a more luminous object has a smaller magnitude.

Neither Figure 6.14 nor Figure 6.15 show a clear relationship between host luminosity and  $B_{gq}$ . Indeed, the Spearman’s rank correlation coefficient shows there is no evidence for a correlation when 3C295 is excluded from the analysis (89% or  $1.6\sigma$  significance in Figure 6.7 and 92% or  $1.8\sigma$  in Figure 6.8, as listed in Table 6.7). As in Section 6.3.2, re-testing the correlations using the Zucca et al. (2006) luminosity function does not cause a great change in these significances, as listed in Table 6.8. Therefore, in a similar fashion to Section 6.2.2, I find very little evidence for a link between host galaxy magnitude and environmental density.

## 6.4 Overdensities and Radio Jet Position Angle

The results presented in Sections 6.2 and 6.3 suggest that whilst there may be a link between the environmental density of a ZP5 object and its radio luminosity and radio morphology, the picture is more complicated than a straightforward dependence of one on the other. For example, whilst there is evidence for a positive correlation between radio luminosity and overdensity in Figures 6.3, 6.12 and 6.13, it is noticeable that some objects with high radio luminosities still reside in environments which are not particularly

dense.

In this section I investigate another possible element of the picture; whether there exists a link between the angular profile of the overdensities and the position angle (PA) of the radio jets of the ZP5 objects. If there is indeed a link between the radio luminosity and the environmental density due to the impact of the jets on the dense intra-cluster medium, then we would expect there to be some link between the direction of the radio jets and the direction of greatest environmental overdensity.

In order to investigate this, I once again used sources from the central chips which matched the colour cuts of Section 6.1.2. However, here I restricted my analysis to sources falling within the three innermost annuli used of Section 6.2 (a concentric area of  $3 \times 10^6$  kpc<sup>2</sup>), where the source density deviates most significantly from the background level. For each source remaining in the catalogues I then calculated the angle with respect to the radio jet PA made by the line joining the source to the central ZP5 object, as illustrated in Figure 6.16. Each source therefore has a calculated angle in the range 0–90° (where 0° means an object is aligned with the radio jet). Then, for each ZP5 object, I determined the number of surrounding objects whose angle thus calculated fell into each of six equal size bins: 0–15°, 15–30°, 30–45°, 45–60°, 60–75° and 75–90°, and corrected these number counts for completeness according to Section 5.3.2. Finally, I divided the ZP5 sample according 151 MHz radio luminosity using the same bins as used in Section 6.2.1:  $L_{151} < 10^{25.3}$  W Hz<sup>-1</sup> sr<sup>-1</sup>,  $L_{151}$  from  $10^{25.3}$  to  $10^{25.8}$  W Hz<sup>-1</sup> sr<sup>-1</sup>,  $L_{151}$  from  $10^{25.8}$  to  $10^{26.3}$  W Hz<sup>-1</sup> sr<sup>-1</sup>,  $L_{151}$  from  $10^{26.3}$  to  $10^{26.8}$  W Hz<sup>-1</sup> sr<sup>-1</sup> and  $L_{151} > 10^{26.8}$  W Hz<sup>-1</sup> sr<sup>-1</sup>. For each of these radio luminosity bins, I added together the completeness-corrected source counts, binned in angular segments, for all of the objects in the radio luminosity bin. I then calculated the relative density of sources in each angle bin as a fraction of the number of sources contained in all of the angle bins for that radio luminosity bin, along with the Poisson error. The resulting fractional overdensities are shown in Figure 6.17.

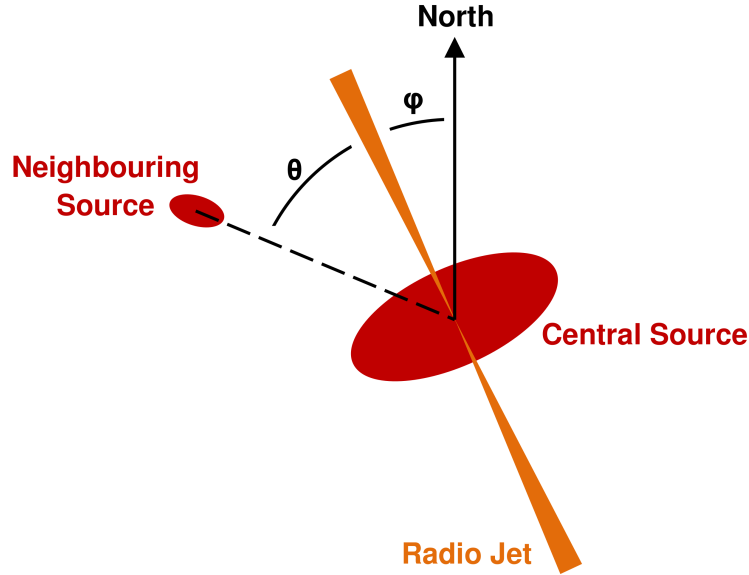


Figure 6.16: An illustration of how the source angles used in Section 6.4 were calculated. For each source, the angle ( $\theta$ ) made by a line connecting the source to the central  $z \sim 0.5$  object was calculated with respect to the radio jet position angle ( $\phi$ ).

It is apparent from Figure 6.17 that there is no evidence in the first four radio luminosity bins for any relation between environmental overdensity and radio jet PA. However, the most radio luminous bin ( $L_{151} > 10^{26.8} \text{ W Hz}^{-1} \text{ sr}^{-1}$ ) shows evidence for an alignment between overdensity and the PA of radio the jet. A Kuiper test rejects at the 99.8% ( $3.1\sigma$ ) level the null hypothesis that the distribution is uniform. However, once again excluding 3C295 from the analysis reduces this significance to 95% ( $2.0\sigma$ ), thus only providing tentative evidence of an alignment effect. Furthermore, since there are only 13 objects in the  $L_{151} > 10^{26.8} \text{ W Hz}^{-1} \text{ sr}^{-1}$  bin (or 12 when 3C295 is excluded) these statistics must be taken as giving an indication of trends only, and not with the robustness that would be obtained with a larger sample.

However, these hints of an alignment between overdensity and radio jet PA for the most radio luminous objects are consistent with the suggestion that the highest luminosity radio sources require the densest IGM medium on which to work (as discussed in Section

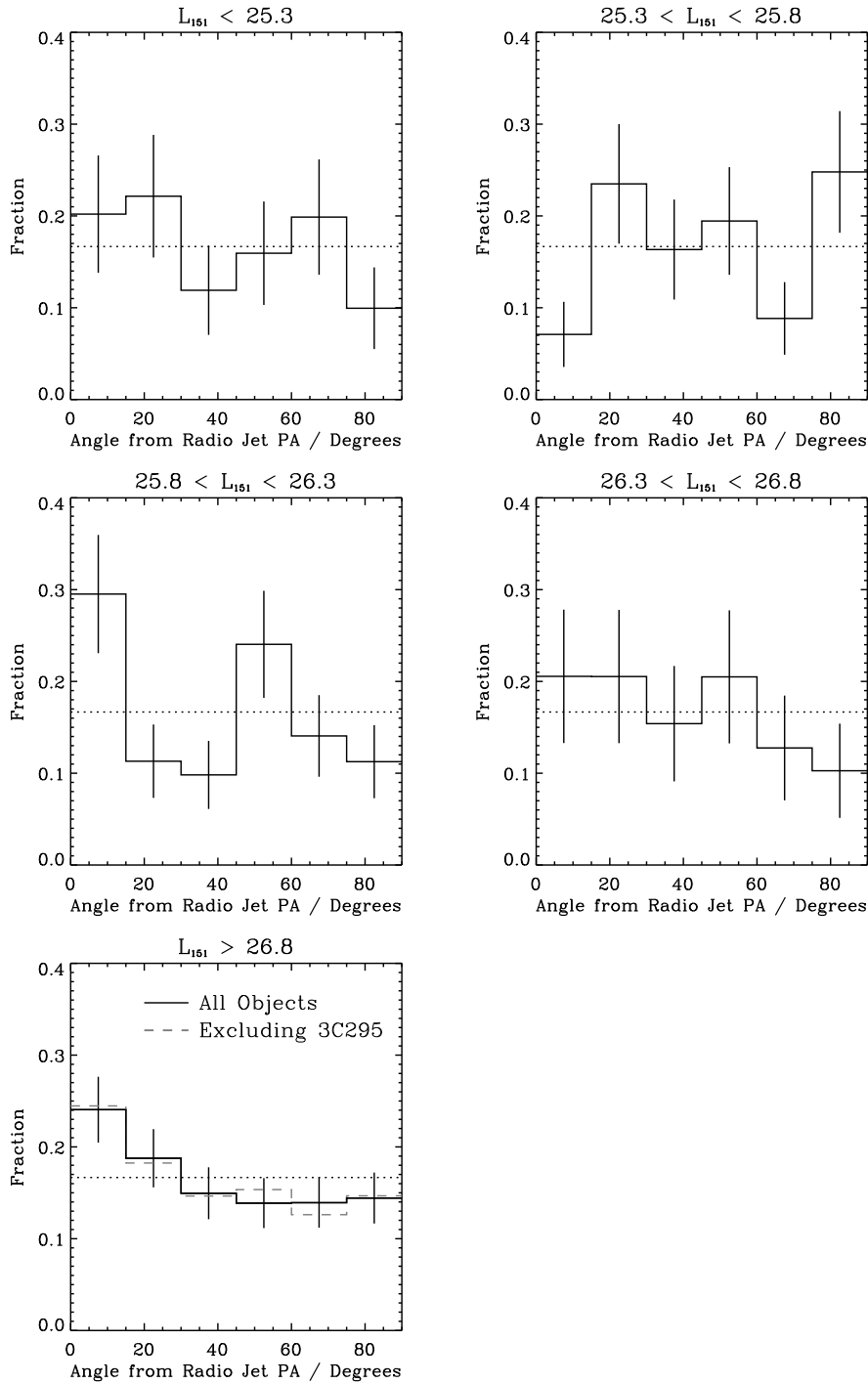


Figure 6.17: The fractional overdensity versus the angle from the radio jet position angle for the  $z \sim 0.5$  objects, separated by 151 MHz radio luminosity,  $L_{151}$  (Section 6.4). The fractional overdensities are shown in  $15^\circ$  bins, and the dotted line in each subfigure illustrates a uniform distribution. The black line in each subfigure shows the fractional overdensity for all of the objects contained within the radio luminosity bin. The grey dashed line in the final bin ( $L_{151} > 10^{26.8} \text{ W Hz}^{-1} \text{ sr}^{-1}$ ) shows the fractional overdensity when the object 3C295 is excluded from the results.

6.2.1). It is also a possible explanation for the observation made in Sections 6.2.1 and 6.3.2 that some objects with high radio luminosities have relatively low environmental densities; it is possible that a source with a high radio luminosity may sit in an environment with a relatively low global environmental density but have radio jets aligned with an axis of particularly high local density. Thus the radio jets could be enhanced by the dense IGM medium leading to a high radio luminosity for a source which resides in a region of relatively low global environmental density.

## 6.5 Overdensities and Host Position Angle

As discussed in Chapter 1, many studies have found that the major axes of Brightest Cluster Galaxies (BCGs) are aligned with the major axes of their host clusters (the Binggeli effect, e.g. Sastry 1968; Binggeli 1982; Trevese, Cirimele & Flin 1992; Fuller, West & Bridges 1999; Torlina, De Propriis & West 2007), and that these alignments were already present by  $z \sim 0.5$  (Donoso, Mill & Lambas 2006). In Chapter 4 I noted that the ZP5 objects may evolve into BCGs. One test of this is therefore whether there exists an alignment between environmental overdensity and the host galaxy PA (the angle of the major axis) for the ZP5 objects.

To test this I repeated the procedure described in Section 6.4, but rather than use the direction of the radio jets as my reference point for the angle calculation I used the direction of the host galaxy PA from McLure et al. (2004). Each source in the immediate vicinity of a ZP5 object thus has a calculated angle in the range  $0\text{--}90^\circ$ , where  $0^\circ$  means an object is aligned with the ZP5 galaxy host PA. For each ZP5 object I again binned these angles into six angle bins of equal size. I then divided the ZP5 sample according to host magnitude using the same three bins as in Section 6.2.2:  $M_R > -22.98$ ,  $-23.46 < M_R < -22.98$  and  $M_R < -23.46$ . For each of these host magnitude bins I calculated the

---

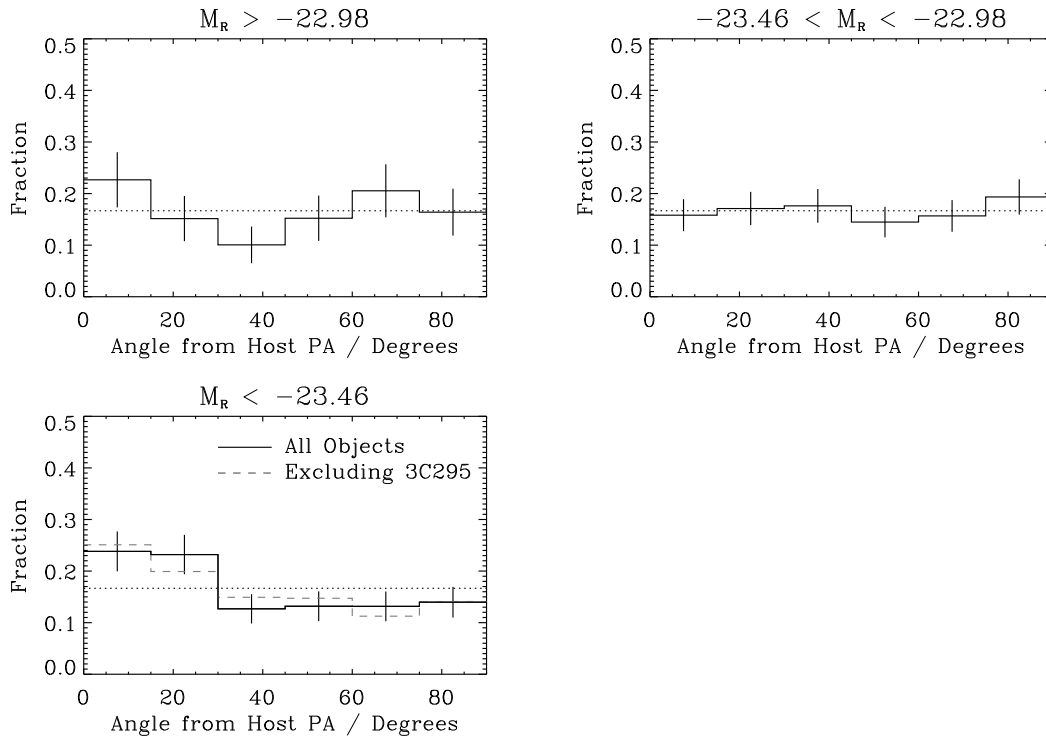


Figure 6.18: The fractional overdensity versus the angle from the host galaxy position angle for the  $z \sim 0.5$  objects, separated by host magnitude,  $M_R$  (Section 6.5). The fractional overdensities are shown in  $15^\circ$  bins, and the dotted line in each subfigure illustrates a uniform distribution. The black line in each subfigure shows the fractional overdensity for all of the objects contained within the host magnitude bin. The grey dashed line in the final bin ( $M_R < -23.46$ ) shows the fractional overdensity when the object 3C295 is excluded from the results.

fractional overdensity distribution in the same manner as in Section 6.4. The results are shown in Figure 6.18.

No alignment effects are seen in Figure 6.18 for the faintest and middle host magnitude bins ( $M_R > -22.98$  and  $-23.46 < M_R < -22.98$ ). However, the most optically luminous objects ( $M_R < -23.46$ ) show hints of an alignment between environmental density and host galaxy PA. A Kuiper test rejects at the 99.5% ( $2.8\sigma$ ) level the null hypothesis that the distribution is uniform, although this drops to an insignificant 93% ( $1.8\sigma$ ) when 3C295 is excluded. In addition, there are only 14 objects in this bin (13 without 3C295) meaning we are unable to regard these statistics as completely robust. Mindful

of these caveats, the tentative hints of the Binggeli effect seen for the most optically luminous objects ( $M_R < -23.46$ ) suggests that these objects may evolve into BCGs as suggested in Chapter 4, but that the rest of the sample show little evidence for this, albeit with limited number statistics.

## 6.6 Conclusions

In order to investigate whether properties of radio galaxies are linked to the environments in which the galaxies reside, in this chapter I use both a straightforward overdensity and a  $B_{gq}$  analysis with appropriate colour cuts to determine the environmental density of the radio galaxies in the ZP5 sample and compare this to the radio luminosity and the host magnitude of the galaxies. I also investigate how the density may be related to radio morphology and excitation state, and whether there is a preferred orientation of the cluster environment around these sources.

- I find a positive correlation between  $L_{151}$  and environmental overdensity, significant at the 99.7% ( $3.0\sigma$ ) level for  $r < 977$  kpc. This is consistent with the suggestion (e.g. Barthel & Arnaud 1996; Kauffmann, Heckman & Best 2008; Falder et al. 2010) that radio jets are enhanced in denser environments.
  - I also find hints of an alignment between overdensity and radio jet PA for the most radio luminous objects in the sample ( $L_{151} > 10^{26.8}$  W Hz<sup>-1</sup> sr<sup>-1</sup>). As well as once again being consistent with the suggestion that the highest luminosity radio sources require the densest IGM on which to work, this finding also provides a possible explanation for the objects in the sample with high radio luminosities but relatively low overdensities; it may be that whilst the global overdensity is low for these objects the radio jet is aligned with an axis of particularly high local density, giving rise to the high radio luminosity.
-

- The FRIs in my sample appear to have a very different environmental density distribution to the FRIIs, significant at the  $>99.9\%$  ( $>3.3\sigma$ ) level, with FRIIs possessing a greater number of close companions than the FRIs. This is consistent with Chapter 4, where I found that FRIIs need to evolve in order to move onto the local Fundamental Plane (plausibly through mergers) but the FRIs do not. However, the small number of FRIs in the sample (nine) mean that this finding remains a tentative one. I find no difference in the environmental density distribution between LEGs and HEGs.
  - Finally, I find tentative hints of an alignment between the major axes of ZP5 galaxies and their clusters (the Binggeli effect), but only for the most optically luminous objects in the sample ( $M_R < -23.46$ ). This suggests that these objects may evolve into BCGs as suggested in Chapter 4, but that the rest of the sample do not.
-

# Chapter 7

## Conclusions

In this thesis I have investigated the hosts and cluster environments of a sample of 41 radio galaxies at  $z \sim 0.5$  (the ZP5 sample; McLure et al. 2004). In this chapter I summarise my main findings (Sections 7.1 and 7.2), describe the links between them (Section 7.3) and indicate possible areas of future work that build upon them.

### 7.1 Host Galaxies

My investigations into the hosts of the  $z \sim 0.5$  radio galaxy sample, and their links to the AGNs themselves, have focussed on two areas: the star formation histories of the host galaxies and the Fundamental Plane of the host galaxies.

To study the star formation histories of my host galaxies (Chapter 3) I used spectroscopic data for a 24 object subsample of the full ZP5 sample. The observations and data reduction were described in Chapter 2. I used the strength of the 4000Å break [ $D_n(4000)$ ] as an indicator of recent star formation and found that my radio galaxies fall into one of two distinct populations in the  $D_n(4000)$  – radio luminosity plane. The lower radio luminosity population is composed entirely of Low Excitation Galaxies (LEGs), whereas the population at higher radio luminosity contains all of the High Excitation Galaxies

(HEGs) in the sample as well as a few LEGs. I found that the lower radio luminosity population has systematically higher  $D_n(4000)$  indices than the higher radio luminosity population. This dichotomy is well explained by the presence of a younger stellar population in the higher radio luminosity (or HEG) population. These results are consistent with the hypothesis (Hardcastle, Evans & Croston 2007) that HEGs are powered by the accretion of cold gas, possibly supplied to the galaxy by mergers (which would also trigger the observed star formation). The LEGs on the other hand may have experienced no recent influx of cold gas (explaining their general lack of recent star formation) and thus be powered by the accretion of the hot phase of the inter-stellar medium.

In Chapter 4 I used the same spectroscopic data in order to study the Fundamental Plane of 18 of my radio galaxies, combining the host galaxy data from McLure et al. (2004) with velocity dispersion data determined using a direct fitting procedure. I showed that the Fanaroff-Riley type I objects (FRIs), once corrected for passive evolution, lie on the Fundamental Plane of local radio galaxies (Bettoni et al. 2001) but the Fanaroff-Riley type II objects (FRIIs) do not. However, both types of object appear to lie on the same  $z \sim 0.5$  plane. I thus found evidence for evolution of the Fundamental Plane of these radio galaxies between  $z \sim 0.5$  and  $z = 0$ , at least for the more powerful FRII type objects. Considering the source of this evolution, I found that neither passive evolution, nor a mass-dependent evolution in the mass-to-light ratios, nor an evolution in the size of the host galaxies can by themselves provide the necessary rotation in the Fundamental Plane. However, I suggested that a combination of all three effects, with merger-induced size evolution as the dominant factor, may provide the solution.

---

## 7.2 Environments

In Chapter 6 I used wide field multi-band imaging data (described in Chapter 5) to investigate the cluster environments of all but one of the objects in the ZP5 sample. I found that the cluster overdensity is positively correlated with the radio luminosity, in agreement with the suggestion that radio jets are enhanced in denser environments (e.g. Barthel & Arnaud 1996; Kauffmann, Heckman & Best 2008; Falder et al. 2010). I also found a difference in the overdensity distribution between the FRI and FR II type radio galaxies, observing a greater number of close companions around FR IIs than FR Is. However, the small number of FR Is in the sample (nine) means that this finding remains tentative.

Furthermore, I found that the cluster environments of those objects which have the largest optical host luminosities show tentative evidence for an alignment between the major axes of the galaxies and the major axes of their clusters (the Binggeli effect, see e.g. Sastry 1968; Binggeli 1982) This suggests that these objects evolve into BCGs in the local universe (e.g. Binggeli 1982; Trevese, Cirimele & Flin 1992; Fuller, West & Bridges 1999; Torlina, De Propris & West 2007). Finally, the radio galaxies with the highest radio luminosities show tentative hints of an alignment between the cluster major axis and the position angle of the radio jet. This is consistent with the idea that high luminosity radio sources require a dense surface for the jets to work on in order to provide the necessary synchrotron losses. In turn, it also provides a possible explanation for those objects in the sample observed to have high radio luminosities but relatively low overdensities; it may be the case that whilst the global overdensity is low for these objects the radio jet is aligned with an axis of particularly high local density, giving rise to the high radio luminosity.

---

### 7.3 Radio Galaxies, Hosts & Environments

The results outlined in Sections 7.1 and 7.2 support a scenario in which there are strong links between radio galaxies, their hosts and their environments.

On the one hand we see a picture in which the powerful FR II type radio sources reside in particularly rich cluster environments at  $z \sim 0.5$ . The first effect of this is merger activity between  $z \sim 0.5$  and  $z = 0$ , leading to the merger-induced size evolution which I suggest is the principle mechanism whereby these FR IIs are moved onto the local Fundamental Plane. Secondly, the high density of the inter-galactic medium (IGM) provides an abundance of material on which the radio jets can work, resulting in high synchrotron losses and thus the high radio luminosity. Thirdly, the presence of close companions means that many, but not necessarily all, of these objects will have undergone a recent merger. This merger would have provided an influx of cold gas, leading both to star formation and to the efficient accretion of the cold gas by the black hole, leading to the HEGs with evidence of recent star formation seen in Chapter 3.

On the other hand we find that the less powerful FR I type radio sources reside in less rich cluster environments at  $z \sim 0.5$  (although still in overdense regions when compared to the background count, as described in Chapter 6). Mergers are rarer for these objects, and thus they move onto the local Fundamental Plane by passive evolution alone. Since they are less likely to have undergone a recent merger there is less likely to be a supply of cold gas for star formation and for accretion onto the black hole, resulting in LEGs with little evidence of recent star formation. In addition, the lower density of the IGM does not provide as much material for the radio jets to work on as in the case of those objects in denser environments, leading to the lower radio luminosities observed. In certain cases, however, a radio galaxy located in an environment with a modest global overdensity may have its radio jet aligned with an axis of particularly high local density, giving rise to objects with a high radio luminosity without a correspondingly high global overdensity.

---

In this picture, therefore, the radio properties of a  $z \sim 0.5$  radio galaxy are principally determined by the environment, which also plays a key role in determining the evolution of the host galaxy. Also, whilst the emission line properties of the AGNs are driven by the nature of the material accreted onto the black hole, this is also greatly influenced by the environment, leading to the overlap seen in the morphological and spectral properties of radio galaxies. However, if this picture is correct, it remains unclear as to how the environments of the FRI and FR II type objects evolve into their local counterparts, where FRIs inhabit moderately rich clusters whilst FR IIs are found in isolation or in small groups (Longair & Seldner 1979; Prestage & Peacock 1988, 1989; Hill & Lilly 1991), although there is substantial overlap between the populations.

Finally, my findings provide some evidence in support of the AGN-driven feedback included in the current models of galaxy evolution and formation. The link between star formation history and spectral classification is consistent with the suggestion of two separate modes of accretion onto the central black hole of an AGN, as included in various models (e.g. Croton et al. 2006; Sijacki et al. 2007). However, the evolution of the radio galaxy hosts themselves appears to be satisfactorily explained by processes which do not include feedback, and thus AGN-driven feedback does not appear to be a dominant factor in the evolution of radio galaxy hosts since  $z \sim 0.5$ .

## 7.4 Future Work

A valuable extension of this work would be to obtain spectra for the remainder of the ZP5 sample. This would enable the results concerning the Fundamental Plane, in particular the position of the FRI type objects with respect to the  $z \sim 0$  and  $z \sim 0.5$  planes, to be placed on a sounder footing. In a similar vein, further investigations into the environments of  $z \sim 0.5$  FRIs would allow a more definite conclusion regarding the possible differences

---

between the cluster densities of FRIs and FRIIs.

Further work beyond this would be to acquire spectroscopic and imaging data of the hosts and environments of complete samples of radio galaxies over the entire  $z = 0$  to  $z = 1$  redshift range. This would enable us to trace the evolution of the hosts and environments of powerful radio galaxies between  $z = 1$  and  $z = 0$  as a function of radio luminosity, velocity dispersion and bulge luminosity, as well as investigating differences in this evolution as a function of spectral or morphological type. At  $z < 0.5$  this data could be obtained in a straightforward manner using similar techniques and telescopes to those described in this thesis, thus enabling us to investigate the current gap in redshift between my work and that of Bettoni et al. (2001) with respect to the Fundamental Plane, and between my work and that of McLure & Dunlop (2001a) with respect to the environments.

Extending this work to higher ( $z = 0.5$  to  $z = 1$ ) redshifts would require deeper radio samples. Such samples could be constructed from a deep survey over a relatively wide area, such as the VIDEO survey.<sup>1</sup> Bulge luminosities and effective radii could be measured using the near-infrared data from VIDEO, which could also be used to investigate the cluster environments. Dedicated spectroscopic follow-up with 8-metre class telescopes would be required to determine the velocity dispersions of galaxies in these samples. The star formation histories at these higher redshifts could be investigated in the far-infrared using Herschel (e.g. Hardcastle et al. 2010).

Further into the future, it will be possible to investigate the Fundamental Plane of quasar host galaxies using integral field unit (IFU) technology on forthcoming instruments. For example, using the HARMONI IFU on the European Extremely Large Telescope (E-ELT) together with adaptive-optics-corrected observations it will be possible to determine the velocity dispersion of these galaxies out to  $z \sim 2$  using the redshifted CaII triplet or Mg*b* complex. This data can also be used to create reconstructed, nuclear-

---

<sup>1</sup><http://www.star.herts.ac.uk/~mjarvis/video/>

---

subtracted 2D images of the quasar host galaxies, from which the effective radii and surface brightnesses can be measured. Combining these with the velocity dispersions, we will be able to study the evolution of the Fundamental Plane of quasar hosts from  $z \sim 2$  to the present day, and see whether similar trends are present as found for radio galaxies (as we would expect from unified models). Such an investigation is already possible at lower redshifts ( $z \lesssim 0.3$ ) using the SINFONI IFU on the Very Large Telescope (VLT).

---



# Bibliography

Akiyama M., Ueda Y., Ohta K., 2002, *ApJ*, 567, 42

Alexander D. M., Smail I., Bauer F. E., Chapman S. C., Blain A. W., Brandt W. N., Ivison R. J., 2005, *Nature*, 434, 738

Alexander D. M., Swinbank A. M., Smail I., McDermid R., Nesvadba N. P. H., 2010, *MNRAS*, 402, 2211

Allen S. W., Dunn R. J. H., Fabian A. C., Taylor G. B., Reynolds C. S., 2006, *MNRAS*, 372, 21

Almaini O., Boyle B. J., Griffiths R. E., Shanks T., Stewart G. C., Georgantopoulos I., 1995, *MNRAS*, 277, L31

Antonucci R. R. J., Miller J. S., 1985, *ApJ*, 297, 621

Aretxaga I., Terlevich E., Terlevich R. J., Cotter G., Díaz Á. I., 2001, *MNRAS*, 325, 636

Babić A., Miller L., Jarvis M. J., Turner T. J., Alexander D. M., Croom S. M., 2007, *A&A*, 474, 755

Bahcall J. N., Kirhakos S., Saxe D. H., Schneider D. P., 1997, *ApJ*, 479, 642

Baldi R. D., Capetti A., 2008, *A&A*, 489, 989

Balogh M. L., Morris S. L., Yee H. K. C., Carlberg R. G., Ellingson E., 1999, *ApJ*, 527, 54

Barthel P. D., 1989, *ApJ*, 336, 606

Barthel P. D., Arnaud K. A., 1996, *MNRAS*, 283, L45

Battye R. A., Browne I. W. A., 2009, *MNRAS*, 399, 1888

- Begelman M. C., Cioffi D. F., 1989, *ApJ*, 345, L21
- Benson A. J., Bower R. G., Frenk C. S., Lacey C. G., Baugh C. M., Cole S., 2003, *ApJ*, 599, 38
- Best P. N., 2000, *MNRAS*, 317, 720
- Best P. N., Longair M. S., Röttgering H. J. A., 1998, *MNRAS*, 295, 549
- Best P. N., Lehnert M. D., Miley G. K., Röttgering H. J. A., 2003, *MNRAS*, 343, 1
- Best P. N., von der Linden A., Kauffmann G., Heckman T. M., Kaiser C. R., 2007, *MNRAS*, 379, 894
- Bettoni D., Falomo R., Fasano G., Govoni F., Salvo M., Scarpa R., 2001, *A&A*, 380, 471
- Binggeli B., 1982, *A&A*, 107, 338
- Birkinshaw M., Davies R. L., 1985, *ApJ*, 291, 32
- Bondi H., 1952, *MNRAS*, 112, 195
- Bonning E. W., Cheng L., Shields G. A., Salviander S., Gebhardt K., 2007, *ApJ*, 659, 211
- Boyle B. J., Terlevich R. J., 1998, *MNRAS*, 293, L49
- Brooks A. M., Governato F., Quinn T., Brook C. B., Wadsley J., 2009, *ApJ*, 694, 396
- Brandt W. N., Alexander D. M., 2010, *Proceedings of the National Academy of Science*, 107, 7184
- Bryant J. J., Broderick J. W., Johnston H. M., Hunstead R. W., Gaensler B. M., De Breuck C., 2009, *MNRAS*, 394, 2197
- Burns J. O., White R. A., Hough D. H., 1981, *AJ*, 86, 1
- Calzetti D., Armus L., Bohlin R. C., Kinney A. L., Koornneef J., Storchi-Bergmann T., 2000, *ApJ*, 533, 682
- Canalizo G., Stockton A., 2000, *AJ*, 120, 1750
-

- Canalizo G., Stockton A., 2001, *ApJ*, 555, 719
- Chiaberge M., Capetti A., Celotti A., 2002, *A&A*, 394, 791
- Chiaberge M., Capetti A., Macchetto F. D., 2005, *ApJ*, 625, 716
- Cimatti A., di Serego-Alighieri S., Fosbury R. A. E., Salvati M., Taylor D., 1993, *MNRAS*, 264, 421
- Ciotti L., Ostriker J. P., 2007, *ApJ*, 665, 1038
- Clarke D. A., Bridle A. H., Burns J. O., Perley R. A., Norman M. L., 1992, *ApJ*, 385, 173
- Clavel J., Wamsteker W., Glass I. S., 1989, *ApJ*, 337, 236
- Clewley L., Jarvis M. J., 2004, *MNRAS*, 352, 909
- Cole S., Lacey C. G., Baugh C. M., Frenk C. S., 2000, *MNRAS*, 319, 168
- Cole S., Norberg P., Baugh C. M. et al., 2001, *MNRAS*, 326, 255
- Cowie L. L., Songaila A., Hu E. M., Cohen J. G., 1996, *AJ*, 112, 839
- Crenshaw D. M., Kraemer S. B., George I. M., 2003, *ARA&A*, 41, 117
- Croom S. M., Richards G. T., Shanks T. et al., 2009, *MNRAS*, 399, 1755
- Croton D. J., Farrar G. R., Norberg P. et al., 2005, *MNRAS*, 356, 1155
- Croton D. J., Springel V., White S. D. M. et al., 2006, *MNRAS*, 365, 11
- Daly R. A., 1990, *ApJ*, 355, 416
- Davis M., Meiksin A., Strauss M. A., da Costa L. N., Yahil A., 1988, *ApJ*, 333, L9
- De Breuck C., van Breugel W., Stanford S. A., Röttgering, H., Miley G., Stern D., 2002, *AJ*, 123, 637
- Dekel A., Birnboim Y., 2006, *MNRAS*, 368, 2
- Dekel A., Birnboim Y., Engel G. et al., 2009, *Nature*, 457, 451
-

- de Kool M., Arav N., Becker R. H., Gregg M. D., White R. L., Laurent-Muehleisen S. A., Price T., Korista K. T., 2001, *ApJ*, 548, 609
- Deng X.-F., He J.-Z., Jiang P., 2007, *ApJ*, 671, L101
- di Serego Alighieri S., Vernet J., Cimatti A. et al., 2005, *A&A*, 442, 125
- Djorgovski S., Davis M., 1987, *ApJ*, 313, 59
- Donoso E., O'Mill A., Lambas D. G., 2006, *MNRAS*, 369, 479
- Dressler A., Lynden-Bell D., Burstein D., Davies R., Faber S. M., Terlevich R., Wegner G., 1987, *ApJ*, 313, 42
- Dunlop J. S., Peacock J. A., 1990, *MNRAS*, 247, 19
- Dunlop J. S., McLure R. J., Kukula M. J., Baum S. A., O'Dea C. P., Hughes D. H., 2003, *MNRAS*, 340, 1095
- Eales S., Rawlings S., Law-Green D., Cotter G., Lacy M., 1997, *MNRAS*, 291, 593
- Edge D. O., Shakeshaft J. R., McAdam W. B., Baldwin J. E., Archer S., 1959, *MNRAS*, 68, 37
- Elbaz D., Jahnke K., Pantin E., Le Borgne D., Letawe G., 2009, *A&A*, 507, 1359
- Ellingson E., Yee H. K. C., Green R. F., 1991, *ApJ*, 371, 49
- Elvis M., Wilkes B. J., McDowell J. C. et al., 1994, *ApJS*, 95, 1
- Emonts B., Morganti R., Oosterloo T., van Gorkom J., 2008, in Beswick R. J., Diamond P. J., Schilizzi R., eds, *Proc. Sci., The Modern Radio Universe: From Planets to Dark Energy*
- Faber S. M., Jackson R. E., 1976, *ApJ*, 204, 668
- Faber S. M., Dressler A., Davies R. L., Burstein D., Lynden-Bell D., Terlevich R., Wegner G., 1987, in Faber S.M., ed., *Nearly Normal Galaxies: From the Planck Time to the Present*. Springer, New York, p. 175
- Falder J. T., Stevens J. A., Jarvis M. J. et al., 2010, *MNRAS*, 405, 347
- Fanaroff B. L., Riley J. M., 1974, *MNRAS*, 167, 31P
-

- Farrah D., Geach J., Fox M., Serjeant S., Oliver S., Verma A., Kaviani A., Rowan-Robinson M., 2004, MNRAS, 349, 518
- Ferrarese L., Merritt D., 2000, ApJ, 539, L9
- Filippenko A. V., 1996, *The Physics of Liners in View of Recent Observations*, 103, 17
- Fine S., Jarvis M. J., Mauch T., 2011, MNRAS, 412, 213
- Franceschini A., Vercellone S., Fabian A. C., 1998, MNRAS, 297, 817
- Fritz A., Ziegler B. L., 2009, AN, 330, 1010
- Fritz A., Jørgensen I., Schiavon R. P., Chiboucas K., 2009, AN, 330, 931
- Fritz A., Jørgensen I., Schiavon R. P., 2010, in Bruzual G., Charlot S., eds, *Proc. IAU Symp. 262, Stellar populations – planning for the next decade*. Cambridge University Press, Cambridge, 335
- Fuller T. M., West M. J., Bridges T. J., 1999, ApJ, 519, 22
- Geach J. E., Simpson C., Rawlings S., Read A. M., Watson M., 2007, MNRAS, 381, 1369
- Gebhardt K., Bender R., Bower G. et al., 2000, ApJ, 539, L13
- Gebhardt K., Faber S. M., Koo D. C. et al., 2003, ApJ, 597, 239
- Goldschmidt P., Kukula M. J., Miller L., Dunlop J. S., 1999, ApJ, 511, 612
- Graham A., Lauer T. R., Colless M., Postman M., 1996, ApJ, 465, 534
- Granato G. L., Danese L., Franceschini A., 1997, ApJ, 486, 147
- Greene J.E., Ho L.C., 2006, ApJ, 641, 117
- Grimes J. A., Rawlings S., Willott C. J., 2004, MNRAS, 349, 503
- Groth E. J., Peebles P. J. E., 1977, ApJ, 217, 385
- Gültekin K., Richstone D. O., Gebhardt K. et al., 2009, ApJ, 698, 198
-

- Hall P. B., Green R. F., 1998, ApJ, 507, 558
- Hamilton A. J. S., 1988, ApJ, 331, L59
- Hansen S. M., McKay T. A., Wechsler R. H., Annis J., Sheldon E. S., Kimball A., 2005, ApJ, 633, 122
- Hardcastle M. J., 2004, A&A, 414, 927
- Hardcastle M. J., Evans D. A., Croston J. H., 2006, MNRAS, 370, 1893
- Hardcastle M. J., Evans D. A., Croston J. H., 2007, MNRAS, 376, 1849
- Hardcastle M. J., Evans D. A., Croston J. H., 2009, MNRAS, 396, 1929
- Hardcastle M. J., Virdee J. S., Jarvis M. J. et al., 2010, MNRAS, 409, 122
- Harvanek M., Ellingson E., Stocke J. T., Rhee G., 2001, AJ, 122, 2874
- Hasinger G., 2004, Nuclear Physics B Proceedings Supplements, 132, 86
- Heckman T. M., 1980, A&A, 87, 152
- Herbert P. D., Jarvis M. J., Willott C. J., McLure R. J., Mitchell E., Rawlings S., Hill G. J., Dunlop J. S. 2010, MNRAS, 406, 1841
- Herbert P. D., Jarvis M. J., Willott C. J., McLure R. J., Mitchell E., Rawlings S., Hill G. J., Dunlop J. S. 2011, MNRAS, 410, 1360
- Hill G. J., Lilly S. J., 1991, ApJ, 367, 1
- Hill G. J., Rawlings S., 2003, NewAR, 47, 373
- Hill G. J., Goodrich R. W., Depoy D. L., 1996, ApJ, 462, 163
- Hine R. G., Longair M. S., 1979, MNRAS, 188, 111
- Ho L. C., 1996, The Physics of Liners in View of Recent Observations, 103, 103
- Ho L. C., 2002, ApJ, 564, 120
- Ho L. C., 2009, ApJ, 699, 626
-

- Ho L. C., Filippenko A. V., Sargent W. L. W., 1997, *ApJ*, 487, 568
- Holt J., Tadhunter C. N., González Delgado R. M., Inskip K. J., Rodriguez J., Emonts B. H. C., Morganti R., Wills K. A., 2007, *MNRAS*, 381, 611
- Hopkins A. M., Beacom J. F., 2006, *ApJ*, 651, 142
- Hopkins P. F., Bundy K., Hernquist L., Wuyts S., Cox T. J., 2010, *MNRAS*, 401, 1099
- Huang J.-S., Glazebrook K., Cowie L. L., Tinney C., 2003, *ApJ*, 584, 203
- Hutchings J. B., Crampton D., Morris S. L., Durand D., Steinbring E., 1999, *AJ*, 117, 1109
- Ilbert O., Tresse L., Zucca E. et al., 2005, *A&A*, 439, 863
- Irwin M., Lewis J., 2001, *NewAR*, 45, 105
- Jackson N., Rawlings S., 1997, *MNRAS* 286, 241
- Jarvis M. J., McLure R. J., 2002, *MNRAS*, 336, L38
- Jarvis M. J., McLure R. J., 2006, *MNRAS*, 369, 182
- Jarvis M. J., Rawlings S., Eales S., Blundell K. M., Bunker A. J., Croft S., McLure R. J., Willott C. J., 2001a, *MNRAS*, 326, 1585
- Jarvis M. J., Rawlings S., Willott C. J., Blundell K. M., Eales S., Lacy, M., 2001b, *MNRAS*, 327, 907
- Jørgensen I., Franx M., Kjørgaard P., 1995, *MNRAS*, 276, 1341
- Jørgensen I., Franx M., Kjørgaard P., 1996, *MNRAS*, 280, 167
- Jørgensen I., Chiboucas K., Flint K., Bergmann M., Barr J., Davies R., 2006, *ApJ*, 639, L9
- Jørgensen I., Chiboucas K., Flint K., Bergmann M., Barr J., Davies R., 2007, *ApJ*, 654, L179
- Kauffmann G., Heckman T. M., White S. D. M. et al., 2003, *MNRAS*, 341, 33
- Kauffmann G., Heckman T. M., Best P. N., 2008, *MNRAS*, 384, 953
-

- Kelson D. D., Illingworth G. D., van Dokkum P. G., Franx M., 2000, *ApJ*, 531, 184
- Kereš D., Katz N., Weinberg D. H., Davé R., 2005, *MNRAS*, 363, 2
- Kereš D., Katz N., Fardal M., Davé R., Weinberg D. H., 2009, *MNRAS*, 395, 160
- Khachikian E. Y., Weedman D. W., 1974, *ApJ*, 192, 581
- Khochfar S., Silk J., 2006, *ApJ*, 648, L21
- Kocevski D. D., Faber S. M., Mozena M. et al., 2011, arXiv:1109.2588
- Kochanek C. S., Pahre M. A., Falco E. E. et al., 2001, *ApJ*, 560, 566
- Kormendy J. G., 1977, *ApJ*, 217, 406
- Kukula M. J., Dunlop J. S., McLure R. J., Miller L., Percival W. J., Baum S. A., O’Dea C. P., 2001, *MNRAS*, 326, 1533
- Lacy M., Rawlings S., Hill G. J., Bunker A. J., Ridgway S. E., Stern D., 1999, *MNRAS*, 308, 1096
- Lacy M., Laurent-Muehleisen S. A., Ridgway S. E., Becker R. H., White R. L., 2001, *ApJ*, 551, L17
- Lacy M., Storrie-Lombardi L. J., Sajina A., et al., 2004, *ApJS*, 154, 166
- Laing R. A., Bridle A. H., 1987, *MNRAS*, 228, 557
- Laing R. A., Riley J. M., Longair M. S., 1983, *MNRAS*, 204, 151
- Laing R. A., Jenkins C. R., Wall J. V., Unger S. W., 1994, in Bicknell G. V., Dopita M. A., Quinn P.J., eds, *ASP Conf. Ser. Vol. 54, The Physics of Active Galaxies*. Astron. Soc. Pac., San Francisco, p. 201
- Laor A., 2000, *ApJ*, 543, L111
- Lawrence A., 1991, *MNRAS*, 252, 586
- Lawrence A., Elvis M., 2010, *ApJ*, 714, 561
- Ledlow M. J., Owen F. N., 1995, *AJ*, 110, 1959
-

- Lilly S. J., 1989, ApJ, 340, 77
- Lilly S. J., Longair M. S., 1982, MNRAS, 199, 1053
- Lilly S. J., Longair M. S., 1984, MNRAS, 211, 833
- Lilly S. J., Longair M. S., Allington-Smith J. R., 1985, MNRAS, 215, 37
- Longair M. S., 1966, MNRAS, 133, 421
- Longair M. S., Seldner M., 1979, MNRAS, 189, 433
- Luo B., Brandt W. N., Xue Y. Q. et al., 2011, arXiv:1107.3148
- Mackay C. D., 1971, MNRAS, 151, 421
- Macklin J. T., 1982, MNRAS, 199, 1119
- Magorrian J., Tremaine S., Richstone D. et al., 1998, AJ, 115, 2285
- Mancini C., Daddi E., Renzini A. et al., 2010, MNRAS, 401, 933
- Martínez-Sansigre A., Rawlings S., Lacy M., Fadda D., Marleau F. R., Simpson C., Willott C. J., Jarvis M. J., 2005, Nature, 436, 666
- Martínez-Sansigre A., Rawlings S., Lacy M. et al., 2006, MNRAS, 370, 1479
- Matthews T. A., Sandage A. R., 1963, ApJ, 138, 30
- McAlpine K., Jarvis, M. J., 2011, MNRAS, 413, 105
- McLure R. J., Dunlop J. S., 2001a, MNRAS, 321, 515
- McLure R. J., Dunlop J. S., 2001b, MNRAS, 327, 199
- McLure R. J., Dunlop J. S., 2002, MNRAS, 331, 795
- McLure R. J., Jarvis M. J., 2004, MNRAS, 353, L45
- McLure R. J., Kukula M. J., Dunlop J. S., Baum S. A., O’Dea C. P., Hughes D. H., 1999, MNRAS, 308, 377
-

- McLure R. J., Willott C. J., Jarvis M. J., Rawlings S., Hill G. J., Mitchell E., Dunlop J. S., Wold M., 2004, MNRAS, 351, 347
- Merritt D., Ferrarese L., 2001, ApJ, 547, 140
- Mitchell E. K., 2005, PhD thesis, University of Oxford
- Mullaney J. R., Pannella M., Daddi E. et al., 2011, arXiv:1106.4284
- Nelson C. H., Whittle M., 1996, ApJ, 465, 96
- Niederste-Ostholt M., Strauss M. A., Dong F., Koester B. P., McKay T. A., 2010, MNRAS, 405, 2023
- Norman C., Hasinger G., Giacconi R. et al., 2002, ApJ, 571, 218
- Ocvirk P., Pichon C., Teyssier R., 2008, MNRAS, 390, 1326
- Ohta K., Yamada T., Nakanishi K. et al., 1996, ApJ, 458, L57
- Owen F. N., Laing R. A., 1989, MNRAS, 238, 357
- Pahre M. A., Djorgovski S. G., de Carvalho R. R., 1998, AJ, 116, 1591
- Polletta M. d. C., Wilkes B. J., Siana B., et al., 2006, ApJ, 642, 673
- Prestage R. M., Peacock J. A., 1988, MNRAS, 230, 131
- Prestage R. M., Peacock J. A., 1989, MNRAS, 236, 959
- Rafferty D. A., Brandt W. N., Alexander D. M., Xue Y. Q., Bauer F. E., Lehmer B. D., Luo B., Papovich C., 2011, arXiv:1108.3229
- Rawlings S., Jarvis M. J., 2004, MNRAS, 355, L9
- Rawlings S., Saunders R., 1991, Nature, 349, 138
- Rawlings S., Eales S., Lacy M., 2001, MNRAS, 322, 523
- Rees M. J., 1989, MNRAS, 239, 1P
- Reeves J. N., O'Brien P. T., Ward M. J., 2003, ApJ, 593, L65
-

- Richards G. T., Strauss M. A., Fan X. et al., 2006, *AJ*, 131, 2766
- Rigby E. E., Best P. N., Brookes M. H., Peacock J. A., Dunlop J. S., Röttgering H. J. A., Wall J. V., Ker L., 2011, *MNRAS*, 416, 1900
- Robertson B., Cox T. J., Hernquist L., Franx M., Hopkins P. F., Martini P., Springel V., 2006a, *ApJ*, 641, 21
- Robertson B., Hernquist L., Cox T. J., Di Matteo T., Hopkins P. F., Martini P., Springel V., 2006b, *ApJ*, 641, 90
- Roche N., Eales S. A., 2000, *MNRAS*, 317, 120
- Sadler E. M., Cannon R. D., Mauch T. et al., 2007, *MNRAS*, 381, 211
- Sanders D. B., Mirabel I. F., 1996, *ARA&A*, 34, 749
- Sanders D. B., Soifer B. T., Elias J. H., Madore B. F., Matthews K., Neugebauer G., Scoville N. Z., 1988a, *ApJ*, 325, 74
- Sanders D. B., Soifer B. T., Scoville N. Z., 1988b, *Science*, 239, 625
- Sastry G. N., 1968, *PASP*, 80, 252
- Schechter P., 1976, *ApJ*, 203, 297
- Scheuer P. A. G., 1987, in Zensus J. A., Pearson T. J., eds, *Superluminal Radio Sources*, Cambridge University Press, Cambridge, p. 104
- Schmidt M., 1963, *Nature*, 197, 1040
- Schmidt M., Green R. F., 1983, *ApJ*, 269, 352
- Seyfert C. K., 1943, *ApJ*, 97, 28
- Shaver P. A., Wall J. V., Kellermann K. I., Jackson C. A., Hawkins, M. R. S., 1996, *Nature*, 384, 439
- Sijacki D., Springel V., Di Matteo T., Hernquist L., 2007, *MNRAS*, 380, 877
- Silk J., Rees M. J., 1998, *A&A*, 331, L1
- Simpson C., 2005, *MNRAS*, 360, 565
-

- Simpson C., Rawlings S., 2000, MNRAS, 317, 1023
- Simpson C., Rawlings S., Lacy M., 1999, MNRAS, 306, 828
- Smith E. P., Heckman T. M., Illingworth G. D., 1990, ApJ, 356, 399
- Smith P. S., Balonek T. J., Elston R., Heckert P. A., 1987, ApJS, 64, 459
- Steffen A. T., Barger A. J., Cowie L. L., Mushotzky R. F., Yang Y., 2003, ApJ, 596, L23
- Stern D., Eisenhardt P., Gorjian V., et al., 2005, ApJ, 631, 163
- Surace J. A., Sanders D. B., 1999, ApJ, 512, 162
- Surace J. A., Sanders D. B., Vacca W. D., Veilleux S., Mazzarella J. M., 1998, ApJ, 492, 116
- Surace J. A., Sanders D. B., Evans A. S., 2000, ApJ, 529, 170
- Tadhunter C. N., Scarrott S. M., Draper P., Rolph C., 1992, MNRAS, 256, 53P
- Tadhunter C. N., Dickson R. C., Shaw M. A., 1996, MNRAS, 281, 591
- Tadhunter C., Dickson R., Morganti R., Robinson T. G., Wills K., Villar-Martin M., Hughes M., 2002, MNRAS, 330, 977
- Tasse C., Röttgering H. J. A., Best P. N., Cohen A. S., Pierre M., Wilman R., 2007, A&A, 471, 1105
- Torlina L., De Propris R., West M. J., 2007, ApJ, 660, L97
- Tran H. D., Cohen M. H., Ogle P. M., Goodrich R. W., di Serego Alighieri S., 1998, ApJ, 500, 660
- Treister E., Krolik J. H., Dullemond C., 2008, ApJ, 679, 140
- Treu T., Stiavelli M., Bertin G., Casertano S., Møller P., 2001, MNRAS, 326, 237
- Treu T., Ellis R. S., Liao T.X. et al., 2005a, ApJ, 633, 174
- Treu T., Ellis R. S., Liao T. X., van Dokkum P. G., 2005b, ApJ, 622, L5
-

- Trevese D., Cirimele G., Flin P., 1992, *AJ*, 104, 935
- Trichas M., Georgakakis A., Rowan-Robinson M., Nandra K., Clements D., Vaccari M., 2009, *MNRAS*, 399, 663
- Vanden Berk D. E., Richards G. T., Bauer A. et al., 2001, *AJ*, 122, 549
- van der Wel A., Franx M., van Dokkum P. G., Rix H.-W., Illingworth G. D., Rosati P., 2005, *ApJ*, 631, 145
- van der Wel A., Holden B. P., Zirm A. W., Franx M., Rettura A., Illingworth G. D., Ford H. C., 2008, *ApJ*, 688, 48
- van der Wel A., Bell E. F., van den Bosch F. C., Gallazzi A., Rix H.-W., 2009, *ApJ*, 698, 1232
- van Dokkum P. G., Franx M., 1996, *MNRAS*, 281, 985
- van Dokkum P. G., Stanford S. A., 2003, *ApJ*, 585, 78
- Vardoulaki E., Rawlings S., Hill G. J. et al., 2010, *MNRAS*, 401, 1709
- Villar-Martín M., Tadhunter C., Humphrey A., Encina R. F., Delgado R. G., Torres M. P., Martínez-Sansigre A., 2011, *MNRAS*, 416, 262
- West M. J., 1994, *MNRAS*, 268, 79
- Whysong D., Antonucci R., 2004, *ApJ*, 602, 116
- Wiita P. J., 2004, *AP&SS*, 293, 235
- Willott C. J., Rawlings S., Blundell K. M., Lacy M., 2000, *MNRAS*, 316, 449
- Willott C. J., Rawlings S., Blundell K. M., Lacy M., Eales S. A., 2001, *MNRAS*, 322, 536
- Willott C. J., Rawlings S., Jarvis M. J., Blundell K. M., 2003, *MNRAS*, 339, 173
- Wold M., Lacy M., Lilje P. B., Serjeant S., 2000, *MNRAS*, 316, 267
- Wold M., Lacy M., Lilje P. B., Serjeant S., 2001, *MNRAS*, 323, 231
- Wold M., Armus L., Neugebauer G., Jarrett T. H., Lehnert M. D., 2003, *AJ*, 126, 1776
-

Wolf M. J., Sheinis A. I., 2008, *AJ*, 136, 1587

Woo J.-H., Urry C. M., 2002, *ApJ*, 579, 530

Woo J., Urry C. M., Lira P., van der Marel R. P., Maza J., 2004, *ApJ*, 617, 903

Worthey G., Ottaviani D. L., 1997, *ApJS*, 111, 377

Yee H. K. C., Green R. F., 1987, *ApJ*, 319, 28

Young S., Axon D. J., Robinson A., Capetti A., 2009, *ApJL*, 698, L121

Zakamska N. L., Strauss M. A., Krolik J. H. et al., 2003, *AJ*, 126, 2125

Zandivarez A., Martínez H. J., 2011, *MNRAS*, 415, 2553

Zucca E., Ilbert O., Bardelli S. et al., 2006, *A&A*, 455, 879

---

# Appendix A

## WHT Spectra

In Figures A.1 to A.4 I show the final galaxy and signal-to-noise spectra for each of the objects observed using the William Herschel Telescope (WHT). Respectively Figures A.1, A.2, A.3 and A.4 show the spectra as extracted over the different apertures discussed in Section 2.2.6 and Section 2.3: full width at three-quarters intensity (FWTQI), full width at half maximum (FWHM), full width at zero intensity, and the aperture corresponding to the effective radius ( $r_e$ ). The observations and data reduction for these data are described in Section 2.3.

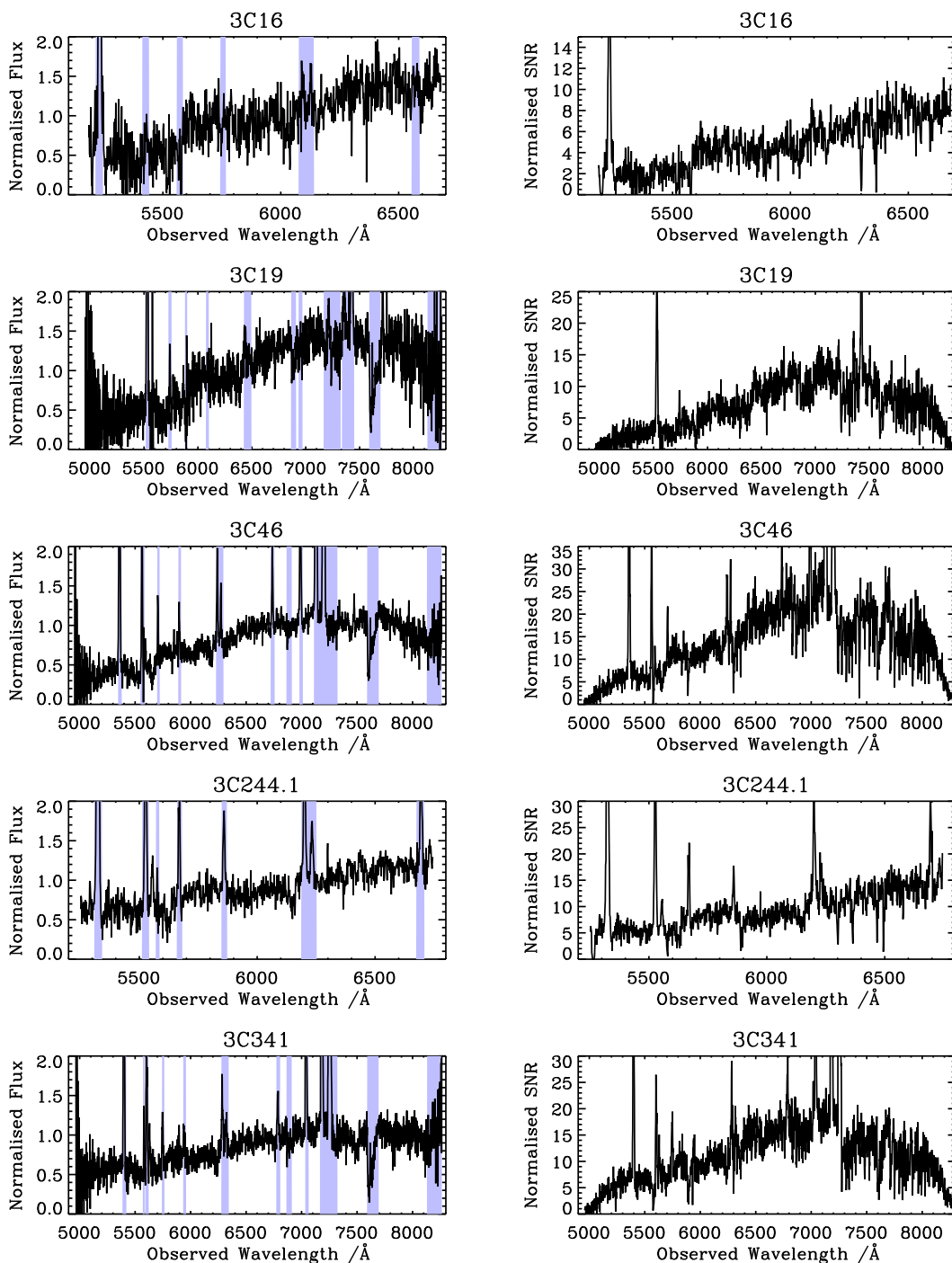


Figure A.1: The final galaxy (left panels) and signal-to-noise (right panels) spectra of objects observed using the William Herschel Telescope (WHT) for the full width at three-quarters intensity (FWTQI) aperture (see Section 2.3). Each galaxy spectrum is normalised to a mean flux of one, and the corresponding noise spectrum is divided by the same normalisation factor before conversion to a signal-to-noise spectrum (Section 2.2.7). The shaded areas indicate regions which are masked due to the presence of emission or telluric absorption features or chip artefacts, as discussed in Sections 2.2.7 and 2.3.

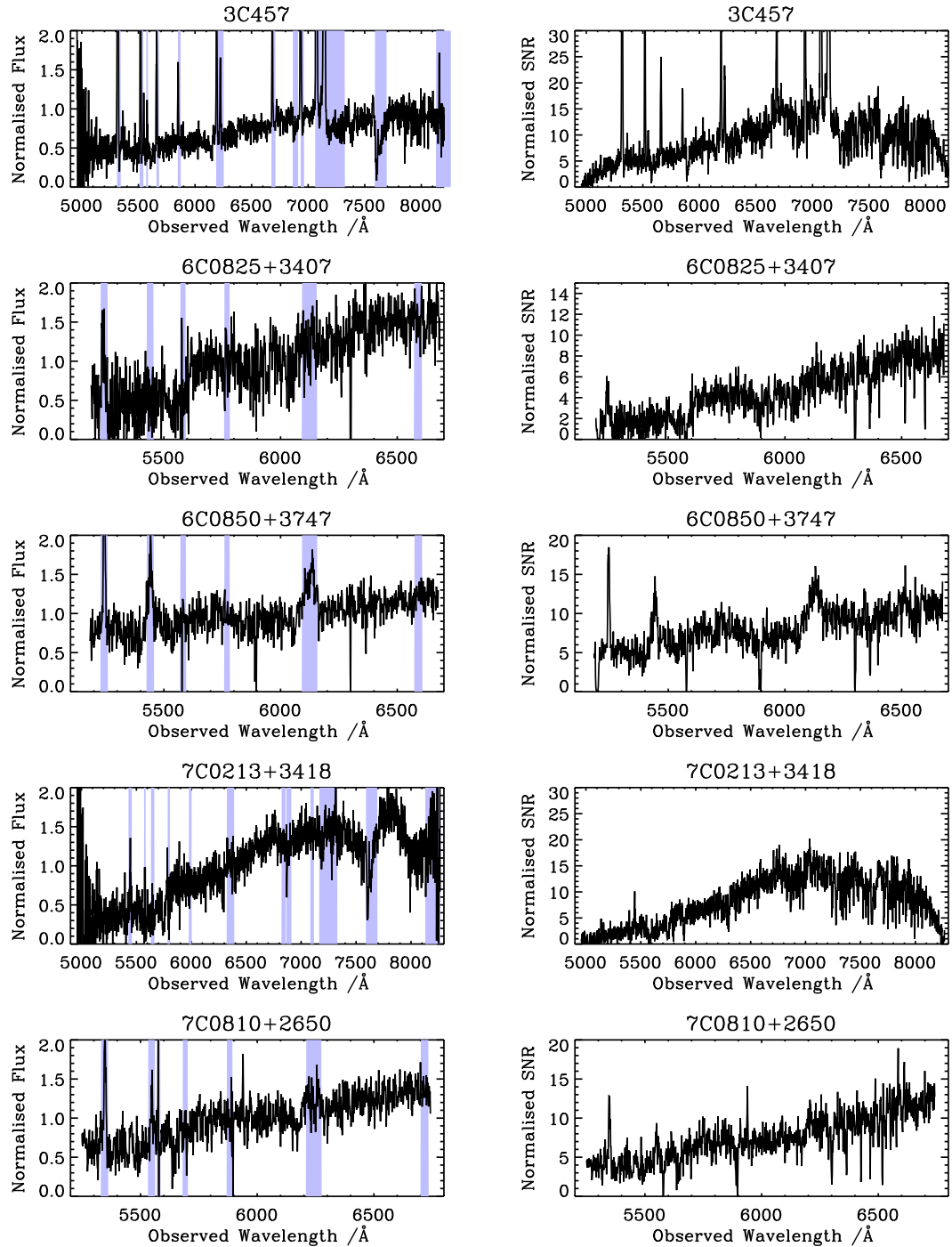


Figure A.1 continued.

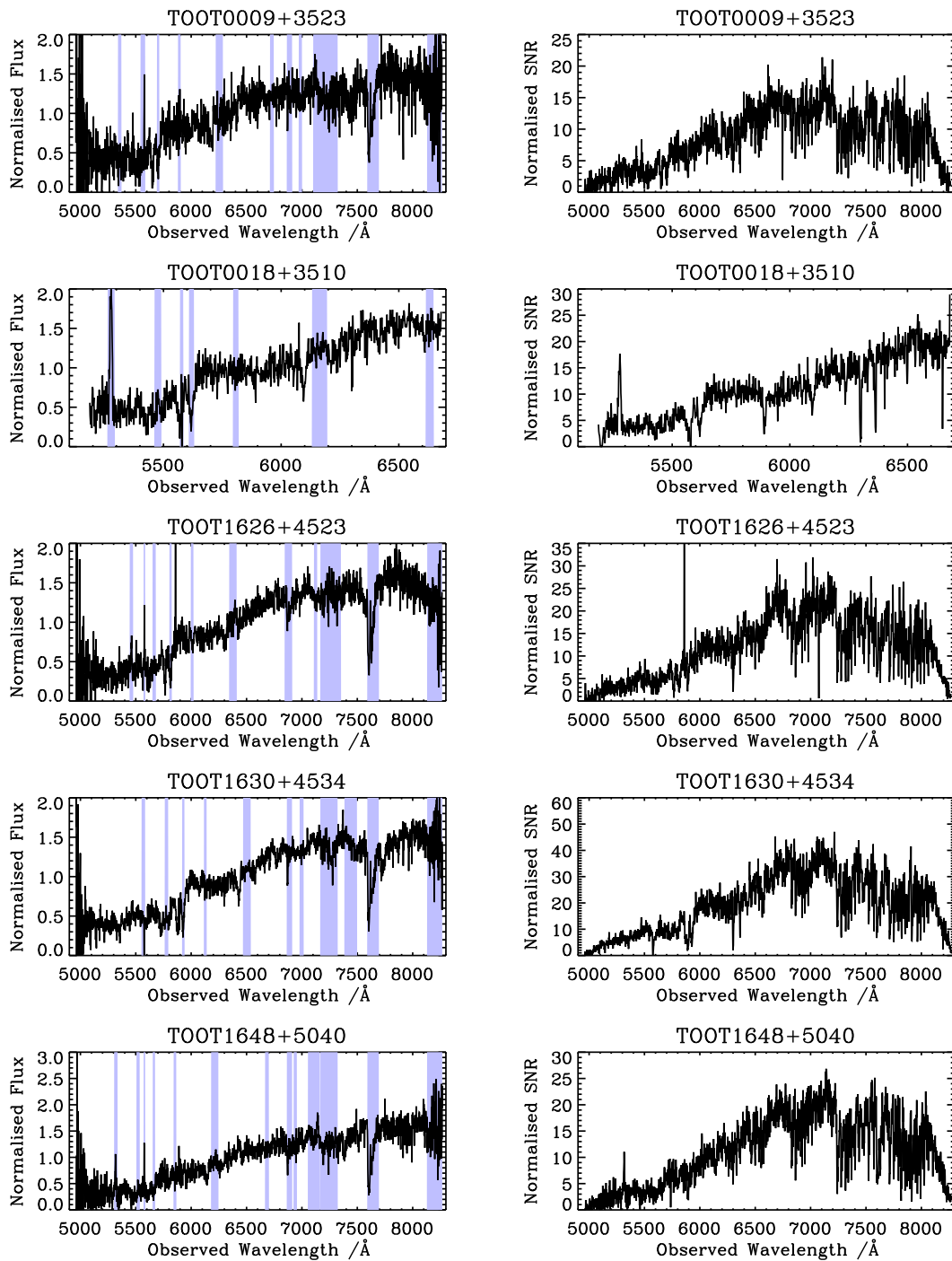


Figure A.1 continued.

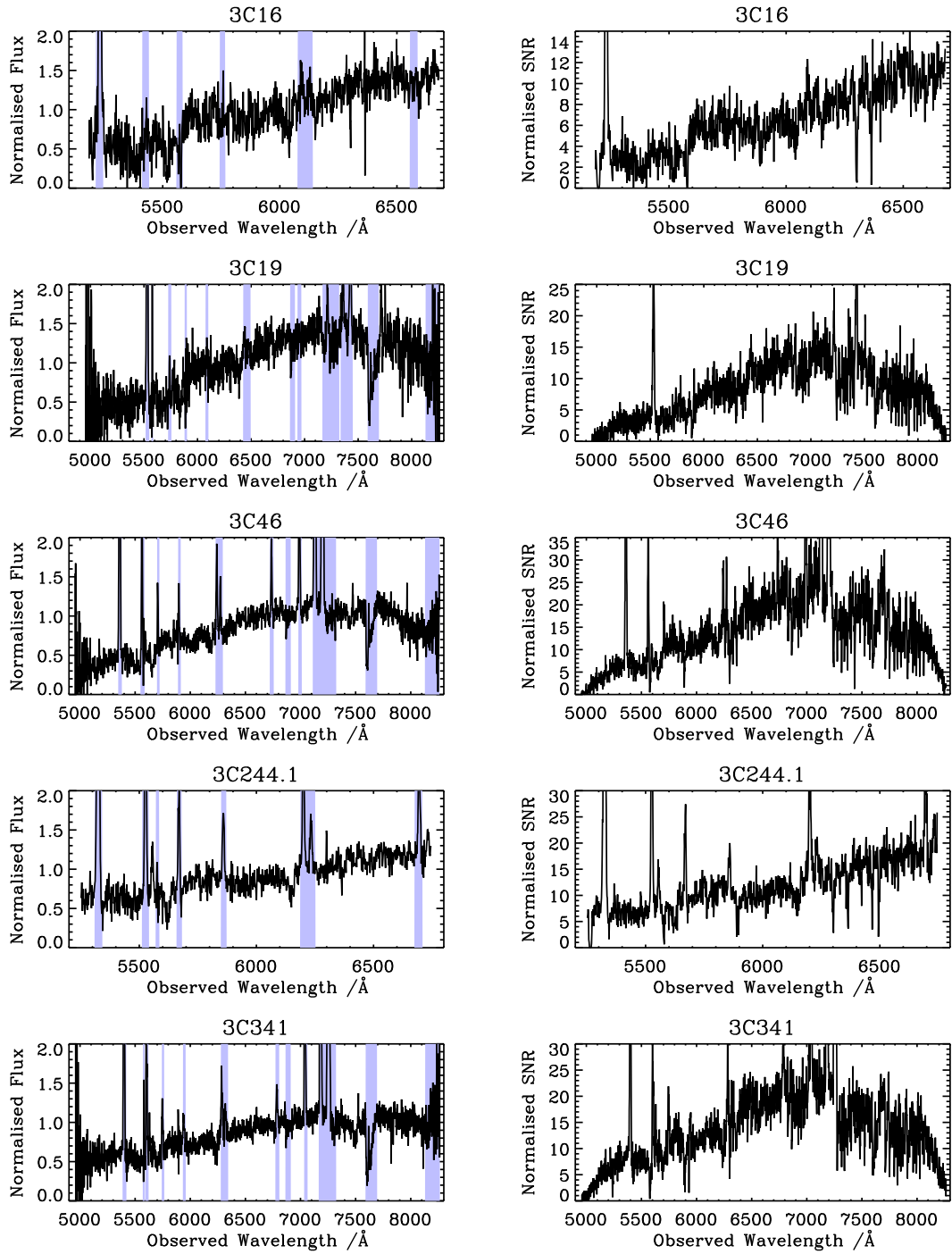


Figure A.2: The final galaxy (left panels) and signal-to-noise (right panels) spectra of objects observed using the William Herschel Telescope (WHT) for the full width at half maximum (FWHM) aperture (see Section 2.3). Each galaxy spectrum is normalised to a mean flux of one, and the corresponding noise spectrum is divided by the same normalisation factor before conversion to a signal-to-noise spectrum (Section 2.2.7). The shaded areas indicate regions which are masked due to the presence of emission or telluric absorption features or chip artefacts, as discussed in Sections 2.2.7 and 2.3.

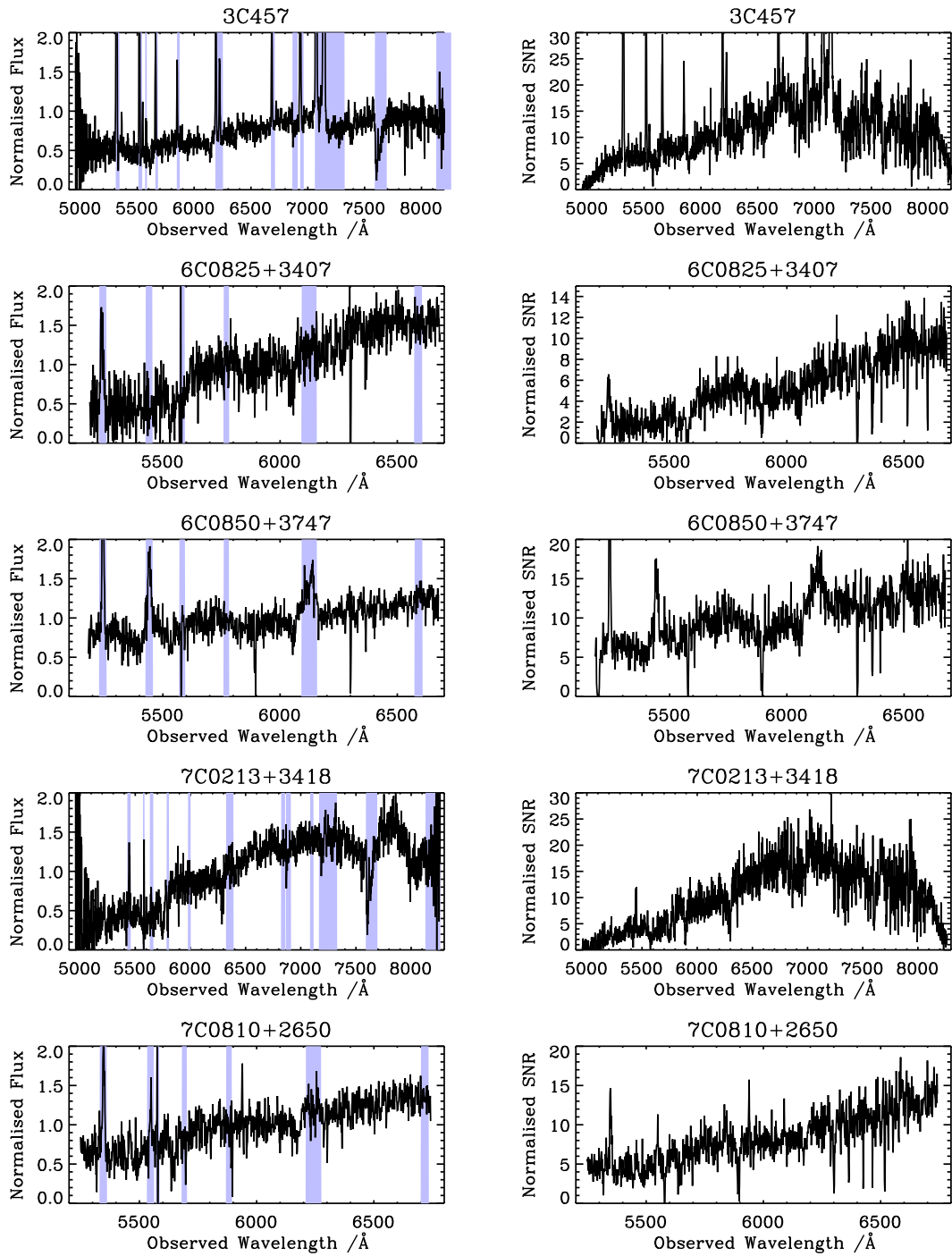


Figure A.2 continued.

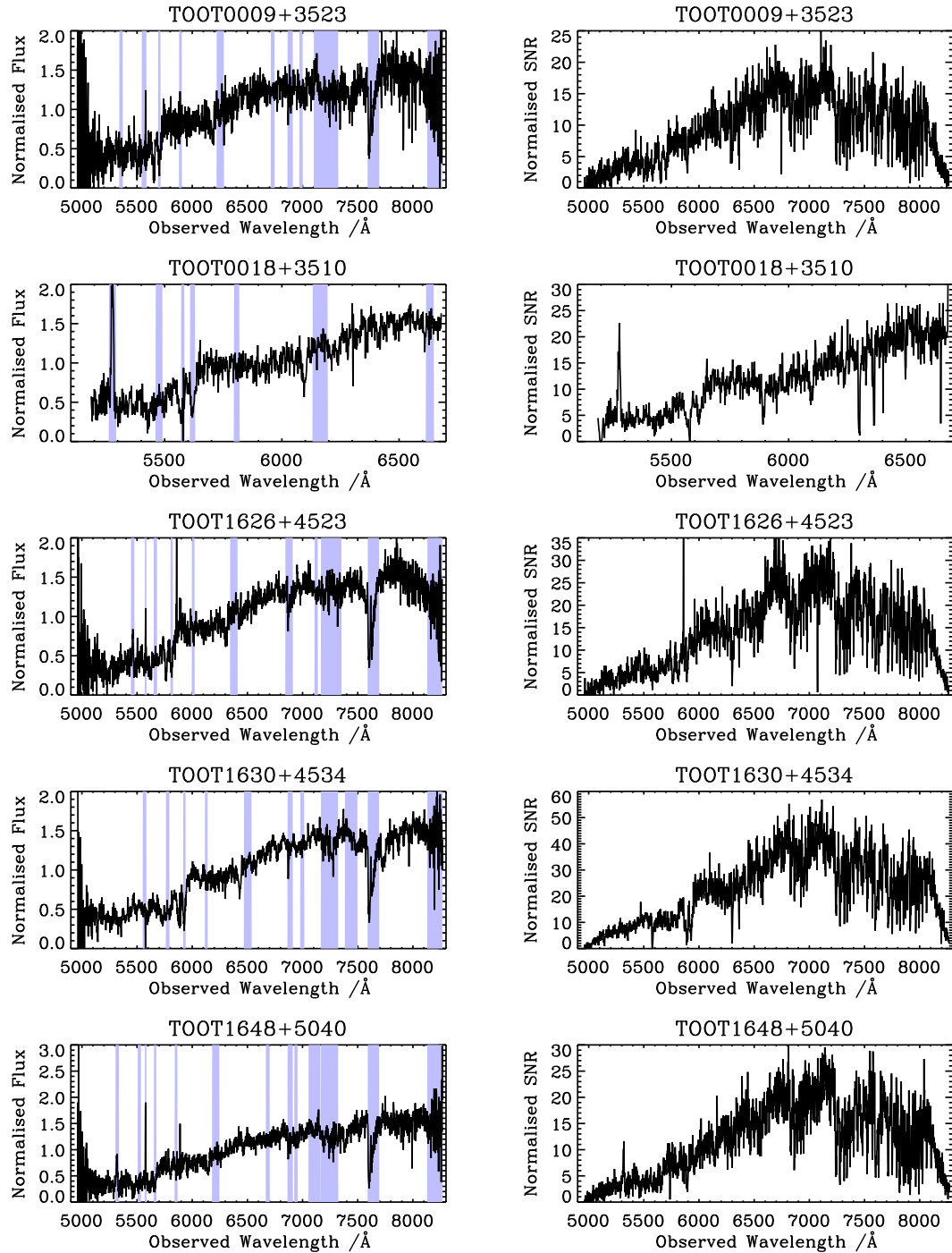


Figure A.2 continued.

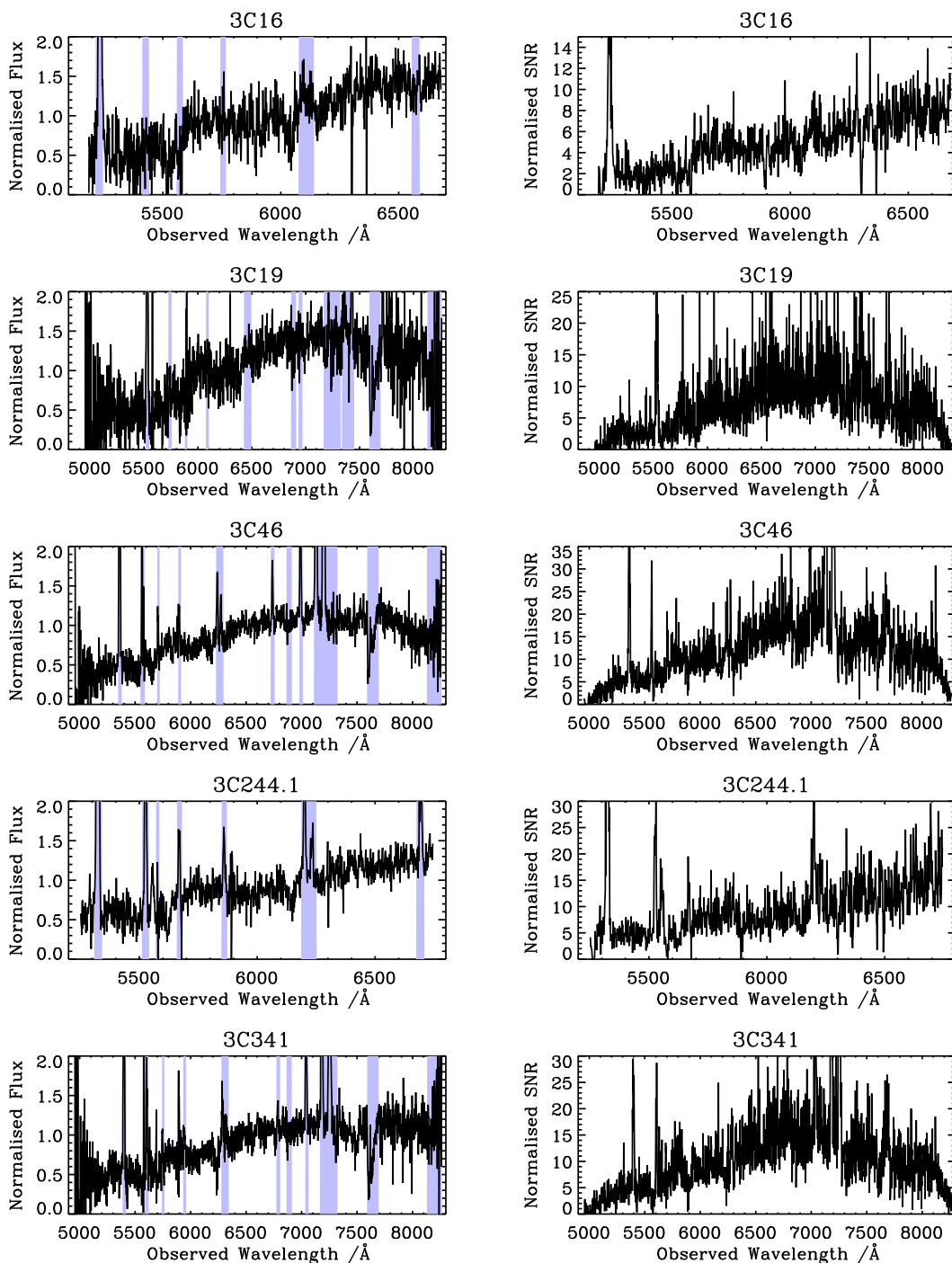


Figure A.3: The final galaxy (left panels) and signal-to-noise (right panels) spectra of objects observed using the William Herschel Telescope (WHT) for the full width at zero intensity (FWZI) aperture (see Section 2.3). Each galaxy spectrum is normalised to a mean flux of one, and the corresponding noise spectrum is divided by the same normalisation factor before conversion to a signal-to-noise spectrum (Section 2.2.7). The shaded areas indicate regions which are masked due to the presence of emission or telluric absorption features or chip artefacts, as discussed in Sections 2.2.7 and 2.3.

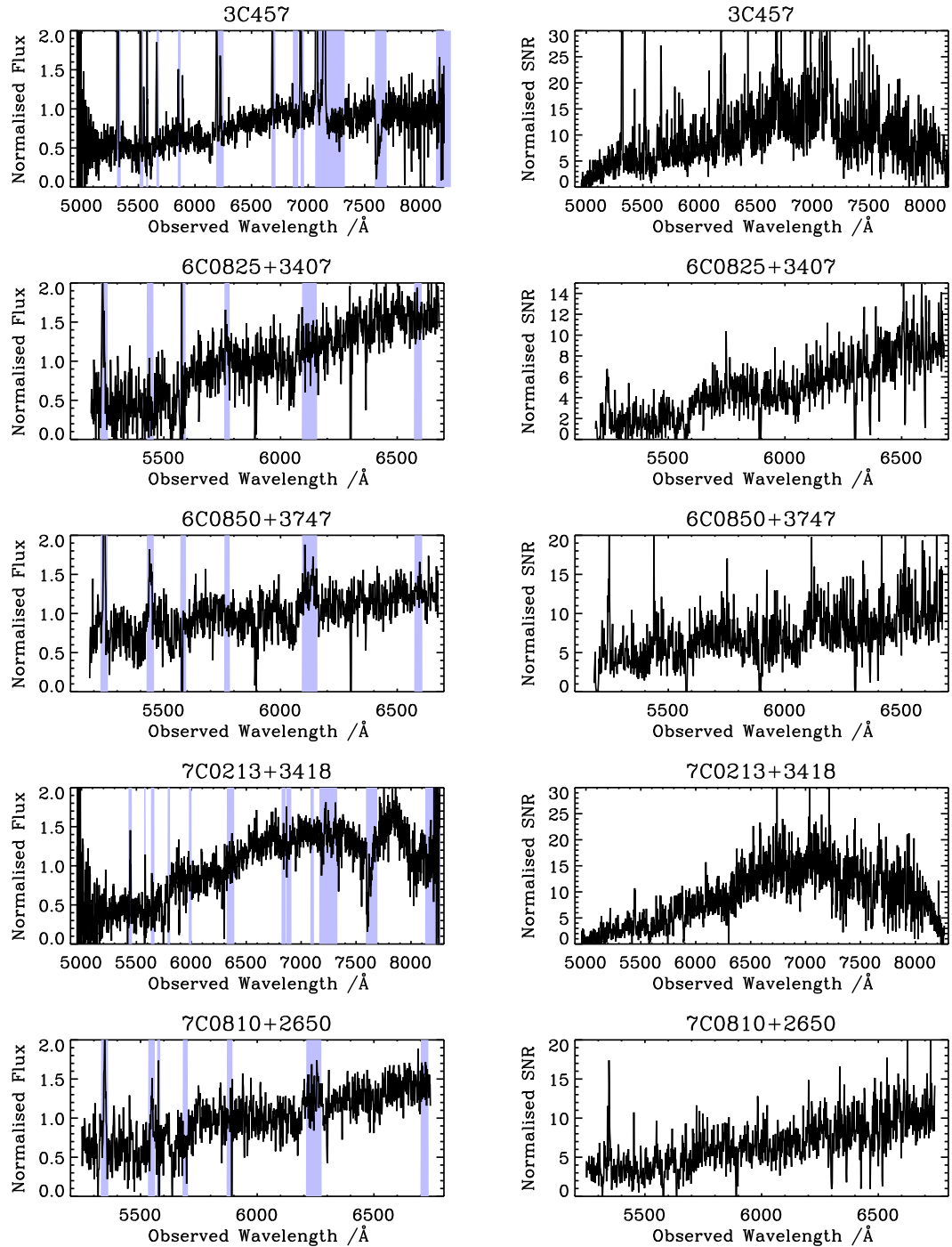


Figure A.3 continued.

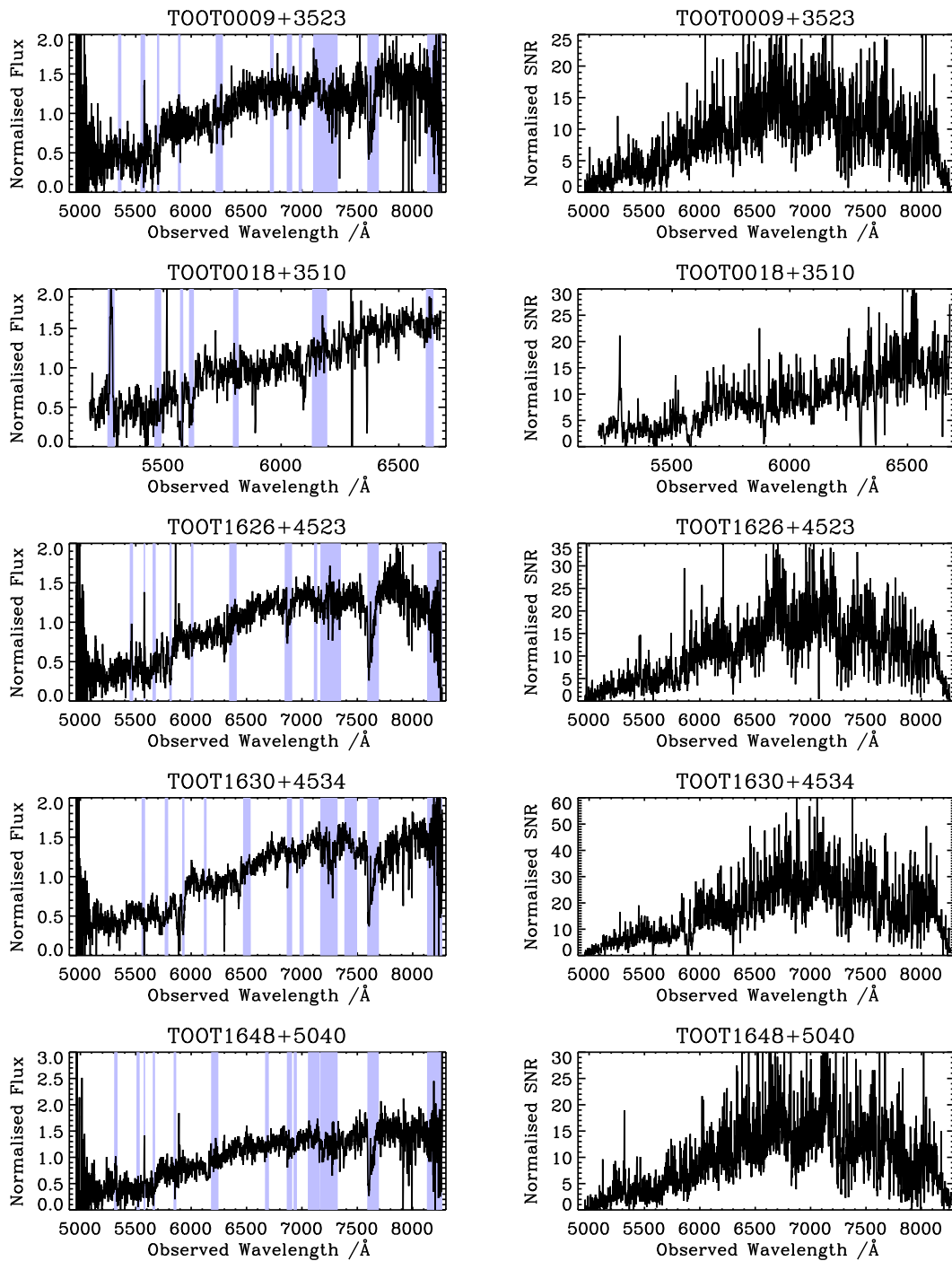


Figure A.3 continued.

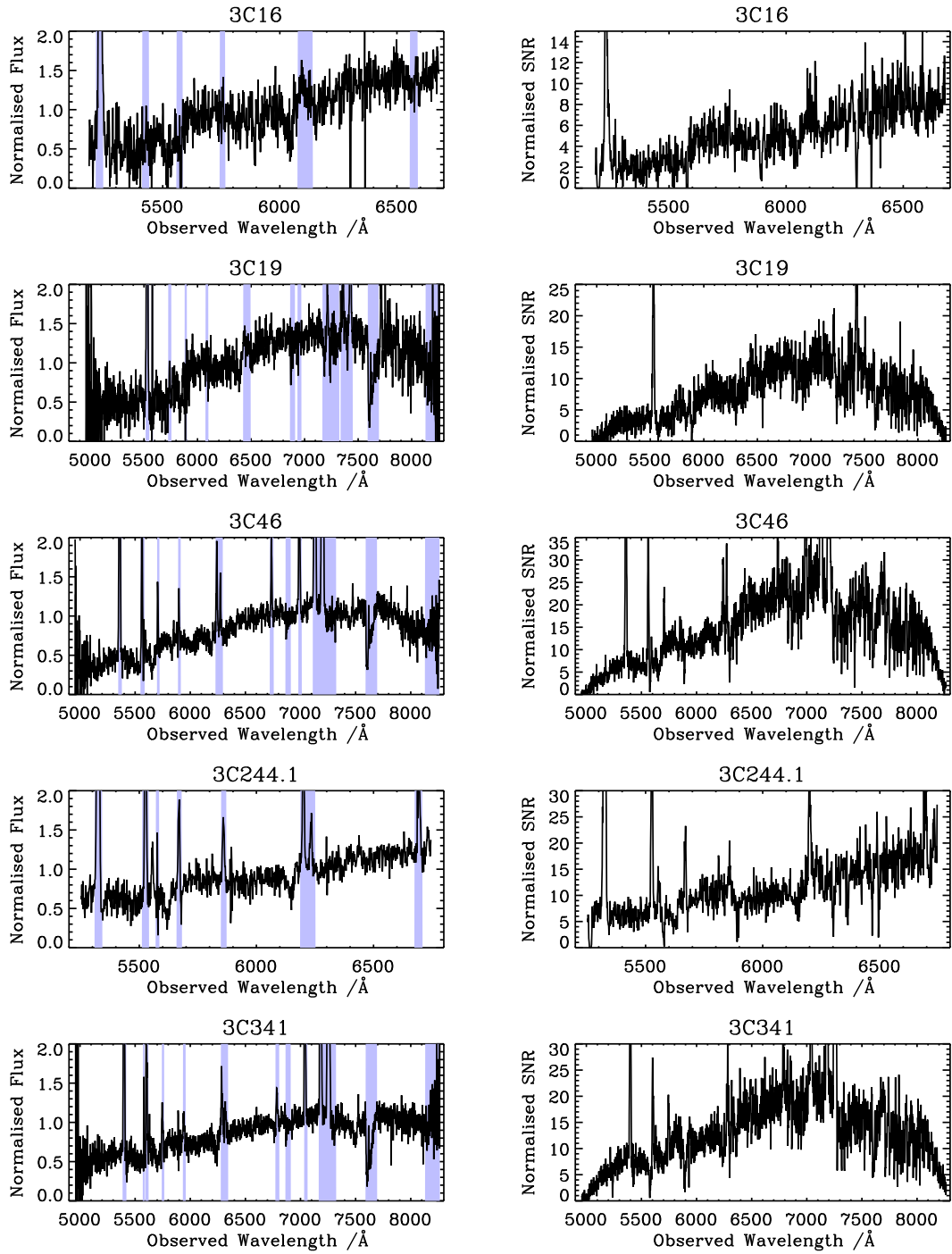


Figure A.4: The final galaxy (left panels) and signal-to-noise (right panels) spectra of objects observed using the William Herschel Telescope (WHT) for the apertures corresponding to the effective radii of the objects (see Section 2.3). Each galaxy spectrum is normalised to a mean flux of one, and the corresponding noise spectrum is divided by the same normalisation factor before conversion to a signal-to-noise spectrum (Section 2.2.7). The shaded areas indicate regions which are masked due to the presence of emission or telluric absorption features or chip artefacts, as discussed in Sections 2.2.7 and 2.3.

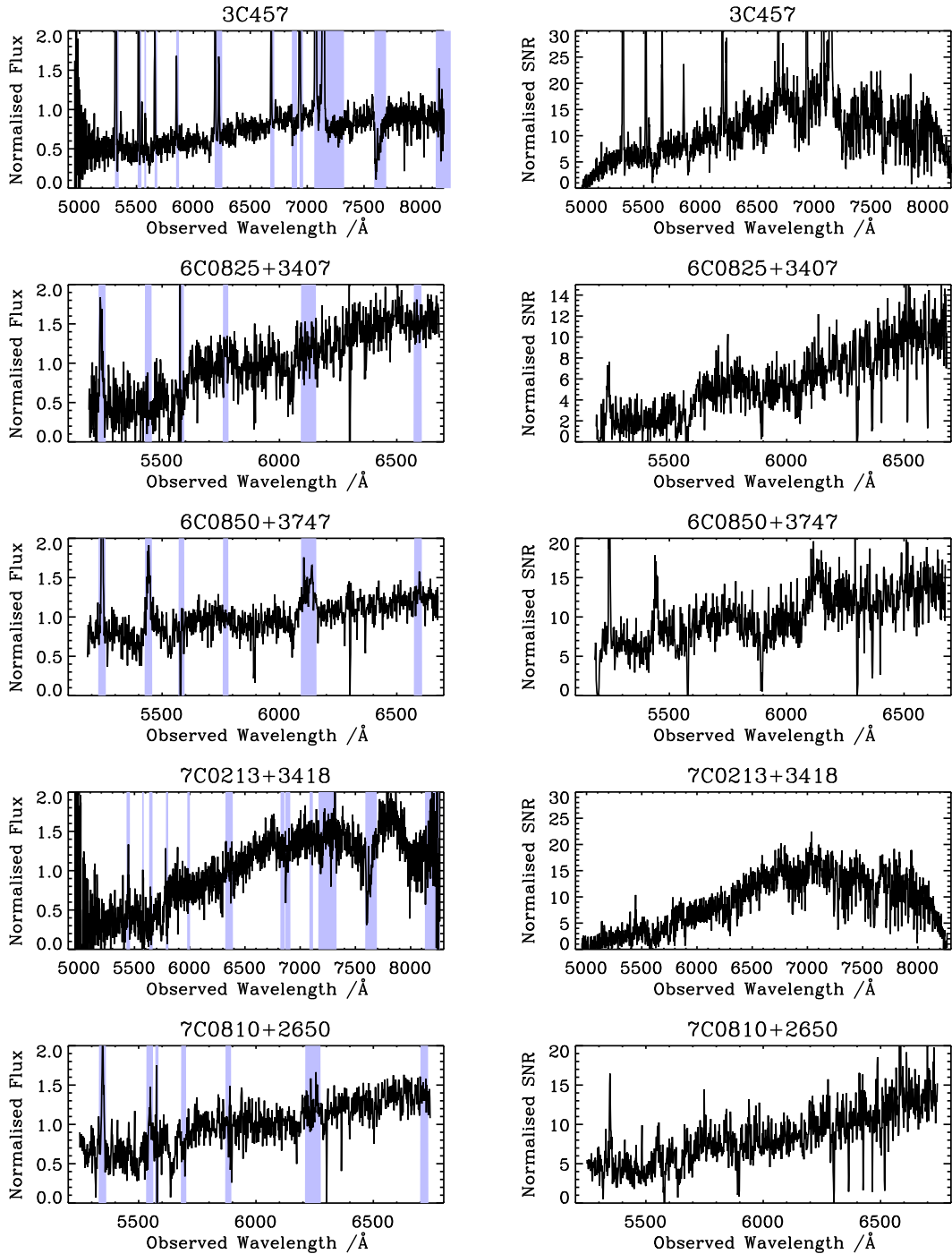


Figure A.4 continued.

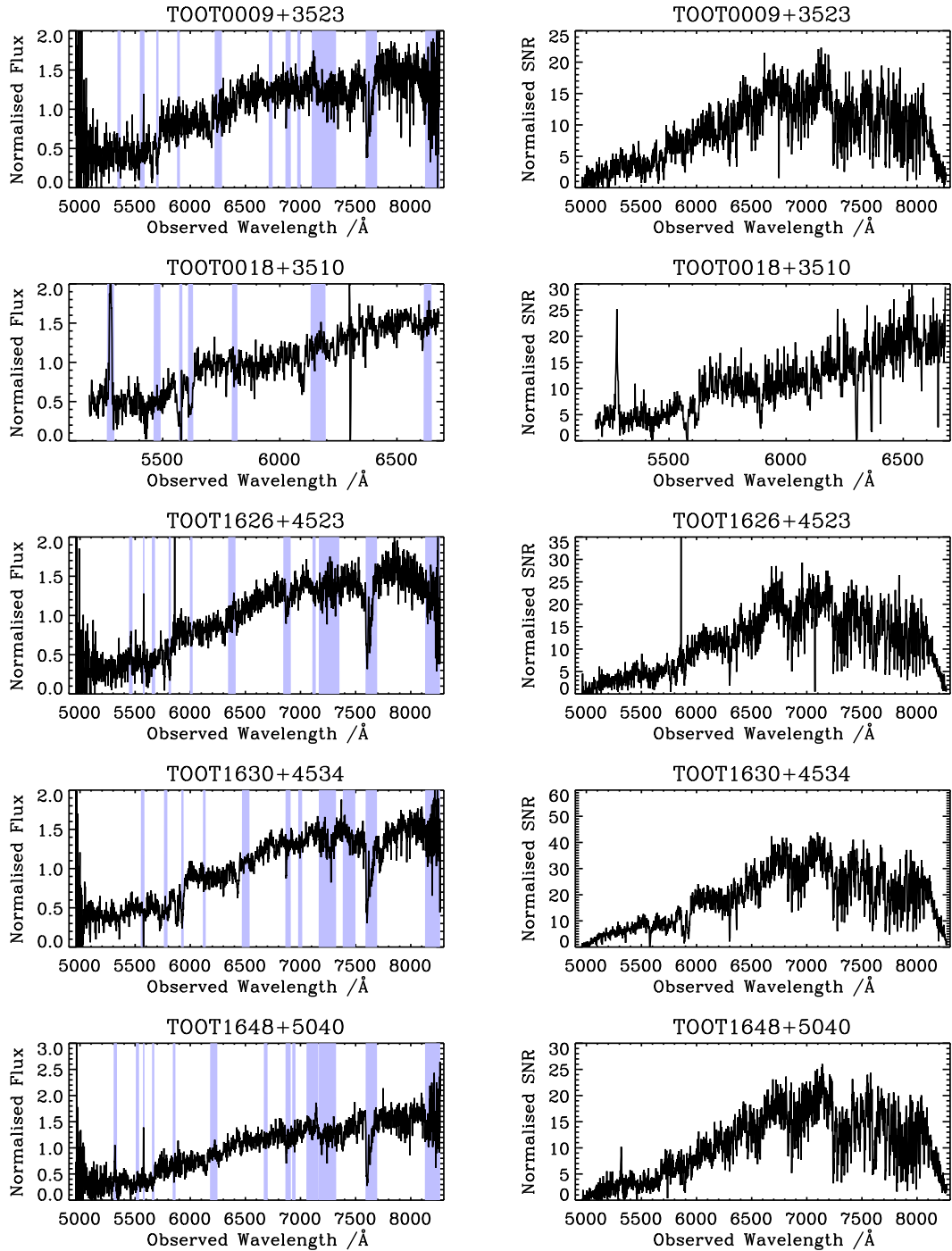


Figure A.4 continued.